Heriot-Watt University

Non-local models of cell-cell interactions in development

Jennifer Martha Bloomfield

April 2011

Submitted for the degree of
Doctor of Philosophy in Mathematics
on completion of research in the
Department of Mathematics,
School of Mathematical and Computer Sciences.

I hereby declare that the work presented in this thesis was carried out by myself at Heriot-Watt University, except where due acknowledgement is made, and not been submitted for any other degree.

Abstract

This thesis explores pattern formation caused by cell-cell interactions in animal tissues during development, whether that patterning be natural or experimental. We produce three non-local integrodifferential equation models that each explore a different driver for pattern formation: cell proliferation, cellular differentiation, and cell migration. We consider how the local environment of a cell – or, more specifically, a cell's neighbours – affects that spatial patterning in each case.

In the first part of this thesis we present mathematical modelling of proliferation-driven patterning in mosaic tissues, where mosaic tissues are those composed of two or more genetically distinct cell types. The results of our modelling suggets that small changes in the type of interaction that cells have with their local environment can lead to very different outcomes for the composition of mosaics. We study two variations of a cellular automaton model based on simple rules for renewal, and then do the same for an integrodifferential equation model. The results of the continuous and cellular automata models are qualitatively the same, and we observe that changes in local environment interaction affect the dynamics for both. Furthermore, we demonstrate that the models reproduce some of the patterns seen in actual mosaic tissues.

In the next model we consider cellular differentiation, which is the process whereby cells form into their final state. We investigate three different versions of the model, with differentiation being cell autonomous, regulated via a community effect, or weakly dependent on the local cellular environment. We consider the spatial patterns that such different modes of differentiation produce, and investigate the formation of both stripes and spots by the model. We show that pattern formation only occurs when differentiation is regulated by a strong community effect.

Finally we present a general model of contact-dependent interactions, and consider the role of both interaction ranges and strengths on patterning formation. Our analysis of the model equations shows that the magnitudes and signs of both of these terms affect whether the system will show instability or stability, as will the initial densities of each cell population. Furthermore, our simulations show that whilst increased ranges lead to increased aggregation widths, and attractive forces lead to stationary aggregations, repulsive forces can cause a range of behaviours, including travelling waves, oscillatory behaviour, and breathing bands.

Acknowledgements

With thanks to my supervisors, Dr. Kevin Painter and Prof. Jonathan Sherratt, who have both been fantastic throughout. Also to my collaborators, Dr. Gabriel Landini and Dr. Alf Gerisch; and to the Engineering and Physical Sciences Research Council who funded this work.

Contents

Chapter 1

Biological Introduction

This thesis explores pattern formation caused by cell-cell interactions in animal tissues, whether that patterning be natural or experimental. To introduce this topic we here provide a brief overview of cell-cell signalling, which mediates interactions between cells, followed by a summary of three drivers for pattern formation: cell proliferation, cellular differentiation, and cell migration, and a brief discussion of cell death. We end this section with an introduction to some of the biological applications to which we later apply our models. Note that for reviews of relevant modelling work and specific biological literature, we refer the reader to the introductory sections of each individual chapter.

1.1 Cell signalling

We consider how the local environment of a cell – or, more specifically, a cell's neighbours – affects the spatial patterning seen in models of cell proliferation, differentiation and migration. For the local environment of a cell to have any impact on that cell at all, the cell in question must be able to receive signals from its local environment. We therefore begin this thesis with a discussion of cell signalling.

Cells communicate in four main ways: through endocrine signalling, where the signalling cell secretes a molecule into the bloodstream so that it diffuses across the body; through paracrine signalling, where a signalling molecule is diffused locally through the extracellular matrix (the medium that surrounds cells); through neuronal signalling, where electrical signals travel along axons to specific target cells; and through contact-dependent signalling, where signalling molecules are passed directly from one cell to another (Alberts et al., 2008). As we are interested in the effect of a cell's local environment on the cell itself, we restrict our interest to the most local and direct form of communication, contact-dependent signalling.

Contact-dependent signalling often involves a membrane bound signalling molecule from a signalling cell attaching to the receptor of a neighbouring target cell, so that the signal passes directly from one to the other without affecting any other cells (Figure 1.1; Alberts et al., 2008). Other mechanisms include gap junctions, which are small channels that directly link the cytoplasms of two cells, allowing signals to pass directly between the cells (Sherer and Mothes, 2008). A cell may receive many signals at once, and the combination of these signals determine cell behaviour (Figure 1.2; Alberts et al., 2008). Note that cells will not necessarily respond to the same signals in the same ways – the response very much depends on the type of cell that receives the signal (Gilberts, 2010). Moreover, a cell that is receiving signals from one set of cells is also likely to independently send out its own signals to other cells (Alberts et al., 2008). This intercellular signalling is essential if a cell is to co-ordinate its decisions with those of its neighbours.

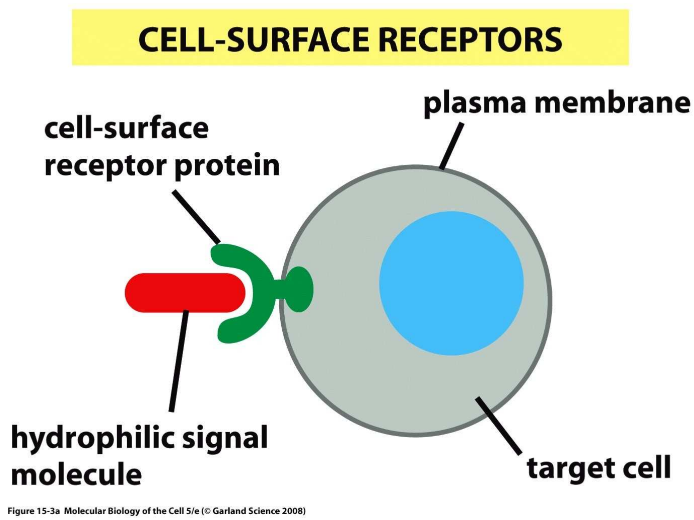

Figure 1.1: The signal molecule (red) binds to the cell-surface receptor (green), which passes on those signals to the inside of the target cell. As the signalling molecule is hydrophilic, and hence will disolve in water, it is unable to travel inside the target cell itself. Note that small hydrophobic signal molecules can simply diffuse through the membrane without the need for a cell surface receptor. Copywright 2008 from Molecular Biology of the Cell by Bruce Alberts et al. Reproduced by permission of Garland Science/Taylor & Francis Books, Inc.

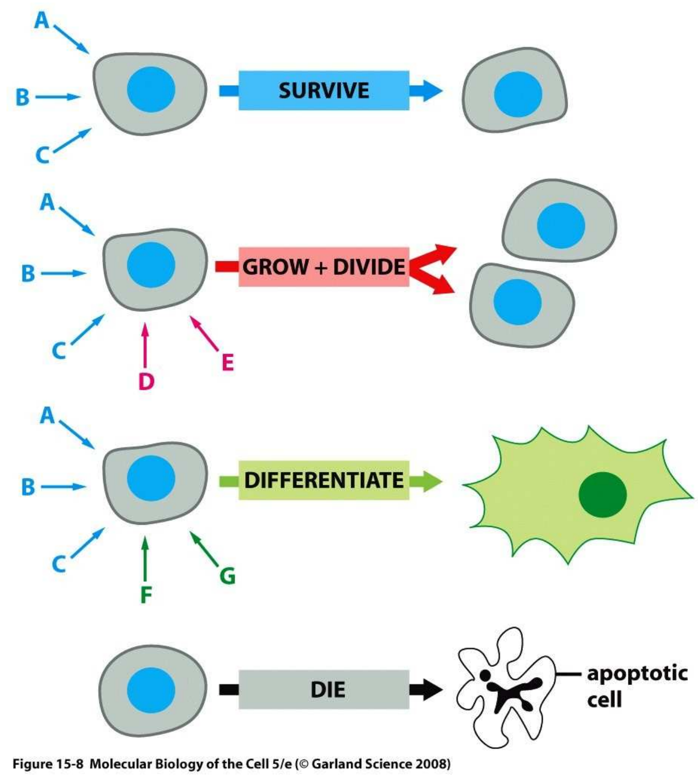

Figure 1.2: A cell receives survival signalling molecules at all times (blue arrows); without these it will die, i.e., become apoptotic (bottom panel). As well as survival signals, a cell may receive other signals such as those to grow and divide (red arrows) or to differentiate (green arrows). Copywright 2008 from Molecular Biology of the Cell by Bruce Alberts et al. Reproduced by permission of Garland Science/Taylor & Francis Books, Inc.

1.1.1 Cell signalling in cellular proliferation, differentiation, migration and apoptosis

In the following chapters we focus on how the signals that a cell receives affects cell proliferation, cellular differentiation, and cell migration, often following the death or apoptosis of a cell. These processes are complex; we provide a brief outline of each of them in turn here.

Proliferation

Proliferation is a fundamental cellular process and has an important role in many situations including embryogenesis and tissue maintenance. In order for a cell to proliferate it must first grow, then replicate and segregate its chromosomes, then divide (Figure 1.3; Alberts et al., 2008); this sequence of events is known as the cell cycle. For this cycle to begin, a cell must receive specific signals (Wolpert, 2004).

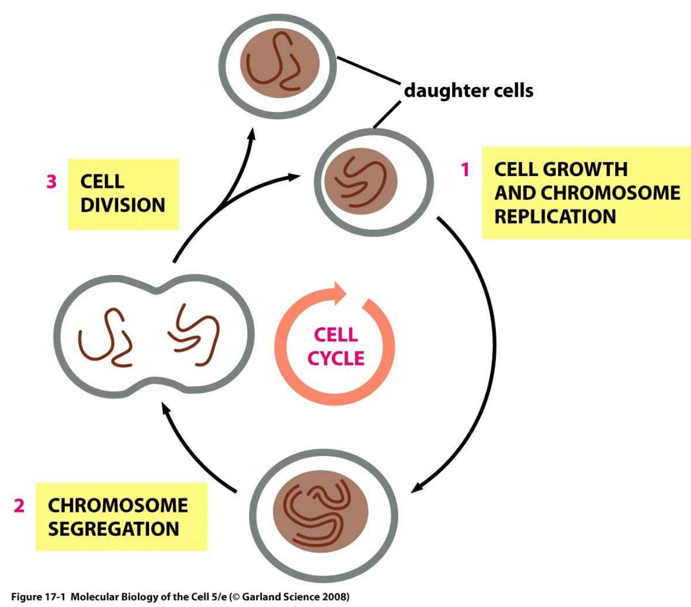

Figure 1.3: Proliferation of cells via the cell cycle. Copywright 2008 from Molecular Biology of the Cell by Bruce Alberts et al. Reproduced by permission of Garland Science/Taylor & Francis Books, Inc.

These extracellular signalling molecules that regulate proliferation can be split into three groups: growth factor signal molecules that promote cell growth, mitogens that stimulate cell division, and survival factors that suppress cell death (Alberts et al., 2008). All of these signals are passed from one neighbouring cell to another via contact-dependent signalling, triggering internal cellular pathways that lead to the required outcome.

Differentiation

Cellular differentiation is a process that occurs in nearly all cells that have not reached their final form. It describes the development of specialised cells, such as bone cells or muscle cells, from the undeveloped precursor cells of which all specialised (i.e., differentiated) cells are made. Differentiation occurs due to external signals that a cell receives; these signals cause it to change the expression of its genes, leading it to become the specialised cell type required (Wolpert, 2004).

There are many ways that differentiation can be induced, some of which are mediated by contact-dependent signalling. For example, it has been widely hypothesised that a cell may sometimes differentiate according to a "community effect", whereby undifferentiated cells that receive signals from other undifferentiated cells in the immediate environment will differentiate together into the same cell type once a threshold level of these signals is reached (Figure 1.4, top panel; Gurdon et al., 2003). This process allows cells in the same spatial area to keep the gene expression necessary for the tissue they create. Homoiogenetic induction is another method of inducing differentiation. Here, cells induced to differentiate first self-induce a signal to send to their neighbours, instructing those cells to do the same (Nieuwkoop, 1997). In this way the signal is passed from cell to cell, until such time has lapsed that any undifferentiated cells no longer respond (Figure 1.4, bottom panel).

Migration

Cell migration occurs throughout the life of many cells, and is particularly important during development and disease. It involves a cell crawling across other cells or the extracellular matrix in the direction in which it has been signalled to move.

In order to migrate in a specific direction, cells must have a front end, or leading edge, that attaches to the surface over which the cell is crawling, whilst the back of the cell contracts to push the cell forwards (Figure 1.5; Alberts et al., 2008). The process of creating these front and back ends is called cell polarisation, a somewhat complicated process that we do not discuss here. However, the direction in which a cell polarises and hence chooses for its leading edge depends on external signals, the upshot of which is that as these signals change, so too does the polarisation of a cell and hence its direction of movement. These signals can be contact-dependent or diffuse, with the two signal types often both in operation in order to direct cells to their required position (Alberts et al., 2008).

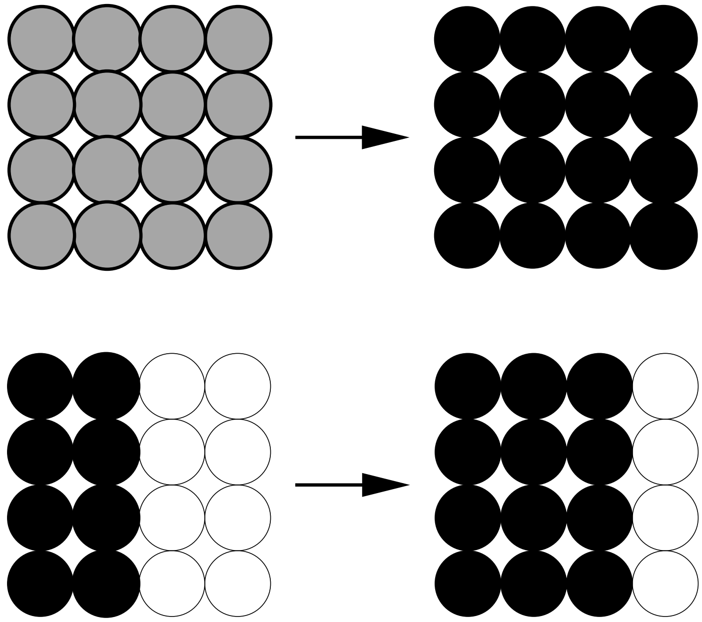

Figure 1.4: Schematic of different neighbour-based differentiation processes. The Community Effect: In the top panel, we see all uncommited cells emitting a signal (grey circles). They all switch to becoming differentiated cells (black) once a threshold signal level has been reached. Homoiogenetic Induction: In the lower panel, we see differentiated cells (black) emitting a signal that leads to uncommited responsive cells (white) becoming differentiated (black) themselves. After Gurdon et al. (2003).

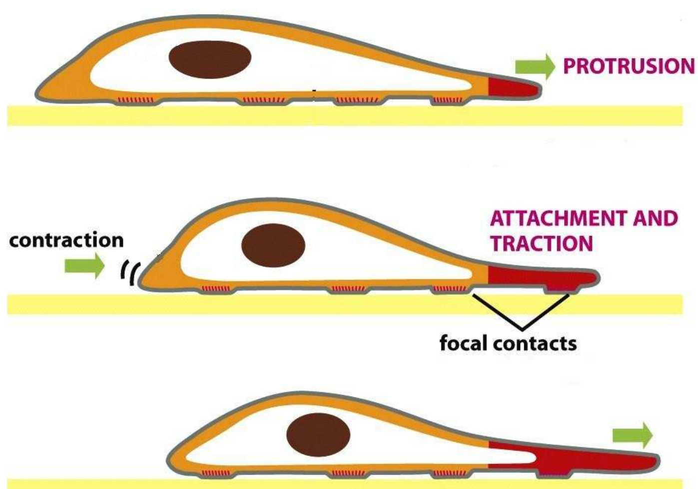

Figure 1.5: Schematic of a crawling cell. The cell protrudes in the direction in which it needs to travel, forming a leading edge (top panel). It then makes new contacts with the surface over which the cell is crawling, and the back end contracts, propelling the body of the cell forward (middle panel). Hence the cell crawls forward (bottom panel). Adapted from Alberts et al. (2008), with permission.

Apoptosis

A cell needs to receive signals in order to survive. Without these survival signals the cell undergoes a form of programmed cell death, usually by apoptosis (Alberts et al., 2008). In a fully formed tissue, this apoptosis is balanced by cell proliferation and differentiation, so that as cells are removed from the tissue by apoptosis, they are directly replaced by new cells. In this way tissue is kept intact, and cells which are abnormal in some way can be removed without damaging the tissue (Alberts et al., 2008). During development on the other hand, apoptosis can be induced to remove superfluous cells (Gilbert, 2010). For example, the cells that make up the tail of a tadpole die during the metamorphosis into a frog, as they are no longer required by the animal. Both of these scenarios are mediated by cell signalling.

1.2 Biological applications

In this thesis we consider various biological applications for our models, and we introduce these applications here.

1.2.1 Mosaic tissues

In the following chapter, we look at mosaic tissues. These are tissues that are composed of two or more genetically distinct cell types. They can occur naturally, or can be created experimentally (Figure 1.6). Both types of mosaics can give useful information about developmental patterns. For example, the experimental mosaics shown in Figure 1.7 highlight differences in the developmental processes of the liver and the adrenal cortex. Whilst the adrenal cortex (panel A) has developed in bands of one population alongside another, the liver (panel B) has developed in a random pattern of both cell types mixed homogeneously across the domain. As regards naturally occuring mosaics, there are certain human diseases involving either genetic mutations or X-chromosome inactivation early in development that can be visible on the skin. The lines that these diseases form are called Blaschko lines (Figure 1.8), and they are thought to demarcate the boundaries of the different cell clones (Happle 2006). Studying the formation of these mosaics provides insight into these diseases.

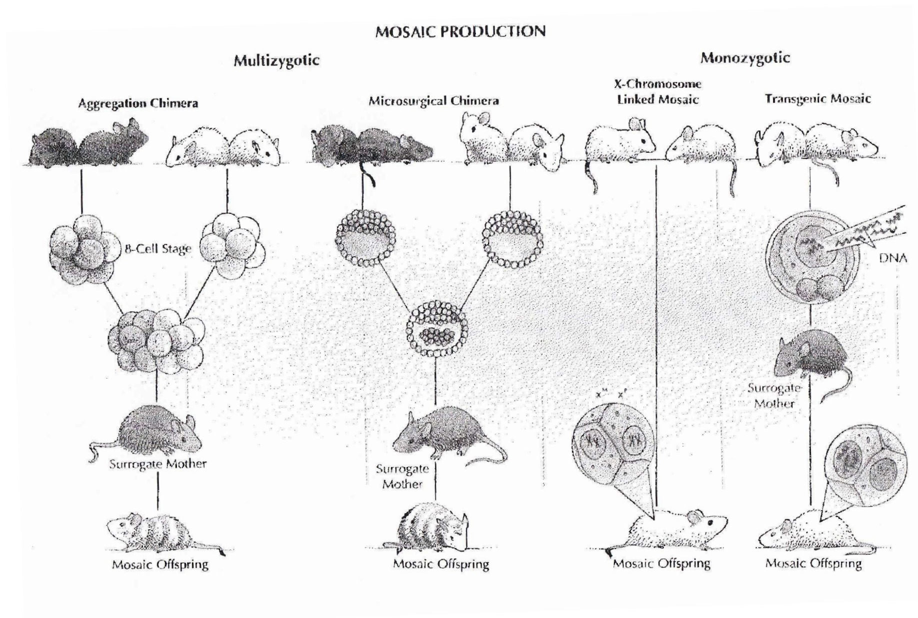

Figure 1.6: Cartoon of mosaic production. The two figures on the left show how chimaeras are produced through manipulation of either early embryos (far left) or of blastocysts (second from left), blatocysts being pre-embryonic cells. By mixing cells from two different sets of parents, and implanting the mixed cells into a surrogate, a chimaera is formed. Mosaics are also be formed naturally in all female mammals due to X-chromosome inactivation which leaves some cells with the maternal X-chromosome active and others with the paternal: without this X-inactivation, female mammal cells would contain too many genes. A similar mosaic can be created artificially by injecting DNA that integrates into the host after the fertilized egg divides, therefore leaving only some of the developing cells with the injected DNA. Drawing Tom Herzberg. Reproduced from Ng & Iannaccone (1992), with permission.

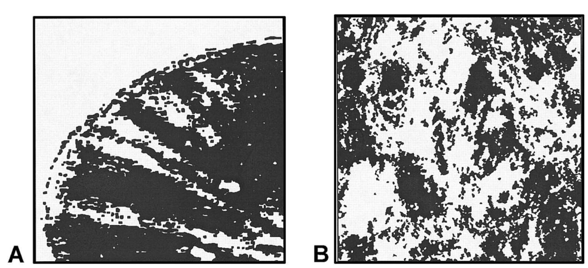

Figure 1.7: Binarized images of the autoradiograms of the adrenal cortex (A) and the liver (B) in a rat chimaera. See Landini & Iannaccone (2000) for metholodgical details. Reproduced from Landini & Iannaccone (2000), with permission.

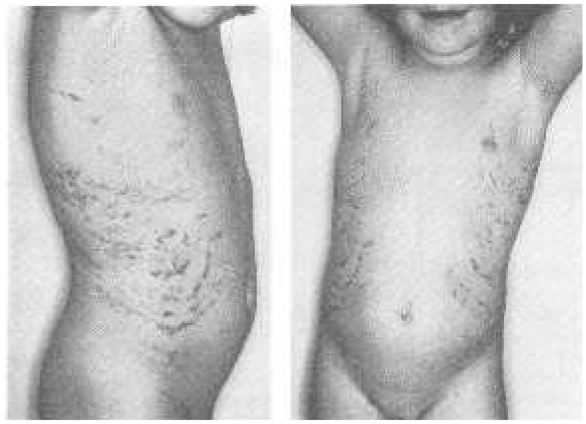

Figure 1.8: Photograph of hyperpigmentation along Blaschko lines in the trunk, caused by incontinentia pigmenti, a rare genetic skin condition linked to X-chromosome mosaicism. We see that broad lines are formed across the trunk. Reproduced from Landy & Donnai (1993), with permission. All rights reserved.

1.2.2 Zebrafish pigmentation

Adult zebrafish are small fish, about 55mm long (Figure 1.9). They are transparent during much of their short development, and they are also relatively easy to breed (Quigley & Parichy, 2002). Furthermore, the underlying conservation of genes and mechanisms between species means that studying the development of the zebrafish very often leads to general insights into the development of many other vertebrates. They are, therefore, a good model organism to study.

Figure 1.9: An adult wild-type zebrafish. Reproduced from Moreira & Deutsch (2005), with permission. All rights reserved.

The development of the zebrafish's pigmentation pattern has been recorded in detail. As we investigate this pigment pattern formation in Chapter 3, we present time series data of zebrafish stripe development here (Figure 1.10). We see that black pigment cells called melanophores arise on the body of the zebrafish, and form dense stripes over the space of three to four weeks. Inbetween these melanophore stripes, yellow xanthophore pigment cells appear, leaving a small space along the border of melanophore stripes. Both types of pigment cells organise into these stripes through both cell differentiation and migration.

1.3 Outline of thesis

In the following three chapters we consider the processes of cellular proliferation, differentiation and migration, presenting an appropriate non-local model for each process in turn. For each model, we explore the spatial patterning that arises and discuss its biological significance.

In Chapter 2, we begin with a look at mosaic tissues and chimaeras in particular. We construct both a cellular automata and integrodifferential model, and use these models to explore different rules for proliferation, or, more specifically, cell renewal. We find that changes in the renewal rule lead to significantly different pattering outcomes in mosaic tissues.

Following on from this work, in Chapter 3 we extend the previous continuous model to look at cell differentiation. We investigate three different versions of the model, with differentiation being cell autonomous, regulated via a community effect, or weakly dependent on the local cellular environment. We show that pattern formation only occurs when differentiation is regulated by a strong community effect.

Then in Chapter 4 we investigate directed cell migration, again using an integrodifferential equation. We investigate both attractive and repulsive cell-cell interactions over various distances, something which we believe has not been looked at in previous modelling work relating to cell biology. We find that attractive forces produce stationary aggregations, and that increased interaction distances increase aggregation width. Meanwhile repulsive forces can produce nonstationary patterns and irregular patterning, including oscillations and travelling waves.

We then present an account of the numerical methods used throughout this work (Chapter 5), including a look at metastability, the process by which a seemingly steady state evolves very slowly over time to the actual steady state solution. We finish with a short discussion (Chapter 6).

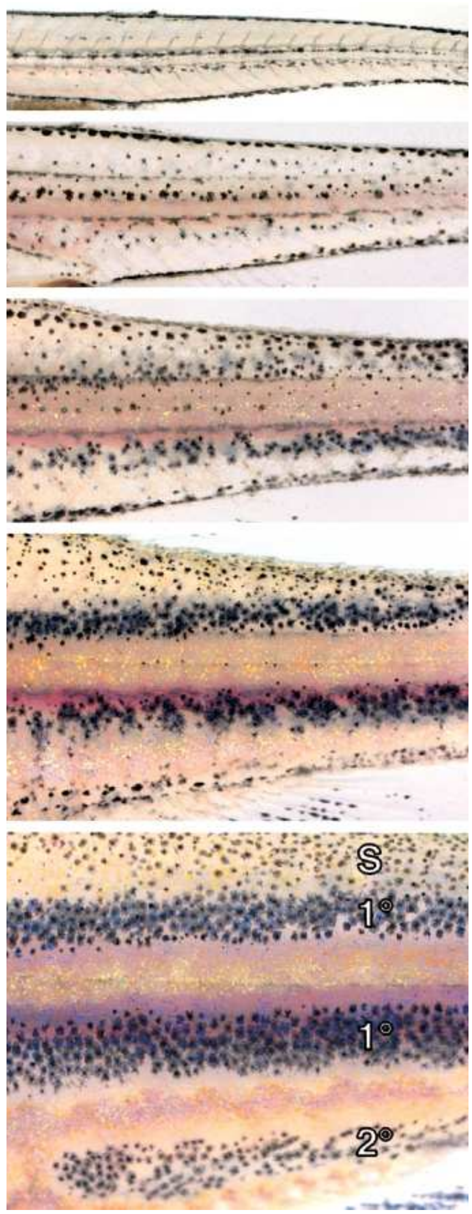

Figure 1.10: Metamorphosis of the zebrafish pigment pattern. Shown are a series of images from a single wild-type larva over the course of 25 days of development. From top to bottom: 1st panel: The early larval pigment pattern persists for about two weeks. 2nd panel: Subsequently, black pigment cells (melanophores) arise dispersed over the flank in regions not previously occupied by these cells. 3rd panel: During a second phase of metamorphosis, additional melanophores begin to arise in prospective melanophore stripe regions. 4th panel: By about 4 weeks of development, two primary adult melanophore stripes border a lighter interstripe region. Final panel: During subsequent growth and development, primary (1) melanophore stripes become more regular and additional, secondary (2) stripes are added to the pattern; scale melanophores (S) can be seen covering the dorsal flank. Reproduced from Quigley & Parichy (2002), with permission. All rights reserved.

Chapter 2

Cellular automata and integrodifferential equation models for cell renewal in mosaic tissues

Mosaic tissues are composed of two or more genetically distinct cell types. They occur naturally, and also provide a useful experimental method for exploring tissue growth and maintenance. By marking the different cell types, one can study the patterns formed by proliferation, renewal and migration. Here we present mathematical modelling suggesting that small changes in the type of interaction that cells have with their local cellular environment can lead to very different outcomes for the composition of mosaics. In cell renewal, proliferation of each cell type may depend linearly or nonlinearly on the local proportion of cells of that type, and these two possibilities produce very different patterns. We study two variations of a cellular automaton model based on simple rules for renewal. We then propose an integrodifferential equation model, and again consider two different forms of cellular interaction. The results of the continuous and cellular automata models are qualitatively the same, and we observe that changes in local environment interaction affect the dynamics for both. Furthermore, we demonstrate that the models reproduce some of the patterns seen in actual mosaic tissues. In particular, our results suggest that the differing patterns seen in organ parenchymas may be driven purely by the process of cell replacement under different interaction scenarios.

Note that this chapter contains much material that was originally published in Royal Society Interface, 7, 1525-1535 (2010), and was a collaboration between Jenny Bloomfield, Jonathan Sherratt, Kevin Painter and Gabriel Landini. Gabriel Landini conceived the cellular automata model. The continuous models were developed by Jenny Bloomfield, Kevin Painter and Jonathan Sherratt, who also worked together on the stability analysis. Kevin Painter and Jenny Bloomfield worked together on the writing of numerical code. Jenny Bloomfield performed all of the continuous numerical studies and wrote the paper, with comments provided by the co-authors.

2.1 Introduction

Proliferation is a fundamental cellular process, forming the basis of renewal in all higher organisms. It has an important role in many situations including embryogenesis and tissue maintenance, although the extent to which it is a driver for such multicellular processes is not known. Cellular proliferation is modulated by cell signalling. This may be contact-dependent, requiring cells to physically touch each other, or it may involve longer range processes (Webb & Owen, 2004; Graham & Ooyen, 2006). Once a cell has received a proliferation signal, it produces a daughter cell of its own type.

The question of how the decision to proliferate is made has appeared in relation to multiple biological problems. One such, which we will concern ourselves with here, is that of mosaicism. Mosaic tissues are composed of two or more genetically distinct cell types, and the mosaic patterns produced by this mix of cells are witnessed in many scenarios. For example, certain human diseases involving mutations early in embryogenesis can exhibit macroscopic patterns in skin along so-called Blaschko lines, which are thought to indicate the limits between different proliferating cell clones (Happle, 2006). Mosaic patterns also arise in all females due to X-chromosome inactivation: females carry two X chromosomes, one of which is inactivated early in embryogenesis to prevent overexpression of X-chromosome genes. This inactivation process is known as Lyonization (Lyon, 1961), and as the inactivation is passed on to daughter cells, it leads to females being a mix of two different cell types, with either the paternal or maternal X-chromosome active. This inactivation may also be related to Blaschko lines becoming visible in some pathological conditions in females, again following boundaries between the two cell types (Happle, 2006).

Experimentally, mosaicism can be explored through the use of chimaeras. Chimaeric animals are individuals that have four or more parents. They are created by the fusion of distinguishable embryos, or by transgenic techniques (incorporating certain cell markers into one of the embryonic cells). Experimentalists have used chimaeras to consider the fate of cell clones, the spread and effect of certain mutations, and the cellular composition of different organs in parenchyma growth (see Ng & Iannaccone (1992) and West (1998) for more detail).

A better understanding of exactly how mosaic patterns arise would provide an important contribution to the problems outlined above. As chimaera experiments in particular have been so successful in the exploration of mosaics, we discuss them in detail here, with particular reference to their relevance for the growth and maintenance of organ parenchyma, the base tissue of organs. Although the patterns formed in chimaeras during the development of organ parenchymas can only be viewed after their creation, they do provide a tool against which hypotheses for growth and maintenance can be tested. In situ analysis of chimaeras has revealed different complex patterns in different organs. In the rodent liver, for example, cell lines appear to mix randomly, whereas the adrenal cortex produces radial stripes of cell lineages. It has been suggested that mosaics observed in the liver could be caused by cells proliferating randomly (Kokha et al., 1994; Iannaccone et al., 2002) while in the adrenal cortex, the placement of daughter cells may be biased centripetally (Iannaccone & Weinberg, 1987; Landini & Iannaccone, 2000; Iannaccone et al., 2002).

The suggestion that two very different organ parenchyma mosaics could both be caused by differences in proliferation (modulated, perhaps, by cellular contact (Landini & Iannaccone, 2000)), opens up the possibility that all organ parenchyma growth might be guided by cell proliferation and renewal alone, as opposed to other factors such as cell migration (Morley et al., 1996). Until experimental techniques can be improved, a theoretical approach such as mathematical modelling provides a valuable method of testing different hypotheses. Before we consider our own model, we discuss the models seen in the current literature that consider chimaera experiments, and also those that look at more general issues concerning the regulation of cell renewal by the local environment.

Few models have been produced to specifically describe the chimaera experiments above; those that have are mainly cellular automata (CA). A population of cells is arranged on a grid with rules imposed to govern the movement, growth and death of each cell according to both the position of neighbouring cells and the age of the cell itself. These models reproduce various chimaeric patterns (Landini & Iannaccone, 2000), but only explicitly consider the proliferation hypothesis, not the cell migration/proliferation hypothesis. A CA model for an experiment involving chick and quail cells in the intestine, very similar to the chimaeras already discussed, is explored in Simpson et al. (2007a). This paper considers both cell migration and proliferation, and the results of the CA are successfully matched to that of experimental data; it is also noted that the dynamics produced by the CA match those of the Fisher partial differential equation (see Murray (1989), Vol. I, Ch. 11), demonstrating a successful multi-scale modelling process. In Simpson et al. (2007b) and Simpson et al. (2006), a general continuous mathematical model of cell invasion is created and validated with experimental data. Proliferation is shown to be the key mechanism in driving the invasion process.

In this paper we take both a discrete and a continuous approach. It is possible to link discrete and continuous models formally as is done, for example, in the liver growth model of Green et al. (2010), but we do not attempt that here. Instead we take a more phenomenological approach. Following on from the successful discrete models of Kokha et al. (1994) and Landini & Iannaccone (2000), and the experimental work discussed above (particularly the observations made by both Simpson et al. (2006) and Landini & Iannaccone (2000) regarding the importance of cell proliferation), we assume cell proliferation, or more precisely, cell renewal to be the driving force for the dynamics. Through modelling, we can exclude all other factors from the system, such as mechanical effects, cell ageing, migration etc., thereby testing whether cell renewal on its own is able to create the empirically observed variety of mosaics. We explore two different replacement mechanisms, both of which incorporate the effect of neighbouring cells on cell renewal. Although our model is designed for the investigation of organ parenchymas, it is also applicable to a range of other cell replacement problems.

Section 2.2 outlines the conceptual framework behind our theoretical models, and Section 2.2.1 considers a discrete cellular automata (CA) model for a cell renewal problem based on chimaera experiments. We then begin Section 2.2.2 by describing the derivation of the continuous model, which has two slightly different versions, and which is the main focus of this paper. We consider the behaviour of the model for cells in two space dimensions in Section 2.3, and demonstrate the ability of the model to form organ parenchyma mosaics as witnessed in both the adrenal cortex and liver, as well as showing some more general results. In Section 2.4 we discuss our findings, and go on to discuss another biological application for the model: that of Blaschko lines. We end by discussing potential directions for future work.

The key finding of this work is that, by changing the way in which the local cellular environment regulates cell renewal in our models, we can radically alter the patterns produced. In cell renewal, proliferation of each cell type may depend linearly or nonlinearly on the local proportion of cells of that type, and these two possibilities produce very different patterns. This observation offers possible answers to the question of why different organ parenchymas produce different mosaics, as observed in chimaera experiments and discussed in this section. Our results suggest that these various patterns may be created by different cell replacement scenarios mediated by different reactions to the local cellular environment.

2.2 Modelling Chimaera Experiments

Chimaera experiments are used to explore tissue dynamics by observing patterns generated by subpopulations of cells. These subpopulations have no functional difference but are genetically distinct, and so can distinguish between themselves. The subpopulations can be artificially marked by distinct markers to enable their dynamics to be observed.

We outline two conceptual models, both of which are based on biological hypotheses of cell renewal. Of course, various other conceptual models could also be suggested, but as the mechanism that regulates cell renewal in various organs has not been fully elucidated, we choose two different but likely mechanisms here. First, we suggest that a mix of two differently marked, but otherwise identical cell types die and are reborn according to a "voting" principle: a cell dies randomly, and is replaced by a cell of whichever type is in the majority in its immediate neighbourhood. If there is an even mix of neighbouring cell types, replacement is allocated randomly. We call this the Majority conceptual model, and it is akin to the idea that proliferation is biased towards the cell type which is in the majority locally. Although we are not aware of specific data supporting this hypothesis in cell renewal, such community effects are well documented in the regulation of other cell behaviours (Standley et al., 2001), and certainly would be a likely candidate for renewal in cells that communicate through local mechanisms such as juxtacrine signalling.

A second scenario dictates that a cell is replaced by the same type as a cell selected randomly from those in its immediate neighbourhood. This is the Single-Cell conceptual model, and represents basic cell proliferation whereby empty space is filled via the division of a cell in its immediate neighbourhood.

We model these concepts in two dimensions, thereby considering a monolayer of cells. For both of these scenarios, we assume that the population of cells stays constant, i.e. that death and birth are instantaneous. This means that we are modelling a process of tissue homoeostasis, as opposed to tissue growth. We further assume that there is no empty space, which allows us to think of this model as a one population model: a cell is either of one type or the other. Furthermore, since the two populations are only differentiated by a marker but are otherwise the same, we assume that both birth and death rates in the two populations are the same. Both the Majority and the Single-Cell conceptual models provide a simplified representation of a synthetic chimaera, and we simulate them as such to investigate the emerging patterns.

2.2.1 A Cellular Automata Approach

Individual based models are very well established and come in many different formats (see, for example, Anderson et al., (2007) for review). For our purposes it is sufficient to use a very simple CA model, even though more sophisticated forms are available. CA have been applied to many biological applications as their discrete form lends itself naturally to the modelling of biological cells. We set up two CA "voter" models according to the conceptual models outlined above (see Liggett (1985), Ch.5 for a more general description of voter models). The processes for the two models are outlined in Figure 2.1.

While the algorithms in Figure 2.1 describe asynchronous random choice updating (Schönfisch & de Roos, 1999), we have also implemented a synchronous updating method, meaning that all grid squares across the lattice are updated simultaneously, with new values calculated according to their neighbours at the previous time-step. No qualitative difference in results from the two updating algorithms is observed, beyond that of timescale (see Section 2.5.2). The simulations illustrated here all employ asynchronous updating, since it is the most relevant to biological scenarios.

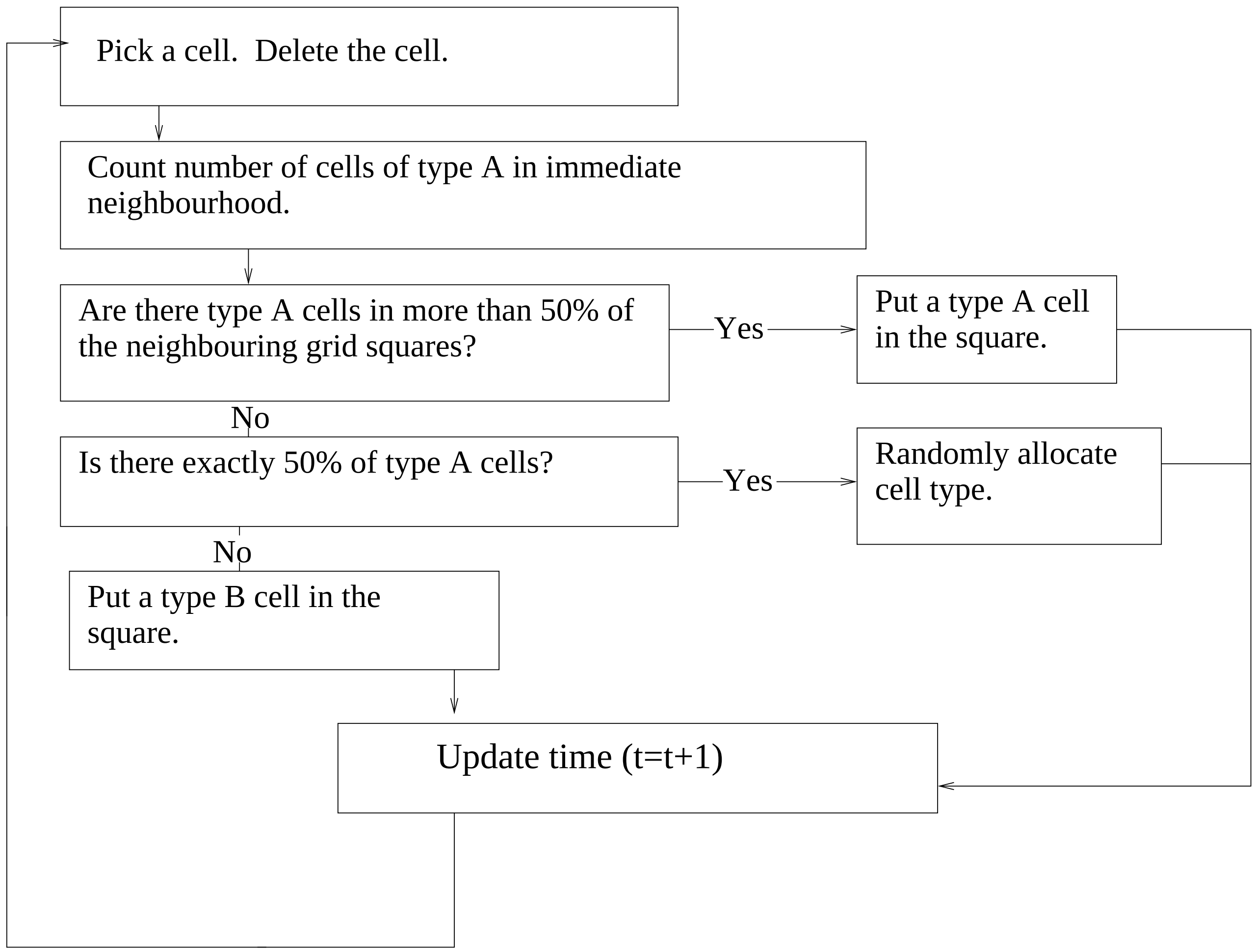

(a) Majority CA

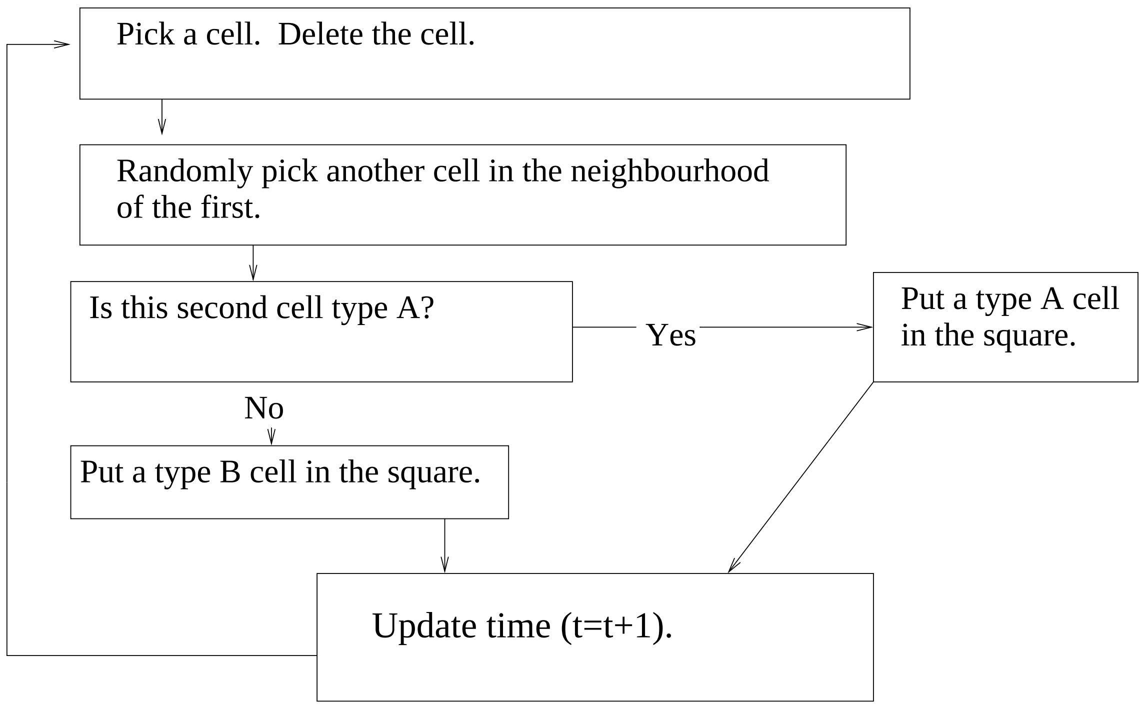

(b) Single-Cell CA

Figure 2.1: The updating process for the asynchronously updated cellular automata. Figure 2.1(a) describes the process for the CA based on the Majority conceptual model, while Figure 2.1(b) describes that of the CA based on the Single-Cell conceptual model.

Bearing in mind our biological application to chimaera experiments, we explore initial conditions of two cell types evenly mixed across the grid for each of the conceptual models. For the domain geometry, we suppose that we are carrying out experiments on an assay with fixed size and presume that cells at the boundaries of our tissue receive no information from outwith the tissue. That is to say, on the boundary and at the corners of the domain only cells in the domain are considered, and an average is taken over that reduced number of cells in the Majority model, whilst in the Single-Cell model a cell that picks a neighbour outside the domain does not change state. These boundary conditions are of a type that has minimal impact on patterning within the domain.

For the Majority conceptual model the end result is either domination by a single cell type across the grid (Figure 2.2, top panels), or a split domain in the form of one large block of each cell type (Figure 2.2, middle panels). The change in proportion of black cells over time can be seen in Figure 2.3 for both cases. This result is seen both for our choice of neighbourhood (an eight cell "Moore" neighbourhood), and in a more preliminary simulation study using a four-neighbour "von-Neumann" neighbourhood, which involves just cells that share a complete edge with the empty site. The significance of the von Neumann neighbourhood is that it is the predominant formalism in the extensive literature on so-called threshold voter models, which are otherwise similar to our Majority conceptual model. In the threshold-2 voter model, cells switch type at a given rate if a least two (out of four) neighbours are of the opposite type (Cox & Durrett, 1991). While this is not quite the same as our Majority model, both models do have the possibility of switching only when half of the neighbours are of opposite type. Cox & Durrett (1991) conjecture that such a model will evolve to all of either one cell type or the other dominating across the domain, depending on which cell type has the greater initial density, with a density of precisely 1/2 being the critical value at which the switch between these two scenarios occurs. This is consistent with our observation that with initial conditions of two cell types mixed approximately evenly across the grid, we see either the steady state solution of all one species, all another, or split between the two (Figure 2.3).

For the Single-Cell conceptual model we do not observe the system evolving to a single cell type, even when the simulations are run on a long timescale (Figure 2.3). Rather, cell types agglomerate in a constantly changing pattern (Figure 2.2, bottom panels), forming solid groups. We see this over long timescales (we investigated up to $t = 10^9$, and still saw this spatially unstable movement). Again, preliminary investigations show no qualitative difference between simulations using a von Neumann neighbourhood and those carried out on a Moore neighbourhood, making the literature on voter models relevant. The literature states that for models similar to this one, clustering is the expected result i.e. cell types group into larger and larger blocks,

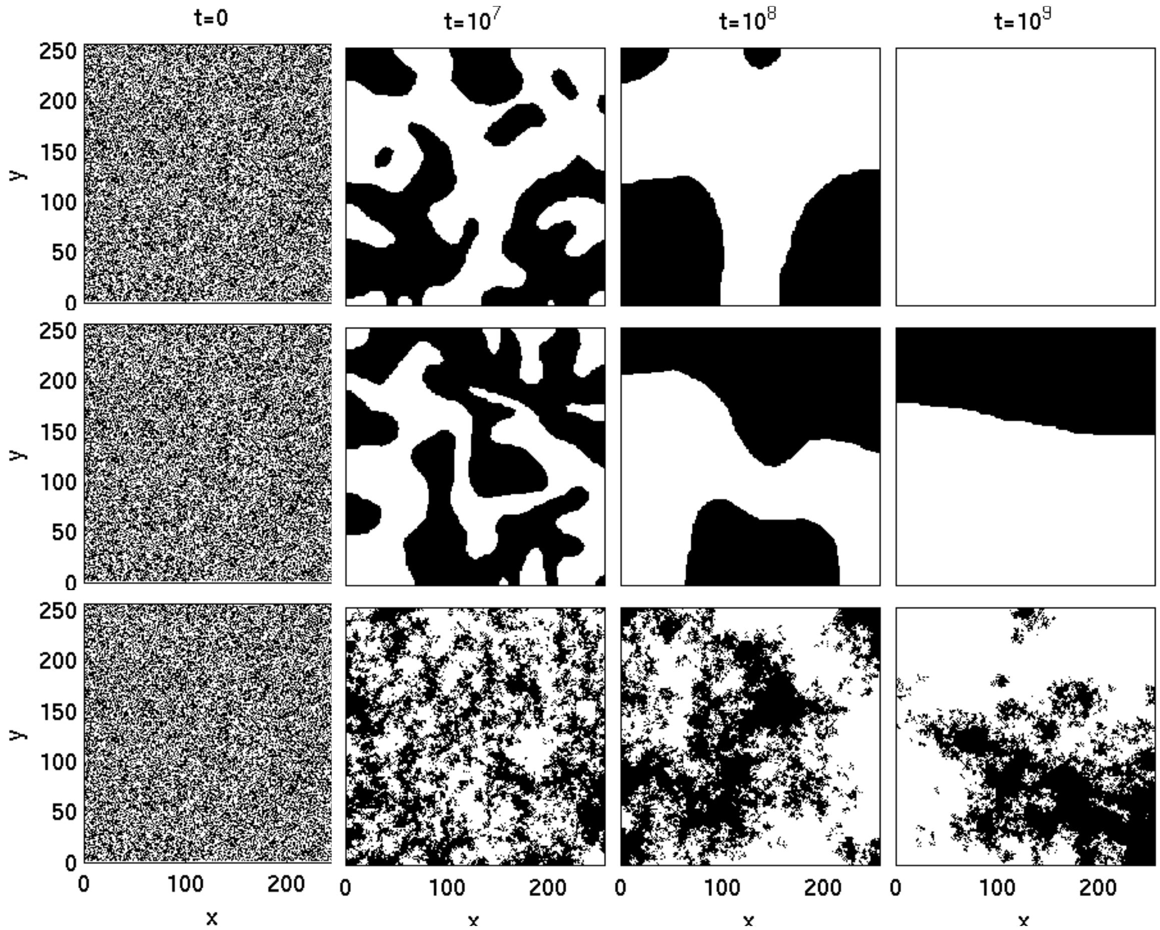

Figure 2.2: Solution of the Cellular Automata (CA) as described above, at times $t = 0$, 10^7, 10^8 and 10^9. Note that these are equivalent to biological times 0, 3, 30 and 300 years if cells are replaced every seven days (see Section 2.4 for details of this calculation). Here, we use mixed initial conditions by randomly assigning to each grid square the value of 0 or 1. In the top set of panels, left to right, we consider the Majority conceptual model, and see cells quickly forming large agglomerations, before they either die out completely or dominate the grid. Out of 1000 runs, we see quick domination by a single cell type across the entire domain in about 30% of cases, while the remaining 70% end with both species present as seen in the second set of panels. No qualitative change in behaviour is seen after 10^9. In the bottom set of panels, a solution to the Single-Cell conceptual model is shown, demonstrating persistence of both cell lines over time. For the upper and middle panels, cells are updated according to the process described in Figure 2.1(a), while the CA in the third set of panels is updated according to the process described in Figure 2.1(b). All CAs are carried out on a grid of size 256×256, and use an eight neighbour Moore neighbourhood. On the boundary and at the corners of the domain, only cells in the domain are considered, and an average is taken over that reduced number of cells in the Majority model, whilst in the Single-Cell model a cell that picks a neighbour outside the domain does not change state. See Chapter 5 for more numerical details.

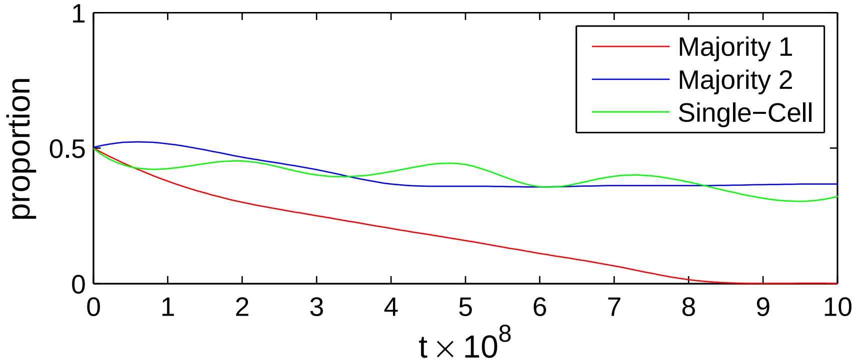

Figure 2.3: We plot the proportion of black cells over time for each of the three simulations shown in Figure 2.2. Whilst for the Majority model, we see either a steady decrease in black cells (red), or a mix of both cell types (blue), for the Single-Cell model we always see a mix of both cell types (green).

until the solution runs to a single species steady state as $t \to \infty$ with probability 1 (Cox & Durrett, 1991; see also Cox & Griffeath, 1986; Dornic et al., 2001). We do not see this end state; rather, our simulations show (in, for example, Figure 2.2, bottom panels) the initial clustering process where the two cell types form larger solid blocks as time increases. The much longer timescale over which a single species emerges is not likely to be biologically relevant.

These results show that different types of contact-mediated renewal produce very different patterns. Note that whilst here we have not considered irregular lattices such as Voronoi tesselations or other geometries such as hexagonal lattices, both of which perhaps model cell shapes better than our regular square lattice, our cellular automata do provide good preliminary results into the type of behaviours that we can expect from our conceptual models. With these results in mind we now develop a continuous framework that is more amenable to mathematical analysis, in order to understand the origin of the distinct pattern outcomes that our cellular automata produce.

2.2.2 Development of a Continuous Model

We first attempted to develop a continuous model by taking a discrete model to its continuous limit. Such an approach seems sensible given the discrete nature of cells. However, it always resulted in the loss of key information as a result of the scaling process (see Section 2.5.1), and this led us to take a more phenomenological approach that we detail here.

To model our problem continuously, we must decide how to represent the local environment of cells that influence cell renewal. We first use an integral term I to calculate the proportion of one cell type in the local environment, and then apply various functions f to this integral to explore different renewal scenarios. Such a representation of cell environment via an integral term has been used previously in contexts including cell sorting (Armstrong et al., 2006), development (Armstrong et al., 2009; Green et al., 2010), and cancer (Gerisch & Chaplain, 2008; Sherratt et al., 2009; Painter et al., 2010). Since we again wish to model a monolayer of cells, the integral I is in two dimensions, and is taken over a region dictated by a sensing radius R, representing the capacity of a cell to directly sense its environment via, for example, filopodial contact. Increasing R allows us to consider different sizes of the neighbourhood that influences cell renewal, and therefore allows us to consider different types of cell communication. For example, a small R can represent local contact-dependent communication such as juxtacrine signalling (Owen et al., 1999; Webb & Owen, 2004), whilst a larger R may be chosen to explore a longer range communication such as a locally diffusing signalling molecule (Monk, 1997) or filopodial contact to distant cells (Sherer & Mothes, 2008).

Since we are concerned with modelling chimaera experiments, we have a closed system where the birth of cells simply replaces those cells lost to death i.e. there is no empty space. We further assume that the replacement rates of the two cell lines are the same, as expected in mosaic tissues where the distinction between cell populations may often only be at a genetic level and not in terms of their behaviour. This enables the model to be formulated as a single equation for the proportion of cells that are of one of the two types. We refer to the two cell types as A and B, with $a(\underline{x}, t)$ being the proportion of cells of type A; thus a fraction $1 - a(\underline{x}, t)$ of the cells are of type B.

Our complete model is therefore:

$$\frac{\partial a}{\partial t} = \alpha(f(I_a) - a), \tag{2.1}$$

where I_a is the integral $\frac{1}{area} \int_0^R \int_0^{2\pi} a(\underline{x} + r\underline{\eta}) r d\theta dr$. Other cells within the domain of integration in I_a are located relative to $a(\underline{x}, t)$ by reference to both the distance r along the sensing radius R, and $\underline{\eta} = (\cos\theta, \sin\theta)$. The constant α is the cell replacement rate, and can be thought of as a representation of the mean life time of cells which would be expected to vary between tissues and cell types. In terms of the CA model, α is related to the time step since it regulates the rate at which the cell population changes through time. A more accurate relationship could be obtained if a more formal link between the two models was attempted, but as we are primarily interested in the long term dynamics of the model, and not its rate of change, we do not attempt to derive such a link here. The integral is normalised over the area, which is πR^2 away from the boundaries of the domain. We assume a finite sheet of cells, and hence on the boundary the integral is truncated i.e. cells that lie outside the domain are not included in our calculations, neither in the integral itself, nor in the calculation of area over which the integral is normalised. We will solve this model numerically, using a Methods of Lines approach to transform our equation into a systm of ODEs and then applying ROWMAP, after first completing some mathematical analysis. See Chapter 5 for more on this.

We now consider two different scenarios that explore different local environment dependencies, and that match our CA simulations and conceptual models. We choose a smooth approximation to a step-function f as this matches the idea of a 'community-effect' type patterning; we choose a linear f as this is most similar to a standard cell-renewal process, whereby one cell that neighbours an open space will produce a single daughter cell to fill it, without communicating with other cells around it.

- Locally Biased Model
  - Renewal is biased towards the cell type in the local majority.
  - This is equivalent to the Majority conceptual model and corresponding CA simulation.
  - We choose f as illustrated in Figure 2.4(a): a cell will be replaced with a type biased towards those in the majority around it, in a scenario that mimics that of the community effect witnessed in cell differentiation (Standley et al., 2001).
- Locally Unbiased Model
  - Renewal is non-biased.
  - This is equivalent to the Single-Cell conceptual model and CA simulation.
  - We choose f as illustrated in Figure 2.4(b): a daughter cell will be of a certain type with a probability equal to the proportion of that cell type present, corresponding to basic cell proliferation.

Note that a must lie between 0 and 1 since it is a proportion, and moreover $f(0) = 0$ and $f(1) = 1$ since both $a = 0$ and $a = 1$ must be steady states.

2.2.3 Linear Stability Analysis of Homogeneous Steady States

In order to explore the long term behaviour we can expect from the model, we carry out some analysis, looking at the location and stability of steady states. Steady states for $f \in [0, 1]$ of the Locally Biased model, found by setting $\frac{\partial a}{\partial t} = 0$ in (2.1), are given by $a = 0$, $1/2$ and 1. We then perturb the steady states homogeneously through space

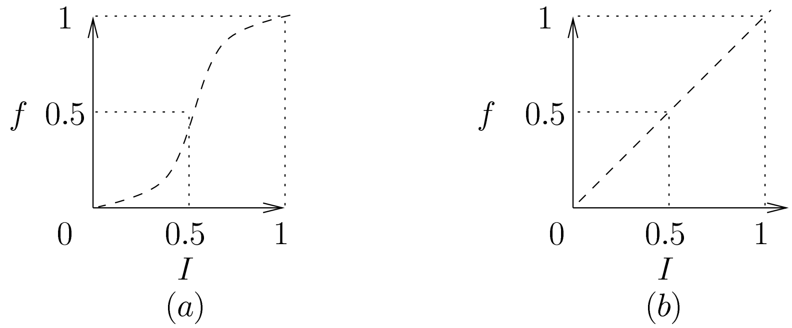

Figure 2.4: Schematic of renewal function in the continuous model. (a) A smooth continuous approximation to a step function, symmetric about 1/2, representing the Locally Biased model. (b) Linear f, representing the Locally Unbiased model.

to explore their stability: we put $a = a_s + \tilde{a}(t)$, where a_s is our steady state and $\tilde{a}$ is a small homogeneous perturbation. Then

$$\frac{\partial \tilde{a}}{\partial t} = \alpha \left(f(I_{a_s+\tilde{a}}) - (a_s + \tilde{a}) \right). \tag{2.2}$$

At $a_s = 0$ and $a_s = 1$, $f'(I_{a_s}) < 0$, while at $a_s = 1/2$, $f'(I_{a_s}) > 0$. Therefore $a = 0$ and $a = 1$ are stable, while $a = 1/2$ is unstable. For the Locally Biased model, we therefore expect only one scenario close to the steady state: depending on the initial proportion of A, we expect that the system will always evolve to either all A or all B.

In the same manner, we explore the Locally Unbiased model. Here there is a continuum of steady states at $a = a_s$, with any $a_s \in [0, 1]$ possible. The steady states are neutrally stable. This means we expect the system to remain at whatever proportion of A and B it begins with, which is consistent with the simulations in Figure 2.2 (bottom panels).

MODEL TYPE	STEADY STATE	STABILITY
Locally Biased	0	stable
	1/2	unstable
	1	stable
Locally Unbiased	$a_s \in [0, 1]$	neutral

Table 2.1: A summary table of stability of the steady states of (2.1)

This analysis of the two variations of the model suggests that a cell's reaction to its local environment can significantly alter the patterns we can expect to see. With the Locally Biased version of the model we expect locally to see all cells having a single type, either A or B, whereas in the Locally Unbiased model we expect to see a persistence of both cell lines. This is consistent with the proliferation hypothesis for the development of organ parenchymas, which suggested that proliferation was the driver behind the creation of differing mosaic patterns (see Section 2.1).

2.3 Numerical Simulations of the Continuum Models

Whilst the linear analysis provides some insight into the expected model behaviour, a numerical study is required for further understanding. Our numerical code discretises the circular domain of the integral, and then sums the integral over each of the grid squares within the circle. Although some of the area of the circle is lost at the boundaries, the calculation is fast and, with a fine lattice, it is accurate – see Chapter 5 for more on this. More sophisticated numerical schemes for integrodifferential equations using techniques such as fast Fourier transforms to evaluate the integral are possible: see in particular Gerisch & Chaplain (2008) and Gerisch (2010). To discretise time, we used ROWMAP (Weiner et al., 1997), a method that is particularly suited to solving stiff ODE initial value problems, and that automatically controls and adjusts time-step size. For more numerical details, see Chapter 5.

2.3.1 The Two Dimensional Model Results

We begin by investigating initial conditions corresponding to a homogeneous, equal mix of cell types A and B across the grid, so that we set $a = 0.5\pm$small noise (see Figure 2.5). This is a biologically realistic scenario for a group of cells at the start of a chimaera experiment. These initial conditions also allow comparisons with our CA simulations. Note that in preliminary investigations, we have found that varying the amplitude of noise present in the initial conditions makes no qualitative difference to the results. We did not consider extreme initial conditions as these have little biological relevance. We investigate each f in turn. We carry out all simulations on a two dimensional grid with boundary conditions equivalent to the biological scenario of a chimaera experiment: we imagine a sheet of cells with no cells present outside the boundary.

For the Locally Biased model, we find that the solution usually goes to all A or all B across the entire domain, as expected from our linear analysis (see Section 2.2.3). However, sometimes the long-term solution involves a division of the domain into two parts, one solely of type A, and the other solely of type B (Figure 2.6). This occurred in a total of 6 out of 20 runs. Note that these results are qualitatively the same as those seen in the cellular automata model (see Section 2.2.1 and Figure 2.2, top and

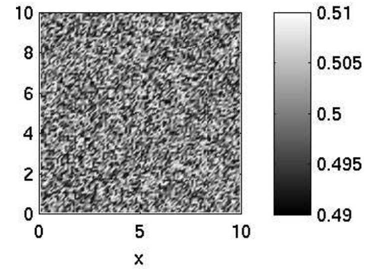

Figure 2.5: The homogeneous mixed initial conditions used for the two dimensional model. The two cells are evenly mixed across the domain. The domain is a square with sides of length 10 dimensionless space units.

middle panels). They are not quantitatively the same, since while for our CA we see mixed conditions 70% of the time in the Majority case, for our continuous model in the equivalent Locally Biased case we see mixing only 30% of the time. However, increasing the gradient of f, moving it closer towards a step-function, causes an increase in the number of times the long-term solution evolves to a domain of one part A, one part B. Intuitively this is not surprising, as in moving f closer to a step function we move closer to the discrete CA scenario in which 70% of our simulations ended with both cell populations present.

For the Locally Unbiased model, we see the two cell populations A and B merge into a single homogeneous state (Figure 2.8). This suggests that biologically, the two cell lines will persist over time alongside one another (corresponding to $b = 1 - a$ with $0 < a < 1$ in (2.1)). This result is also similar to our cellular automata simulations for the Single-Cell model (see Section 2.2.1 and Figure 2.2, bottom panels), although the continuous model loses the fine-grained spatial dynamics of the discrete model (not shown).

Biologically, solutions of the type shown in Figure 2.6 are reminiscent of the growth patterns of both the adrenal cortex, which involve large blocks of a single cell type alongside one another, and the liver, which involves random patterning. For certain domain sizes our simulations of the Locally Biased model show repeated stripes, as is seen in the adrenal cortex (see Figure 2.7; note that in this figure, we deliberately use a long, thin domain to encourage stripe formation – for more on stripe formation, see Section 2.5.3). These stripes are stable to spatial perturbations, suggesting that something similar to Locally Biased proliferation could be the driver for the dynamics seen in this organ, although there is no concrete evidence on whether or not this is the case. Moreover, the similarity between our discrete simulations and the patterns observed *in vivo*, along with the continuous model results also showing cell line persistence, suggests that the growth of liver parenchyma may be driven by the cell renewal process as described in the Locally Unbiased model, although again there is

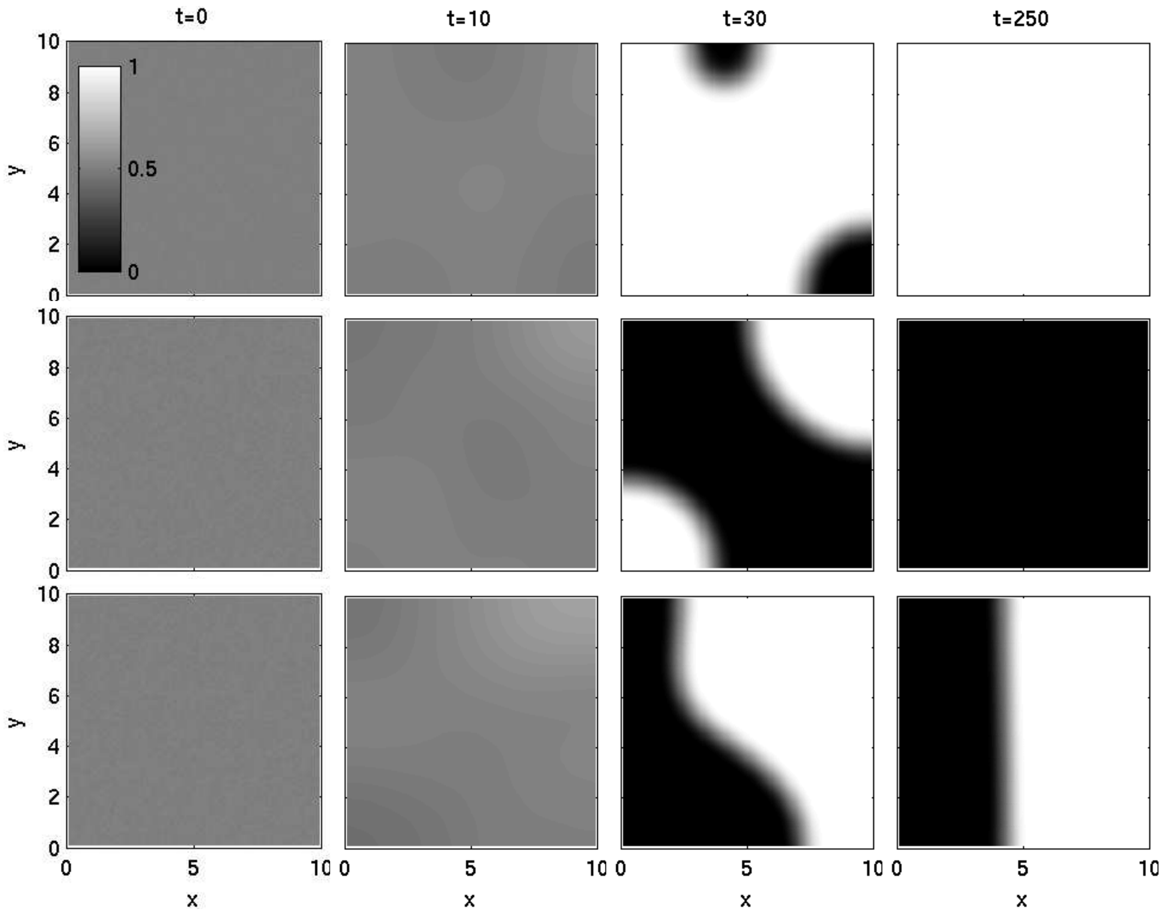

Figure 2.6: A solution of the two dimensional Locally Biased model equations (2.1) with homogeneous initial conditions. We plot the proportion of cells of type A in space at dimensionless times $t = 0$, $t = 10$, $t = 30$ and $t = 250$. The top set of panels show the domain quickly evolving to an all white domain of A cells, while the middle set shows quick dominance by B (black). The bottom panels show dominance by neither cell type, which held for long times (solutions were found to be stable in runs up to $t = 10^8$; not shown). Out of 20 runs, A dominated 10 times, B 4 times, and neither 6 times. Note that if we assume a cell has a half-life of 5 days then $\alpha = ln2/5$. Therefore, with $\alpha = 1$ as here, each timestep is equivalent to $5/ln2 \approx 7.2$ days. Thus outputs are approximately at dimensional times 0, ten weeks, seven months, and at 5 years. Note also that if we assume that the integral radius R is 0.025mm for example, then our dimensional domain size is 0.25mm. We begin with initial conditions of $a = 0.5 + 0.02 \times c$ where c is chosen randomly between -0.5 and 0.5 at each numerical grid point. The function f is given by $f(I) = 0.5\tanh(\tan(I\pi - 0.5\pi)) + 0.5$, a continuous approximation to a step function. The dimensionless parameter values are $R = 1.0$, $\alpha = 1.0$. The domain is of size 10 dimensionless space units. We set absolute error tolerance in the ROWMAP scheme to 10^{-6}. Space discretisation is $\delta x = 0.1$. See Chapter 5 for more numerical details.

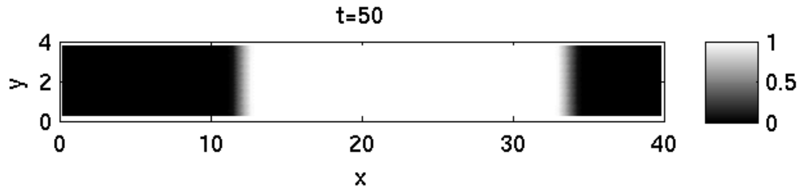

Figure 2.7: A solution of the two dimensional Locally Biased model equations (2.1) with mixed homogeneous initial conditions. We plot the proportion of cells of type A in space at dimensionless time $t = 50$. We see the formation of stable stripes. The domain is 40 dimensionless space units wide, and 4 high. All other numerical details are as in Figure 2.6.

no empirical evidence to confirm this suggestion. In Section 2.4 we suggest possible future experiments to test this prediction.

Overall, the result of the Locally Unbiased model in comparison to that of the Locally Biased model shows that by merely changing the influence of the local environment on the renewal term, two very different results are observed. This suggests that the way cells react to and communicate with their local environment has a very significant role in the dynamics of homoeostasis.

2.3.2 Extending the Two Dimensional Results

We now consider three further sets of initial conditions, in order to gain insight into the behaviours discussed above. In Section 2.3.1, the Locally Biased model sometimes resulted in a split domain. In order to investigate this phenomenon further, we repeat our experiments, this time starting with split conditions similar to those seen in Figure 2.6, bottom panel, at time $t = 250$ (see Figure 2.9(a)). With such initial conditions, the interface between the two species does not move over long times, suggesting that we are indeed at a steady state (not shown). Furthermore, we repeat our experiments with a curved interface (see Figure 2.9(b)) in order to discover whether a non-flat interface could cause movement due to mean curvature. We see a flattening of the interface (see Figure 2.10), but no further movement. This coincides with the previous result, and leads us to conclude that a coexistence steady state in the Locally Biased model will always display a flat interface between the two species. Finally, we investigate "island" initial conditions (see Figure 2.9(c)), in order to explore the dynamics of a localised group of cells. Again, we see movement driven by mean curvature i.e. movement is fastest where curvature is greatest. This leads to the "island" rapidly shrinking until it disappears (see Figure 2.11), explaining both why we sometimes see the dominance of a single species in the Locally Biased model, and why we do not see spotted patterns, as each small group of cells is engulfed by the larger local population

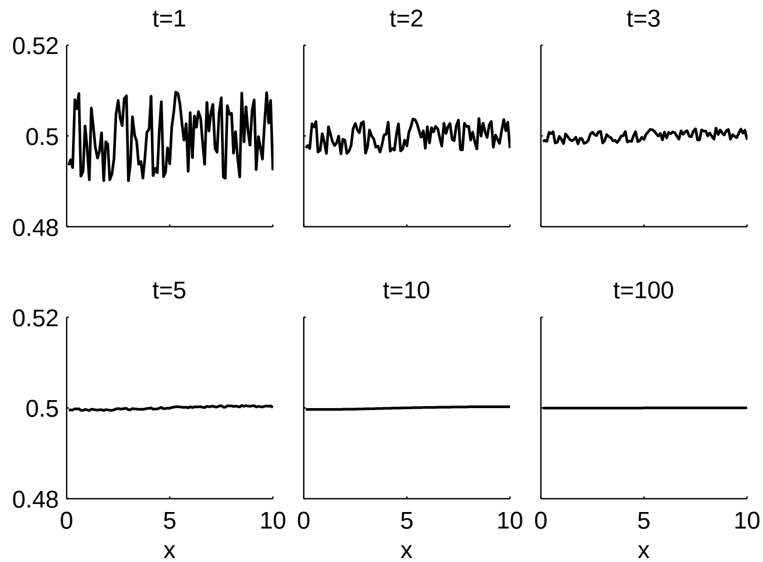

Figure 2.8: Time evolution plots of the two dimensional Locally Unbiased model equations (2.1). The domain is initially an even mix of the cell populations A and B, as in Figure 2.5, and is of size 10 dimensionless space units. We plot the proportion of cell type A across space in the x direction for $y = 2$ at various times t, until $t = 100$. We see the proportion of A spreading homogeneously across the domain over time until $A = 0.5$ everywhere. All parameter values and numerical details are as in Figure 2.6, although with a linear f as stipulated by this model (see Figure 2.4(b)).

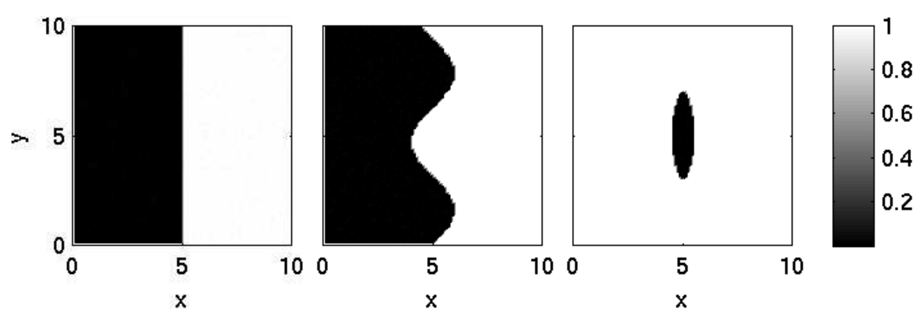

(a) Split i.c.s (b) Curved i.c.s (c) Island i.c.s

Figure 2.9: More initial conditions used for the two dimensional model. The domain is again a square with sides of length 10 dimensionless space units.

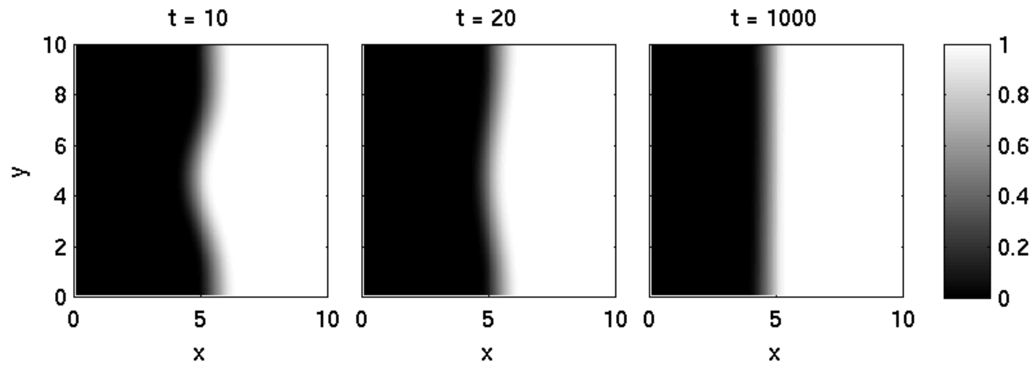

Figure 2.10: Solutions to the two dimensional Locally Biased model equations (2.1) with curved initial conditions as in Figure 2.9(b). We plot the density of cells in space at $t = 10$, $t = 20$ and $t = 1000$. Neither cell type dominates over long times. All numerical details and parameter values are as in Figure 2.6.

(see Figure (2.6) at time $t = 30$)[1]. While further investigation of curved boundaries

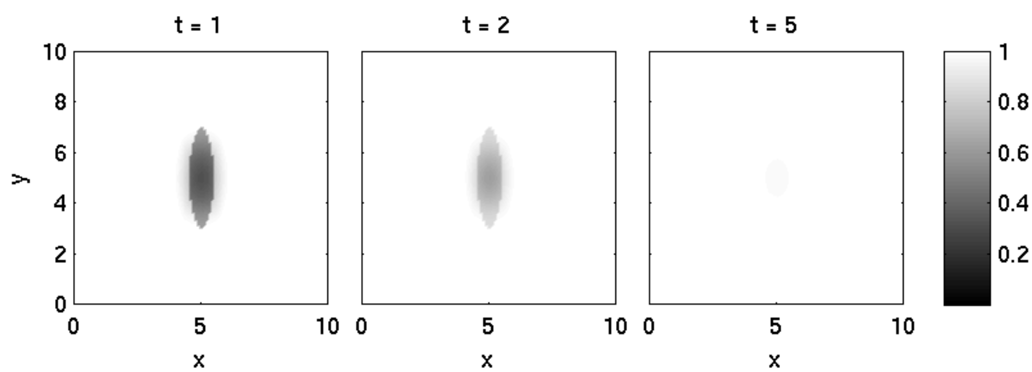

Figure 2.11: Solutions to the two dimensional Locally Biased model equations (2.1) with island initial conditions as in Figure 2.9(c). We plot the density of cells in space at $t = 1$, $t = 2$ and $t = 5$. The dominant cell type rapidly engulfs the "island", demonstrating that we will not see spotted patterns. All numerical details and parameter values are as in Figure 2.6.

and their movement is not the focus of the present paper, it is a natural area for future work, building on the literature of the movement of "islands" in the two dimensional Ginzburg-Landau equation, a generic balanced, bistable partial differential equation (Rougemont, 2000).

[1] Note that such a test was repeated with the Majority conceptual CA, and led to the same results (see Section 2.5.2).

2.4 Discussion

The results of our mathematical models are qualitatively consistent with biological experiments, and suggest that the way a cell reacts to its local environment has a significant part to play in cellular patterning in mosaics. Our key finding is that a small change in the reaction to the local cellular environment can produce a very different outcome for the overall composition of the tissue. In cell renewal, proliferation of each cell type may depend linearly or nonlinearly on the local proportion of cells of that type, and these two possibilities produce very different patterns. Moreover, by looking at the results of chimaera experiments that explore rat livers and adrenal cortices, we have found that the proliferation hypothesis previously discussed in Simpson et al. (2006) and Landini & Iannaccone (2000) (see Section 2.1) could indeed offer an accurate description of the mechanisms that drive organ parenchyma maintenance, with the different patterns seen being caused by different reactions to cellular contact. If this hypothesis is correct, we predict that cells in the liver renew according to the linear Locally Unbiased mechanism, and cells in the adrenal cortex renew according to the non-linear Locally Biased mechanism. This is something that could be tested with the use of fluorescent markers: by marking and following mosaic cells from cell lines of various organs *in vitro* and taking regular images of them, one could discover whether cells are renewing according to the Locally Biased or Locally Unbiased mechanisms, or according to a different mechanism altogether.

To be satisfied about the biological predictions of the model for specific systems in a quantitative manner, we could investigate timescales. In the CA models, we employ asynchronous updating on a grid of 256×256 cells, meaning that a cell on average will be replaced every 65536 timesteps. Thus $t = 10^7$, as in Section 2.2.1, Figure 2.2, corresponds to approximately 150 cell replacements. If a cell is replaced on average every 7 days, this corresponds to about 3 years, meaning that the patterns seen at 10^9 are certainly not biologically relevant if cells are indeed replaced every 7 days. Our results suggest therefore that patchy mosaics are the most likely outcome, whilst stripes or single species populations might need an additional mechansim (migration for example, as suggested by Morely, 1996) in order to form within a suitable timescale.

In terms of the continuous model, α is the cell replacement rate. So if cells have a half-life of 5 days, $\alpha = ln2/5$. Since in Section 2.3.1, Figure 2.6 we set $\alpha = 1$, each dimensionless timestep is equivalent to $5/ln2 = 7.2$ days. Therefore the patterns in Figure 2.6 are shown at approximately 0, 10, 30 and 250 weeks, the last of which is equivalent to approximately 5 years. This is very different to the final dimensional timestep seen in the CA model simulations, that ran until a dimensional time of approximately 300 years. One possibility for the similarity in patterning but the discrepancy in timescale could be the difference in domain size between the two simulations: we carried out the continuous model simulations on a domain of length 10, with a cell radius of 1, as opposed to a domain of 256×256 cells as in our CA simulations. In order to apply the results from the continuous model more directly to mosaic patterns we would need to consider a much larger spatial domain that would relate to actual tissue size, and to our CA simulations. However, without a specific derivation of the continuous model from the discrete, it will always be hard to link the two in a precise quantiative manner.

These time calculations demonstrate the importance of having access to data on cell replacement and on the number of cells in or size of a particular biological system, in order to make accurate predictions regarding the relevance of time-dependent patterning behaviour.

In Section 2.1 we discussed the phenomenon of X-chromosome inactivation mosaicism in females, and the hypothesis that the appearance of Blaschko lines in mammals may be related to the patterned placement of activated and inactivated X-chromosomes in the skin (Happle, 2006). In the majority of females, cells with one or other X-inactivated chromosome appear mixed evenly across the skin in a fine mosaic (Asplund et al., 2001), as is suggested by the Locally Unbiased model. This model is an effective represention of the proliferation of a single daughter cell from one mother cell, as occurs in normal cell proliferation. This suggests that the patterns created by lesions that occur along Blaschko lines in females could be governed by an interruption of normal proliferation processes. This could cause the different cell lines to appear in large blocks alongside each other with merging of the two cell lines across their boundary, as is seen in the Locally Biased model (see Figures 2.6, 2.7 and 2.10). Again, experiments could be done with fluorescent markers to see whether this is the case. However, the issue of what could make such a change occur in the normal proliferation process remains to be explored.

Future theoretical work may involve analysing heterogeneous steady states to explore the structure and scale of patterns. This would enable us to investigate more fully the spatial aspects of, for example, the stripe patterns of adrenal cortex chimaeras. We could also investigate more fully different proliferation functions f to represent other possible cell contact scenarios, in order to explore the different patterns seen in various organs in chimaera experiments. Extending the model to three dimensions would allow much better comparisons with experimental work, as currently most of the quantitative results gathered from chimaeras is in the form of two dimensional sections from three dimensional tissues. Considering the corresponding model on a growing domain would also allow more precise comparisons. In a similar vein, one could attempt a continuous model that is more closely derived from a discrete model. The parameters in a discrete model can in some cases be reliably estimated from microscopic data, and thus could then be used to estimate parameters in the macroscopic model. One possible method of deriving a continuous model would be to consider the probabilities of a cell in the CA becoming type A, say, over a large number of realisations, and to use the variance as a basis for the function f in the continuous model. We have not attempted such a derivation as we do not have the precise biological data that would be required to make the link between the model types of real value. However, this step would be useful in the creation of a three dimensional model for which there is good microscopic data available.

Our model could also be extended to explore scenarios that are outside the closed system necessitated by chimaera experiments. As it stands, the continuum model could be used to study the role of community effects in cell differentiation, and we plan to apply the model to this cellular process in the following chapter. A variation of the model may also be used to explore more general cell proliferation: this would require a factor of a being included in the proliferation term of (2.1). Such an amended model would explicitly relate the total population of one cell type to the proliferation rate of that cell type, and would allow us to consider growing cell populations. However, for the particular application we have considered, our rather different renewal term is appropriate, and the resulting model has highlighted the importance of correct formulation in exploring the tissue dynamics arising from cellular renewal.

2.5 Supplementary material

This section contains additional material on both CA and continuous model simulations that was not included in the published paper that makes up the bulk of this chapter, but which is relevant to our investigations. It begins with an alternative modelling technique that was not persued in the published paper.

2.5.1 The search for a suitable continuous model – taking a discrete model to its continuous limit

As mentioned in Section 2.2.2, we began our continuous modelling attempts by forming a discrete model and taking it to its continuous limit. Although such an approach failed (in the sense that we did not see the full range of patterning expected from our CA simulations), leading us to turn to the phenomenological modelling techniques of Section 2.2.2, we present our discrete attempts below for completeness. We consider a straightforward nearest-neighbour model. Note that we arbitrarily chose to first model the Majority conceptual model (Section 2.2). As its failure led to us abandoning this line of enquiry, we did not carry out similar attempts for the Single-Cell conceptual model (Section 2.2), and so do not present such work here.

Time-step attempt

Creating a discrete model of the Majority conceptual model presented in Section 2.2 seems an obvious first choice in this problem, which is clearly discrete. To begin, we consider only the one dimensional case for ease of calculation. In the $1D$ case, the dead cell at position x, say, is only affected by its neighbours at positions $x - h$ and $x + h$ i.e. we consider a nearest-neighbour model.

We begin by considering a simple time-step method: we assume that the probability of a cell at position x and time t being of type A is given by $p(x, t)$. (Note that if a cell is not of type A, it must be type B. Therefore we can find the probability of a cell being type B from looking at the probability of that cell being type A, and so do not need to consider both cell types in our equations.) For now, we assume that the cell at x has already died at time t; we are just interested in the cell type produced at position x at time $t+\tau$. We further assume that the probabilities themselves are a sufficient representation of the "voting" method outlined in the Majority conceptual model (Section 2.2). Then the following equation represents the probability of a cell at position x being of type A at time $t + \tau$, with h being the length of a typical cell:

$$p(x, t + \tau) = \tfrac{1}{2}[p(x - h, t) + p(x + h, t)]. \tag{2.3}$$

This very simple equation, on expansion via Taylor series, collapses down to a basic diffusion equation as $\tau \to 0$ with $\frac{h^2}{\tau} = \mathcal{O}_s(1)$ when considering only terms up to second order. It therefore fails to replicate the behaviour seen in our Majority CA simulations (see Section 2.2.1, Figure 2.2, top and middle panels). It also fails to represent our Majority conceptual model correctly, as the posed algorithm is certainly not one of diffusion. Therefore a more considered approach is needed.

Time-step with a probability function, f

We now explicitly model the "voting" system of the Majority conceptual model that very firmly causes the dead cell to become either of type B or A, not a diffused mix of the two, in an attempt to prevent the model from collapsing down to a diffusion equation in the continuous limit. We introduce a probability function f, where f is a symmetric function that goes from 0 to 1. This function allows that a dead cell will become either fully of type A or fully of type B.

Such a function can be applied to our $1D$ probability problem very easily: a cell at position x can either be surrounded by two A cells, two B cells, or an A and a B cell (twice). Then the probability that the cell in question will become type A, when taking our strictly symmetric function into account, is given by the probability that it is surrounded by two A cells ($p(x-h,t)\,p(x+h,t)$), plus half the probability that is surrounded by an A and a B cell ($\frac{1}{2}\,[p(x+h,t)(1-p(x-h,t)) + p(x-h,t)(1-$

$p(x+h,t))]$). So

$$p(x,t+\tau) = p(x-h,t)p(x+h,t) + \tfrac{1}{2}[p(x+h,t) - p(x+h,t)p(x-h,t) + p(x-h,t) - p(x-h,t)p(x+h,t)]$$

$$= p(x-h,t)p(x+h,t) + \tfrac{1}{2}[p(x+h,t) + p(x-h,t) - 2p(x+h,t)p(x-h,t)]$$

$$= \tfrac{1}{2}[p(x-h,t) + p(x+h,t)],$$

which is in fact the same probability as in (2.3), and so we once again obtain a diffusion equation.

Time-step with a death term

We now alter our assumption regarding cell death, and instead include the probability of the death of a cell in our model, again to try to prevent the model from collapsing into a diffusion equation in the continuous limit. We again stick to modelling the Majority conceptual model, and remain in one dimension as in the previous sections. Let the probability of cell survival per time step be given by the constant Q (so that one expects survival probability to decrease with the length of time involved). Then the probability of a cell dying is given by $1-Q$, and (2.3) becomes

$$p(x,t+\tau) = Q\,p(x,t) + (1-Q)\,\tfrac{1}{2}[(p(x-h,t) + p(x+h,t)]. \qquad (2.4)$$

Again, Taylor expanding and letting $\tau \to 0$ with $\frac{h^2}{\tau} = \mathcal{O}_s(1) = D$, say, leads us to obtain

$$\frac{\partial p}{\partial t} = (1-Q)D\frac{\partial^2 p}{\partial x^2}, \qquad (2.5)$$

which is simply a variant of the diffusion equation.

A two dimensional approach

In a final attempt to see if taking a discrete model to a continuous limit will produce an equation which is not just one of diffusion, we remove our simplifying assumption that we are operating in a $1D$ domain, as our CA are in $2D$. We therefore create a $2D$ model of the Majority conceptual model i.e. one that considers all eight neighbouring cells, not just the cells immediately to the right and left of the central cell.

If $p_{i,j}(t)$ is the probability of a cell at position (x_i, y_j) and time t, being of type A, then $\frac{1}{8}\left[\,8p_{i,j}(t) + 3h^2\frac{\partial^2 p}{\partial x^2} + 3h^2\frac{\partial^2 p}{\partial y^2}\,\right]$ is the average probability of the neighbouring eight cells being type A (by Taylor expansion and simplification; h is the length of a lattice site). Let everything be as in equation (2.4), except that now we make Q time dependent, and we replace our $1D$ probability (2.3) with our $2D$ probability for eight cells. This brings us closer to our Majority conceptual model. Then $Q_{i,j}(t, t+\tau)$ is the probability of the cell at position (x_i, y_j) staying alive in the interval $t \to t+\tau$, and so the probability of a cell at (x, y) being type A at time $t+\tau$ is given by:

$$p_{i,j}(t+\tau) = p_{i,j}(t)\, Q_{i,j}(t, t+\tau) + (1 - Q_{i,j}(t, t+\tau)[(p_{i,j}(t+\tau) + (\delta h)^2]$$

where $(\delta h)^2 = \frac{3}{8}\, h^2\, \frac{\partial^2 p}{\partial x^2} + \frac{3}{8}\, h^2\, \frac{\partial^2 p}{\partial y^2}$. Let $Q_{i,j}(t, t+\tau) = 1 - \tau\hat{Q}$, $\hat{Q}$ constant. Then as $\tau \to\ 0$, $Q \to 1$ i.e. the probability of staying alive over the time interval increases as that time interval decreases. With this substitution, we can rewrite our model as

$$p_{i,j}(t+\tau) = p_{i,j}(t)\,(1 - \tau\hat{Q}) + \tau\hat{Q}\,[(p_{i,j}(t+\tau) + (\delta h)^2]$$

which, by considering terms of order 1 only, and by letting $\tau \to\ 0$ as before, reduces to a diffusion model.

Limitations of our discrete approaches

It is natural at this point to reflect on why the discrete approach that we employed led to a simple diffusion equation that does not represent our system correctly. In the continuous limit of a discrete model we become concerned not with the state of an individual cell, but with the change in phenotype across the whole lattice. In the discrete scheme this movement depends – with equal emphasis – on the phenotype of neighbouring cells. Although all discrete models are, by their nature, non-local, our particular problem requires this non-locality to be retained in the continuous limit. That is to say, the type of cell that is born always depends on the types of some surrounding cells – the problem cannot be collapsed down to a point. However, in our derivation of continuous limits of discrete models, the change in cell type across the lattice becomes dependent on the phenotype of all cells in the lattice, with equal emphasis placed everywhere. So the models simply become a representation of diffusion, which fails to represent our algorithm accurately.

It is not only our particular algorithm which will fail in this way. Any phenomenon which relies on a permanently non-local term will experience similar difficulties, for those reasons stated above. To avoid this problem, one could look at correlations. Correlations account for interactions between sites, for example, the dependence between the probabilities between two positions A and B in space. This is something that may be pursued in future work.

In terms of modelling actual biology, the failure of our modelling attempts above reflect most closely the difficulty found in obtaining a model of cell adhesion, which is an intrinsically non-local process. Although many lattice-based models have been developed for this process (see Deutsch & Dormann, 2005, for a review), and some lattice-free models (see the review by Galle et al, 2006), there has been little in the way of explicit continuous modelling. Various attempts have been made, mainly by treating cell adhesion as a surface tension on the boundary of a growing tumour (see Chaplain, 1996; Byrne & Chaplain, 1996; Cristini et al., 2003; Frieboes et al., 2006; Macklin & Lowengrub, 2007). This paucity of models is due to the difficulty of representing an intrinsically non-local phenomenon in a continuous framework, and contrasts with the many successful models seen of biologically local phenomena such as chemotaxis (for a recent review of chemotaxis models, see Hillen & Painter, 2007). Meanwhile, the most successful continuous model of cell adhesion so far has been that of Armstrong et al. (2006) which uses an integral term to retain the non-local element of the problem in the continuous case.

2.5.2 Cellular Automata

Updating methods

During the course of our investigations, we considered whether a difference in updating method will affect the outcome of our CA simulations, as mentioned in Section 2.2.1. To investigate this possibility fully, we ran simulations of the Single-Cell model twice, once with the CA updated synchronously and the other with it updated asynchronously. The results are shown in Figure 2.12. As can be seen, there is very little difference between the two sets of figures, with the asynchronously updated figures showing slightly more coarsening than the synchronous ones. However, the result of both populations being mixed across the domain is the same for each type of updating method, leaving us able to choose our preferred updating method without concern for numerical artifacts. The end results for the Majority model are also the same whether updated asynchronously or synchronously (not shown).

Island initial conditions

In Section 2.3.2, we mention that we investigate what happens to 'island' initial conditions in the CA Majority model. The outcome of that simulation is in Figure 2.13. We see that the island does indeed shrink over time until it disappears, as previously stated. We now also investigate island initial conditions for the CA Single-Cell model. Here, the island does not shrink, but rather breaks up and spreads across the domain (Figure 2.14). This is as expected from our analysis and simulations in Sections 2.2.3 and 2.3.1 – both cell lines persist over time, with neither cell type dying out completely. Whilst in the continuous model simulations this leads to a homogeneous spread of evenly mixed cell types across the domain, in this CA simulation we see an inhomogeneous mix of both populations, much as in the mixed initial conditions

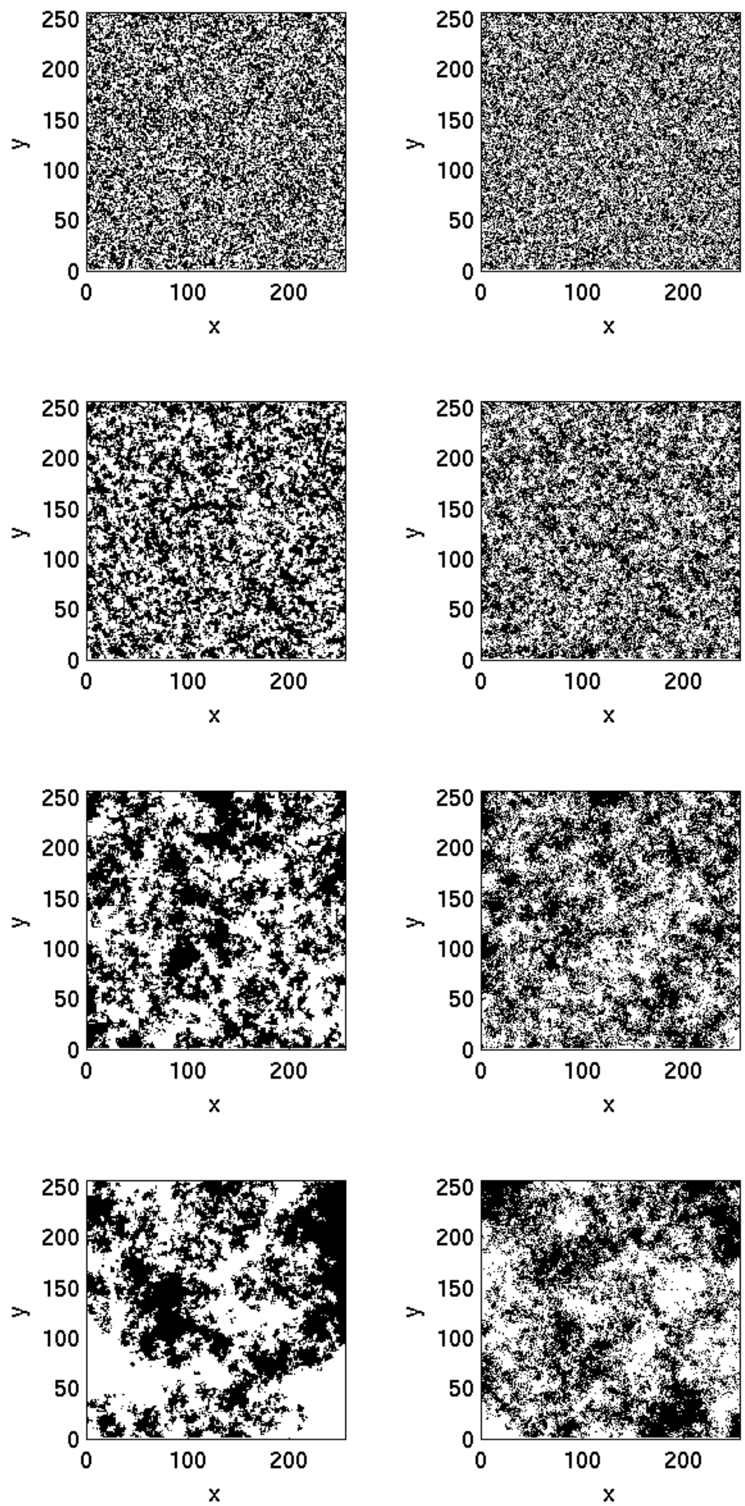

Figure 2.12: Legend on next page.

Figure 2.12: Comparison of asynchronous (left) and synchronous (right) updating for solution of the CA for the Single-Cell conceptual model as described in Section 2.2.1. Figures are at times $t = 256 \times 256 \times n$ for the asynchronously updated model, and at times $t = n$ for the synchronously updated one, for, from top to bottom, $n = 1, 10, 100, 1000$. Although direct comparisons cannot be made, similar aggregating behaviour is seen in both figures. The CA is updated according to the process described in Figure 2.1(b) for the asynchronous model, with the synchronous model following the same algorithm apart from the change to updating time as described in Section 2.2.1. The grid used was of size 256×256. On the boundary, only those cells in the domain are considered in the neighbourhood i.e. the neighbourhood is reduced in size. For more numerical details, see Chapter 5.

scenario for the CA (Figure 2.2, lower panels).

2.5.3 Attempts at generating stripes with the continuous model

As can be seen throughout this chapter, stripes nearly always fail to be generated. This is partly due to the fact that the system for generating patterns is not robust but depends very much on the initial conditions being used, and partly due to the wavelengths of stripes being larger than the domain length used in the two dimensional simulations. Since our two dimensional code is very time consuming, running simulations on a much larger domain is impractical. However, since preliminary one dimensional results suggest that we will see stripes on sufficiently large domains (see the following Chapter, Section 3.4.1, for some one dimensional results for a similar model), we attempt to create stripes in various ways, with some success. We discuss these attempts below.

Decreasing the sensing radius

From looking at one dimensional results for the model (3.7) (see Chapter 3, Section 3.4.1), which when $\alpha_1 = \alpha_2$ and $a = 1 - b$, is the same as the model (2.1), we can see that stripes form over a length scale that is wider than our two dimensional domain. So, using precisely the same two dimensional initial conditions and parameters for the simulation of the Locally Biased model which produced the stripe boundary in Figure 2.6, bottom panels, we decrease the sensing radius from 1 to 0.3 to simulate a larger domain, whilst keeping the actual domain size the same, namely 10×10 with 100×100 grid points; thus $\delta x = 0.1$, as in previous simulations. The expectation is that, as decreasing the sensing radius mathematically has the same effect as increasing the domain length, we will see stripes without having significantly increased the simulation time in the way that a larger domain with more grid points would. Note that for this simulation we use an exact copy of the randomly generated initial conditions that were used in Figure 2.6, bottom panels, since these are initial conditions which we

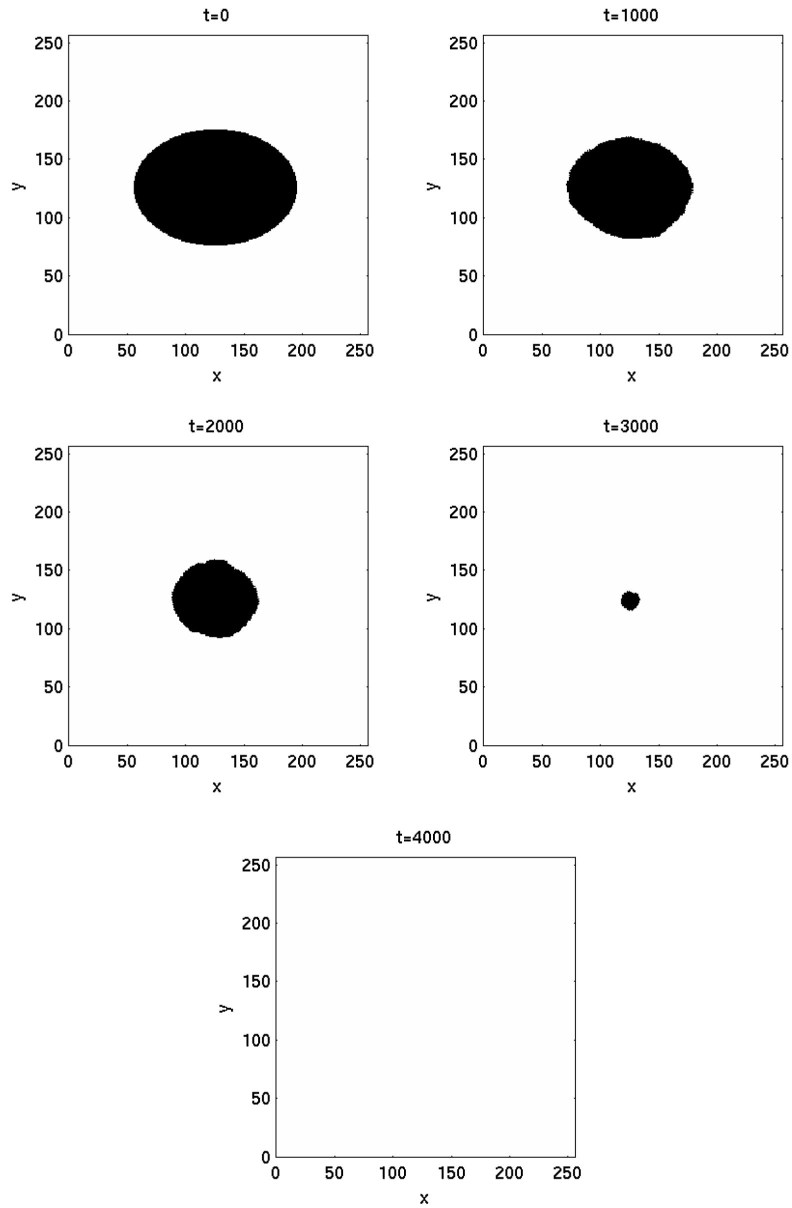

Figure 2.13: Solution of the Majority CA with island initial conditons at times $t = 0$, $t = 1000$, $t = 2000$, $t = 3000$ and $t = 4000$, updated as in Figure 2.1(a), although synchronously as discussed in Sections 2.2.1 and 2.5.2. Here we see domination by the cell type with greater initial proportion. The CA is carried out on a grid of size 256×256. Cells are updated according to the proportion of cells of their type within their 8 cell neighbourhood: if this numbers more than 0.5, the cell remains of its type; if less than 0.5, the cell becomes the opposing cell type; if the proportion is exactly 0.5, the updated cell type is chosen randomly. On the boundary and at the corners of the domain, only the cell type of those cells in the domain are considered, and an average is taken over that reduced number of cells. The initial island is an ellipse centred at in the domain at $(x, y) = (125, 125)$, with a height from the centre of 50 grid points and a width from the centre of 70 grid points.

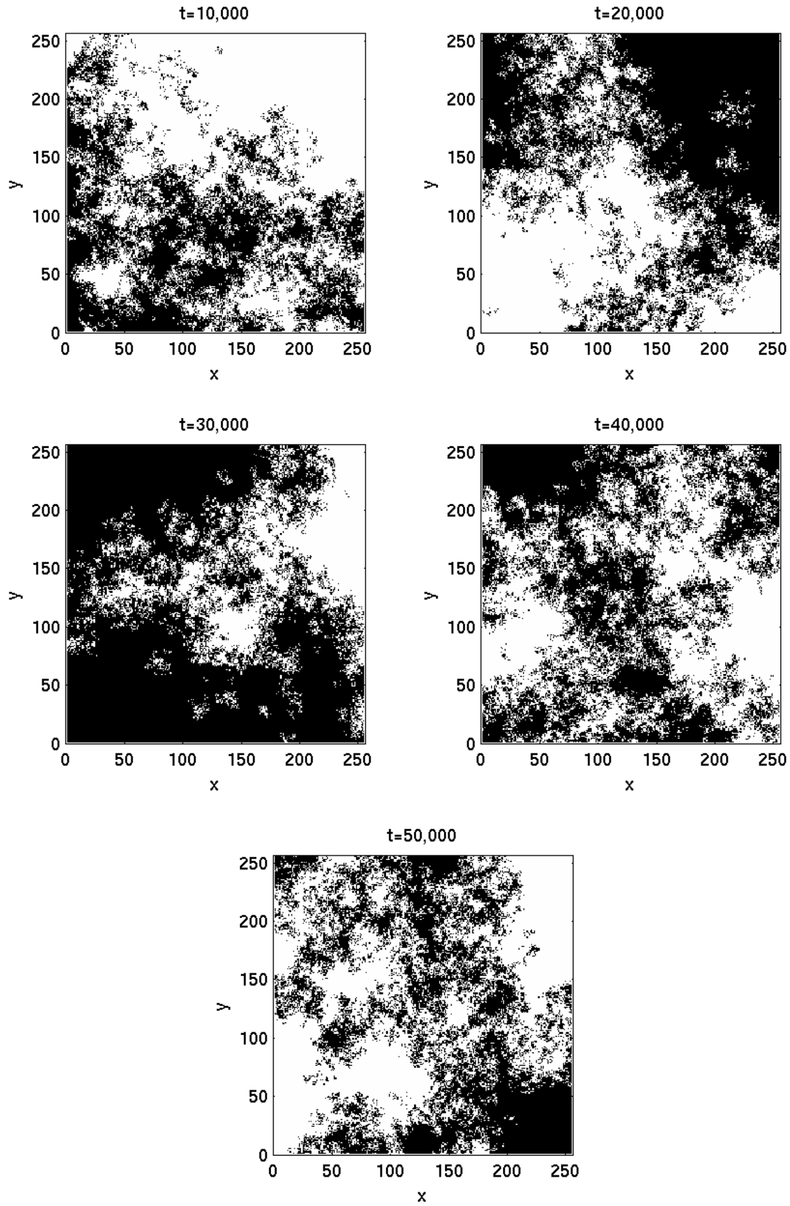

Figure 2.14: Solution of the Single-Cell CA with island initial conditions as in Figure 2.13, recorded at dimensionless times $t = 100,000$, $t = 200,000$, $t = 300,000$, $t = 400,000$ and $t = 500,000$. We see that neither cell type dominates over time. The CA is updated using a synchronous version of the algorithm described in Figure 2.1(b) according to a single rule: a cell chooses randomly one of its 8 neighbours, and updates to become the same cell type of that neighbour. All other details are as in Figure 2.13

know can generate a stripe boundary. This particular simulation does not, however, produce vertical or horizontal stripes, but rather a single stripe of sorts across the diagonal of the domain. Over time this "stripe" expands until the entire domain consists only of one population, leaving us without any patterning (Figure 2.15).

Decreasing the sensing radius and increasing grid points

We now keep the sensing radius at its new value of 0.3, but increase the number of grid points to 300×300. This means that there will be the same number of grid points inside each integral as in the original simulation. This should mean that our randomly generated initial conditions will be closer to those used in Figure 2.6 than those in Figure 2.15, since our initial conditions are generated at each grid point. We again use exactly the same seed for the random number generator used in the initial conditions as we did in Figure 2.6, bottom panels. Again, however, we fail to see multiple stripes, and are left with just a single cell type across the domain.

Original sensing radius on a larger domain

We move on to consider the effect of simply increasing the original domain size and number of grid points, whilst keeping $R = 1$ and again using the same seed for the random number generator as was used previously. On a 20×20 domain with 200×200 grid points, no stripes or stripe boundaries appear – the system goes to a one population steady state (not shown).

Mirroring the initial conditions

Finally we try to mirror the random initial conditions of the original stripe boundary-producing simulation across a widened domain. That is, we extend the domain to a 20×10 domain, and reflect the exact inital conditions of domain points 1 to 10 from the simulation in Figure 2.6, bottom panels, along domain points 11 to 20, thereby ensuring that the initial conditions which first created a stripe boundary are reflected exactly in the second half of the domain (choosing the same seed for the random number generator ensures that exactly the same random initial conditions are produced at each grid point as before). Recall that stripes nearly always fail to be generated in our system, partly as the system for generating patterns is not robust, and partly due to the wavelengths of stripes being larger than the domain length used in the original two dimensional simulations. Hence, through mirroring, we extend the random initial conditions that produced a stripe boundary in the original simulations in order to produce an entire stripe across the domain. This simulation does produce three stripes, and these stripes remain stable over long times, proving that our model has the ability to generate stipe patterns (Figure 2.17).

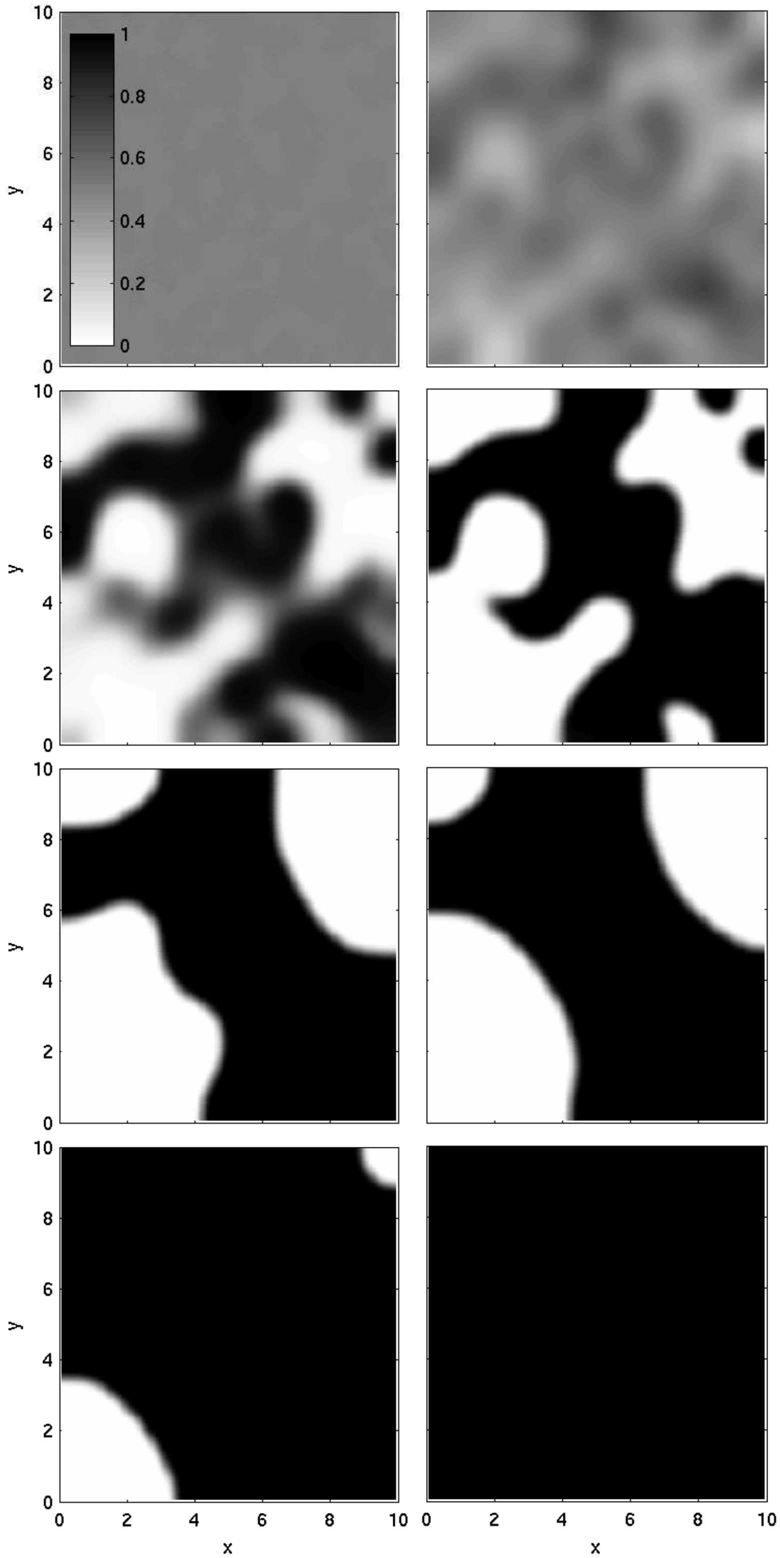

Figure 2.15: Results for the Locally Biased model (2.1) with mixed initial conditions, plotted at output times $t = 0.001$, $t = 0.005$, $t = 0.007$, $t = 0.01$, $t = 0.05$, $t = 0.1$, $t = 0.5$ and $t = 0.7$. We see that whilst a pattern resembling a diagonal stripe does form initially, this is transient, and we are soon left with a one population steady state. All details are as in Figure 2.6, lower panel, except for $R = 0.3$.

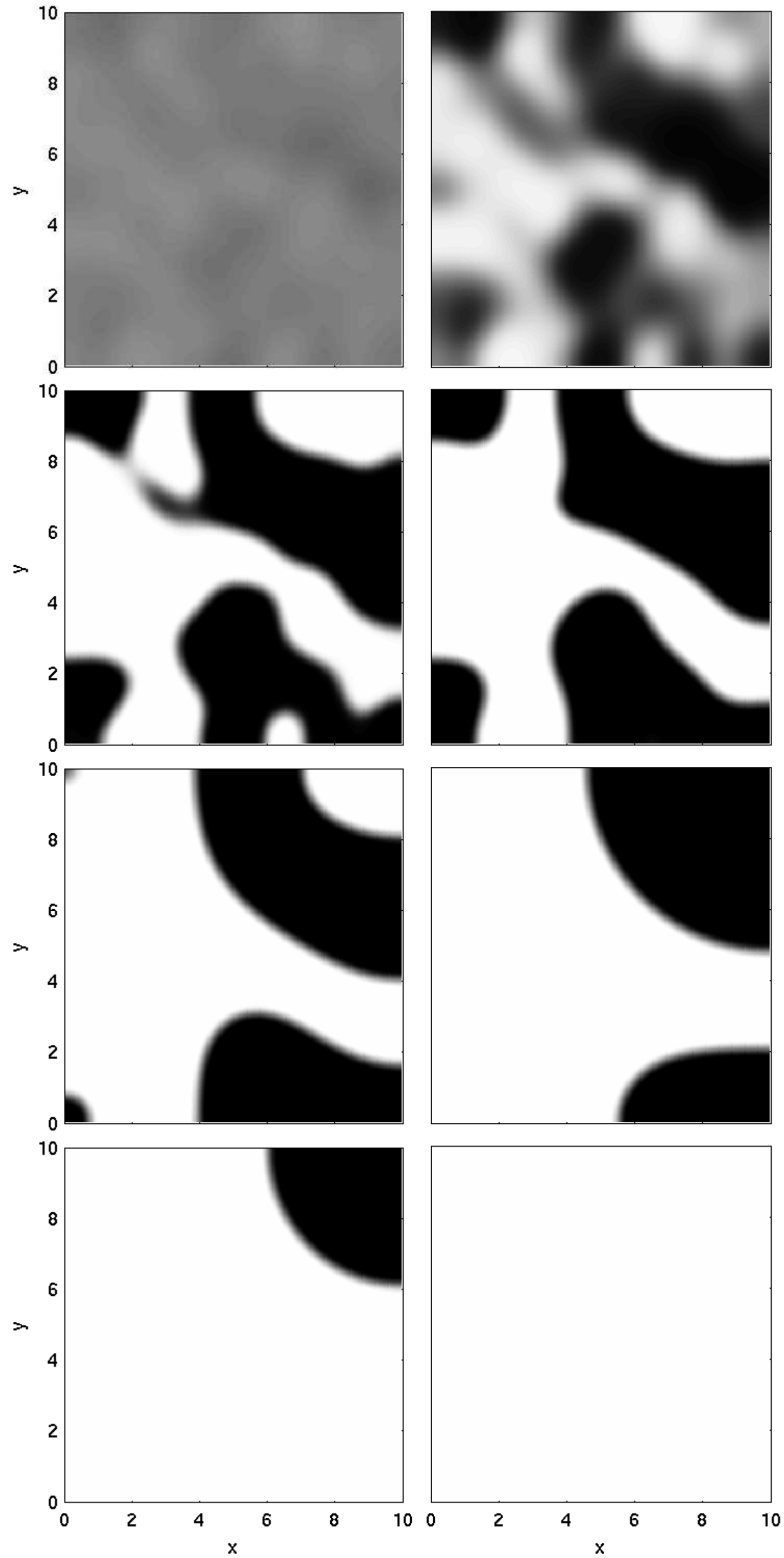

Figure 2.16: Results for the Locally Biased model (2.1) with mixed initial conditions, plotted at output times $t = 0.01$, $t = 0.015$, $t = 0.02$, $t = 0.04$, $t = 0.2$, $t = 1$, $t = 5$ and $t = 9$. We see that only blobs form, and that we are soon left with a one population steady state. All details are as in Figure 2.15, except for $nx = ny = 300$.

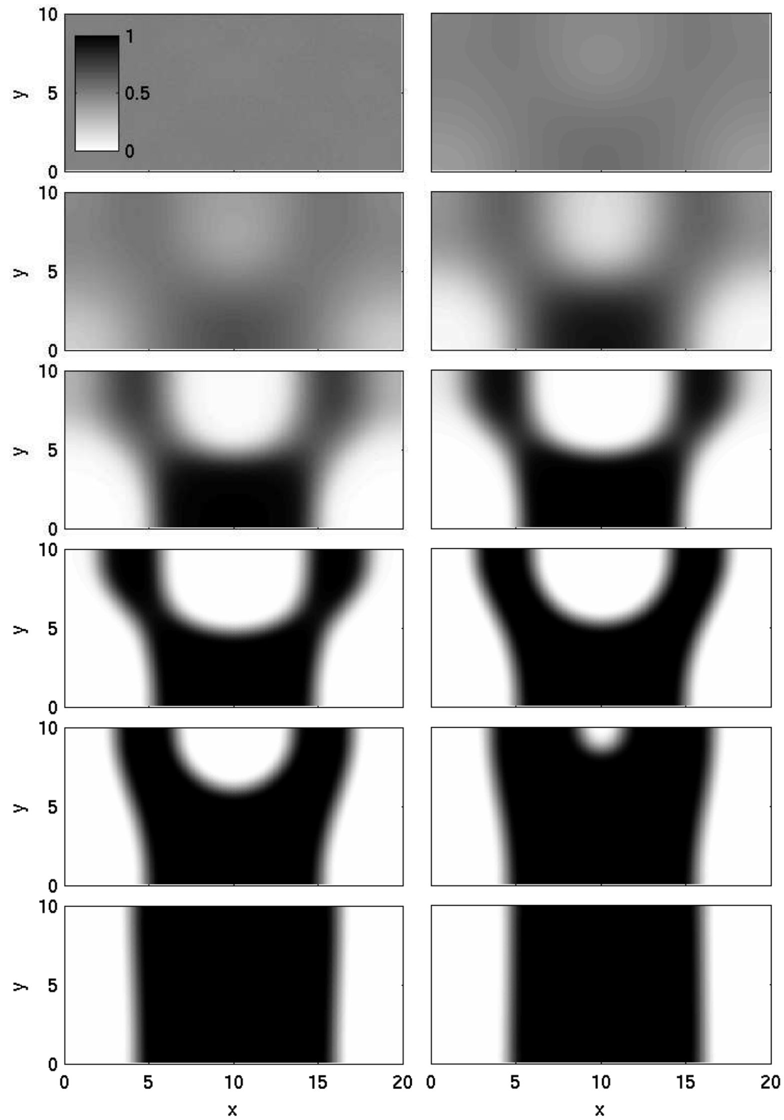

Figure 2.17: Results for the Locally Biased model (2.1) with mixed initial conditions as in Figure 2.6 from $x \in (0, 10]$, mirrored in $x \in (10, 20]$. We see the formation of stable stripes. Times shown are at $t = 0.001$, $t = 0.005$, $t = 0.006$, $t = 0.007$, $t = 0.008$, $t = 0.009$, $t = 0.01$, $t = 0.02$, $t = 0.03$, $t = 0.05$, $t = 0.1$ and $t = 2$. All numerical details areas in Figure 2.6, except for the domain which is extended to a 20×10 domain, and the initial conditions as detailed in the text.

We also try repeating, rather than mirroring, the initial conditions across the extended domain, so that in the second half of the domain the initial conditions at point $n/2 + x$ say, where n is our total number of points, are the same as those at point x. We again generate stable stripes (Figure 2.18), this time four of them. The stripes here are of noticably different widths, showing that not only can the model produce multiple stripes, but that it is also not bound to producing stripes of even widths. This suggests that the Locally Biased mechanism could be the driver behind a wide range of stripe patterns.

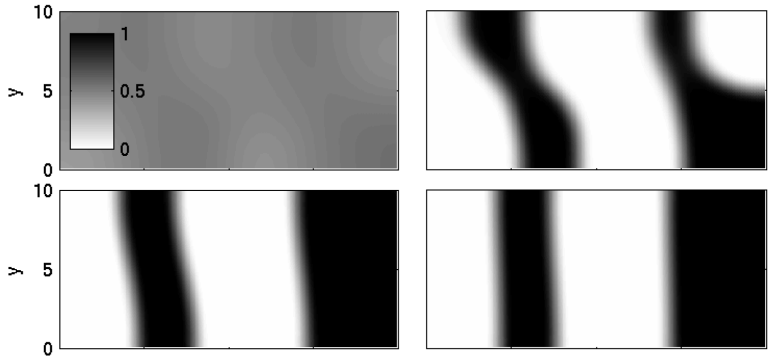

Figure 2.18: Results for the Locally Biased model (2.1) with mixed initial conditions as in Figure 2.6 from $x \in (0, 10]$, repeated for $x \in (10, 20]$. We again see the formation of stable stripes. Times shown are at $t = 0.01$, $t = 0.02$, $t = 0.1$ and $t = 0.2$. All numerical details areas in Figure 2.6, except for the domain which is extended to a 20×10 domain, and the initial conditions as detailed in the text.

Chapter 3

How Does Cellular Contact Affect Differentiation Mediated Pattern Formation?

In this chapter, we move on our investigation of how the local environment affects spatial patterns by considering various mechanisms for cellular differentiation. Using the work in Chapter 2 as a starting point, we now extend the model, presenting a two population continuous integrodifferential model of cell differentiation, using a non-local term to describe the influence of the local environment on differentiation. We investigate three different versions of the model, with differentiation being cell autonomous, regulated via a community effect, or weakly dependent on the local cellular environment. We consider the spatial patterns that such different modes of differentiation produce, and investigate the formation of both stripes and spots by the model. We show that pattern formation only occurs when differentiation is regulated by a strong community effect. In this case, permanent spatial patterns only occur under a precise relationship between the parameters characterising cell dynamics, although transient patterns can persist for biologically relevant timescales when this condition is relaxed. In all cases, the long lived patterns consist only of stripes, not spots.

This chapter contains material that was originally published in Bulletin of Mathematical Biology (2011), 73: 1529-1558, and was a collaboration between Jenny Bloomfield, Kevin Painter and Jonathan Sherratt. The continuous models were developed by Jenny Bloomfield, Kevin Painter and Jonathan Sherratt. Jenny Bloomfield and Jonathan Sherratt worked together on the proof and analysis in Section 3.3. Kevin Painter and Jenny Bloomfield worked together on the writing of numerical code. Jenny Bloomfield did all of the numerical studies and wrote the paper, with comments provided by the co-authors.

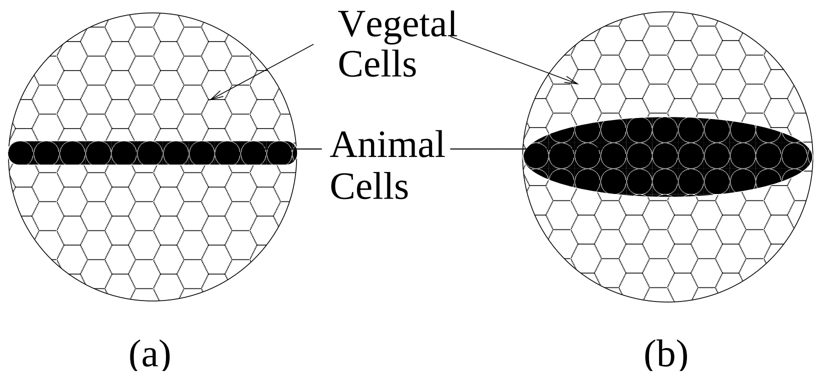

Figure 3.1: Schematic of the sandwich experiments originally carried out by Gurdon (1988) to demonstrate the community effect. Part (a) shows a monolayer of blastula derived animal cells in a vegetal sandwich, while part (b) shows a solid grouping. Gurdon saw differentiation take place only in the latter case. See Gurdon (1988) for more details.

3.1 Introduction

Cellular differentiation describes the development of specialised cells from undeveloped precursor cells. This process occurs in nearly all cells but the mechanisms that drive it are not well understood. Further investigation is necessary to increase our understanding of this fundamental process.

There are many ways that differentiation is induced in cells. For example, it has been widely hypothesised that a cell may sometimes differentiate according to a "community effect". This term was first coined by Gurdon (1988) to explain the phenomenon seen in experiments in which clusters of cells differentiate into a particular tissue type, but individual cells from the same undifferentiated group do not (Gurdon, 1988). Gurdon postulated that undifferentiated cells, which receive signals from other undifferentiated cells in the immediate environment, will differentiate together into the same cell type once a threshold level of these signals is reached. This process allows cells in the same spatial area to keep the correct gene expression necessary for the tissue they create. The community effect has since been widely investigated, with many studies expanding on Gurdon's original experiment and explanation. In his original experiments, Gurdon (1988) placed *Xenopus* ectoderm cells in a sandwich of endoderm (see Figure 3.1). A monolayer of ectodermal cells did not differentiate into muscle, whereas a solid group of cells did. Gurdon and colleagues went on to explore other similar experiments in *Xenopus*, all with the same results (Kato and Gurdon, 1993; Gurdon et al., 1993a). Similar experiments with blastula cells of zebrafish and dorsal ectoderm cells of Drosophila were also carried out (reviewed by Gurdon et al., 1993b). They too showed that groups of cells were needed for the normal differentiation fate of these cells to be achieved.

Weston et al. (1994) explored a different cell group within *Xenopus* to see if cells other than those fated to differentiate into muscle were also driven by the community effect. They studied *Xenopus* notochord, and through sandwich experiments similar to those described above, they concluded that a community effect was also necessary for notochord differentiation. Meanwhile, Cossu et al. (1995) discovered a community effect in mouse myoblast differentiation (Cossu et al., 1995). Work on mice continued, and a community effect was observed at work in the survival of melanoblasts (Aubin-Houzelstein et al., 1998), and even postulated as a possible explanation for the correct migration of Purkinje cells in the cerebellar cortex of mice (Yang et al., 2002), taking the concept of the community effect a long way from its original definition.

Experimental work on a community effect continues, with the latest work looking at cardiomyonocite cells and heartbeat stabilisation (Kaneko et al., 2007; Kojima et al., 2006), but even though a community effect has been explored for over twenty years there are still some fundamental questions that remain unanswered. One of these is how a community effect is achieved biochemically, and this question has been considered to some extent both experimentally and theoretically. Kim et al. (1999) postulated that neuregulin may act as an induction signal for the community effect in myogenic differentiation in rats, while eFGF protein is suggested as the likely factor in *Xenopus* (Standley et al., 2001). Various other community factors have been suggested for different cells and species (see Buckingham (2003) for a review). Meanwhile in his theoretical paper, Monk (1997) created continuous diffusion-based models to explore mechanisms for the community effect in *Xenopus* myogenesis. The biochemical basis of a community effect remains an important research question, but we do not consider it further in this paper.

Rather, we focus on what the community effect means for the spatial structure of tissues; more concretely, what kind of spatial structure does the community effect permit that other forms of differentiation do not? This question has not previously been explored, with research effort concentrated on the underlying biochemistry. However, it is an important question, as answering it will give insight into the geometries of tissues that the community effect can construct and, conversely, those that it cannot. We begin by briefly considering various forms of differentiation, before moving on to look at the community effect in the context of a specific example.

As mentioned above, cell differentiation is not always regulated by the community effect. For example, "autonomous differentiation" may occur at a certain stage in the cell cycle. In this scenario, the local environment of a cell has no effect on its fate; the cell's progress is intrinsic (Salazar-Ciudad et al., 2003). An example of this is the differentiation of mature somites (Buckingham, 2003).

Homoiogenetic induction is another method of inducing differentiation. Here, cells induced to differentiate first self-induce a signal to send to their neighbours, instructing those cells to do the same. In this way the signal is passed from cell to cell, until such time has lapsed that any undifferentiated cells no longer respond. This process, like the community effect, allows a sharp boundary to be formed between different tissues; for example, it has been suggested as an explanation for the formation of spatial patterns seen in the neural plate of amphibians (Nieuwkoop, 1997).

However, as we are interested mainly in a community effect, and the influence it has on the spatial structure of tissue, we focus on that phenomenon here, paying particular attention to the example of a community effect in zebrafish pigmentation. While Gurdon (1993a) provides a very precise definition of the community effect, stating that it is "an interaction among many nearby progenitor cells, as a result of which these cells activate tissue-specific genes and differentiate coordinately as a uniform population", the term has picked up a wider, more general use, as seen in the literature discussed above. In the case of zebrafish pigmentation, the term has been used to describe the preference of pigment cells for their own kind.

The stripes on adult zebrafish form during metamorphosis, which begins at about 14 days post fertilisation (Parichy, 2000). The stripes are mainly made up of two cell types, melanophores (black) and xanthophores (yellow), while iridiphores (translucent) are found spread across the body. These pigmented cells, or chromatophores, arise from latent precursors during metamorphosis. These form black and yellow horizontal stripes across the body of the zebrafish, creating two melanophore stripes by 28 days (Parichy, 2000). It has been postulated that the death of melanophores in areas of high xanthophore density is due to a community effect: melanophores require other melanophores nearby in order to survive, and a sole melanophore is not viable (Parichy, 2000; Buckingham, 2003). This suggests that an undifferentiated precursor will be biased into differentiating into the same type as those differentiated pigment cells surrounding it, as otherwise it will fail to survive.

It is worth noting that biological experiments such as the sandwich experiments described above (see Figure 3.1) are intrinsically disruptive. *In vitro* experiments remove cells from their natural environment, and while the *in vivo* grafting of cells may produce useful results, it also alters the natural cellular environment. This leads to potential discrepancies in the interpretation of experimental results (see Nagai et al. (2005), for a discussion of this in zebrafish blastoderm transplantation). Therefore, in order to further understand and isolate the basic process of cell differentiation, we turn to theoretical models.

We are aware of only one previous theoretical model for the regulation of spatial structure by the community effect, which concerns the zebrafish pigmentation example. Moreira & Deutsch (2005) created a cellular automata model which combines ideas about a community effect with those of attraction and repulsion between melanophores and xanthophores. In their model, a cell will differentiate into a melanophore unless there are more xanthophores in the neighbourhood, in which case a xanthophore will arise. The model successfully reproduces the stripe patterns of the zebrafish.

In this paper, we offer an integrodifferential equation model to describe cell differentiation. In contrast to Moreira & Deutsch (2005), who assume intercellular adhesion and precursor cell differentiation to be simultaneous drivers for the pattern formation process, we explore what dynamics can be produced through differentiation alone, without considering any adhesive effects. In this way we are able to explore the extent to which the community effect alone is able to produce the patterns seen in zebrafish patterning.

In Section 3.2 we present the model alongside a comprehensive biological reasoning for its formulation, basing our ideas on the example of zebrafish pigmentation. From this model we create three variations to explore various differentiation scenarios, looking in particular at a community effect and the strength of the response needed in order to create patterning. In Section 3.3, we go on to consider the stability of the homogeneous steady states of the model, and present various mathematical analyses of them. In Section 3.4 we present the results of numerical simulations, while in Section 3.5 we discuss the outcome of these results. We will show that regulation of differentiation by a strong community effect can generate spatial patterns. The patterns always consist of stripes rather than spots. *De novo* pattern formation only occurs for some initial conditions, showing that regulation of differentiation via a community effect is not a robust pattern formation mechanism. However, it is an effective mechanism for pattern maintenance, provided that the death rates of the two cell populations involved are relatively similar. Note that our model of a community effect assumes that differentiation is only influenced by the local environment and not by any other predisposition towards a particular cell type, so that differentiation rates for this case are always equal across the two populations. We will show that permanent patterns require equal death rates, but that long-lived transient patterns occur when the death rates of the two cell populations are different but relatively close to one another.

3.2 Modelling Cellular Differentiation: A continuous approach

As mentioned in Section 3.1, cell differentiation is a complex process. We build our model by considering the biological data available. In the development of our model we bear in mind the particular example of zebrafish pigmentation, although the model we produce is general enough to be applied to many other scenarios, some of which are discussed at the end of this paper. We begin by considering a stem cell population that is both constant in space and time, and multipotent. To explain these two assumptions, we describe the nature of stem cells, and also cite some evidence that a community effect has a role in the final cell fate of precursors produced from multipotent stem cells. Furthermore, we consider available data regarding the specific case of zebrafish.

In epithelia, stem cells lie in the basal layer. Unlike other cells, stem cells do not terminally differentiate, but rather undergo repeated proliferation. After mitosis, in place of one stem cell there is typically one stem cell and one undifferentiated cell, with the latter differentiating and joining the general cell population. Stem cells have in some cases been shown to be multipotent i.e. the precursor cell that a stem cell produces can have a variety of different fates. These precursors may be multipotent themselves, and, in the peripheral nervous system for example, they are seen to display fate restrictions due to a community effect (Paratore et al., 2002; see also Galli et al. (2000) for further discussions of multipotency in stem cells and precursor cells, and of the role of a community effect in affecting cell fates in neural stem cells). Note that in the case of zebrafish, it is not known whether the precursors of chromatophores are stem cells or not, although there has been some recent evidence to suggest that they are (Hultman et al., 2010). Whether the precursors are multipotent or not is also unknown, despite speculation on this point (Parichy, 2007).

In the creation of a general model then, we first begin with separate stem and precursor cell populations. We assume that we have a stem cell population that remains at a constant level due to self renewal. We further assume that it produces precursor cells at a constant rate, and that each time a precursor cell differentiates, a stem cell produces a new precursor. In this way a constant supply of precursor cells is achieved, leading to the population of precursor cells having a constant density p, say, independent of both space and time. Note that we assume that the precursor cells are evenly distributed across the body. In the zebrafish example, although the spatial distribution of precursors across the fish body has not yet been elucidated, in the fin they have been shown to be evenly distributed (Rawls & Johnson, 2000), and so we believe this to be a reasonable assumption.

We now look in detail at our terminally differentiated cells: we assume there to be two populations, similar to the melanophores and xanthophores found in zebrafish. We call these two differentiated cell populations $a(x,t)$ and $b(x,t)$, with

$$\frac{\partial a}{\partial t} = k_1 f_1(a(x,t), b(x,t)) - \tilde{\alpha}_1 a(x,t) \qquad \frac{\partial b}{\partial t} = k_2 f_2(a(x,t), b(x,t)) - \tilde{\alpha}_2 b(x,t). \quad (3.1)$$

Note that the coefficients in the two linear death terms generally differ since the cell populations A and B are different. From the above discussion, we have that the rate of differentiation of precursor cells is constant, and thus

$$k_1 f_1(a(x,t), b(x,t)) + k_2 f_2(a(x,t), b(x,t)) = \tilde{\alpha_0} p, \text{ say, a constant.} \tag{3.2}$$

We now investigate further the differentiation functions f_1 and f_2 of our model. As discussed in Section 3.1, the type of cell that the precursor cell differentiates into may depend very much on the differentiated cells in the local environment, or on a cell's predisposition towards a particular cell type. We will explore three options: autonomous cell differentiation; differentiation according to a community effect; and a third option, in which the response to the ratio of existing differentiated cell types in the local environment is strictly linear.

Bearing the above three scenarios in mind, we propose three different forms for the f_1 and f_2 functions, all satisfying (3.2). Since in each case we wish both cell lines A and B to be produced by the same mode of differentiation, we assume that $f_1(a, b) = f_2(b, a)$. We wish to consider the extent to which the surrounding environment affects the differentiation of precursor cells. We assume that only cells of type A and B affect the fate decisions of the precursor cells. To consider this effect, we first construct an integral which calculates the proportion of differentiated A and B cells within a certain radius R. Such a representation of cell environment via an integral term has been used previously in many contexts including cell sorting (Armstrong et al., 2006), development (Sekimura et al., 1999; Armstrong et al., 2009; Green et al., 2010, Bloomfield et al., 2010), chemotaxis (Hillen & Painter, 2009) and cancer (Gerisch & Chaplain, 2008; Sherratt et al., 2009; Painter et al., 2010). The cell sensing radius R of the integral reflects the capacity of a cell to directly sense its environment via, for example, filopodial contact. The amount of contact made is important as it determines the extracellular signals that a cell receives. For example, Numb is a signalling protein that is widely expressed during embryogenesis. Numb is thought to inhibit Notch activity, thereby altering communication between an undifferentiated precursor cell and other cells in its local environment. This changed level of communication then allows the precursor cell to choose a different fate to that of a second precursor cell which may contain a different amount of Numb, and which hence experiences a different level of cell-cell communication (Zhong, 2008). We use a function $f(I)$, where I is our local environment integral, to vary the contact and communication of precursor cells with differentiated cells.

Our model in one dimension is given by

$$\frac{\partial a}{\partial t} = k_1 f(I_a) - \tilde{\alpha}_1 a, \quad I_a = \frac{1}{\text{area}} \int_{-R}^{R} \frac{a(x+x_0)}{a(x+x_0)+b(x+x_0)} dx_0$$

$$\frac{\partial b}{\partial t} = k_2 f(I_b) - \tilde{\alpha}_2 b, \quad I_b = \frac{1}{\text{area}} \int_{-R}^{R} \frac{b(x+x_0)}{a(x+x_0)+b(x+x_0)} dx_0. \tag{3.3}$$

Note that in this model, the integrals I_a and $I_b \in [0,1]$ since they consider the proportion of A or B cells in the sensing region of a cell; moreover $I_a + I_b = 1$. The integral is normalised over the area. Typically this is simply the length $2R$, but near the edge of the spatial domain being considered, we truncate the integral over the portion of area which lies within our domain. Equations (3.3) can be nondimensionalised: substituting $t = t^* P/\tilde{\alpha_0} p$, $a = a^* P$, $b = b^* P$, $\tilde{\alpha_1} = \alpha_1 \tilde{\alpha_0} p/P$, $\tilde{\alpha_2} = \alpha_2 \tilde{\alpha_0} p/P$, $k_2/k_1 = k^*$, $f(\cdot) = f(\cdot)^* \tilde{\alpha_0} p/k_1$, where P is the dimensionalised measure of the cell population density, and dropping the $*$'s, gives $\partial a/\partial t = f(I_a) - \alpha_1 a$ and $\partial b/\partial t = kf(I_b) - \alpha_2 b$, with condition (3.2) becoming

$$f(I_a) + kf(I_b) = 1. \tag{3.4}$$

The dimensionless parameter k reflects a possible predisposition of precursor cells to differentiate into cells of type A ($k < 1$) or B ($k > 1$); except where specifically stated, we will restrict our attention to the unbiased case $k = 1$.

Note that the integral I is undefined if $a = b = 0$. Since we are modelling the differentiation of precursor cells into A and B cells from an initial precursor cell layer, the case $a = b = 0$ is definitely relevant in applications. A reasonable assumption is that precursor cells would differentiate into cells of type A and B at equal rates in this case. Therefore, we could amend the model to cover the case $a = b = 0$ via a differentiation function that varied between $1/2$ and $f(I_a)$ (for cell type A) as the overall cell density increased. Such an alteration would be a significant complication mathematically, and would be important for the transient behaviour of populations with low initial density. However, it would not affect long term behaviours, and so we restrict our attention to a model of the form (3.3).

To more fully represent epithelia, which we model as a monolayer, we extend (3.3) to two dimensions. The complete dimensionless equations are then

$$
\begin{aligned}
\frac{\partial a}{\partial t} &= f(I_a) - \alpha_1 a \\
I_a &= \frac{1}{\text{area}} \int_0^R \int_0^{2\pi} \frac{a(\underline{x} + r\underline{\eta})}{a(\underline{x} + r\underline{\eta}) + b(\underline{x} + r\underline{\eta})} r d\theta dr \\
\frac{\partial b}{\partial t} &= k f(I_b) - \alpha_2 b \\
I_b &= \frac{1}{\text{area}} \int_0^R \int_0^{2\pi} \frac{b(\underline{x} + r\underline{\eta})}{a(\underline{x} + r\underline{\eta}) + b(\underline{x} + r\underline{\eta})} r d\theta dr.
\end{aligned} \tag{3.5}
$$

Here $a(\underline{x}, t)$ and $b(\underline{x}, t)$ are our populations of cell types A and B respectively at two dimensional position $\underline{x}$ and time t; other cells within I_a and I_b are located relative to $a(\underline{x}, t)$ and $b(\underline{x}, t)$ by reference to both the distance r along the sensing radius R, and the unit vector $\underline{\eta} = (\cos\theta, \sin\theta)$; α_1 and α_2 are our nondimensional death rates and k is the nondimensional differentiation rate; and finally the integral is normalised over the area of the integration region, which is πR^2 at points away from the boundaries of the domain, and truncated appropriately at points whose distance from the boundaries is less than R. The function f is different for our three differentiation scenarios, and we discuss its form below.

3.2.1 The Three Models

Model one: differentiation is independent of the local environment

First we consider cell autonomous differentiation. In this scenario, differentiation into A or B cells will simply occur at a constant rate, predetermined by various internal cell factors such as the presence of different gene regulatory proteins, without reference to the local environment. Such a mechanism occurs in mature somites which are differentiating into muscle (see, for example, Buckingham (2003)). Differentiation into the two cell types is assumed to occur at different rates, so we allow $k \neq 1$ for this model. We put $f(I_a) = f(I_b)$ a constant, which must equal $1/(1+k)$ to satisfy condition (3.4). Then (3.5) becomes

$$
\frac{da(t)}{dt} = 1/(1+k) - \alpha_1 a(t) \quad \text{and} \quad \frac{db(t)}{dt} = k/(1+k) - \alpha_2 b(t). \tag{3.6}
$$

We call this our **Cell Autonomous Model**.

Models two and three: differentiation is dependent on the local environment

We now turn to modelling a community effect. As we do not wish precursor cells to have a predisposition to differentiate into one cell type over another, i.e. we wish differentiation to be only affected by the local environment, we fix $k = 1$. The mathematical formulation of f requires only that: (i) f is monotonically increasing, so that a larger proportion of cell type A, say, in the sensing region makes it more likely that a precursor cell will differentiate into A; and (ii) $f(I_a) = 1 - f(I_b)$, with $f(1/2) = 1/2$, to avoid any bias between the two cell types. Condition (3.4) is then immediately satisfied.

To model a strong community effect, we are interested in an f which, although continuous, is close to a step function. We choose f as described in Figure 3.2(a). This represents the idea that an undifferentiated precursor cell is strongly biased towards differentiating into the same type as those in the majority around it, as occurs in the community effect described in Section 3.1. We call this version of the model the **Community Model**, and it is given by

$$\frac{\partial a}{\partial t} = f(I_a) - \alpha_1 a \quad \text{and} \quad \frac{\partial b}{\partial t} = f(I_b) - \alpha_2 b, \tag{3.7}$$

with I_a, I_b and all other details as in Section 3.2, equation (3.5).

Another quite distinct case that is also biologically relevant involves f being linear (Figure 3.2(b)). This relates to two different biological scenarios. One of these is that contact with only one surrounding cell is made, and that contact alone determines the outcome of differentiation; such behaviour would be more likely when contact with cells is inhibited, for example due to the presence of Numb as described above. An alternative scenario is that contact occurs with all neighbouring cells, but that the resulting effect on differentiation pathways is linear; this would depend on underlying biochemical details. In either case the response to the signals produced is linear. We call this version the **Single Cell Model**; mathematically it is represented as in (3.7), but with a linear f.

Note that although our two choices of f for the two local environment models (3.7) are not comprehensive, with many other reasonable options, f must be monotonic to reflect a community effect as described in Section 3.1, and symmetric in the sense that $f(1/2 - x) + f(1/2 + x) = 1, \forall x \in (0, 1/2)$. This symmetry ensures that differentiation is unbiased towards either of the two cell types. Then our two choices of f represent two extremes of this understanding of a community effect and should therefore encompass all types of community effect related behaviour.

We now explore the long term behaviour we can expect from the three models by carrying out some analysis, looking at the location and stability of spatially homoge-

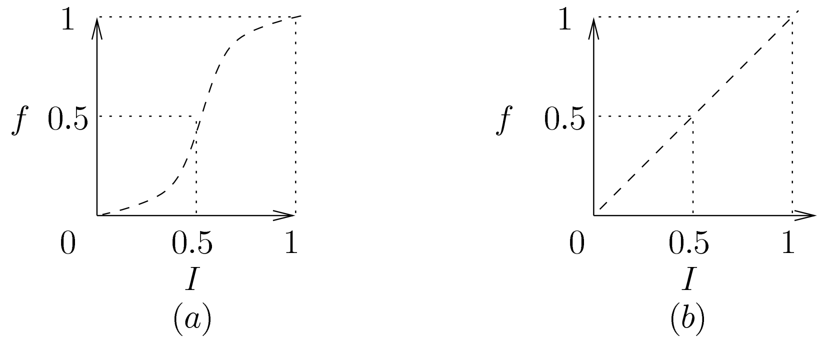

Figure 3.2: The above figure demonstrates the two chosen f functions for differentiation in our model (3.7). Figure (a) shows a smooth continuous function that is close to a step function. This case represents our Community Model. Figure (b) shows a linear f, which represents our Single Cell Model.

neous steady states.

3.3 Analysis of the Three Models

3.3.1 Analysis of the Autonomous Model

We have that (3.6) is given by $\frac{da(t)}{dt} = 1/(1+k) - \alpha_1 a(t)$ and $\frac{db(t)}{dt} = k/(1+k) - \alpha_2 b(t)$. The only steady state of this simple model is given by $(1/\alpha_1(1+k), (k/\alpha_2(1+k))$, with $k \neq 1$. Noting that this is a system of two uncoupled ordinary differential equations, it is immediately clear that this steady state is globally stable for all positive constants α_1 and α_2. This means that this system will always go to, and remain at, a homogeneous mixing of both cell types, in a proportion that is dictated by the relative rates of differentiation and apoptosis.

3.3.2 Analysis of the Community Model

Here the model (3.7) is given by $\frac{\partial a}{\partial t} = f(I_a) - \alpha_1 a$ and $\frac{\partial b}{\partial t} = f(I_b) - \alpha_2 b$ with all details as in Section 3.2, equation (3.5), and f a continuous approximation to a step function as is described in Section 3.2.1, and illustrated in Figure 3.2(a). The question is what homogeneous steady states are possible, and what combination of stabilities can occur as parameters are varied. Knowing this will allow us to see what the likely long term scenarios for the system are, and when they might occur. Biologically, this gives us further insight into the type of differentiation dynamics we can expect in real systems.

Sufficient condition for only three steady states

Let $x = a/(a+b)$. Then $1 - x = 1 - a/(a+b) = b/(a+b)$, and so we have uniform steady states at

$$a = \tfrac{1}{\alpha_1} f(x) \quad \text{and} \quad b = \tfrac{1}{\alpha_2} f(1-x). \tag{3.8}$$

Since $bx = a(1-x)$, (3.8) implies that $\frac{1}{\alpha_1} f(x)(1-x) = \frac{1}{\alpha_2} f(1-x)x$ at a steady state, i.e. $0 = F(x) \equiv (1-x)f(x) - \gamma x f(1-x)$, where $\gamma = \alpha_1/\alpha_2$. Therefore there are steady states at $x = 0$ and $x = 1$, corresponding to populations composed entirely of cell type B and cell type A respectively[1]. Coexistence steady states must satisfy

$$f(x) = \frac{\gamma x}{1 - x + \gamma x}. \tag{3.9}$$

We now show that for a large class of functional forms of f there is only one non-trivial solution of (3.9), i.e. there is only one coexistence steady state.

Proposition Let f be a smooth, monotonically increasing function, $f : [0,1] \longrightarrow [0,1]$ such that the following hold:

$$f(x) = 1 - f(1-x) \,\forall\, x \in (0,1) \tag{3.10}$$

$$f(x) = x \text{ for } x = 0, \tfrac{1}{2}, 1;\ f(x) \neq x \text{ otherwise} \tag{3.11}$$

$$f'(x) = 0 \text{ for } x = 0, 1;\ f'(x) \neq 0 \text{ otherwise} \tag{3.12}$$

$$\begin{aligned} &f''(x) > 16\gamma(1-\gamma)/(\gamma+1)^3 \,\forall\, x \in (0, \tfrac{1}{2}) \text{ when } \gamma \in (0,1) \\ &f''(x) < 16\gamma(1-\gamma)/(\gamma+1)^3 \,\forall\, x \in (\tfrac{1}{2}, 1) \text{ when } \gamma > 1. \end{aligned} \tag{3.13}$$

Then the equations (3.7) have exactly three steady state solutions.

Note that these conditions are sufficient but not necessary. Mathematically, the restriction on the size of f'' prevents multiple steady states on $(0,1)$ by limiting the curvature of f.

Proof. Let $\gamma \in (0,1)$. We begin by defining $g(x) = \gamma x/(1 - x + \gamma x)$; then (3.9) implies that steady states satisfy $f(x) = g(x)$. Trivially $f(0) = g(0) = 0$ and $f(1) = g(1) = 1$, giving us our first two solutions. We now just need to prove the uniqueness of solutions on $(0,1)$ under the above conditions.

We have that $g'(0) = \gamma > f'(0)$, and $g'(1) = \frac{1}{\gamma} > f'(1)$. Therefore $f(x) = g(x)$ must have at least one solution with $x \in (0,1)$. Suppose first that $\gamma \in (0,1)$. Then

[1] Note that the trivial case $(0,0)$ is also a steady state.

straightforward calculation shows that $g(x) < x \, \forall \, x \in (0,1)$, while (3.11) and (3.12) imply that $f(x) \geq x \, \forall \, x \in [\frac{1}{2}, 1)$. Therefore there are no solutions of (3.9) on $[\frac{1}{2}, 1)$. Moreover, (3.13) implies that $f''(x) > g''(1/2) > g''(x) \quad \forall \, x \in (0, \frac{1}{2})$. This ensures that $g(x)$ does not meet $f(x)$ more than once for $x \in (0, \frac{1}{2})$ giving us exactly one more solution to $f(x) = g(x)$ as required. The proof is similar in the $\gamma > 1$ case. Note that for $\gamma = 1$ the case is trivial, as here $g(x) = x$, and so by (3.11) there are only three steady states. $\square$

Stabilities of steady states

Calculation of the stability matrix of (3.7) shows that the single species steady states are both stable. We now show that when there are just three homogeneous steady states of the Community Model (3.7), where f satisfies conditions (3.10) – (3.13), the (unique) coexistence steady state is unstable. Define $F(x) = (1-x)f(x) - \gamma x f(1-x)$ as before. Then, by (3.10),

$$F'(x) = f(x)(\gamma - 1) + f'(x)(1 - x - \gamma x) - \gamma. \tag{3.14}$$

Then, assuming (3.11) and (3.12) hold, $F'(0) = -\gamma < 0$ and $F'(1) = -1 < 0$ by direct substitution into (3.14). Therefore by continuity there must be a point $x^* \in (0,1)$ with $F(x^*) = 0$ and through which F increases with x. Since we assume only three steady states, this must be the unique coexistence steady state. We now calculate the stability matrix of the spatially uniform version of (3.7). The equations in question are $\frac{\partial a}{\partial t} = f(x) - \alpha_1 a$ and $\frac{\partial b}{\partial t} = f(x) - \alpha_2 b$. The stability matrix is then

$$\begin{pmatrix} f'(x)b(a+b)^{-2} - \alpha_1 & -f'(x)a(a+b)^{-2} \\ -f'(1-x)b(a+b)^{-2} & f'(1-x)a(a+b)^{-2} - \alpha_2 \end{pmatrix},$$

and the determinant is given by

$$-\alpha_2/(a+b)\left(f'(x)(1-x) + \gamma x f'(1-x) - \alpha_1(a+b)\right).$$

Since at the steady states, $f(x) = \alpha_1$ and $f(1-x) = \alpha_2$, straightforward calculation shows that the determinant is $-\alpha_2 F'(x)/(a+b)$. Therefore if $F'(x^*) > 0$, the steady state is unstable, so that the only stable homogeneous states consist of populations composed of only one of the cell types. We have not attempted an investigation of the behaviour when $F'(x^*) = 0$, which would require a calculation of the centre manifold of the ODE system, but our expectation is that the coexistence steady state will always be unstable in this case also.

3.3.3 Analysis of the Single Cell Model

This model (3.7) is again given by $\frac{\partial a}{\partial t} = f(I_a) - \alpha_1 a$ and $\frac{\partial b}{\partial t} = f(I_b) - \alpha_2 b$, with f linear as discussed in Section 3.2.1 and illustrated in Figure 3.2(b). The steady states are either a continuum of steady states if the death rates α_1 and α_2 are equal, or single species steady states at $(1/\alpha_1, 0)$ or $(0, 1/\alpha_2)$ if α_1 does not equal α_2 (the steady states are found in the usual way i.e., by setting the model equations (3.7) equal to 0).

As the number of spatially uniform steady states in the Single Cell Model varies according to whether the death rate parameters are equal or not, we investigate the stability of the two cases separately.

Case 1: $\boldsymbol{\alpha_1 = \alpha_2}$

If $\alpha_1 = \alpha_2 = 1/c$, say, this model has a continuum of non-trivial spatially uniform steady states at $(a, b) = (a_s, c - a_s)$, $0 \leq a_s \leq c$. Straight-forward linear analysis shows that these steady states exhibit neutral stability. This means that we expect the system to remain at whatever population density of each cell type it began with. This is of particular interest biologically, as it suggests that in this case, there will be a persistence of both cell types over time. This also occurred in the Autonomous Model, but is in marked contrast to the behaviour seen in the Community Model.

We now explore what happens if, when $\alpha_1 = \alpha_2 = 1/c$, $a + b \neq c$ initially. Then we do not begin along the line of neutral stability – our populations must move onto it. To investigate this, we consider the case of two spatially homogeneous cell populations. We have

$$\frac{da}{dt} = a[1/(a + b) - 1/c] \tag{3.15a}$$

$$\frac{db}{dt} = b[1/(a + b) - 1/c] \tag{3.15b}$$

by simple rearrangement of the spatially homogeneous version of (3.7), with $c = 1/\alpha_1 = 1/\alpha_2$ as stated above. Combining (3.15a) and (3.15b) gives $da/dt = (a/b).(db/dt)$, which leads to

$$a = b/\Gamma \tag{3.16}$$

where Γ is a constant of integration. (3.16) can then be substituted back into (3.15a) to give a single equation for $a(t)$ only:

$$\frac{da}{dt} = a[1/(a + \Gamma a) - 1/c]. \tag{3.17}$$

Since Γ is constant, it can be found by looking at the initial values of a and b, i.e.

$$\Gamma = b_0/a_0, \tag{3.18}$$

where a_0 and b_0 are our initial conditions. Substituting (3.18) into (3.8) and (3.17) implies that a steady state with $a > 0$ must satisfy

$$a = ca_0/(a_0 + b_0), \quad b = cb_0/(a_0 + b_0)\,. \tag{3.19}$$

By looking at (3.17), we can further show that this solution is stable: if a is larger than our positive solution given by (3.19), then $\frac{da}{dt} < 0$, while if a is smaller, $\frac{da}{dt} > 0$.

Case 2: $\boldsymbol{\alpha_1 \neq \alpha_2}$

For this scenario, we have only the steady states $(a, b) = (\frac{1}{\alpha_1}, 0), (0, \frac{1}{\alpha_2})$ i.e. there is no coexistence steady state. Straight-forward linear analysis shows these states to be stable. This suggests that in this case, the system will always evolve to a single species steady state, suggesting dynamics that will be different to the Autonomous Model, but which may have some agreement with the Community Model.

3.3.4 Summary

This analysis of the three variations of our model has shown that the way in which differentiation is regulated by the contact between precursor cells and their local environment significantly alters the balance of cell types we can expect to see, as summarised in Table 3.1. This analysis of steady states and their stability provides a firm foundation for the numerical analysis of the spatiotemporal dynamics that develop from different initial conditions.

MODEL TYPE	STEADY STATE	TYPE	STABILITY
Community	$(\frac{1}{\alpha_1}, 0)$ or $(0, \frac{1}{\alpha_2})$	single species	stable
	(a_s, b_s)	coexistence	unstable
Autonomous	$(1/\alpha_1(k+1), k/\alpha_2(k+1))$	coexistence	stable
Single Cell	$(a_s, b_s) \in [0, c], c = 1/\alpha_1 = 1/\alpha_2$ if $\alpha_1 = \alpha_2$	coexistence	neutral
	$(\frac{1}{\alpha_1}, 0)$ or $(0, \frac{1}{\alpha_2})$ if $\alpha_1 \neq \alpha_2$	single species	stable

Table 3.1: A summary of stability of the steady states of the three models.

3.4 Numerical Analysis of the Three Models

While the linear analysis provides some insight into the expected model behaviour, we carry out a numerical study for further understanding. We first consider a one dimensional version of the model, using a simple numerical scheme that discretises the line integral through space, summing the integral over each point and averaging over the length. Similarly, our two dimensional numerical code discretises the circular domain of the integral, and then sums the integral over each of the grid squares within the circle. Although some of the area of the circle is lost at the boundaries, the calculation is fast and, with a fine lattice, it is reasonably accurate – for more on this, see Chapter 5. For the two dimensional case, more sophisticated numerical schemes for integrodifferential equations using techniques such as fast Fourier transforms to evaluate the integral are possible: see in particular Gerisch & Chaplain (2008) and Gerisch (2010). To solve the resulting system of ODEs, we use a fast and straightforward Euler method in the simple one dimensional case, while in the more complicated two dimensional case, we use ROWMAP (Weiner et al. 1997), a method that is particularly suited to solving stiff ODE initial value problems, and which automatically controls and adjusts time-step size. For more on all numerical methods used, see Chapter 5.

3.4.1 The one dimensional model results

We begin by investigating a homogeneous mix of cell populations with noise in order to explore the patterns created from a randomly mixed group of cells. Such random mixing is seen, for example, in the regeneration of ablated pigment cells in experiments on zebrafish, suggesting that pigment precursor cells in the zebrafish are distributed randomly (Yamaguchi et al., 2007). We investigate the Autonomous, Community and Single Cell Models in turn.

The Autonomous Model

First we look at the Autonomous Model (3.6). For all α_1's and α_2's, the system moves quickly to the steady state $(1/\alpha_1(k+1), k/\alpha_2(k+1))$, $k \neq 1$ as expected (not shown). The initial noise rapidly disappears, leaving solutions that are homogeneous across the domain, demonstrating that the system does not produce patterning.

The Community Model

We now consider the Community Model (3.7) with f as in Figure 3.2(a). We see that here, stripes sometimes develop from the random initial conditions, although they are transient unless $\alpha_1 = \alpha_2$ – this case is special as only here is the model balanced and bistable (i.e. there is a symmetry between the basins of attraction of the two stable steady states). Clearly stripe formation is not robust, as it is not always seen even if $\alpha_1 = \alpha_2$; we believe that the random initial conditions must not be too smooth if we want to see transient stripes, as the mechanism that drives patterning in the model is not strong enough to do so from flat initial conditions. Also, while stripes persist for longer as α_1 approaches α_2, they are permanent only if the death rates of the two cell populations are equal (Figure 3.3). The width of the stripes is dependent on the length of the sensing radius used (Figure 3.4, upper panel). This is as expected, since on an infinite domain, changing the sensing radius is equivalent to rescaling space. Obviously, both the timescale and the stripe width of interest depends on the biological system we are investigating; we discuss this for the specific case of pigmentation stripes on zebrafish in Section 3.5.

Finally, simulations with initial conditions consisting of stripes perturbed by a small amount of random noise indicate that the permanent stripes of the $\alpha_1 = \alpha_2$ case are stable to small perturbations (Figure 3.4, lower panel), while when $\alpha_1 \neq \alpha_2$, this is not the case even for α_1 close to α_2 (not shown). This has relevance to the concept of stripe maintenance, which we again discuss in detail in the context of the zebrafish example in Section 3.5.

The Single Cell Model

We complete our one dimensional study by considering the Single Cell Model (3.7), with f as in Figure 3.2(b). When $\alpha_1 \neq \alpha_2$, the system evolves to a homogeneous steady state as suggested by the analysis in Section 3.3.3 (not shown). However, when $\alpha_1 = \alpha_2$, we see a mix of both cell lines homogeneously across the domain, as suggested by the results in Section 3.3.3, with the long-term steady state being as predicted by equation (3.19) (Figure 3.5). Despite this difference in behaviour between the cases $\alpha_1 \neq \alpha_2$ and $\alpha_1 = \alpha_2$, the key implication is the same in both: we do not see patterning. Therefore only one of our three model types produces spatial patterns in one dimension: the Community Model, with $\alpha_1 = \alpha_2$ a necessary condition for permanent, stable patterns in that case.

We will now go on to investigate simulations on a two dimensional domain, in order to more effectively explore the spatial aspects of the models.

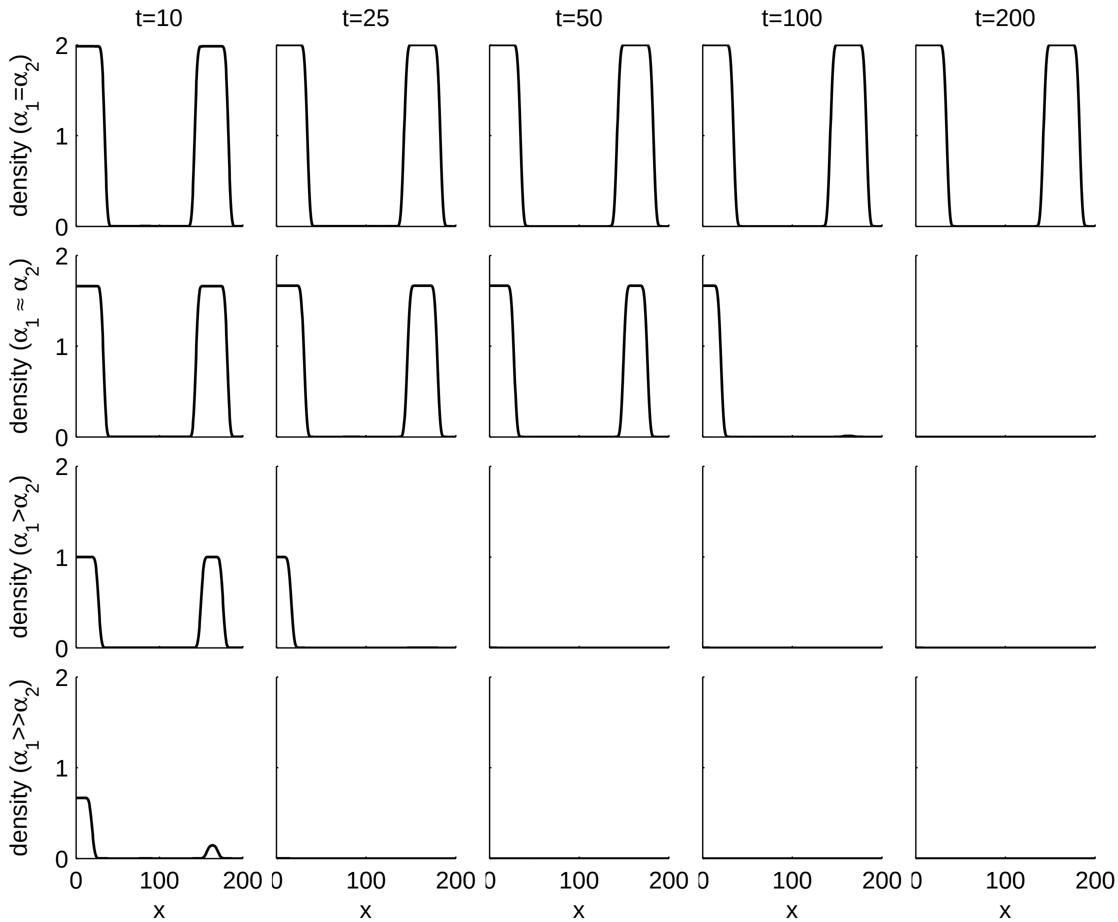

Figure 3.3: Solutions of the Community Model (3.7) with f as in Figure 3.2(a), in one dimension. We begin from random initial conditions. We plot the density of cell type A through space at dimensionless times indicated, and vary the death rates (note that the density of B is omitted for clarity, but satisfies $b \approx 1 - a$ throughout). The death rate $\alpha_2 = 0.5$ in all four cases, with $\alpha_1 = 0.5, 0.6, 1.0, 1.5$ (from the upper panel down). When the death rates of the two populations are equal (upper panel), stripes develop about 70% of the time (706 out of 1000 runs produced stripes that persisted for long simulation times). However, different death rates always eventually produce dominance of a single species across the domain, with the time taken for one species to dominate decreasing as the difference between the two death rates increases. Note that despite their piecewise linear appearance at this magnification scale, the solutions are in fact smooth. All other numerical details are as described in Section 3.4. Initially, random values between 0 and 0.02 are chosen for a and b at each numerical grid point, from a uniform distribution. The domain is of length 200 dimensionless space units. The function f is given by $f(I) = 0.5 \tanh(2 \tan(I\pi - 0.5\pi)) + 0.5$, a continuous approximation to a step function. The dimensionless parameter value $R = 10$. The space discretisation is $\Delta x = 0.5$, and the time discretisation is $\Delta t = 0.01$. For more details, see Chapter 5.

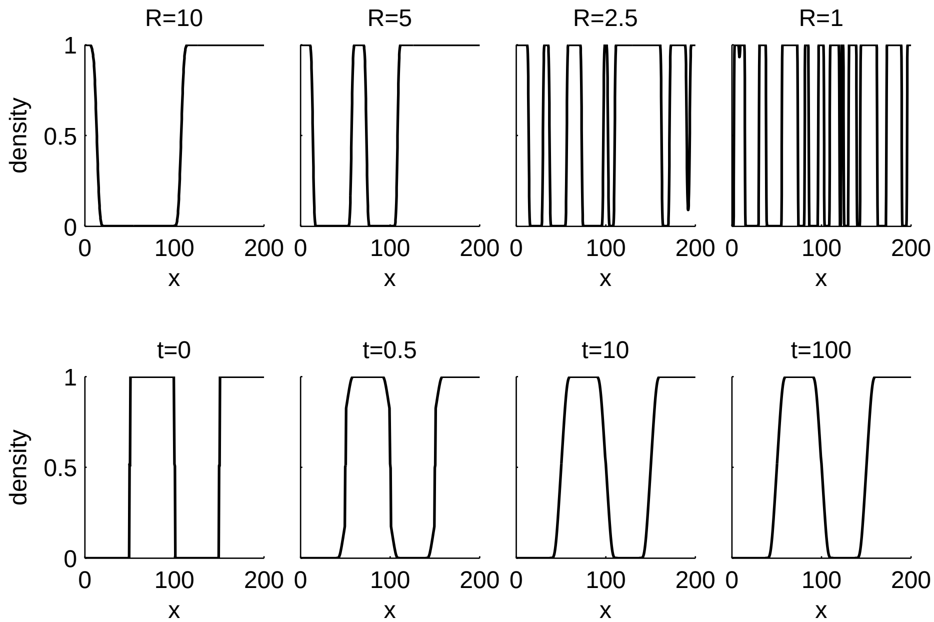

Figure 3.4: Upper panel: Solutions of the Community Model (3.7) with f as in Figure 3.2(a) in one dimension at time $t = 10$, demonstrating that different sizes of sensing radii produce differently sized stripes. We set $\alpha_1 = \alpha_2 = 1$, and adjust R as indicated. We see that decreasing R produces a decrease in stripe width. We set $\Delta x = 0.2$. All other numerical details are as in Figure 3.3. Lower panel: A solution of the Community Model (3.7) with f as in Figure 3.2(a) in one dimension at times $t = 0$, $t = 0.5$, $t = 10$ and $t = 100$, with initial conditions of stripes, perturbed by random noise. This shows that stripes are stable over time. The initial conditions are $a = 0.0$ for $x \in (0, 49.5)$ and $x \in (100.5, 149.5)$, $a = 1$ for $x \in (50.5, 99.5)$ and $x \in (150.5, 200)$, and $a = 0.5 + n_1/50$, $b = 0.5 + n_2/50$ for $x \in (49.5, 50.5)$, $x \in (99.5, 100.5)$ and $x \in (149.5, 150.5)$, where both n_1 and n_2 are random numbers between 0 and 1, chosen from a uniform distribution, calculated at each numerical grid point. The function f is given by $f(I) = 0.5\tanh(\tan(I\pi - 0.5\pi)) + 0.5$, a continuous approximation to a step function. We set $\alpha_1 = \alpha_2 = 1$, with all other numerical details as in Figure 3.3.

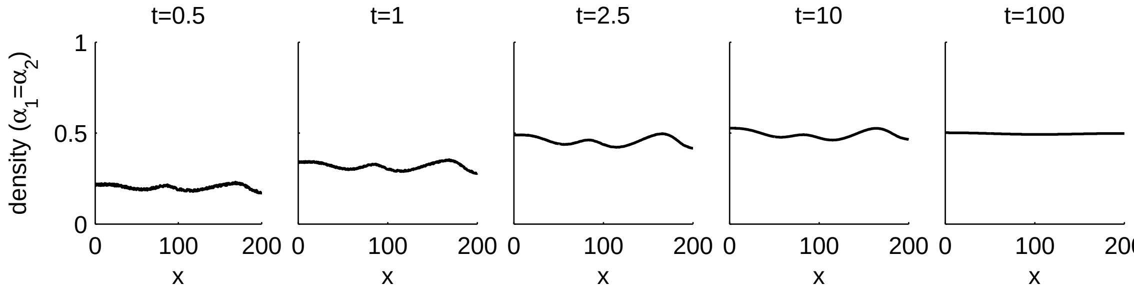

Figure 3.5: Solutions of the Single Cell Model (3.7) with f as in Figure 3.2(b) in one dimension, beginning from random initial conditions, and with equal death rates. We again plot the density of cell type A through space at dimensionless times indicated. We see that the system evolves to a homogeneous steady state, as expected from equation (3.19) and the analysis of Section 3.3.3. In 1000 simulations, we never saw stripes. We set $f(I) = I$ and $\alpha_1 = \alpha_2 = 1$, with all other numerical details as in Figure 3.3.

3.4.2 The two dimensional model results

We turn to $2 - D$ so that we can better explore the patterning seen in biological scenarios. We again begin by investigating a homogeneous mix of cell populations with a small amount of noise, for reasons discussed in Section 3.4.1.

The Autonomous Model

In this model, we see each cell population evolving to the steady state suggested in Section 3.3.1, spread homogeneously across the domain (not shown). These states are stable over time, and show that cell autonomous differentiation results in the persistence of both cell types. For our zebrafish example, this suggests that autonomous differentiation is not the sole process behind the differentiation of chromatophore precursors, since such a mode of differentiation will always fail to produce patterning.

The Community Model

We look at two separate cases, as suggested by our one-dimensional results in Section 3.4.1. We first consider the case where $\alpha_1 \neq \alpha_2$ i.e. the death rates of the two cell populations are distinct. We ran simulations with a variety of different $\alpha_1 \neq \alpha_2$ pairs, and a variety of different seeds for the noise in the initial conditions, for a 10×10 domain. In this case, the system always moves rapidly to a steady state, at which only the cell type with the smaller death rate is present, even when α_1 is close to α_2 (including, for example, $\alpha_1 = 0.99$, $\alpha_2 = 1.01$). In contrast to the one dimensional case, where transient stripes form when death rates are sufficiently close, here patterning is not seen across the domain. This could be to do with the size of our domain as well as the death rates, since the time-consuming nature of the simulations requires us to use a domain that is too small to show stripes of the wavenumber seen in the one dimensional simulations in Section 3.4.1 (each simulation currently takes a few days, so to carry out twenty simulations would be in the order of weeks). In a one dimensional simulation on a domain of length 10 (which is the side-length of our two dimensional domain) with equal death rates, we do not see multiple stripes as in Figure 3.3, but rather a single stripe (not shown). We discuss this in more detail below.

We now turn to the case $\alpha_1 = \alpha_2$. The death rates are then the same for the two populations, suggesting that they are of very similar type. Again we consider only a 10×10 square spatial domain. The system moves directly to a single species steady state in 15 out of 20 runs, and to a split domain in the other 5 runs (see Figure 3.6), showing the capability of the model to produce distinct boundaries between the two populations, in a manner consistent with the formation of stripes. The proportion 5/20 is much lower than that in the one dimensional case, which saw full stripes in 70% of cases. As mentioned above, this difference in proportions makes sense, since the one-dimensional geometry encourages stripes and, moreover, the domain is sufficiently long to see stripes of various wavenumbers. In contrast, the two dimensional 10×10 domain is too small to see such complete stripes form. In cases where we do not see a split domain, the final single species steady state is dependent on the initial conditions, with whichever cell type has the greater initial density being dominant.

The Single Cell Model

Again, we first consider the case $\alpha_1 \neq \alpha_2$ i.e. the death rates for the two populations are distinct. As in the Community Model, the system goes to a single species steady state, as suggested by our stability analysis (not shown). It is again the cell type with the smaller death rate to which the system evolves.

Next we let $\alpha_1 = \alpha_2 = 1/c$, where c is a constant as in Section 3.3.3. Here, stability analysis suggests that we will see a merging of the two initial populations into one spatially uniform population spread across the domain, with the two individual cell types being in the same proportion as they were at the beginning of the simulation, although now spread homogeneously. This is indeed what we see (Figure 3.7). Note that the short timescale shown in Figure 3.7 is relevant as the model has then reached a steady state. This behaviour contrasts with that in the Community Model, but is similar to the results of our Autonomous Model. When $a + b \neq c$ initially, the two cell types go to the densities suggested in Section 3.3.3, equation (3.19) (Figure 3.8).

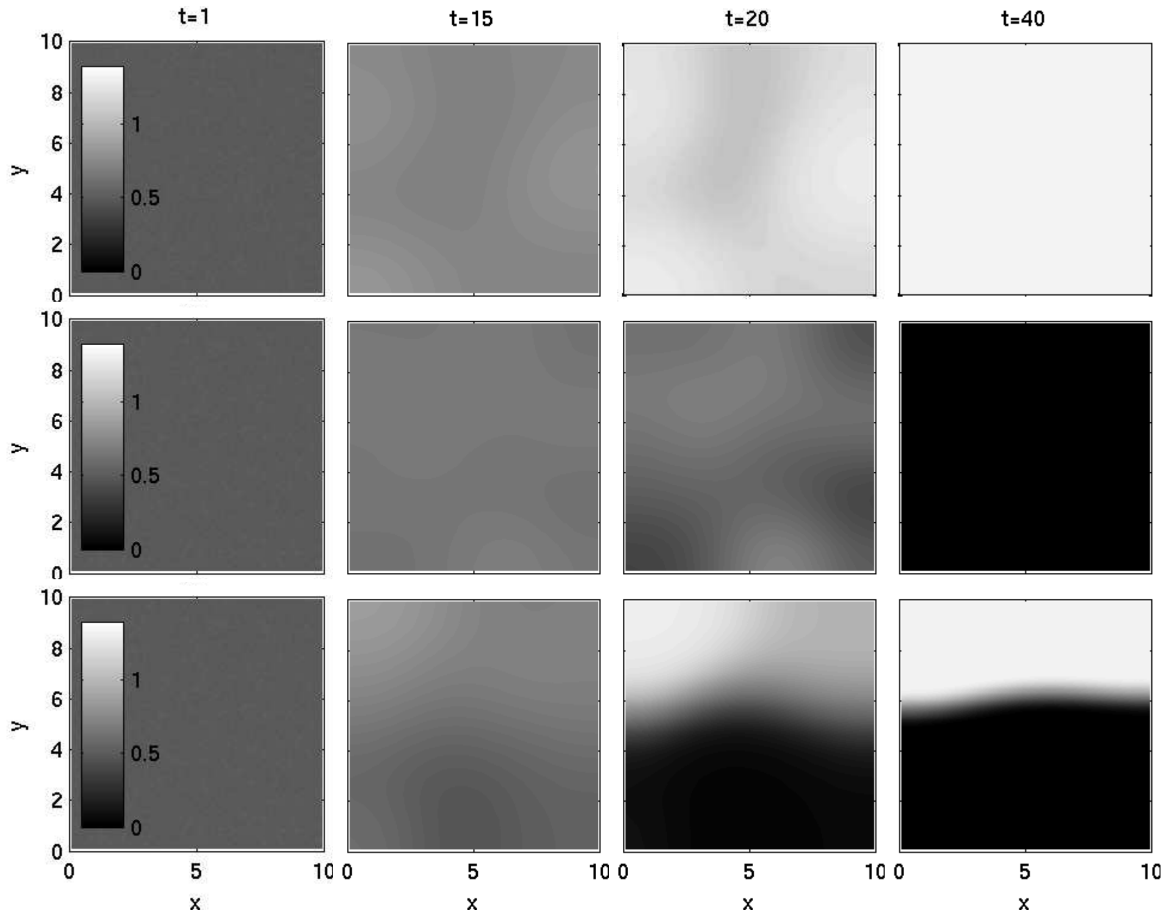

Figure 3.6: A solution to the Community Model (3.7) with f as in Figure 3.2(a) and with random initial conditions as described below. All numerical details are as described in Section 3.4. We plot the proportion of cells of type A in space at dimensionless times $t = 1$, $t = 15$, $t = 20$ and $t = 40$. The upper two panels show dominance of a single species across the grid. The lowest panel shows dominance by neither cell type, which held for long times (solutions were found to be stable in runs up to $t = 10^8$; not shown). Out of 20 runs, A dominated 7 times, B 8, and neither 5. We begin with initial conditions of $a = 0.5 + 0.02 \times n$ where n is chosen randomly between 0 and 1 from a uniform distribution at each numerical grid point. The dimensionless parameter values are $R = 1.0$, $\alpha_1 = \alpha_2 = 0.75$. The domain is of length 10 dimensionless space units. We set the absolute error tolerance in the ROWMAP scheme to 10^{-6}. For more details, see Chapter 5.

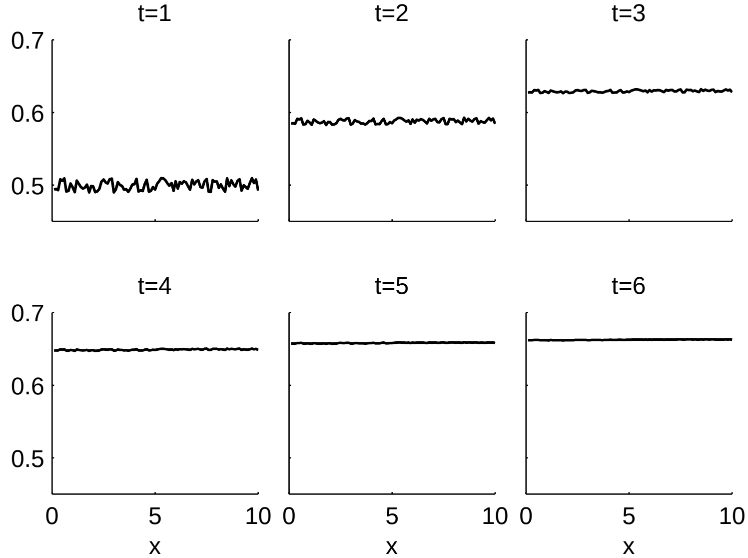

Figure 3.7: Time evolution plots of the two dimensional Single Cell Model equations (3.7). The domain is initially an even mix of the cell populations A and B, as described in Figure 3.6. We plot the density of cell type A across space in the x direction for $y = 2$ at various times t, until $t = 6$. We see the density of A increasing quickly, with the spatial variation in the initial density rapidly smoothing out, and with the density of A approaching 2/3 everywhere, as expected from equation (3.19). All parameter values and numerical details are as in Figure 3.6, although with $f = I$ as stipulated by this model (see Figure 3.2(b)).

3.4.3 Extending the two dimensional model results

We now consider three other initial conditions, in order to further explore some of the behaviours discussed above. In Section 3.4.2, the Community Model in the case $\alpha_1 = \alpha_2$ sometimes resulted in a split domain with different cell types present in the two parts. In order to investigate this phenomenon further, we repeat our experiments, this time starting with split conditions similar to those seen in the lowest panel of Figure 3.6 at time $t = 40$. With these split initial conditions, the interface between the two species does not move over long times, suggesting that we are indeed at a steady state (not shown). Furthermore, we repeat our experiments with a curved interface (see Figure 3.9) in order to discover whether the speed of propagation depends on curvature. We observe a flattening of the interface (Figure 3.9), but no further movement. This coincides with the previous result, and suggests that a coexistence steady state in the Community Model will typically display a flat interface between the two species.

Finally, we investigate "island" initial conditions (see Figure 3.10, first column), in order to explore the dynamics of a localised group of cells. As in the previous result, we find that movement was fastest where curvature was greatest, with the motion roughly proportional to the mean curvature of the wavefront. This leads to

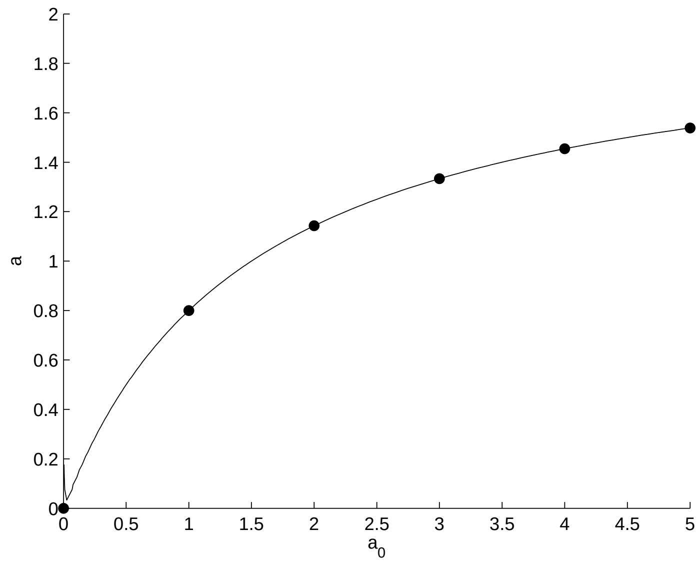

Figure 3.8: The solid line shows the solution to (3.19) with $c = 2$, so that $\alpha_1 = \alpha_2 = 1/2$, and $b_0 = 1.5$. Equation (3.19) gives estimated steady state values in the solution of (3.7) for a when $a + b \neq c$ initially. We fix $b_0 = 1.5$, and plot the steady state a as a function of a_0, where both $b = b_0$ and $a = a_0$ initially. Spots indicate the actual numerical steady state values of (3.7) given by the initial conditions indicated. Note the near identical match between the integrodifferential equation and ODE solutions. In the numerical simulations of (3.7), initial conditions are set to $b = 1.5$ across the domain, and $a = a_0 + 0.02 \times n$, where n is chosen randomly from a uniform distribution between 0 and 1 at each numerical grid point and values of a_0 chosen are 0, 1, 2, 3, 4 and 5. All other parameter values and numerical details are as in Figure 3.7.

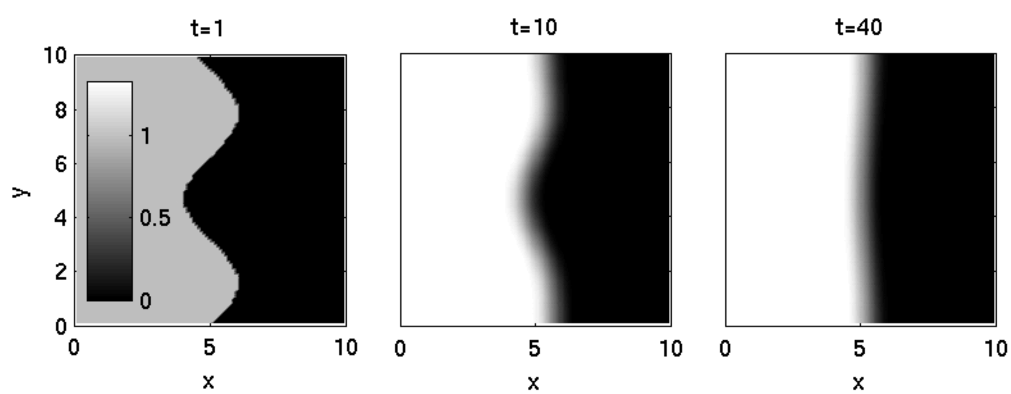

Figure 3.9: Solutions to the two dimensional Community Model equations (3.7) with curved initial conditions. We plot the density of B cells in space at $t = 1$, $t = 10$ and $t = 40$. Neither cell type dominates over long times. All numerical details and parameter values are as in Figure 3.6.

the "island" shrinking until it disappears in nearly all cases (see Figure 3.10, upper panel), explaining both why we sometimes see the dominance of a single species in the Community Model, and why we do not see stable spotted patterns, as each small group of cells would be engulfed by the larger local population. However, if the death rate of the "island" is sufficiently small in comparison to the death rate of the other cell population, then an "island" will grow and dominate the domain (see Figure 3.11 for details of this for circular islands).

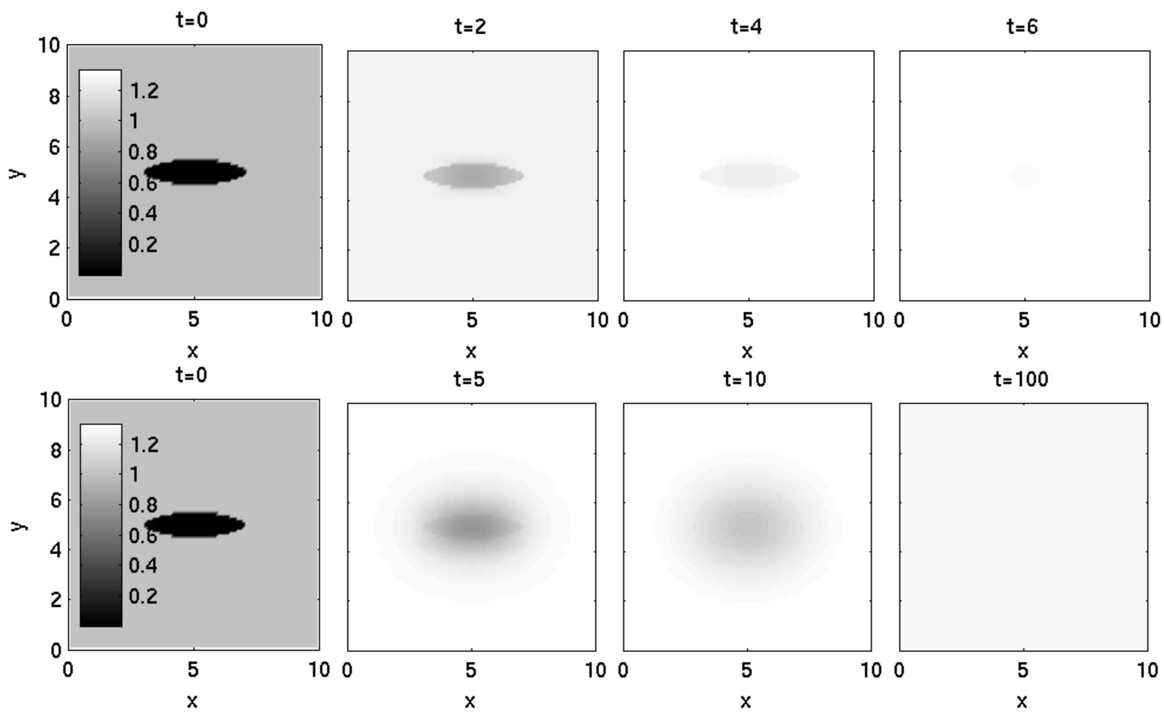

Figure 3.10: Solution of both the two dimensional Community Model and Single Cell Model equations (3.7) with island initial conditions. The domain is initially split with type A the "sea", and B the "island". We plot the density of cell type A in space at the dimensionless times indicated. Community Model (upper panel): A dominates across the domain. The dimensionless parameter values are $\alpha_1 = 0.75$, $\alpha_2 = 1.5$. All other parameter values and numerical details are as in Figure 3.6. Single Cell Model (lower panel): With equal death rates, the initially localised population of cell type B spreads across the domain, merging with the population of cell type A and eventually becoming homogeneous. The dimensionless parameter values are $\alpha_1 = 0.75 = \alpha_2$. All other parameter values and numerical details are as in Figure 3.6, although with a different f as stipulated by this model.

We now consider the same "island" initial conditions for the Single Cell Model in order to see how a small group of cells evolves over time under this differentiation rule. When $\alpha_1 \neq \alpha_2$, we find a direct relationship between the death rates of the two

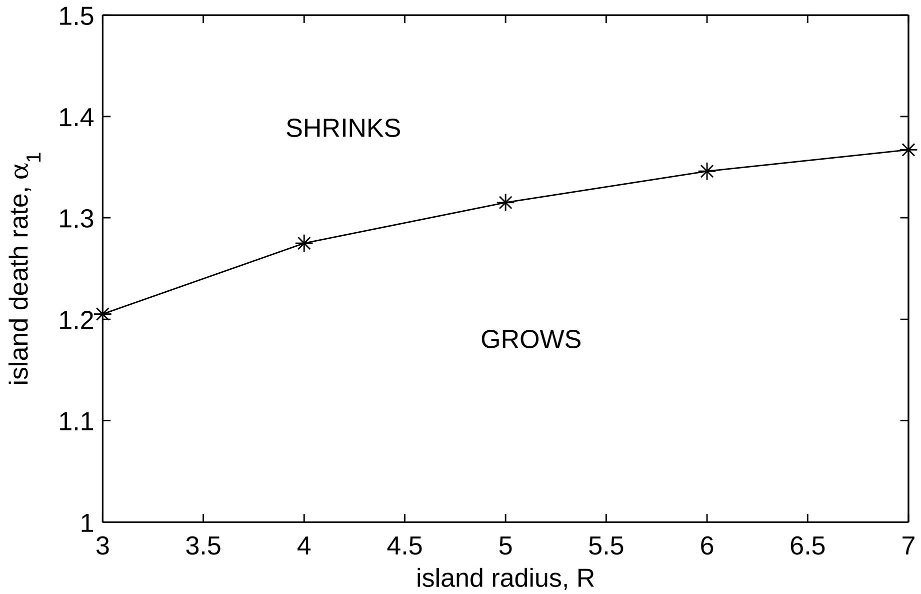

Figure 3.11: Plot of island radius versus death rate for a circular island, showing the parameter regions in which the island will shrink or grow. We set the second cell population to have a death rate of 1.5. We see that as the island increases in size, a higher death rate of the island cell population is required in order for the island to shrink. Critical values were calculated by reducing the problem to one dimension, making use of the circular symmetry; this makes numerical solutions very much faster than the corresponding two dimensional simulations – see Chapter 5, Section 5.7 for more details. Initially, random values between 0 and 0.02 are chosen for a from a uniform distribution at each numerical grid point if $x \leq$the island radius being investigated, while $b = 1 - a$. The island radii chosen are $R = 3$, 4, 5, 6 and 7. Various death rates for the island population are investigated in order to find the critical value to 4 significant figures. The domain is of length 100 dimensionless space units, the dimensionless parameter value $R = 1$, and the space discretisation is $\Delta x = 0.1$. All other numerical details are as in Figure 3.3.

populations and the final steady state for all sizes of "island", with the population with the smaller death rate dominating across the domain, and having a density of either $a = 1/\alpha_1$ or $b = 1/\alpha_2$ (not shown). However, when $\alpha_1 = \alpha_2$, our analysis in Section 3.3.3 has suggested we will see a merging of the two cell populations across the domain, as was seen in Figure 3.7. This is indeed what we find in our simulations, with the overall ratio of cell densities remaining constant (Figure 3.10, lower panel). From a biological viewpoint, this suggests that even a small initial population of cells will persist over time under this differentiation scenario.

3.4.4 Summary of two dimensional results

These results suggest that only the Community Model (3.7), which represents a strong community effect, has the ability to generate spatial patterns consisting of two distinct groups of cells through differentiation alone. These stripes exist permanently only if the death rates of the two cell populations are equal. The requirement of a nonlinear function f means that patterning requires a markedly nonlinear response to the local environment i.e. we need our function f to be of the form shown in Figure 3.2(a) rather than that shown in Figure 3.2(b). Without this nonlinear response, no patterns will be seen for any death rates. One simple implication of this result is that a community effect may be in play in scenarios where we do not see patterning.

3.5 Discussion

Our results demonstrate that patterning can only be obtained in the model via a nonlinear response to the local environment: the fate of a differentiating cell must be strongly biased by the ratio of cell types in its local environment. This is the only way to achieve patterning through a local environment-dependent differentiation process alone; the Community Model, which follows this nonlinear process, does produce patterns in some cases, but neither the Cell Autonomous or the Single Cell Model do. Even with a strong effect, the formation of stripes depends on initial conditions and is therefore not robust: a small bias towards stripe formation in the initial conditions is required for stripes to form. We also note that, significantly, for permanent stripes to form it is necessary that the two death rates are equal. However, transient stripes are seen for distinct death rates (see Figure 3.3 and Section 3.4.1). This shows that on a short timescale, a community effect can produce patterns with unequal death rates. Obviously the timescale of interest varies according to the biological system being investigated, and we discuss timescales in relation to the zebrafish example below.

In investigating the relevance of the model to zebrafish stripe formation, we first consider the width of the stripes seen in our simulations; these should match realistic zebrafish stripe widths if our model is to be relevant. The typical width of a melanophore stripe is 6 cells, while a xanthophore stripe is typically wider once fully formed (Moreira & Deutsch, 2005). If we assume that the sensing radius of a cell is equal to its physical radius, then the stripes formed in Figure 3.3 are not sufficiently wide to be realistic melanophore stripes. Therefore, although our system is clearly able to produce patterning for other systems which contain narrower stripes, we conclude that a community effect is insufficient in itself as a mechanism for creating stripes and other patterns in zebrafish; permanent and accurate stripe formation requires coupling with a stronger mechanism such as homotypic cellular attraction (Caicedo-Carvajal & Shinbrot, 2008; Maderspacher & Nusslein-Volhard, 2003), intercellular adhesion (Moreira & Deutsch, 2005), or indeed, perhaps something entirely different such as a reaction-diffusion system (see Kondo et al. (2009) for a review).

We now look to see whether a strong community effect is sufficient for stripe maintenance in zebrafish. We begin our simulation on a rectangular domain with a central stripe running parallel to the long edge. Over long times, the stripe remains if $\alpha_1 = \alpha_2$ (not shown), and widens or shrinks if the two death rates vary (Figure 3.12). To make our observations specific to zebrafish, we carry out further simulations again with a realistic stripe width, fixed in comparison to the sensing radius: we again assume that the sensing radius of a cell is equal to its physical radius, and impose stripe widths of 6 cells for melanophores and 9 cells for xanthophores (Moreira & Deutsch, 2005). These stripes are wider than those formed transiently in Figure 3.3. We now define maintenance to occur if the stripe width changes by less than 25%, with a density of no less than 75% of the original stripe density. With the stripe initial conditions stated, we vary the death rates and find that for various values we see stripe maintenance over a finite period of time.

In order to understand the extent to which these transient dynamics are relevant to zebrafish pigmentation patterns, we first estimate the dimensional time over which patterns develop, as implied by the model (3.7). Note that this means the dimensional half-life value is implicitly related to the dimensional death rate of the cells. As a somewhat arbitrary estimate for the half-life of a zebrafish melanophore (population A in our model, say), we use 5 days, so that

$$\ln 2/\alpha_1 \times P/\tilde{\alpha_0}p = 5 \text{ days},$$

following the non-dimensionalization in Section 3.2. In Figure 3.3, say, we used a dimensionless melanophore death rate of $\alpha_1 = 1$ in the third panel, and see two stripes at dimensionless $t = 10$. The corresponding dimensional time is then

$$10 \times P/\tilde{\alpha_0}p = 10 \times 1/\ln 2 \times 5 \text{ days} \approx 72 \text{ days}.$$

In the absence of data on the half-life of a melanophore, we present the results for different possible values (Table 3.5). If the half-life of a melanophore is 5 days, then stripes are maintained for at least one year even if the half-life of the xanthophores is 30% more than that of melanophores, or 20% less. The asymmetry between increased and decreased half-lives is due to the absolute difference in values of the associated death rates of the two populations. Whilst this difference is present in all cases, it is greatest in this 30% variation case. Here, while in the +30% case the death rate of xanthophores is 0.17 less than that of melanophores, in the −30% case it is 0.32 greater than that of melanophores, leading to the fast spreading of the melanophore stripe and hence a lack of stripe maintenance. If we decrease the half-life of melanophores to 2.5 days, stripes are still maintained for at least one year when the difference between the half-lives of the two populations is 10%, showing that stripes are maintained under the Community Model over a wide range of half-lives. Therefore, although we do not know exact half-life values, we conclude that a strong community effect is plausible as a mechanism for stripe maintenance in zebrafish. A possible future extension would be to explore the capacity of the model to replicate pattern regeneration following experimental ablation of the pigmentation stripes (Rawls & Johnson, 2000; Yamaguchi et al., 2007).

We now move away from the zebrafish example, and return to more general implications of our model. We began our model construction in Section 3.2 by assuming that stem cells produce precursor cells at a constant rate, and also self-renew as they do so. However, another possible outcome of stem cell mitosis is the production of two precursors, and no stem cells, or two stem cells and no precursors (see Watt et al. (2006), for a discussion of this in the epidermis). One could model both of these scenarios and see what effect they had on the final outcome of the model, and, since so little is known about stem cells and precursor cells in many systems, the mathematical modelling of such scenarios would provide insight into plausible possibilities for different systems. Note also that our two choices of f for the two local environment models are not comprehensive, and there are many other options that one may consider. Further work could reconsider our interpretation of a community effect (Section 3.2.1) to see how our results would be affected by a different f.

Note that in Section 3.4.1, Figure 3.4, the width of the stripe produced depends on the size of the sensing radius R. Stripe widths are typically larger than R, and so if we interpret R to be simply the average radius of cells, then the stripes produced are of dimensions of multiple stripe diameters. They are also irregularly spaced, suggesting that the mechanism of the model is not efficient at generating regularly spaced patterns as seen in many cases of embryonic pattern formation.

Further note that in the model we use an integral term to measure the density of cell types in the local environment, and hence to calculate which cell type is in the

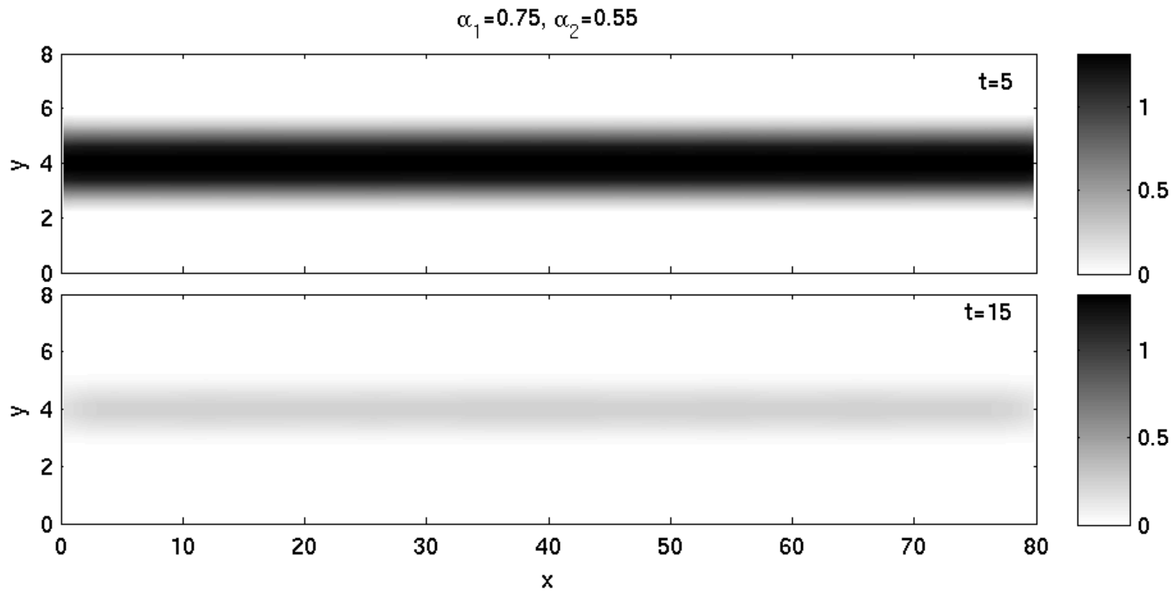

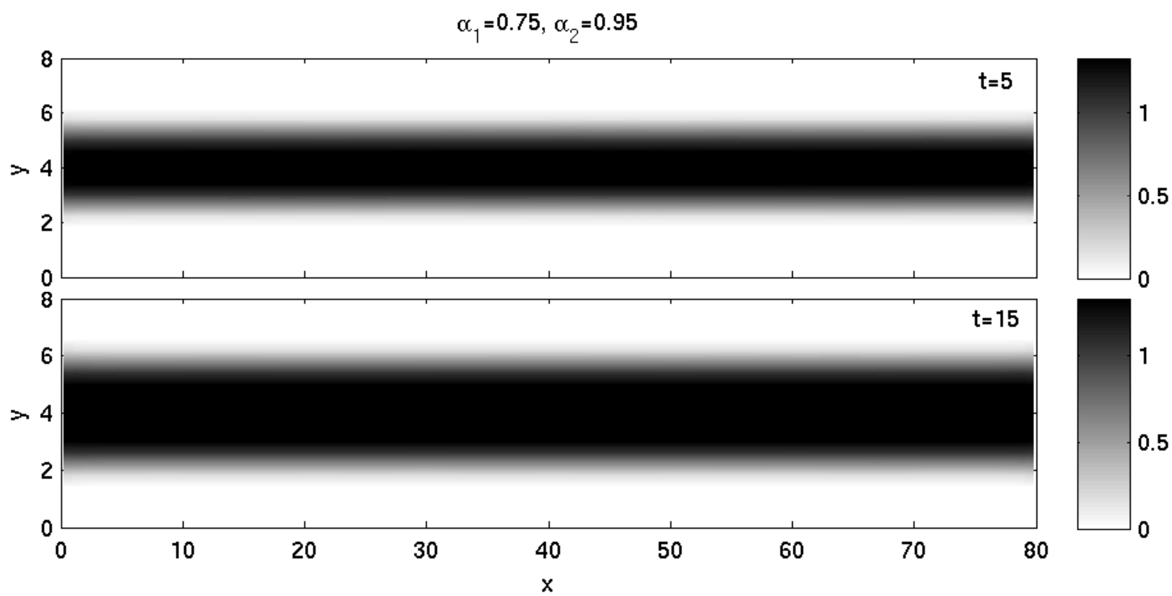

Figure 3.12: A simulation of stripe maintenance. We plot the density of A at the time points indicated. We begin with a striped domain, and see the stripe alter over time. When the death rate of A is greater than that of B, the stripe width decreases (top two panels), while stripe width increase is seen in the converse case (lower two panels). We see that the system is able to maintain stripes for a finite period of time. Note that the stripe width and density do not change over time when death rates are equal (not shown). We use $\alpha_1 = 0.75$, $\alpha_2 = 0.55$ in the upper panel, and $\alpha_1 = 0.75$, $\alpha_2 = 0.95$ in the lower panel. The initial conditions are $a = 1$, $b = 0.02 \times n$ for $y \in [3, 5]$, $a = 0.02 \times n$, $b = 1$ otherwise, where n is a random number chosen from a uniform distribution $\in (0, 1)$ generated at each point. The domain is of size 8×80 dimensionless space points. All other details are as in Figure 3.6.

Do we see stripes maintained after one year?						
xanthophore half-life (% of m.h.-l.) / melano-phore half-life	10%		20%		30%	
	+	−	+	−	+	−
25 days	Yes	Yes	Yes	Yes	Yes	Yes
5 days	Yes	Yes	Yes	Yes	Yes	No
2.5 days	Yes	Yes	No	No	No	No
1 day	No	No	No	No	No	No

Table 3.2: Simulation results on the ability of the Community Model (3.7) to maintain stripes; the function f is as in 3.2(a). We fix our melanohphore half-life, and vary our xanthophore half-life by the percentages shown. We see that a stripe is maintained over the course of a year for a wide variety of half-lives. We set the melanophore death rate at $\alpha_1 = 0.75$ and, from left to right, we set $\alpha_2 = 0.68$, 0.83, 0.63, 0.94, 0.58, 1.07. The initial conditions for the one dimensional simulations used for this table are $a = 1$, $b = 0 + 0.02 \times n$ for $x \in [18, 30]$, $a = 0 + 0.02 \times n$, $b = 0$ otherwise, where n is a random number chosen from a uniform distribution $\in (0, 1)$ generated at each point. The domain is of size 48 dimensionless space points. All other details are as in Figure 3.3.

majority. This calculation depends on the size of the sensing radius R, representing the effective reach of cells. This means that through varying the size of R we could examine the effects of different sensing methods on the model results, and so consider both direct cell-cell contact generated 'decision making' such as that mediated by juxtacrine signalling (small R), and also chemical-based methods such as quorum sensing in bacteria (Atkinson & Williams, 2009), where we can make R larger to suggest a diffusive chemical. In this second scenario the presence of more cells of one type is directly associated with more inductive chemicals of that type. We would use our nonlinear function f as in Figure 3.2(a) to describe the threshold level of chemical necessary for a change in bacterial activity to take place.

The model (3.5) could be further extended and altered to look at various other phenomena in which a community effect may be implicated. For example, we could use it to explore Gurdon's work on myogenesis in *Xenopus* (Gurdon, 1988; 1993a). In these experiments, Gurdon took a small collection of undifferentiated animal cells and observed them collectively differentiating into muscle. Gurdon hypothesised that fully differentiated cells have no effect on the differentiating cells, but rather the cells differentiate when the number of undifferentiated cells reaches a threshold value. Denoting undifferentiated precursors by P, differentiating cells by A, differentiated cells by $\tilde{A}$, a suitable model would be

$$\begin{aligned}
\frac{\partial p}{\partial t} &= -kpf(I_p) \\
\frac{\partial a}{\partial t} &= kpf(I_p) - \alpha a \\
I_p &= \frac{1}{\pi R^2} \int_0^R \int_0^{2\pi} \frac{p(\underline{x} + r\underline{\eta})}{a(\underline{x} + r\underline{\eta}) + p(\underline{x} + r\underline{\eta}) + \tilde{a}(\underline{x} + r\underline{\eta})} r d\theta dr \\
\frac{\partial \tilde{a}}{\partial t} &= \alpha a.
\end{aligned} \tag{3.20}$$

Here $a(\underline{x}, t)$, $p(\underline{x}, t)$, $\tilde{a}(\underline{x}, t)$ are the densities of the cell types A, P and $\tilde{A}$ respectively at two dimensional position $\underline{x}$ and time t, α is the rate at which differentiating cells a become differentiated cells $\tilde{a}$, f is as described in Figure 3.2(a) and k is a positive constant.

We could again vary our contact function f to explore which contact scenario produces the results witnessed by Gurdon, and hence which is most likely to be the method adopted by *Xenopus* during myogenesis. More specifically, there is experimental data regarding the size of the initial precursor population that is necessary for differentiation via the community effect to take place (see Gurdon 1993a), and the time it takes to occur. The model could use this data to obtain estimates of the distances over which these cells can sense their local cellular environment. Note that in this experiment the population of undifferentiated precursor cells is not constant. Therefore our differentiation term in (3.20) is proportional to the varying population P, and this is an important difference from the corresponding term in (3.5). Note also that our integral term I_p calculates the proportion of undifferentiated precursor cells out of all cells present, including fully differentiated cells $\tilde{A}$. Thus the true proportion of P cells within the sensing radius is considered: this is essential to create Gurdon's threshold effect.

We could also use the model to explore homoiogenetic induction, as discussed in Section 3.1 (see also Nieuwkoop, 1997; Gurdon, 1993b). Here we would simply have two cell populations: the precursors P and the differentiated cells A. The appropriate model would have a very similar form to that discussed for Gurdon's experiments above, but without the equation for $\tilde{a}$. The main difference would be in the integral term: I_p would be replaced with the term I_a, as homoiogenetic induction is brought about by the presence of differentiated cells, not by a precursor threshold. Using such a model would again allow us to uncover in more detail the relationships between various components of the process, as discussed above.

Other future work could involve analysing heterogeneous steady states to explore the structure and scale of patterns. This would enable us to investigate more fully the spatial aspects of zebrafish pigmentation stripes and in other examples, allowing us to look at the sharpness of the interface between stripes. Extending the model to three dimensions would allow better comparisons with experimental work, as would considering the corresponding model on a growing domain. Since fish are indeed three dimensional and – in development – grow quite rapidly, we would expect such a model to more closely represent the *in vivo* scenario, and one could explore how stripe formation is affected by the stretching of the domain as the fish grows and changes shape. Again, we could adjust parameter values to explore their effect on the outcomes: for example, altering the cell sensing radius may affect the width of stripes on a growing, curved domain. Furthermore, for better direct comparisons with experimental data, one could attempt a continuous model that is more closely derived from a discrete framework, allowing for the direct application of experimentally derived parameter values. Considering the effects of other cellular processes such as cellular attraction is also a possibility for a more complete model of cellular differentiation. Since our model's very generality means that it can be adjusted to fit numerous biological scenarios as demonstrated above, we hope it will be used to provide further insight into cell differentiation dynamics.

3.6 Supplementary material

This section contains extra material on the two dimensional simulations shown in this Chapter, which were not included in the published paper. We begin, however, with a comparison of the results of Chapters 2 and 3.

3.6.1 Comparing results

Although the models presented in this chapter and in Chapter 2 are of quite different biological scenarios, mathematically they are very similar. Whilst the two continuous Locally Biased and Locally Unbiased models presented in Chapter 2 have both birth and death rates equal, the Community and Single Cell models of this chapter do not. The models presented in this chapter allow the two cell populations A and B to have different death rates, something which is not permitted in Chapter 2 where the density of B is simply given by 1 minus the density of A. However, apart from these differences the models are comparable, with all simulations carried out in the same manner and with the same boundary conditions.

How, then, do the results of these different models compare? In the previous chapter, we saw that the Locally Biased model produced three outcomes: all cells across the domain becoming population A, all cells becoming population B, or an even split between the two populations with a flat interface demarcating the boundary between the two cell populations (Figure 2.6). The Community model in this chapter also produces these outcomes (Figure 3.6). In addition to this, the Community model allows the formation of transient stripes, something which the Locally Biased does not produce. This can be seen in Figure 3.3 (note that the results we would get from a simulation of the Locally Biased model can be easily inferred from the top panel of this figure where the death rates of A and B are equal). These stripes are unstable over time and are unstable to small perturbations.

In terms of the Locally Unbiased model of the previous chapter and Single Cell model of this chapter, we again see differing results. For the Locally Biased model, we see the two cell populations spreading homogeneously across the domain, with both cell populations ending with the same density that they had in the initial conditions (Chapter 2, Figure 2.8). We also see this behaviour for Single Cell model when death rates are equal (this chapter, Figure 3.7). However, when death rates are distinct, the Single Cell model goes to a single cell population across the entire domain, something that is not seen in the Locally Unbiased model.

Furthermore, whilst with the Locally Biased model 'island' initial conditions always lead to the island shrinking until it disappears (Chapter 2, Figures 2.9(c) and 2.11), for the Community model with unequal death rates the island can grow if the death rate of the island is sufficiently small (Figure 3.11). The Single Cell model with equal death rates, and by inferrence, the Locally Unbiased model, sees the island population spread homogeneously across the domain (Figure 3.10, lower panel), whilst the Single Cell model with unequal death rates sees dominance across the domain of whichever cell type has the lowest death rate.

From this discussion it is clear that whilst the four models have many similarities, the ability of the models included in this chapter to have distinct death rates leads to significant behavioural differences with the models of Chapter 2.

Further results of the two dimensional system

Here, we consider our model (3.7), extending the results of Section 3.4.2 by considering curved and split initial conditions as in Section 3.4.3, but with unequal as opposed to equal death rates. We begin by considering curved initial conditions (Figure 3.9), and see that in this case, the system first evolves to a smoothly split domain between the two opposing cell types before the cell type with lowest death rate takes over (Figure 3.13), as suggested by our analysis in Section 3.3.4. We then consider split initial conditions, similar to those seen in Figure 3.6 (lower panel) at $t = 40$, and see that again the cell type with the lowest death rate quickly dominates as expected (Figure 3.14).

These results confirm the importance of death rates to the stability of the system: with unequal death rates in the two populations, we always see dominance of the cell type with the lowest death rate, whilst with equal death rates, we see the long term presence of both cell types (Figure 3.9), as suggested by our analysis (Section 3.3).

With these results we conclude our investigation into differentiation-mediated pattern formation. We now move on to consider the role of attraction and repulsion in tissue patterning.

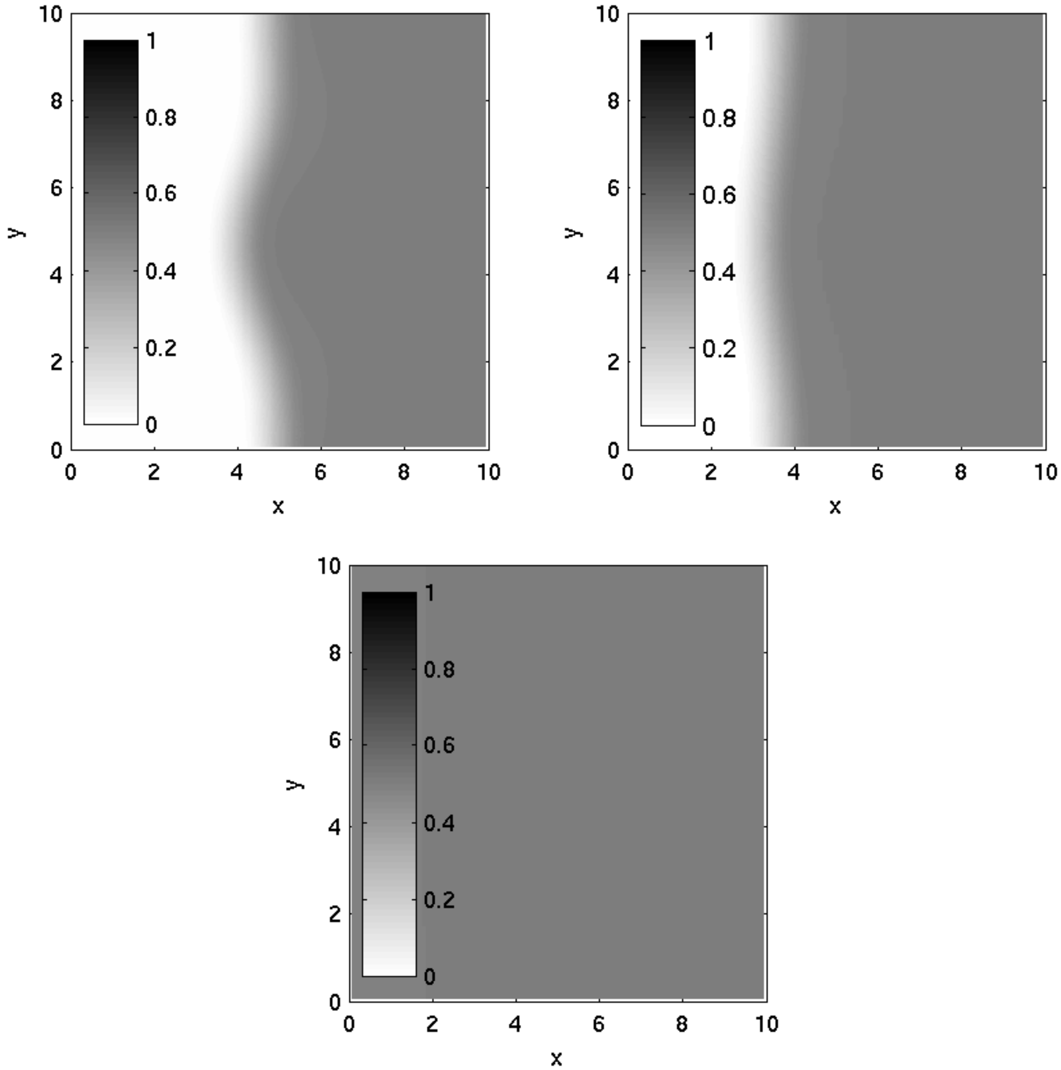

Figure 3.13: Solutions to the two dimensional version of the model equations (3.7) for unequal death rates, with curved initial conditions. We plot the density of cell types in space at the specific time points $t = 5$, $t = 10$, and $t = 25$. The first figure shows the curved initial conditions rapidly flattening out, while the second figure demonstrates the dominance of a, our cell type with the lower death rate of the two, until a homogeneous steady state of $1/\alpha_1 = 0.5$ is reached in the third panel. We begin with initial conditions of $a = 0 + 0.02 \times s$, s a randomly chosen number $\in (0, 1)$ for $x < \sin y + 5$, $a = 1 - 0.02 \times s$ otherwise, and $b = 1 - a$. The domain is of length 10 dimensionless space units, and the solutions are plotted in dimensionless time. The dimensionless parameter values are $R = 1.0$, while the death rates are given by $\alpha_1 = 2$, $\alpha_2 = 3$. The model equations were solved numerically using a Method Of Lines approach, while the integral was calculated as discussed in Section 3.4.

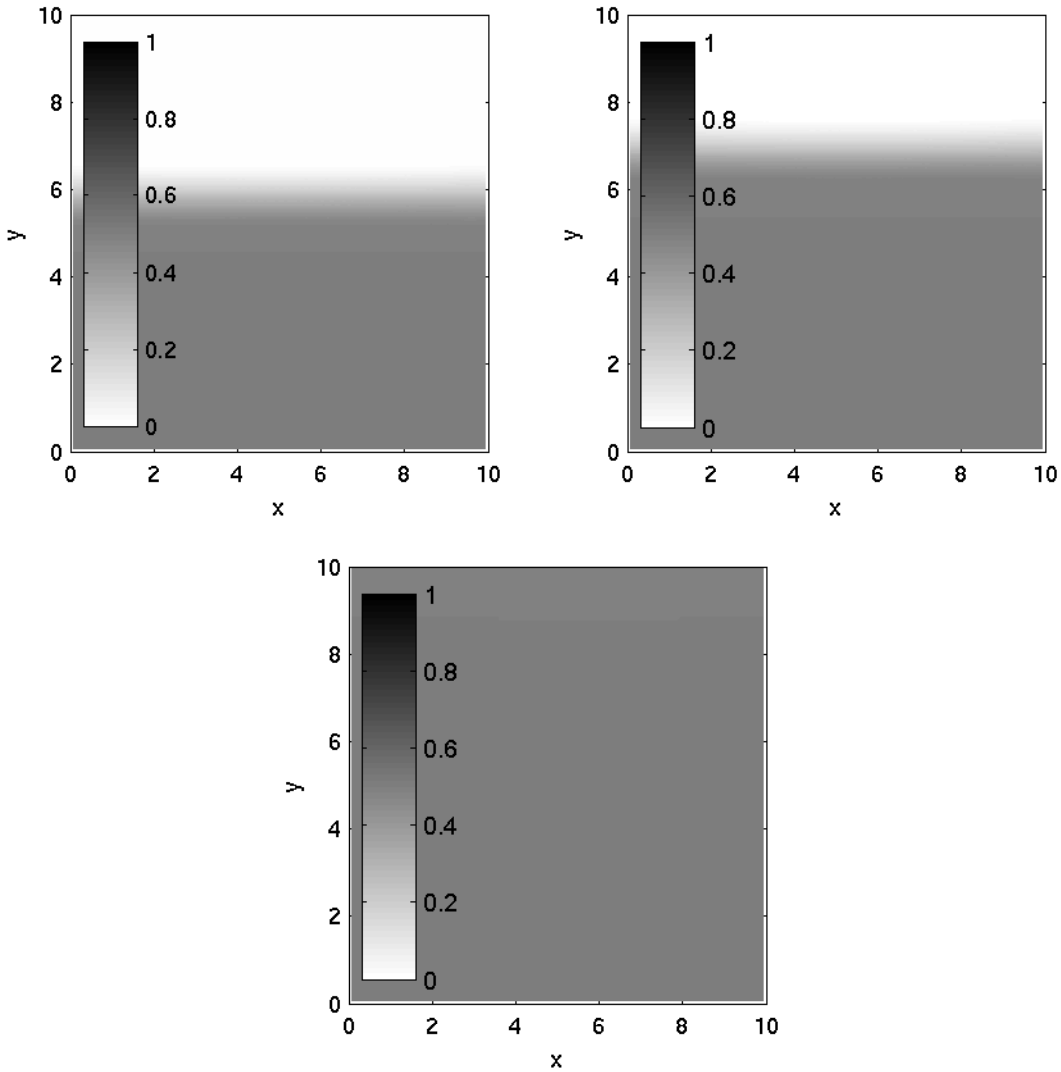

Figure 3.14: Solutions to the two dimensional version of the model equations (3.7) for unequal death rates, with split initial conditions. We plot the density of cell types in space at $t = 5$, $t = 10$ and $t = 25$. The figure shows the dominance of a, our cell type with the lower death rate, with a homogeneous steady state of $1/\alpha_1 = 0.5$ reached by $t = 25$. We begin with initial conditions of $a = 0 + 0.02 \times s$, s a randomly chosen number $\in (0, 1)$, $b = 1 - a$ for $y \in [0, 5]$, and $a = 1 - b$, $b = 0 + 0.02 \times s$ for $y \in (5, 10]$. All other numerical details and parameter values are as in Figure 3.13.

Chapter 4

An integrodifferential equation model for directed cell migration

4.1 Introduction

In previous chapters we investigated the spatial patterning that occurs as a consequence of cell renewal and cell differentiation. However, we have not yet considered the spatial patterns that arise from directed cell movement, and it is this that we turn to here. We begin this section by discussing how cells communicate, as this communication is essential if directed movement is to take place.

Cells communicate in four main ways: through endocrine signalling, where the signalling cell secretes a molecule into the bloodstream so that it diffuses across the body; through paracrine signalling, where a signalling molecule is diffused locally through the extracellular matrix (the medium that surrounds cells); through neuronal signalling, where electrical signals travel along axons to specific target cells; and through contact-dependent signalling, where signalling molecules are passed directly from one cell to another. We are here interested in the effect of a cell's local environment on its position, and so we restrict our interest to the most local and direct form of communication, contact-dependent signalling.

Contact-dependent signalling involves a membrane bound signalling molecule from a signalling cell attaching to the receptor of a neighbouring target cell, so that the signal passes directly from one to the other, without affecting any other cells (Alberts et al., 2008). Once a signal has been received by a target cell, that target cell responds accordingly. If, for example, the signal received is an instruction to repel, the target cell will do so in the direction insisted upon by the signal (see Xu et al., 2000, for details of this in segmental patterning). It should be noted that contact-dependent signalling is not restricted to short distances: some cells send out protrusions such as filopodia that carry receptors at their tips (Sherer & Mothes, 2008). These filopodia can be long (up to ten times the cell diameter in newt pigment cells for example

(Tucker & Erickson, 1986)) and are able to receive the signalling molecules of other cells. Therefore the range of distances over which contact-dependent signalling can take place is wide. Furthermore, note that for the target cell to receive a signal it must have the correct receptor for such a signal (Alberts et al., 2008). Without the correct receptor the signal will not be passed on.

We are interested in contact-dependent communication as a regulator of cell movement, instructing cells when to move and in what direction. It is necessary, therefore, to understand exactly what movement is able to occur as a result of contact-dependent signalling. Some recent insights into this have been made by studying neural crest cells *in vivo* (Carmona-Fontaine et al., 2008). In this study, neural crests cells were for the first time shown to exhibit contact inhibition; that is, when a migrating neural crest cell encounters another neural crest cell they send repulsive signals to one another with the net effect that they both change direction and move away from one another. A repulsive effect is also thought to occur between the yellow xanthophores and black melanophores of zebrafish pigmentation cells at short ranges, whilst at long ranges they are thought to attract, showing that the range over which a signal is sent is relevant to the information in that signal (Maderspacher and Nüsslein-Volhard, 2003). Less specifically, inhibition of movement and the organisation of differing cell types within various tissues has been found to be regulated by Ephrin signals, which are contact-dependent, and which can also promote adhesion and hence attractive movement (for a review, see Poliakov et al., 2004).

Attractive signals have mainly been investigated in terms of cell-cell adhesion (see Gerisch & Painter, 2010, for a review of cell adhesion in patterning). In cell-cell adhesion, cells physically adhere to one another; the forces created by those adhesive bonds cause cells to move. The Differential Adhesion Hypothesis, proposed by Steinberg (1963), suggests that the spatial patterning that arises from mixing two cell types together is due to their relative self-adhesive and cross-adhesive strengths, with various patterns being possible (see Steinberg, 2007, for a review). Similar patterns to those seen as a result of adhesive forces are expected for any attractive signals that cause movement. For more on cell-cell attraction via contact-dependent signalling, see the review by Rørth (2009).

We now turn to look at theoretical models of movement via contact-dependent cell signalling, beginning with spatially discrete models. One of the most widely used of these is the cellular Potts model (Glazier & Graner, 1992, 1993), a lattice-based model that uses energy minimisation ideas to determine the migration and organisation of cells. Interactions occur with neighbouring sites, and hence mimic short-range contact-dependent interactions. This model has therefore proved popular in the modelling of many cell-cell interaction scenarios (see, for example, Bauer et al., 2007; Savill & Sherratt, 2003; Turner & Sherratt, 2002), although longer range interactions cannot take place within this model and the concept is still difficult to link to specific mechanisms. An alternative approach is presented by Shinbrot (2006), who adopts an algorithmic approach used in dissipative particle-dynamics simulations. Here cells move according to a force proportional to their distance from the interacting cell, and a large interaction range is allowed. This model has been adapted to look at pigmentation patterns in zebrafish (Caicedo-Carvajal & Shinbrot, 2008).

We now consider continuous approaches to modelling contact-dependent signalling and migration. Early attempts used ideas of surface tension (Byrne & Chaplain, 1996) and non-linear diffusion (Perumpanani et al., 1996) to try and model the restriction of cell movement as caused by adhesion, a form of contact-dependent directional migration. The most recent successful approach has used a non-local integral term to model the signalling interactions that occur between cells. Such a representation of cell environment via an integral term has been used successfully in many contexts including cell sorting (Armstrong et al., 2006), development (Sekimura et al., 1999; Armstrong et al., 2009; Green et al., 2010) and cancer (Gerisch & Chaplain, 2008; Sherratt et al., 2009; Painter et al., 2010). The use of such a non-local term is flexible, allowing both attractive and repulsive forces to be considered over various ranges. However, all of the models so far have considered only attractive forces over a fixed range.

Although obviously different from modelling contact-dependent signalling processes in cells, swarm modelling also considers non-local interactions between moving particles, and so is instructive. A non-local integral term is used to model the interactions between individual animals over a fixed range, and various swarming patterns have been recorded as a result of these interactions (Mogilner & Edelstein-Keshet, 1999; Eftimie et al., 2007a; Eftimie et al., 2007b; Eftimie et al., 2009). One such model has been used to study the effect that varying interaction ranges has on spatial organisation (Topaz & Bertozzi, 2004). It reveals that in the case of potential motion and non-local repulsion, a short range leads to a smoothing of the density profile whilst a larger range leads to increased movement. With attraction, the greater the interaction range, the fewer aggregations form and the larger those aggregations are. In the case of incompressible motion, which occurs when animals are at a fixed density that they must maintain, spirals form, with the range of the interaction determining the degree of spiral formation (Topaz & Bertozzi, 2004). No such investigation into the effect of ranges on patterning has been carried out in relation to cells as far as we are aware.

We will carry out a detailed investigation into the effects of interaction range and attraction and repulsion on the organisation of cells within a tissue. Note that a thorough investigation into repulsive effects in patterning in animal tissue has not yet been undertaken in continuous modelling since the cell biology investigations mainly focus on adhesion, an attractive force. In discrete modelling, only the models of Shinbrot (Shinbrot, 2006; Caicedo-Carvajal & Shinbrot, 2008) have, as far as we are aware, investigated repulsive effects under this scenario. We undertake this modelling as it allows us to explore the breadth of behaviours that can be achieved from specific cell-cell interactions. Unlike biological experiments, we are not restricted to considering one system, nor must we consider the practicalities of manipulating living tissue. We adopt a continuous approach as it has fast computational time for large cell populations, and allows for the easy incorporation of other continuous models into our work.

We begin this chapter with a derivation of the model, illustrated by two example cell-cell interaction functions. This is followed by some analysis in Section 4.3, including a discussion of this analysis in terms of our two examples introduced in Section 4.2, and a thorough numerical investigation into which instability scenarios we expect to see for the second of these examples. Section 4.4 offers numerical simulations in one dimension, highlighting the patterning behaviour, while in Section 4.5 we discuss the results, their biological significance, and future work.

4.2 Creating a model

We wish to analyse the effect of both interaction strengths and ranges on pattern formation, as how these various interactions affect patterning in tissues is a question that we believe has not yet been fully explored by modellers. Given the lack of previous work that considers both signalling ranges and attractive and repulsive signals, we formulate a general model. This allows us to understand the broad dynamics of the system, with the hope that the model will then be adapted by others to answer specific biological questions.

4.2.1 The equations

We choose a continuous model as it allows for mathematical analysis of pattern formation, and for easy incorporation into existing models. We begin by creating a partial differential equation for each of the cell populations we wish to consider. For simplicity, we consider just two populations. Since we wish to consider cell movement, we begin with a discussion of intercellular forces.

We employ a mass conservation approach, as here we are interested in the patterning formed only by movement and do not expect any overall losses or gains to our system. We follow Armstrong et al. (2006), so that the cell density of a population u

at position x, time t, is governed by the flux of u. That is, we let

$$\frac{\partial u}{\partial t} = -\nabla \cdot \mathbf{J}$$

where $\mathbf{J}$ represents cell flux. This cell flux can contain various elements according to the biological system being modelled. Note that, for the moment, we do not include any cell birth or cell death, effectively suggesting either that cells that die in the system are immediately replaced by cells of the same type, or that the timescale of the dynamics is shorter than birth and death processes (as can sometimes be the case in embryogenesis). We do this so that we can concentrate exclusively on the dynamics that are a result of cell-cell interactions. Kinetic terms may be incorporated at a later date. Here, we are interested in both random cell movement, and in movement caused by attractive and repulsive interactions. The former of these we will model in the usual way as Fickian diffusion, so that $\mathbf{J}_{random} = -D\nabla u$ where D is the coefficient of cell diffusion.

To model the movement caused by attraction and repulsion, we acknowledge the forces that occur between interacting cells. Whilst a cell that is attracted to another will be pulled towards it, a cell that is repulsed will be pushed away. These forces between cells drive the overall movement of the cell population. The interactions occur at a local level, and the resultant force will always be in the direction of the attracting cell, or opposite to the direction of the repulsing cell. Since we are interested in a continuum and not a discrete model, we attribute the resultant force to local cell density, so that a locally high cell density will produce a large force, and a low density a small one. We justify this by thinking about the biological scenario: the more cells there are in an area, the more likely it is that cell-cell contacts, which pass on attractive or repulsive signals, form. The more cell-cell contacts that form, the stronger the overall signal received, and hence the greater the resultant movement. Moreover, as cells are more likely to form contacts to cells nearby rather than further away, the distance at which the signalling cell is positioned from the receptor cell also has a role to play in the total strength of the signal received. Then the local force created at position x due to interaction signals at $x + s$ is postulated to be given by

$$f(x, s) = \Omega(s, \xi_i)u(x + s, t).$$

The function Ω is our signalling function which dictates the strength and direction of the signal, and hence the relevant force, related to distance s and to signalling range ξ_i, and $u(x + s, t)$ is simply the density of our cell population u at position $x + s$. So our total force across the entire interaction range of a cell is simply the sum of all of these forces, giving us a nonlocal integral term

$$F(x) = \int_{\mathbb{R}} \Omega(s, \xi_i) u(x+s, t) ds.$$

Finally, assuming negligible inertia and by following Stoke's law which says that the drag of a spherical object is proportional to its velocity (although cells are not spheres, we can approximate them as such for our purposes here), we let

$$\mathbf{J}_{interaction} = u\omega \int_{\mathbb{R}} \Omega(s, \xi_i) u(x+s, t) ds,$$

where ω is a constant of proportionality related to viscosity. We also assign a function $p(u)$ to limit the density of our cells and prevent overcrowding. Note that this flux is proportional to both the forces described above and the cell density.

Then the total mass conservation equation for one cell population in one dimension is given by

$$\frac{\partial u}{\partial t} = D\frac{\partial^2 u}{\partial x^2} - \frac{\partial}{\partial x}\left(u\omega p(u) \int_{\mathbb{R}} \Omega(s, \xi_i) u(x+s, t) ds\right). \tag{4.1}$$

Within the two equations for our system of PDEs covering our two cell populations, we now include the nonlocal term described above for each set of cellular interactions that take place. The nonlocal nature of the terms allows us to explore possible interactions that take place beyond the diameter of a cell due to filopodia say, as discussed in Section 4.1. For our two population system there are four interaction terms in total: two heterotypic, i.e., between different cell populations, and two homotypic, i.e., within the same cell populations. For each of the four nonlocal terms we allow distinct interaction ranges, so that not only do the two cell populations have different ranges, but also within each population the homotypic and heterotypic interaction ranges are distinct. Such a scenario is not unrealistic, and we give a possible example of such a phenomena here.

A cytoneme is a long, thin intercellular structure that enables cell-cell communication over long ranges (Sherer & Mothes, 2008). It is thought that cytonemes may be formed from filopodia that, when they reach another cell, are then bound by it. Such formation, which allows the connection of one cell's ligand (i.e., its extracellular signalling molecule) with another cell's receptor, can only take place if the ligand-receptor pair are compatible. Once such a connection has been formed, signals and receptors can move through the cytoneme, allowing instructions to be passed from one cell to the next (Sherer & Mothes, 2008). Signals passed along the cytoneme may, for example, cause the polarisation of a cell in a certain direction, causing it to reorient and possibly move.

In contrast to these long-range connections, cells may instead communicate with one another through short-range connections such as direct cell-cell contact. Such contact is established directly on the cell's surface or membrane, and is common in the process of cell-cell adhesion (Alberts et al., 2008).

It is not unlikely, therefore, that whilst u cells may send out long range connections to other u cells, say, they may only have compatible connections with v cells over a shorter range, with, for example, u to u cell interactions mediated by cytonemes, and u to v interactions mediated by adhesion molecules (Figure 4.1). Our model represents this type of scenario by allowing a different range for each interaction term.

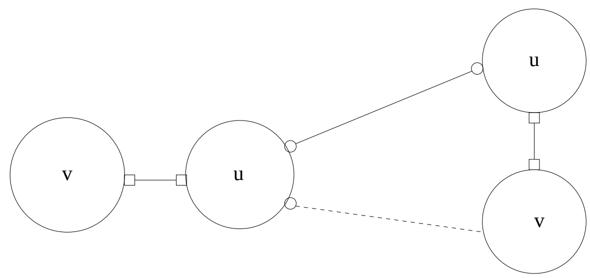

Figure 4.1: Schematic showing possible different connections between two cell populations, u and v. Whilst u cells can signal to each other through long, cytoneme-type connections (solid line, circular ends), u and v type populations only have short range cognate ligand-receptor pairs (solid line, square ends). When a u cell tries to connect to a v cell through the creation of a cytoneme, the v cell is unable to provide the correct receptor, and so a connection is not made (dashed line).

We also allow each signalling function Ω to have its own interaction strength, acknowledging by doing so that cell populations may prioritise one signal over another when determining what action to take. The actual form of Ω we leave unspecified, although we assume that the form of all interaction terms are alike. This is not necessary in the model formation, but as we are able to vary the range and strength of the terms whilst leaving the form of them the same, this seems a reasonable simplification to make.

Then for our two cellular population densities $u(x,t)$ and $v(x,t)$, we have, in one dimension, equations of the form

$$\begin{aligned}\frac{\partial u}{\partial t} =& D_u \frac{\partial^2 u}{\partial x^2} - \frac{\partial}{\partial x}\left(u\omega p(u,v)\left(\mu_{uu}\int_{\mathbb{R}} \Omega(s,\xi_{uu})u(x+s)ds + \right.\right. \\ & \left.\left. \mu_{uv}\int_{\mathbb{R}} \Omega(s,\xi_{uv})v(x+s)ds\right)\right)\end{aligned} \tag{4.2}$$

and

$$\frac{\partial v}{\partial t} = D_v \frac{\partial^2 v}{\partial x^2} - \frac{\partial}{\partial x}\left(v\omega p(u,v)\left(\mu_{vv}\int_{\mathbb{R}}\Omega(s,\xi_{vv})v(x+s)ds + \mu_{vu}\int_{\mathbb{R}}\Omega(s,\xi_{vu})u(x+s)ds\right)\right), \tag{4.3}$$

where Ω is our signalling function, and ξ_i and μ_i ($i = uu,\ vv,\ uv,\ vu$), are our homotypic and heterotypic ranges and strengths respectively. Recall that homotypic is between like cell types, and heterotypic is between differing cell types. Our μ_i can be both positive or negative, depending on whether they are representing attractive or repulsive interactions. Note that our ξ_i do not necessarily represent the entire distance over which signalling takes place, but rather may just be a proportion of it; such a distinction depends on the choice of our signalling function Ω. The diffusion rates D_u and D_v represent random motion by the two cell populations, whilst ω is our drag effect, and $p(u,v)$ is a 'packing' function, limiting the density of the cell populations. This close-packing function $p(u,v)$ could be given by $e^{-(u+v)/P}$ for example, where P limits the population density – the fact that p never reaches 0 models jostling amongst a high density population. (To lower the value of this 'jostling' term, we can let kP be the population density for some $k > 1$, so that at $u+v = kP$, $p = e^{-k} < p = e^{-1}$.) See Table 4.2.1 for a summary of parameters.

Dimensional Parameter	Parameter Name	Typical Dimensions
D_u	diffusion coefficient of u population	cm^2/sec
D_v	diffusion coefficient of v population	cm^2/sec
$\mu_i\omega$	total interaction strength, incl. drag effect	cm/Ns
ξ_i	interaction range	cm

Table 4.1: A summary table of parameters found in the model equations (4.2) and (4.3).

Note that Ω is scaled by the length of each interaction range ξ_i, where this range is either the full distance over which the corresponding cell population can communicate, or a representative measure of it (for example, half the distance). An example of this signalling function Ω could be a monotonic curve chosen to represent a changing strength in signal over the ranges 0 to $-\xi_i$ and 0 to ξ_i, or a constant function with cut offs at $-\xi_i$ and ξ_i chosen to mimic a constant signal followed by a sudden loss of signal beyond ξ_i (Figures 4.2(a) and 4.2(b)). Note that the latter of these options is more likely to occur over short ranges where only direct cell-cell contact is being considered. In the former case we are thinking of filopodia: whilst we do not necessarily expect filopodia to relay a weaker signal at long distances, we do expect fewer filopodia to reach long ranges rather than shorter ones. The cumulative effect of this is for the cell in question to sense fewer signals from further away and so receive a lower overall signal strength at greater distances. This leads to the suggestion of a monotonically decreasing function for Ω (Figure 4.3). We can also vary our types of signal through truncation, i.e., we truncate Ω at a given $c \ll \xi_i$, where $2\xi_i$ is the maximum distance over which a cell can sense other cells, in order to create a strong close range signal; we lengthen c for a more varied long-range signal type (Figure 4.2(c)). Note that to switch from attraction to repulsion, we simply change the sign of our strength terms μ_i from $+$ to $-$.

In terms of boundary and initial conditions there are many possibilities to consider, and the model does not restrict our choices in any way. If we wish to see how patterns emerge under this modelling scheme, we could begin with random initial conditions, as long as these are within the limits imposed by the packing function $p(u, v)$. Biologically, this would pertain to exploring patterning in early development, when cells begin from an unsorted position. Or, one could impose patterned initial conditions to explore the development of that pattern. Such an initial condition could be used to explore the patterns that develop after the establishment of initial patterning that is not mediated by cell-cell interactions, as is seen in the zebrafish for example (Maderspacher and Nüsslein-Volhard, 2003). For boundary conditions, one could implement periodic boundary conditions, no-flux boundary conditions, reflective boundary conditions, fixed boundary conditions, or a mix of any of the above. Each of these would be appropriate for a different biological scenario. For example, periodic boundary conditions are suitable when modelling patterning on a large domain or on a complete organ, whilst no-flux or reflective boundary conditions would be better suited to models of experimental assays or small pieces of tissue.

Whilst not necessary for the model equations, for the remainder of this chapter we assume that the signalling function Ω is odd, as we assume in the above examples (Figure 4.2). This means that whilst cells to the left of a cell at position x, say, push or pull the cell at x in one direction, cells to the right of x push or pull the cell in the opposite direction. This makes sense biologically: we are suggesting that a cell is either pulled towards cells on either side of it through cell adhesion say, or pushed away due to contact inhibition perhaps, but not pulled from one side and pushed from the other (although note that if a cell is already polarised it will have a bias in a particular direction). For example, a cell that is experiencing an Ω that represents an attractive signal must be pulled in a negative direction if total attraction is strongest to the left of the cell, but pulled in a positive direction if total attraction

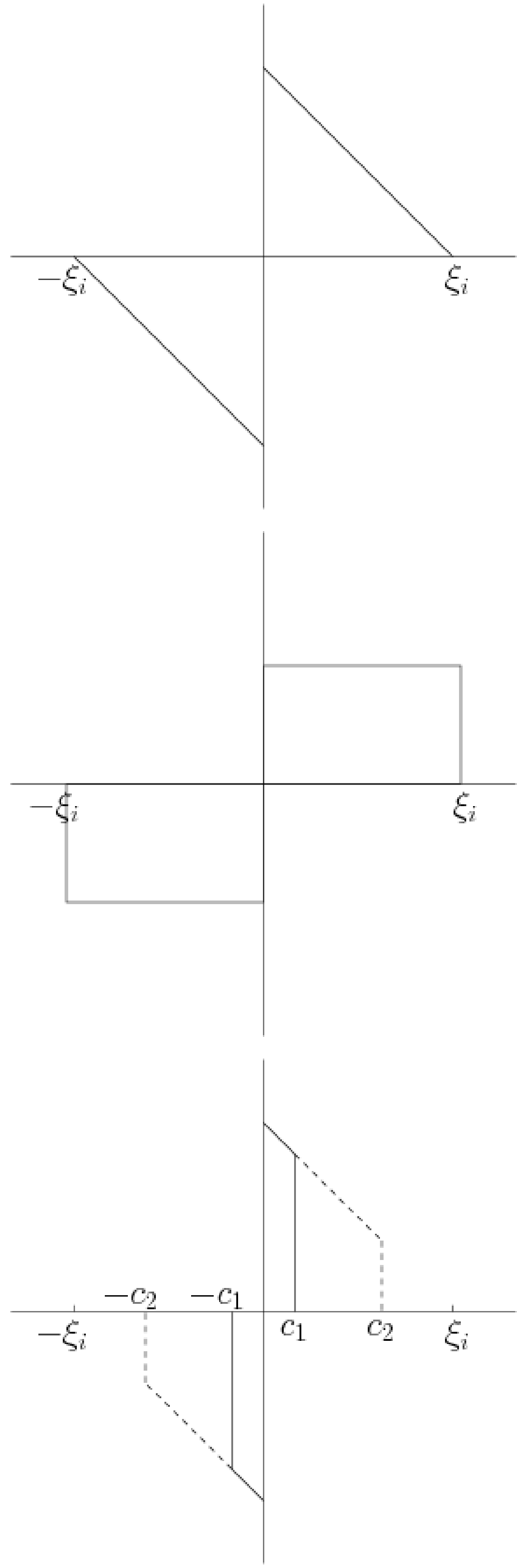

Figure 4.2: Possible signalling functions Ω. See text for further details.

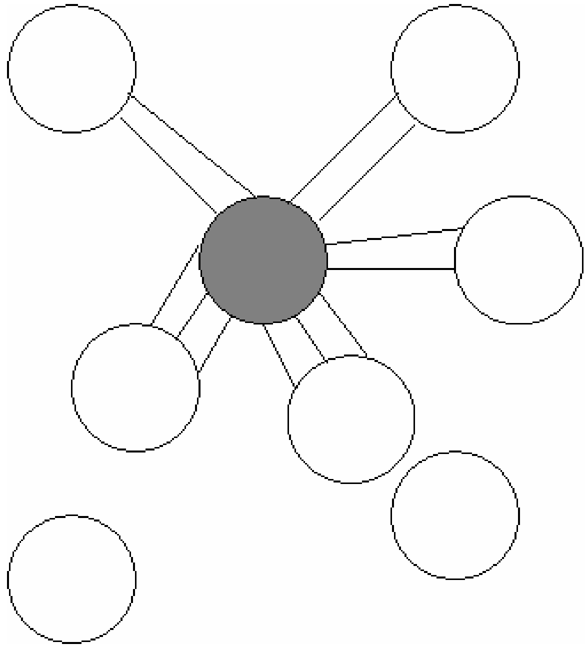

Figure 4.3: Schematic of a cell with filopodia, represented by the central grey circle with thin lines protruding from it, connecting with surrounding cells (represented by surrounding circles). Whilst filopodia can be long, they are likely to make connections with the first compatible cells they encounter. The cumulative effect of this is for filopodia to receive signals from other cells at a decreasing rate as distance from the receptor cell increases. See text for further details.

is strongest to the right of the cell – an odd function will do this (Figure 4.4). We always normalise our integral, so that each integral over its complete range has the same value. For our main example in the following sections, we let $\int_0^\infty \Omega(s, \xi_i)ds = 1$. Note that this means that as we increase the range, the total signal will remain the same, and hence the maximum signal strength will decrease. If we wish to keep the maximum signal strength the same across all ranges we can alter our interaction strengths μ_i accordingly.

As an illustrative example, let $\Omega(x, \xi_i) = 1$ for all $0 < x < \xi_i$, $\Omega(x, \xi_i) = -1$ for all $-\xi_i < x < 0$, and 0 otherwise, as in Figure 4.2(b). Biologically we are assuming that all protrusions pass on the same strength of signal to the cell independent of their distance from that cell, as long as they are within an interaction range ξ_i, which here represents the full distance over which a cell of each type can communicate. This type of example therefore is most suited to cell populations that experience short range cell-cell contact dependent signalling, as discussed above. We let the heterotypic terms $\mu_{uv} = \mu_{vu}$ and $\xi_{uv} = \xi_{vu}$, implying that the effect that u cells have on v cells is equal to the effect of v cells on u cells, as occurs in systems where cells form adhesive bonds with each other. For simplicity, let the packing term $p(u, v) = 1$, $\omega = 1$, and

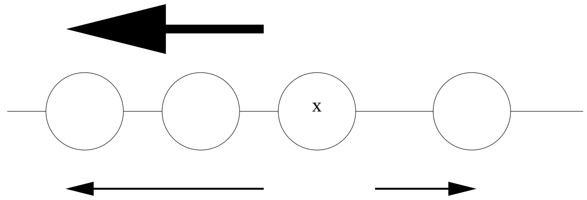

Figure 4.4: Schematic of forces received as a result of signalling from neighbouring cells. The cell at position x receives attractive signals say, and hence attractive forces, from both the cells to its right and those to its left. However, as there are more cells to its left, the strength of signal received from its left is therefore greater than that received from its right. This leads the cell at x to move to the left.

$D_u = D_v = 1$. Then (4.2) and (4.3) become

$$\begin{aligned}\frac{\partial u}{\partial t} =& \frac{\partial^2 u}{\partial x^2} - \frac{\partial}{\partial x}\left(u\left(\mu_{uu}\int_{s=-\xi_{uu}}^{s=\xi_{uu}} \frac{s}{|s|}u(x+s)ds + \right.\right. \\ & \left.\left. \mu_{uv}\int_{s=-\xi_{uv}}^{s=\xi_{uv}} \frac{s}{|s|}v(x+s)ds\right)\right)\end{aligned} \tag{4.4}$$

and

$$\begin{aligned}\frac{\partial v}{\partial t} =& \frac{\partial^2 v}{\partial x^2} - \frac{\partial}{\partial x}\left(v\left(\mu_{vv}\int_{s=-\xi_{vv}}^{s=\xi_{vv}} \frac{s}{|s|}v(x+s)ds + \right.\right. \\ & \left.\left. \mu_{uv}\int_{s=-\xi_{uv}}^{s=\xi_{uv}} \frac{s}{|s|}u(x+s)ds\right)\right),\end{aligned} \tag{4.5}$$

similar to the two population model given in Armstrong et al. (2006). This model was used to investigate cell-cell adhesion in animal cells, and successfully replicated the cell sorting experiments of Steinberg (1962a,b,c).

For another illustrative example, we turn to Mogilner and Edelstein-Keshet (1999), and Eftimie et al. (2007a,b), who let $\Omega(x,\xi_i) = \frac{1}{\xi_i}\tilde{\Omega}(\frac{x}{\xi_i}) = \frac{1}{\xi_i}(\frac{1}{2}\frac{x}{\xi_i}e^{-\frac{1}{2}(\frac{x}{\xi_i})^2})$ (Figure 4.6). Note that the papers cited here actually concern animal swarms, with the signalling function based on the idea that animals in a swarm align themselves in a group, not too close to each other but not too far apart, according to the position of the other animals they can sense around them. In terms of our cell interaction model, we can consider Ω in terms of irregular shaped cells and their protrusions which extend beyond ξ_i, with the majority of signalling taking place at a distance ξ_i from each cell centre (Figure 4.5). Such an interpretation leads to a signalling function of the form shown (Figure 4.6). Using this form for Ω, the equations become

$$
\begin{aligned}
\frac{\partial u}{\partial t} =& D_u \frac{\partial^2 u}{\partial x^2} - \frac{\partial}{\partial x}\left(u\omega p(u,v) \left(\frac{\mu_{uu}}{\xi_{uu}} \int_{\mathbb{R}} (s/2\xi_{uu}) e^{-(s/\xi_{uu})^2/2} u(x+s) ds + \right.\right. \\
& \left.\left. \frac{\mu_{uv}}{\xi_{uv}} \int_{\mathbb{R}} (s/2\xi_{uv}) e^{-(s/\xi_{uv})^2/2} v(x+s) ds \right)\right)
\end{aligned} \tag{4.6}
$$

and

$$
\begin{aligned}
\frac{\partial v}{\partial t} =& D_v \frac{\partial^2 v}{\partial x^2} - \frac{\partial}{\partial x}\left(v\omega p(u,v) \left(\frac{\mu_{vv}}{\xi_{vv}} \int_{\mathbb{R}} (s/2\xi_{vv}) e^{-(s/\xi_{vv})^2/2} v(x+s) ds + \right.\right. \\
& \left.\left. \frac{\mu_{vu}}{\xi_{vu}} \int_{\mathbb{R}} (s/2\xi_{vu}) e^{-(s/\xi_{vu})^2/2} u(x+s) ds \right)\right),
\end{aligned} \tag{4.7}
$$

where this time the integrals are taken over the real line. Whilst obviously cells cannot sense over infinite distances, the value of this Ω is negligible for large x, and calculating integrals over the real line can prove useful when carrying out mathematical analysis.

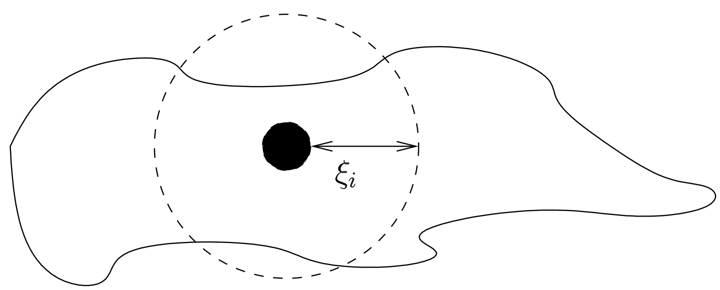

Figure 4.5: An irregular shaped cell (solid line), with an average distance from the centre (black circle) given by distance ξ_i (dashed line). We use this average distance as a representation of our peak signalling distance, whilst noting that some signalling can take place both much closer to the cell centre and much further away dependent on position along the membrane, and on filopodia.

As can be seen from these examples, the generic model is able to consider numerous forms of interactions with ease, making it applicable to many biological scenarios. Below, we investigate this model further by carrying out some stability analysis both of the general model and of the two examples given above, before moving on to numerical investigations.

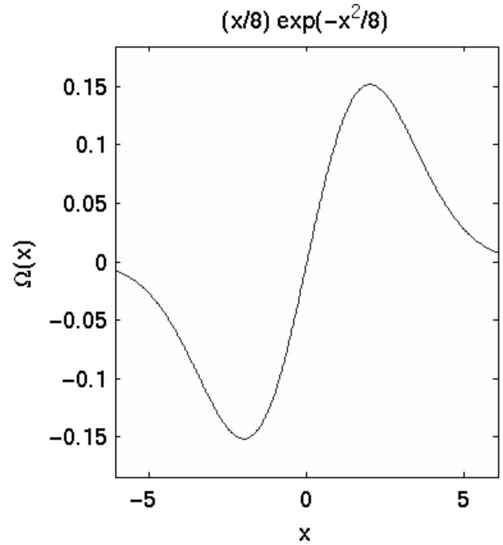

Figure 4.6: Illustration of the function $\Omega(x, \xi_i) = (x/2\xi_i^2)e^{-((x/\xi_i)^2)/2}$, with $\xi_i = 2$ in this case. Cells furthest from the centre attract weakly, whilst cells closer to the centre attract more strongly. Cells very close to the centre attract only weakly. See text for further details.

4.3 Analysis

4.3.1 Scaling the equations

We begin our analysis by reducing the number of parameters in (4.2) and (4.3) through scaling the system, which can be done once we have chosen an appropriate $p(u, v)$ term. Let us assume that $p(u, v) = (1 - (u + v)/P)$, one of the simplest forms of our 'packing' term p. We also let $\Omega(x, \xi_i)$ be of the form $\frac{1}{\xi_i}\tilde{\Omega}(x/\xi_i)$ for some function $\tilde{\Omega}$, so that the width of each $\tilde{\Omega}$ term is scaled by ξ_i. Note that the function $\tilde{\Omega}$ is normalised by ξ_i so that the integral of $\Omega(x, \xi_i)$ over $\mathbb{R}^+$ is one. We let L be an arbitrary length scale; we will consider some different specific values of L later in the chapter. Then by scaling u and v with P, x with L, ξ_{uu}, ξ_{uv}, ξ_{vv}, ξ_{vu} with L, t with L^2/D_u and μ_{uu}, μ_{uv}, μ_{vv}, μ_{vu} with $PL\omega/D_u$, we can rescale our system. We get

$$
\begin{aligned}
\frac{\partial u}{\partial t} =& \frac{\partial^2 u}{\partial x^2} - \frac{\partial}{\partial x}\left(u(1-u-v)\left(\frac{\mu_{uu}}{\xi_{uu}}\int_{\mathbb{R}}\tilde{\Omega}(s/\xi_{uu})u(x+s)ds + \right.\right. \\
& \left.\left. \frac{\mu_{uv}}{\xi_{uv}}\int_{\mathbb{R}}\tilde{\Omega}(s/\xi_{uv})v(x+s)ds\right)\right)
\end{aligned}
\tag{4.8}
$$

and

$$\begin{aligned}\frac{\partial v}{\partial t} =& \tilde{D}\frac{\partial^2 v}{\partial x^2} - \frac{\partial}{\partial x}\left(v(1-u-v)\left(\frac{\mu_{vv}}{\xi_{vv}}\int_{\mathbb{R}}\tilde{\Omega}(s/\xi_{vv})v(x+s)ds+\right.\right.\\ & \left.\left.\frac{\mu_{uv}}{\xi_{vu}}\int_{\mathbb{R}}\tilde{\Omega}(s/\xi_{vu})u(x+s)ds\right)\right),\end{aligned} \tag{4.9}$$

where $\tilde{D} = D_v/D_u$.

Again, boundary conditions and initial conditions can be chosen as appropriate.

4.3.2 Calculating the Dispersion Relation

We explore patterns arising from the arbitrarily chosen uniform initial conditions U and V. Note that since we have our scaled $p(u,v) = (1-u-v)$, we impose that $0 \leq U+V \leq 1$, with also $0 \leq U \leq 1$ and $0 \leq V \leq 1$, to ensure that the initial total tissue cell density is less than the maximum density. We consider (4.8) and (4.9) with $u(x,t) = U + \tilde{u}(x,t)$ and $v(x,t) = V + \tilde{v}(x,t)$, where $\tilde{u}$ and $\tilde{v}$ are small perturbations from U and V respectively. We get

$$\begin{aligned}\frac{\partial \tilde{u}}{\partial t} =& \frac{\partial^2 \tilde{u}}{\partial x^2} - (U(1-U-V))\frac{\partial}{\partial x}\left(\frac{\mu_{uu}}{\xi_{uu}}\int_{\mathbb{R}}\tilde{\Omega}(s/\xi_{uu})\tilde{u}(x+s)ds+\right.\\ & \left.\frac{\mu_{uv}}{\xi_{uv}}\int_{\mathbb{R}}\tilde{\Omega}(s/\xi_{uv})\tilde{v}(x+s)ds\right)\end{aligned} \tag{4.10}$$

and

$$\begin{aligned}\frac{\partial \tilde{v}}{\partial t} =& \tilde{D}\frac{\partial^2 \tilde{v}}{\partial x^2} - (V(1-U-V))\frac{\partial}{\partial x}\left(\frac{\mu_{vv}}{\xi_{vv}}\int_{\mathbb{R}}\tilde{\Omega}(s/\xi_{vv})\tilde{v}(x+s)ds+\right.\\ & \left.\frac{\mu_{uv}}{\xi_{vu}}\int_{\mathbb{R}}\tilde{\Omega}(s/\xi_{vu})\tilde{u}(x+s)ds\right),\end{aligned} \tag{4.11}$$

considering terms linear in $\tilde{u}$ and $\tilde{v}$ only (note that the integral terms $\int_{\mathbb{R}}\tilde{\Omega}U$ and $\int_{\mathbb{R}}\tilde{\Omega}V$ equal 0, as $\tilde{\Omega}$ is an odd function).

We now look for solutions proportional to $e^{\lambda t+iqx}$, setting $\tilde{u} = e^{\lambda t+iqx}$ and $\tilde{v} = Ae^{\lambda t+iqx}$, so that (4.10) and (4.11) become

$$\begin{aligned}\lambda e^{\lambda t+iqx} =& -q^2 e^{\lambda t+iqx} - U(1-U-V)\left(\frac{\mu_{uu}}{\xi_{uu}}\frac{\partial}{\partial x}\int_{\mathbb{R}}\tilde{\Omega}(s/\xi_{uu})e^{\lambda t+iqx+iqs}ds+\right.\\ & \left.\frac{\mu_{uv}}{\xi_{uv}}\frac{\partial}{\partial x}\int_{\mathbb{R}}\tilde{\Omega}(s/\xi_{uv})Ae^{\lambda t+iqx+iqs}ds\right)\end{aligned} \tag{4.12}$$

and

$$A\lambda e^{\lambda t+iqx} = -\tilde{D}Aq^2e^{\lambda t+iqx} - V(1-U-V)\left(\frac{\mu_{vv}}{\xi_{vv}}\frac{\partial}{\partial x}\int_{\mathbb{R}}\tilde{\Omega}(s/\xi_{vv})Ae^{\lambda t+iqx+iqs}ds + \right.$$

$$\left.\frac{\mu_{vu}}{\xi_{vu}}\frac{\partial}{\partial x}\int_{\mathbb{R}}\tilde{\Omega}(s/\xi_{vu})e^{\lambda t+iqx+iqs}ds\right). \tag{4.13}$$

The Leibniz integral rule states

$$\frac{\partial}{\partial x}\int_{a(x)}^{b(x)} f(x,t)dt = f(t,b(x))b'(x) - f(t,a(x))a'(x) + \int_{a(x)}^{b(x)}\frac{\partial}{\partial x}f(x,t)dt.$$

We want to calculate

$$\frac{\partial}{\partial x}\int_{\mathbb{R}}\tilde{\Omega}(s/\xi_i)e^{\lambda t+iqx+iqs}ds = -\frac{\partial}{\partial x}\int_{\mathbb{R}}\tilde{\Omega}(w/\xi_i)e^{\lambda t+iqx-iqw}dw$$

where $w=-s$ since $\tilde{\Omega}$ is odd. So, by the Leibniz integral rule,

$$-\frac{\partial}{\partial x}\int_{\mathbb{R}}\tilde{\Omega}(w/\xi_i)e^{\lambda t+iqx-iqw}dw = -iqe^{\lambda t+iqx}\int_{\mathbb{R}}\tilde{\Omega}(w/\xi_i)e^{-iqw}dw.$$

This is in the form of a Fourier transform of $\tilde{\Omega}$, $\widehat{\Omega}$ say, where $\widehat{\Omega}(x) = \int_{\mathbb{R}}\tilde{\Omega}(x)e^{-iqx}dx$. Note that if the Fourier transform of $\tilde{\Omega}(x)$ is $\widehat{\Omega}(x)$, then the Fourier transform of $\tilde{\Omega}(x/a)$ is $|a|\widehat{\Omega}(ax)$. Substituting this in to (4.12) and (4.13), and dividing through by $e^{\lambda t+iqx}$, we get

$$\lambda = -q^2 + iqU(1-(U+V))\left(\mu_{uu}\widehat{\Omega}(q\xi_{uu}) + \mu_{uv}A\widehat{\Omega}(q\xi_{uv})\right) \tag{4.14}$$

and

$$\lambda = -\tilde{D}q^2 + iqV(1-(U+V))\left(\mu_{vv}\widehat{\Omega}(q\xi_{vv}) + \frac{\mu_{vu}}{A}\widehat{\Omega}(q\xi_{vu})\right). \tag{4.15}$$

Rearranging (4.15) gives

$$\lambda A + A\tilde{D}q^2 - AiqV(1-U-V)\mu_{vv}\widehat{\Omega}(q\xi_{vv}) = iqV(1-U-V)\mu_{vu}\widehat{\Omega}(q\xi_{vu}),$$

so that

$$A = iqV(1-U-V)\mu_{vu}\widehat{\Omega}(q\xi_{vu})/\left((\lambda + \tilde{D}q^2 - iqV(1-U-V)\mu_{vv}\widehat{\Omega}(q\xi_{vv}))\right).$$

Putting A into (4.14) and rearranging, we obtain the following quadratic in λ:

$$\begin{aligned}\lambda^2 + \lambda &\left((1+\tilde{D})q^2 - iq(1-U-V)\left(U\mu_{uu}\widehat{\Omega}(q\xi_{uu}) + V\mu_{vv}\widehat{\Omega}(q\xi_{vv})\right)\right) \\ &+ \left(q^2 - iqU(1-U-V)\mu_{uu}\widehat{\Omega}(q\xi_{uu})\right)\left(\tilde{D}q^2 - iqV(1-U-V)\mu_{vv}\widehat{\Omega}(q\xi_{vv})\right) \\ &+ q^2UV(1-U-V)^2\mu_{uv}\mu_{vu}\widehat{\Omega}(q\xi_{uv})\widehat{\Omega}(q\xi_{vu}) = 0.\end{aligned} \tag{4.16}$$

There exist non-trivial solutions for $\tilde{u}$ and $\tilde{v}$ if and only if (4.16) is satisfied. As $\tilde{\Omega}$ is odd, $\widehat{\Omega}$ is of the form $i\Gamma(q)$, $\Gamma(q) \in \mathbb{R}$. So (4.16) can be written as

$$\lambda^2 + \mathcal{C}(q)\lambda + \mathcal{D}(q) = 0$$

where $\mathcal{C}$ and $\mathcal{D} \in \mathbb{R}$:

$$\mathcal{C}(q) = q^2(1+\tilde{D}) + q(1-U-V)(U\mu_{uu}\Gamma(q\xi_{uu}) + V\mu_{vv}\Gamma(q\xi_{vv})) \tag{4.17}$$

and

$$\begin{aligned}\mathcal{D}(q) =&(q^2 + q(1-U-V)\mu_{uu}\Gamma(q\xi_{uu})U)(\tilde{D}q^2 + q(1-U-V)\mu_{vv}\Gamma(q\xi_{vv})V) \\ &- q^2UV(1-U-V)^2\mu_{uv}\mu_{vu}\Gamma(q\xi_{uv})\Gamma(q\xi_{vu}).\end{aligned} \tag{4.18}$$

We have that if $\mathcal{C}(q) < 0$ for some q, $Re(\lambda_+) > 0$ where $\lambda_+ = 0.5(-\mathcal{C} + \sqrt{\mathcal{C}^2 - 4\mathcal{D}})$ i.e., we have instability. If $\mathcal{C}(q) > 0$ for all q, we can only get instability if there exists some q for which $D(q) < 0$.

4.3.3 Specific analysis of the conditions for instability

If $\mathcal{C}(q) < 0$

We can split the condition $\mathcal{C}(q) < 0$, with $\mathcal{C}(q)$ given by (4.17), into nine cases depending on the signs of the homotypic terms μ_{uu} and μ_{vv} (note that only the terms μ_{uu} and μ_{vv}, as strength terms, can vary from positive to 0 to negative – all other terms, such as interaction ranges and populations, are always positive). This is useful to do as it allows us to immediately understand the restrictions on instability for a given set of strength parameters μ_i and Fourier transforms $i\Gamma$, based on the signs of these terms.

If the homotypic term $\mu_{vv} = 0$, the first sufficient condition for instability is simply given by

$$(1+\tilde{D})/(1-U-V) < -q/q^2(U\mu_{uu}\Gamma(q\xi_{uu})), \tag{4.19}$$

from which we can get our first two cases depending on the sign of μ_{uu}: we let $\mu_{uu} > 0$

Can $\mathcal{C}(q) < 0$?			
Sign of μ_{vv} \ Sign of μ_{uu}	-ve	0	+ve
-ve	Never	Never	Yes
0	Never	Never	Yes
+ve	Yes	Yes	Yes

Table 4.2: Table demonstrating for which signs of μ_{uu} and μ_{vv} instability may occur.

be case one, and $\mu_{uu} < 0$ be case two. We can immediately see that if $\Gamma < 0$, as occurs for the two illustrative examples discussed in detail in Section 4.2.1, only case one will lead to instability. The third and fourth cases are similarly found by setting $\mu_{uu} = 0$ in (4.17). Setting both homotypic terms equal to zero gives us our fifth case. In this case, $\mathcal{C}(q) > 0$ for some q, showing that this fifth case is never satisfied. If $\mu_{vv} > 0$ and $\mu_{uu} > 0$ or $\mu_{vv} < 0$ and $\mu_{uu} < 0$ (cases six and seven), then we simply have

$$(1 + \tilde{D})/(1 - U - V) < -q/q^2 \left(U\mu_{uu}\Gamma(q\xi_{uu}) + V\mu_{vv}\Gamma(q\xi_{vv})\right). \tag{4.20}$$

Here, for $\Gamma < 0$ we may again see this condition satisfied only in case six, leading to instability; in case seven, this condition will never be satisfied. Finally, if $\mu_{uu} < 0$ and $\mu_{vv} > 0$ (case eight), we get

$$(1 + \tilde{D})/(1 - U - V) < q/q^2 \left(U|\mu_{uu}|\Gamma(q\xi_{uu}) - V\mu_{vv}\Gamma(q\xi_{vv})\right), \tag{4.21}$$

with a similar condition obtained in the opposing case (case number nine). If (4.21) holds for the appropriate μ_{uu} and μ_{vv}, then the system will exhibit instability. Unlike in the previous cases, a negative strength term does not imply that (4.21) will not be satisfied. We summarise the above results in Table 4.2.

If $\mathcal{C}(q) > 0$

If $\mathcal{C}(q) \geq 0$, we need $\mathcal{D}(q) < 0$ for instability. Again, we can split condition $D(q) < 0$ with $D(q)$ given by (4.18) into nine cases based on whether μ_{vv} and μ_{uu} are positive, negative or zero. However, within this we must further split our conditions into three more groups, based on the sign of $\mu_{uv}\mu_{vu}$, the product of the heterotypic terms. As such, there are a total of 9×3 cases; we do not list them here as they can be inferred easily from (4.18). However, we take this opportunity to note that, assuming that our Fourier transform $i\Gamma < 0$ as is the case for both of our given examples, if both of the homotypic terms μ_{uu} and $\mu_{vv} \leq 0$, then the product of the heterotypic terms μ_{uv} and μ_{vu} must be > 0 for instability to occur, i.e., the heterotypic terms must either both be attractive, or both repulsive. Note that this means that if all interaction terms are repulsive, instability may occur, distinctly different to the well-documented cell adhesion case (Steinberg, 2007). If one or other or both of the homotypic terms are positive, such a restriction on the heterotypic strengths does not apply.

4.3.4 Specific examples

To further elucidate the system we consider some specific examples. If we take (4.4) and (4.5) of Section 4.2.1, and set $\xi_i = 1$, $i = uu$, uv, vv, vu, (recall that for this example, $p(u, v) = 1$), then we have exactly the same equations as given in Armstrong et al. (2006) (the terms S_u and S_v in their model are equivalent to our μ_{uu} and μ_{vv} terms here, whilst their C is equivalent to our setting $C = \mu_{uv} = \mu_{vu}$; the rationale for setting $\mu_{uv} = \mu_{vu}$ in this way is to consider a cell-cell adhesion scenario, whereby adhesive bonds are formed between each cell and hence interactions across populations are symmetric). For the step function as described in Armstrong et al. (2006), the real part of the Fourier transform is given by $\Gamma(q) = 2(\cos q - 1)/q$, for which $\mathcal{C}(q) = 2\left(q^2 + (\cos q - 1)(U\mu_{uu} + V\mu_{vv})\right)$ and $\mathcal{D}(q) = q^4 + 2q^2(\cos q - 1)(U\mu_{uu} + V\mu_{vv}) + 4UV(\cos q - 1)^2(\mu_{uu}\mu_{vv} - \mu_{uv}^2)$. Combining these, we see that we require $4UV(\mu_{uv}^2 - \mu_{uu}\mu_{vv})X^2 - 2(U\mu_{uu} + V\mu_{vv})X - 1 > 0$ to see instability, where $X = (\cos q - 1)/q^2$, as in Armstrong (2007). See Armstrong (2007) for details on what this implies about instability in this model.

For further understanding we now consider (4.8) and (4.9) with $\tilde{\Omega}(\frac{x}{\xi_i}) = \frac{x}{\xi_i}e^{-x^2/2\xi_i^2}$, similar to equations (4.6) and (4.7) that were first introduced in Section 4.2.1. We stay with this example for the remainder of this chapter, as it provides a good description of cell-cell signalling as described in Section 4.1. Then we have

$$\begin{aligned} \frac{\partial u}{\partial t} =& \frac{\partial^2 u}{\partial x^2} - \frac{\partial}{\partial x}\left(u(1-u-v)\left(\frac{\mu_{uu}}{\xi_{uu}}\int_{\mathbb{R}}(s/\xi_{uu})e^{-(s/\xi_{uu})^2/2}u(x+s)ds + \right.\right. \\ & \left.\left. \frac{\mu_{uv}}{\xi_{uv}}\int_{\mathbb{R}}(s/\xi_{uv})e^{-(s/\xi_{uv})^2/2}v(x+s)ds\right)\right) \end{aligned} \tag{4.22}$$

and

$$\frac{\partial v}{\partial t} = \tilde{D}\frac{\partial^2 v}{\partial x^2} - \frac{\partial}{\partial x}\left(v(1-u-v)p(u,v)\left(\frac{\mu_{vv}}{\xi_{vv}}\int_{\mathbb{R}}(s/\xi_{vv})e^{-(s/\xi_{vv})^2/2}v(x+s)ds + \frac{\mu_{vu}}{\xi_{vu}}\int_{\mathbb{R}}(s/\xi_{vu})e^{-(s/\xi_{vu})^2/2}u(x+s)ds\right)\right), \tag{4.23}$$

where the Fourier transform of $\tilde{\Omega}$ is $i\Gamma(q) = -\sqrt{2\pi}qe^{-q^2/2}$.

Then conditions resulting from inequalities for (4.17) and (4.18) become

$$\alpha + \beta < \mu_{uu}\xi_{uu}Uy^{\xi_{uu}^2} + \mu_{vv}\xi_{vv}Vy^{\xi_{vv}^2}, \tag{4.24}$$

and

$$\alpha\beta < \mu_{uv}\mu_{vu}\xi_{uv}\xi_{vu}UVy^{\xi_{uv}^2+\xi_{vu}^2} + \beta\mu_{uu}\xi_{uu}Uy^{\xi_{uu}^2} + \alpha\mu_{vv}\xi_{vv}Vy^{\xi_{vv}^2} - \mu_{uu}\mu_{vv}UV\xi_{uu}\xi_{vv}y^{\xi_{uu}^2+\xi_{vv}^2}, \tag{4.25}$$

where $\alpha = 1/(\sqrt{2\pi}(1-U-V))$, $\beta = \tilde{D}\alpha$, and $y = e^{-q^2/2}$, all of which are > 0. Note that $y \in (0,1]$.

From these two conditions we can see quite clearly that in the case where the homotypic terms are both negative, the product of the heterotypic terms must be large and positive for there to be instability. If the homotypic terms are positive and sufficiently large, then the sign and magnitude of the heterotypic terms is unimportant with respect to instability of the uniform solution.

To clearly illustrate what these conditions imply in terms of instability for this system, we now carry out some numerical analysis. We consider three specific biological questions:

- How do changes in signalling range affect patterning?
- How do different levels of initial population densities affect patterning?
- How do changes in signalling strength affect patterning, particularly the heterotypic signalling strengths?

Recall that for our normalised Ω, increasing the signalling range has the effect of decreasing maximum signal strength, as total signalling across the range remains the same. Signalling strength is therefore intertwined with signalling range. We do not explore the precise relationship between these two parameters here, as in this initial study we choose to alter just one parameter type at a time.

Some numerical analysis of the instability conditions for a specific example

Since biologists know relatively little about how the distance over which a cell can interact with other cells affects patterning, we will first focus on our range terms in order to provide new insights into cell-cell interaction systems, varying ranges ξ_{uu}, ξ_{vv}, ξ_{uv} and ξ_{vu}. We begin by assuming that our steady states have equal values $U = V = 1/4$ which is in the middle of our range $U + V \in (0, 1]$. We now assume equal random motion for the two cell types (i.e., $\tilde{D} = 1$); biologically, this simply suggests that our two cell types have similar motility in the absence of directional cues. From this we can calculate the parameters α and β in (4.24) and (4.25) as $\alpha = \beta = \sqrt{2/\pi}$. As, at first, we wish to concentrate on the effect of varying range terms only, we fix all strength terms μ_i to be equal. Without a specific biological system in mind, we arbitrarily choose $\mu_i = 1$. Thus all of the parameters that are independent of our ξ_i are fixed. We let our length scale L be the diameter of a cell, and now vary the range parameters ξ_{uu}, ξ_{vv}, ξ_{uv} and $\xi_{vu} \in (0, 5]$ cycling through these values numerically in steps of 0.1 over all values of $y \in (0, 1]$. In the left plot of Figure 4.7, we fix the heterotypic ranges $\xi_{uv} = \xi_{vu} = 1.0$ whilst varying the homotypic ranges ξ_{uu} and ξ_{vv}, whilst in the right hand plot we fix the homotypic ranges to 1.0 whilst varying the heterotypic ones. We see that in both cases, large ranges promote instability.

Intuitively, such a result makes sense. A small range means that a cell interacts only with other cells very close to it, and so only promotes migration over these very short distances. Therefore there is little movement. Interactions over long ranges, however, can lead to migration over long ranges, and hence instability.

Furthermore, with a view to experimentalists who create assays with a fixed initial population of cells, we turn to look at the effect that different initial populations U and V have on stability. We again let our $\mu_i = 1$ and $\tilde{D} = 1$ be as in Figure 4.7, and for the same reasons. Looking at Figure 4.7, we choose $\xi_{uv} = \xi_{vu} = 5.0$ as suitable parameters for which we can see instability. Furthermore, we let $\xi_{uu} = \xi_{vv} = 1.0$. We then vary our initial populations U and V with $U + V < 1$, calculating the appropriate values for α and β for each (U, V) pair. We plot the outcome below (Figure 4.8).

We see that whilst both very small and large values are stable, mid-range and lower values produce instability (Figure 4.8). This suggests that a certain population level of u and v is necessary to see patterning in the first place, but that too large a number leaves little room for instability in the system. If we have just a very low density in an experimental assay, signals will be weak since there will be fewer cells to produce signals, leading to little movement as they fail to receive sufficient signals to encourage them to move. An assay with high population density, on the other hand, will prevent cells from moving due to overcrowding – they physically won't have the space to move.

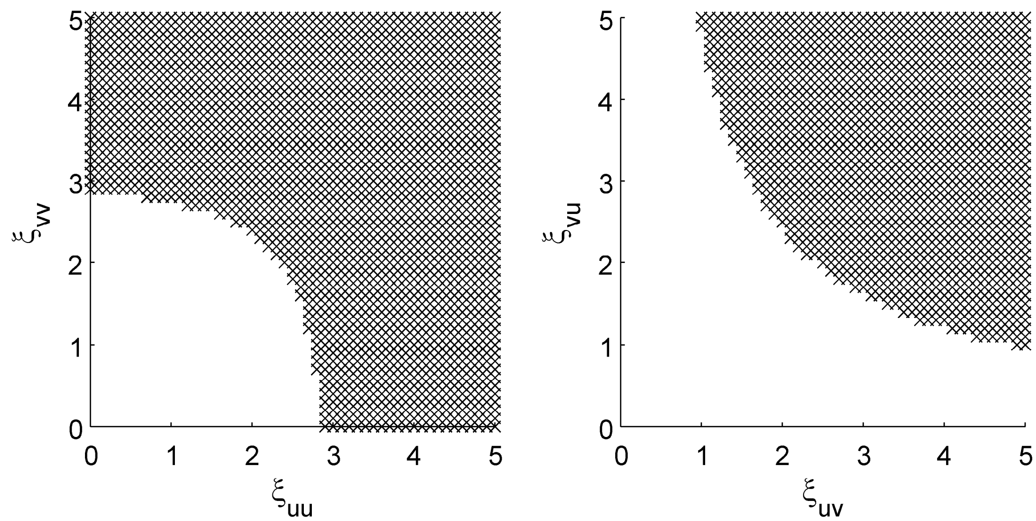

Figure 4.7: Plots showing (ξ_{uu}, ξ_{vv}) (left panel) and (ξ_{uv}, ξ_{vu}) (right panel) parameter regions where instability occurs according to conditions (4.24) and (4.25). We cycle y through 0 to 1 in steps of 0.001 at each plot point to see if these conditions are satisfied for any y. A cross indicates each point where the conditions are satisfied, thus indicating the values of (ξ_{uu}, ξ_{vv}) (left panel) and (ξ_{uv}, ξ_{vu}) (right panel) under which instability occurs in the system of equations given by (4.22) and (4.23). We can see that as ξ_{uu}, ξ_{vv}, ξ_{uv} and ξ_{vu} increase, solutions move further away from the steady state. Parameters used are $\alpha = \beta = \sqrt{2/\pi}$ and $\mu_{uu} = \mu_{vv} = \mu_{uv} = \mu_{vu} = 1.0$. In the left-hand plot we vary the ranges ξ_{uu} and ξ_{vv} from 0.0 to 5.0 in steps of 0.1, whilst we fix $\xi_{uv} = \xi_{vu} = 1.0$. In the right-hand plot we vary ξ_{uv} and ξ_{vu} from 0.0 to 5.0 in steps of 0.1, whilst we fix $\xi_{uu} = \xi_{vv} = 1.0$.

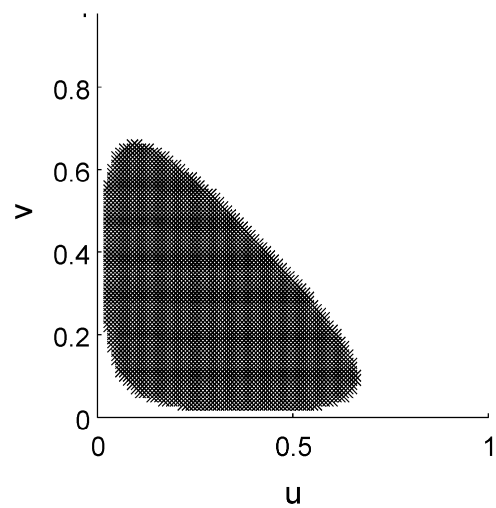

Figure 4.8: Plot showing U, V parameter regions where instability occurs according to conditions (4.24) and (4.25). We again cycle y through 0 to 1 in steps of 0.001 at each plot point to see if these conditions are satisfied for any y. A cross indicates each point where the conditions are satisfied, thus indicating the values of U and V under which instability occurs in the system of equations given by (4.22) and (4.23). We can see that there is a small region of instability for low to mid-sized values of U and V. See text for further details. Parameters used are $\xi_{uv} = \xi_{vu} = 5.0$, and $\xi_{uu} = \xi_{vv} = 1$. We again set $\mu_{uu} = \mu_{vv} = \mu_{uv} = \mu_{vu} = 1.0$, and also $\tilde{D} = 1$, so that $\alpha = \beta = 1.0/(\sqrt{2\pi}(1.0 - U - V))$, which alter as U and V are varied between 0 and 1. The parameters U and $V \in [0, 1]$ are plotted along the $x-$ and $y-$ axis respectively, for values of $U + V \leq 1.0$ only.

Finally, we consider the impact of the homotypic and heterotypic strength terms on stability. Whilst biologists know that cells of the same population have a strong affinity towards each other, little is known about cell interactions between cells of different populations. Bearing this in mind, we here make our homotypic strength terms μ_{uu} and μ_{vv} high (i.e., here we set $\mu_{uu} = \mu_{vv} = 5$), and vary our heterotypic ones. We keep all other parameters as in Figure 4.7, and also fix our range parameters ξ_{uu} and ξ_{vv} at 1.0, and ξ_{uv} and ξ_{vu} at 5.0 as in Figure 4.8. Looking at Figure 4.9, left panel, we notice that if the product of the heterotypic strength terms $\mu_{uv}\mu_{vu}$ is sufficiently large, we see instability. This is as we would expect from considering condition (4.25). There is no instability for cases where one of the heterotypic strengths is attractive and the other repulsive (i.e., where the product is negative), suggesting that in these cases in Figure 4.9 the heterotypic strengths may work to counteract each other, promoting stability. From looking at (4.25), we can see that the only case for which we would see instability with these heterotypic terms would be if the homotypic terms were large. There is also no instability in Figure 4.9 for the case where the heterotypic strengths are 0, and (4.24) and (4.25) are not satisfied, suggesting that heterotypic interaction is essential in this specific case.

For completeness, we also consider the case for fixed heterotypic strength terms and varying homotypic strength terms. Since so little is known about heterotypic interactions, we here fix $\mu_{uv} = \mu_{vu} = 1.0$, and vary our homotypic strength terms, whilst keeping everything else as in our heterotypic strength case. In Figure 4.9, right panel, threshold behaviour is seen, showing that once homotypic strengths have increased above a certain level, instability is guaranteed in this case.

Biologically, the stronger the positive homotypic strengths between cells the more cell-cell attraction there is. Thus strong homotypic attraction encourages cells to move towards their own kind, leading to a separation of cell populations similar to that seen in the cell adhesion scenario explored in the experiments of Steinberg (1962a,b,c). Strong homotypic repulsion, on the other hand, leads to cells of the same type pushing away from each other, leading to mixing of the two cell types. The opposite of this repulsive effect is true of heterotypic strengths. If both u to v and v to u interactions are mediated by a strong repulsive force, the total effect is for u cells to group with other u cells and v cells to group with other v cells, leading to an effect similar to that produced by strong homotypic attraction strengths. On the other hand, if, for example, u attracts v but v repulses u, these two interactions effectively cancel each other out, preventing cells from moving. Finally, strong positive heterotypic interactions in this scenario leads cells to move towards each other, promoting agglomerations.

As can be seen from all of the above analysis, instability can be produced in the system in a variety of ways, whether through varying the heterotypic or homotypic range or strength terms, or even by varying the initial densities of each population.

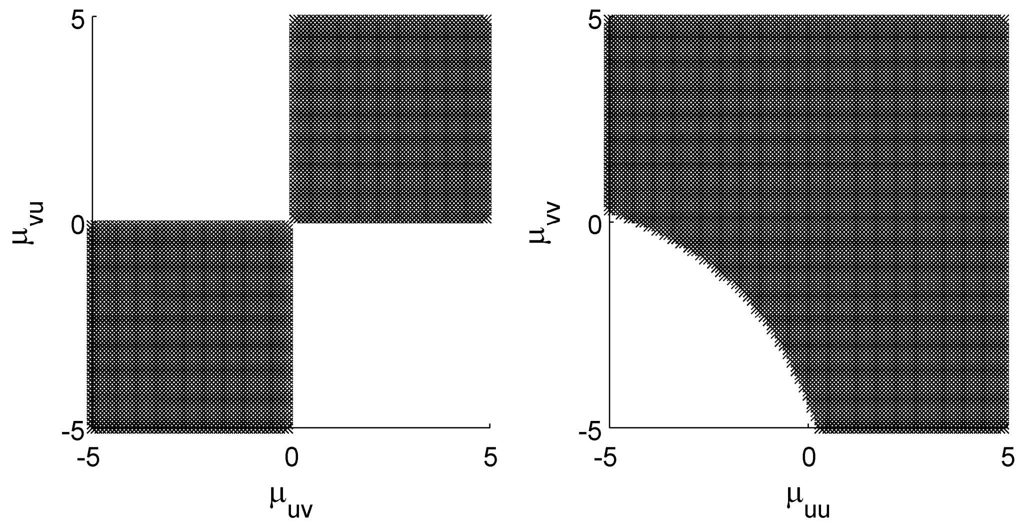

Figure 4.9: Plots showing parameter regions where instability occurs according to conditions (4.24) and (4.25) for varying heterotypic strengths (left panel) and varying homotypic strengths (right panel). We again cycle y through 0 to 1 in steps of 0.001 at each plot point to see if these conditions are satisfied for any y. A cross indicates each point where the conditions are satisfied, thus indicating the parameters under which instability occurs in the system of equations given by (4.22) and (4.23). We can see in the left panel that as $|\mu_{uv}|$ and $|\mu_{vu}|$ increase, solutions move further away from the steady state. See text for further details. The parameters $\mu_{uu} = \mu_{vv} = 3.0$, while μ_{uv} and $\mu_{vu} \in [-5, 5]$ are varied along the $x-$ and $y-$ axis respectively. In the right panel, we can see that there is instability above a given threshold for μ_{uu}, μ_{vv}, as is expected from conditions (4.24) and (4.25). The parameters $\mu_{uv} = \mu_{vu} = 1.0$, while μ_{uu} and $\mu_{vv} \in [-5, 5]$ are varied along the $x-$ and $y-$ axis respectively. For both panels, the ranges are again ξ_{uu} and $\xi_{vv} = 1.0$, ξ_{uv} and $\xi_{vu} = 5.0$, whilst $U = V = 0.25$ and $\tilde{D} = 1.0$ once more. Other parameters are then $\alpha = \beta = \sqrt{2/\pi}$.

It is clear then that there is much possibility for patterning in the model, and we now turn to numerical simulations of equations (4.22) and (4.23) in order to explore the form of some of the patterns.

4.4 Numerical simulations in one dimension

We carry out some numerical analysis of the model equations (4.22) and (4.23). We use a Matlab code which uses the inbuilt Matlab time integrator 'ode45' to solve the system of ODEs which we formulate using the Method of Lines approach, and a Fast Fourier Transform technique to calculate the integral. We thank Dr. Alf Gerisch, the author of this code, who kindly let us use it in this work. For more details on the numerical methods, see Chapter 5.

Note that throughout this entire section, $U = V = 0.25$ plus some noise is our initial condition, $\mu_i = 50$ is our attraction strength for $i = uu, uv, vv, vu$, and $\tilde{D} = 1.0$ is our coefficient of cell diffusion, unless otherwised stated, all chosen so that we see instability according to conditions (4.24) and (4.25). We here let our length scale L represent the maximum signalling range of a u cell; we assume this maximum length to be ten times the diameter of a single cell as is found in newt pigment cells (Tucker & Erickson, 1986). Then a sensible value for our signalling ranges is $\xi_i \geq 0.1$. We can then set our domain to be of length 10. Also note that for the remainder of this chapter we truncate the integral of $\tilde{\Omega}(x)$ in order to implement our finite numerical scheme; instead of calculating $\tilde{\Omega}(x)$ over the real line as in our analysis above, we calculate it from $x = -10\xi_i$ to $x = 10\xi_i$. Such a truncation alters the dynamics of our system very little, since $\tilde{\Omega}(|10\xi_i|)$ is very small, and $\tilde{\Omega}(x) \to 0$ as $x \to \infty$. We use periodic boundary conditions throughout.

4.4.1 Verification of the analysis

We begin by using our numerical code to verify the statements made in Section 4.3.4 regarding conditions for instability. We seek to verify each of our results in turn, beginning with a consideration of the range parameters ξ_i, before moving on to look at initial cell densities U and V, and then strength parameters μ_i.

In order to determine whether the parameter values produce stability or instability, for each time point we calculate the l^2-norm of our population. That is to say, at each time point we calculate $(U - u(x))^2$ for each x within our domain, where U is our initial density of population u, and $u(x)$ is the cell density of u at position x. We sum these together across all x, and take the square root of the total, giving us our l^2-norm for the whole domain. By plotting the l^2-norm for each time point, we can see whether the system is stabilising (the l^2-norm is decreasing towards zero) or becoming more unstable (the l^2-norm is increasing).

Here we present plots of l^2-norm versus time for various parameters, chosen to verify the analysis plots in Section 4.3.4. Recall that the term 'heterotypic' describes interactions between differing cell types, and 'homotypic' describes interactions between cells of the same type. Recall further that whilst most parameter values are positive, the strength terms μ_i,(which, combined with the signalling function $\tilde{\Omega}$, describe the magnitude and direction of cell-cell interaction forces), can be negative to represent cell-cell repulsion. When positive, they represent cell-cell attraction.

Note that for all of the following plots the first plot point is at time $t = 1$, with $t = 0$ omitted for clarity. We begin with a look at range plots (Figure 4.10). We see that instability is found if the homotypic ranges $\xi_{uu} = \xi_{vv} = 4$ but stability is found if $\xi_{uu} = \xi_{vv} = 1$ (Figure 4.10, top panels). The switch between stabilities takes place between $\xi_{uu} = \xi_{vv} = 2$ and $\xi_{uu} = \xi_{vv} = 3$, although plots of these two scenarios are not not shown as the change in stability is harder to see than in the plots shown. We see the same with the heterotypic range case (Figure 4.10, lower panels), as expected from Figure 4.7.

We now consider initial densities of populations u and v (Figure 4.11). We find that, after first seeing stability for values of u and v at 0.05 and below (Figure 4.11, top panel), we then see instability for values between 0.15 and 0.35 (the middle case where $u = v = 0.25$ is shown; Figure 4.11, middle panel), and then stability for values of 0.45 and above (Figure 4.11, bottom panel). This is exactly as we would expect from considering Figure 4.8.

Finally we look at both homotypic and heterotypic strength terms (Figure 4.12). In the heterotypic case, we see instability for positive values of $\mu_{uv}\mu_{vu}$ (Figure 4.12, top and bottom panel, right hand side), but stability in the $\mu_{uv}\mu_{vu} = 0$ case (Figure 4.12, middle panel, right hand side). For the homotypic strength terms, we see instability for positive and zero strength terms (Figure 4.12, top and middle panel, left hand side), and instability when $\mu_{uu} = \mu_{vv} = -1$ and below (Figure 4.12, bottom panel, left hand side). Both of these are as we would expect from considering Figure 4.9.

In conclusion, our numerical simulations match our analysis, suggesting that our conditions for instability (4.24) and (4.25) are indeed accurate. This corroboration in turn provides assurance that the numerical method is implemented correctly.

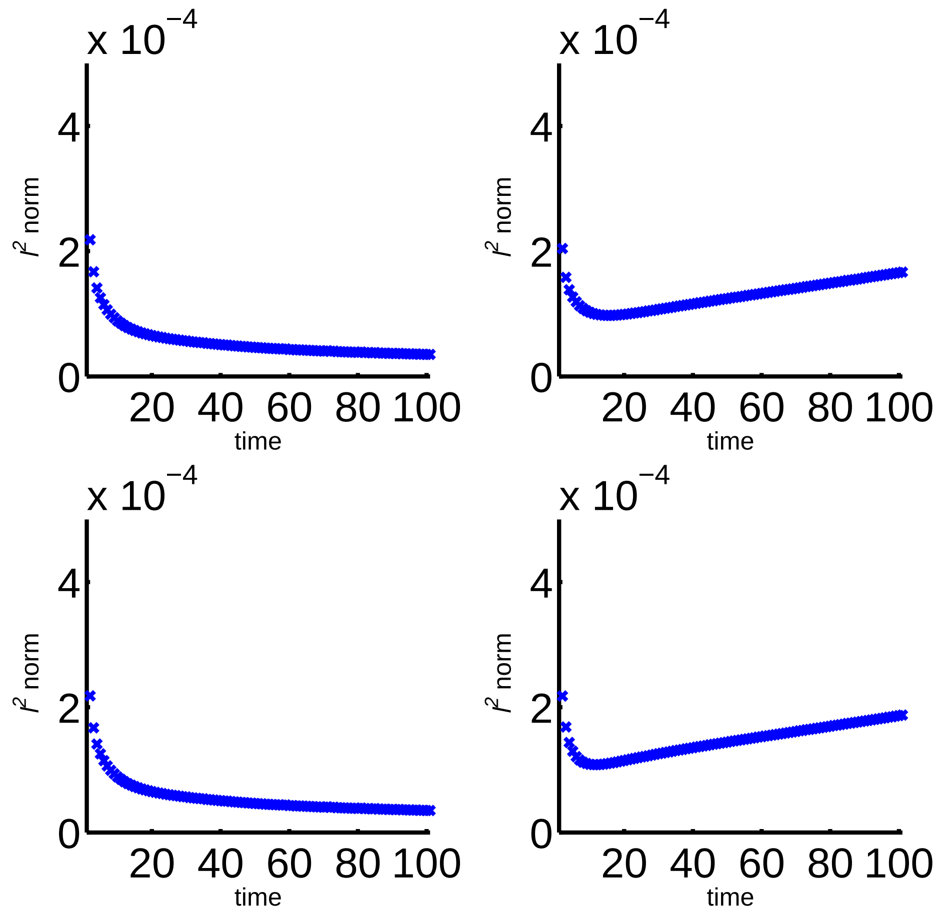

Figure 4.10: Plots of l^2-norm versus time for simulations of equations (4.22) and (4.23) varying homotypic ranges (top) and heterotypic ranges (bottom). In the top left simulation we set $\xi_{uu} = \xi_{vv} = 1$, with $\xi_{uu} = \xi_{vv} = 4$ in the top right plot. In the bottom left simulation we set $\xi_{uv} = \xi_{vu} = 1$, with $\xi_{uv} = \xi_{vu} = 4$ in the bottom right plot. We see stability in the left-hand plots, as represented by the l^2-norm tending to zero, and instability in the right-hand plots as seen by the increase in l^2-norm. All parameters are as in Figure 4.7, with all numerical details for the simulation of (4.22) and (4.23) as detailed in Chapter 5.

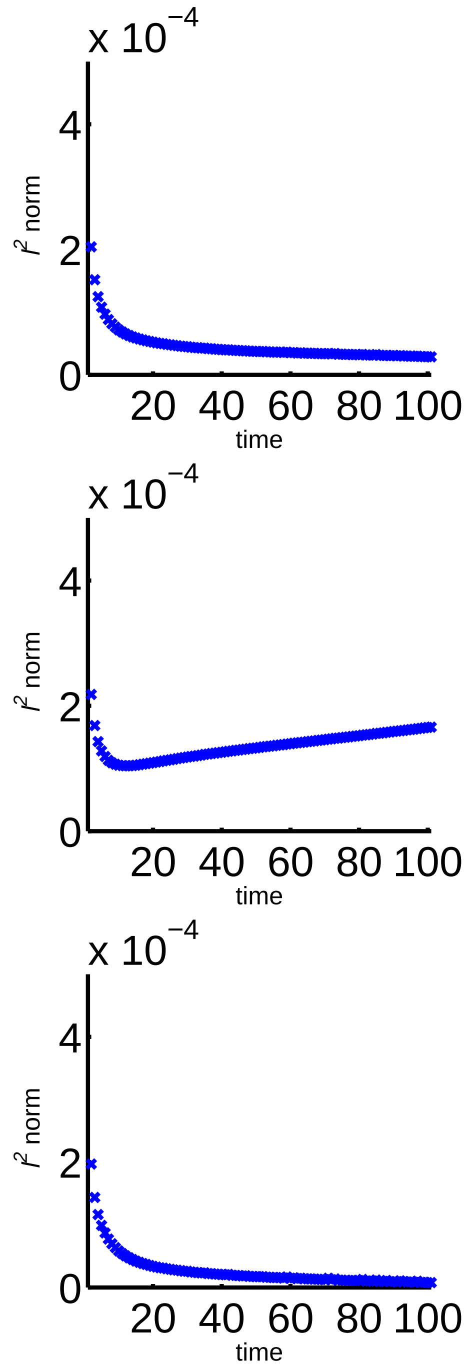

Figure 4.11: Plots of l^2-norm versus time for simulations of equations (4.22) and (4.23) varying initial densities of u and v. We set, from top to bottom, $u = v = 0.05$, $u = v = 0.25$ and $u = v = 0.5$. We see stability in the top and bottom plots, but instability in the middle plot, as expected from considering Figure 4.8. All parameters are as in Figure 4.8, with all numerical details for the simulation of (4.22) and (4.23) as detailed in Chapter 5.

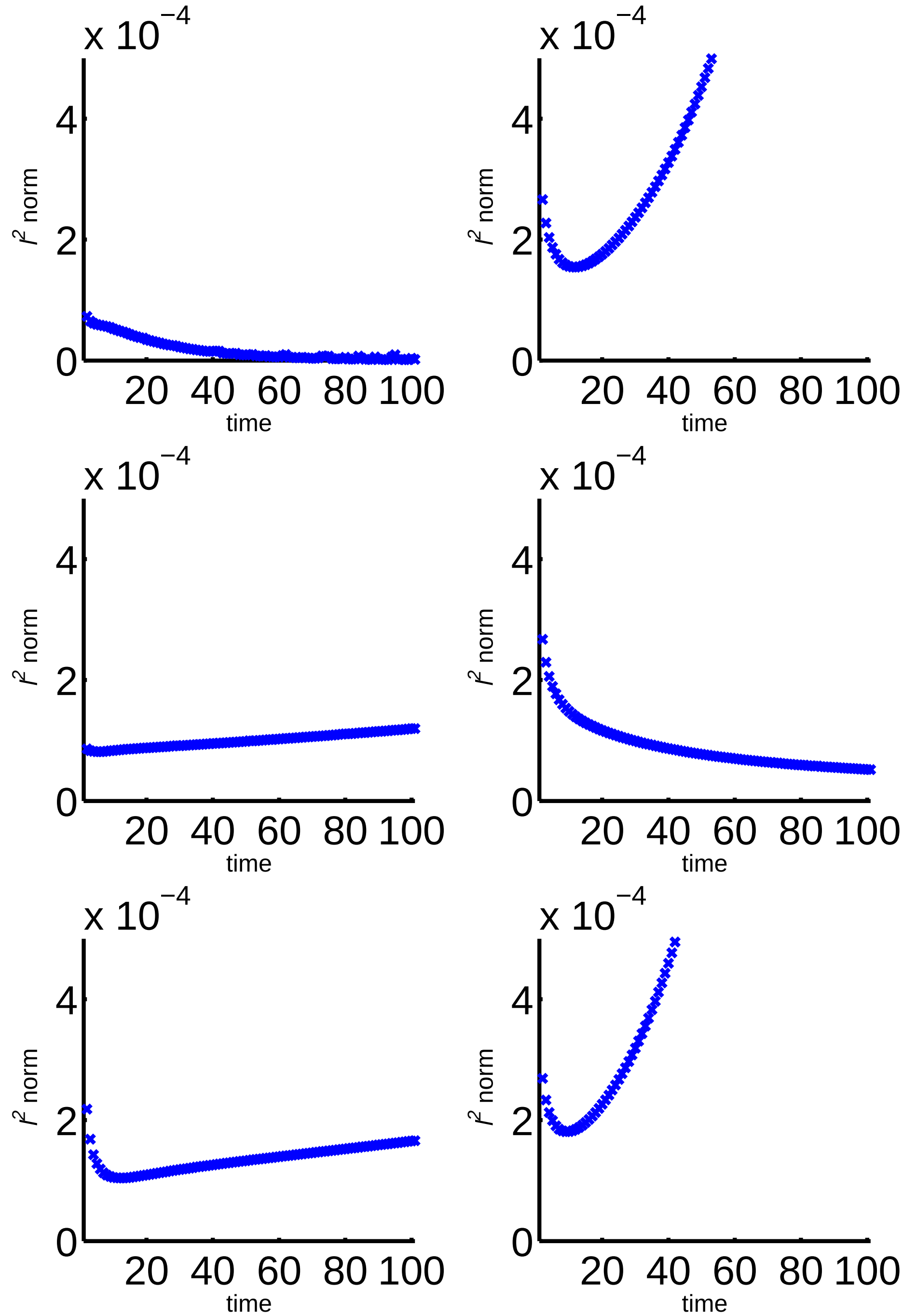

Figure 4.12: Plots of l^2-norm versus time for simulations of equations (4.22) and (4.23) varying homotypic and heterotypic strengths. In the top left simulation we set $\mu_{uu} = \mu_{vv} = -1$, with $\mu_{uv} = \mu_{vu} = -1$ in the top right plot. In the middle left simulation we set $\mu_{uu} = \mu_{vv} = 0$, with $\mu_{uv} = \mu_{vu} = 0$ in the middle right plot. In the bottom left simulation we set $\mu_{uu} = \mu_{vv} = 1$, with $\mu_{uv} = \mu_{vu} = 1$ in the bottom right plot. In the left-hand plots we see a change from stability to instability between -1 and 0, with this change maintained at 1. In the right-hand plots, stability is only apparent in the middle case, whilst the other two plots indicate instability, as expected from Figure 4.9. All parameters are as in Figure 4.9, with all numerical details for the simulation of (4.22) and (4.23) as detailed in Chapter 5.

4.4.2 Preliminary investigations of pattern formation

Having satisfied ourselves that our analysis is accurate we now carry out some preliminary investigations of the model equations (4.22) and (4.23) in order to begin to understand the kind of patterning that may arise, for whilst our analysis tells us when we can expect patterns to occur it does not tell us what these patterns will look like: this will depend on the fully nonlinear equations. Our parameter space is large (we have eleven parameters that we may vary), and so we begin by varying just one or two parameters at a time. We consider:

- one population, varying the interaction range term ξ_i
- one population, varying interaction strength μ_i, only in the attractive case (the repulsive case will always be stable as seen from conditions (4.24) and (4.25))
- two populations, varying homotypic interaction ranges
- two populations, varying homotypic interaction strengths, only in the attractive case (the fully repulsive case will always be stable as seen from conditions (4.24) and (4.25))
- two populations, varying both heterotypic interaction ranges
- two populations, varying one homotypic interaction range and one heterotypic interaction range
- two populations, varying both heterotypic interaction strengths, for both attractive and repulsive cases
- two populations, varying one homotypic interaction strength and one heterotypic interaction strength, for both attractive and repulsive cases.

In this preliminary study we run all simulations to just $t = 0.5$, before moving on in Section 4.4.3 to vary just one heterotypic range term ξ_{uv} and then one heterotypic strength term μ_{uv}, running simulations to $t = 20$ in the former and up to $t = 100$ in the latter. For a biological system where cell diffusion is $10^{-10}\text{cm}^2/\text{sec}$ say, these times are equivalent to approximately 6 days, 33 weeks and 3 years (see Section 4.5 for details of this calculation). Note that the results presented in this section mainly show transient patterning, i.e., a stationary state has not been reached, although at steady states, patterning may still exist.

One population

With only one population (in this case, we arbitrarily set $v = 0$), there are clearly no heterotypic terms to be investigated. We concentrate on considering ranges and

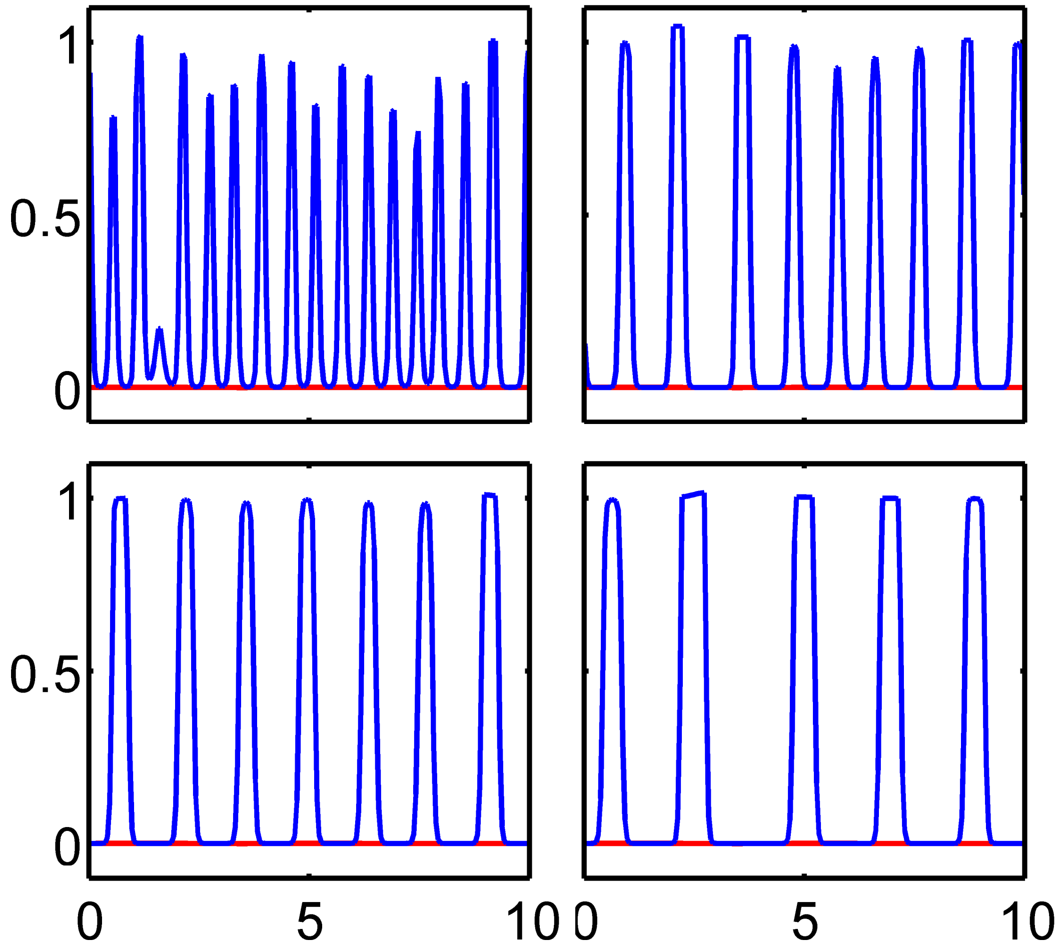

Figure 4.13: Simulations of the model equation (4.22). We plot the density of u (blue) and v (red) at $t = 0.5$ as we increase the range ξ_{uu} from 0.1 to 0.4. We see fewer peaks and wider peaks as the interaction range increases. Parameters are $\mu_{uu} = 100$, $U = 0.25$, $V = 0$, ξ_{uu} varied as described. The domain is of length 10 with 200 grid points, whilst the time discretisation is varied according to the Matlab package 'ode45'. For more numerical details, see Chapter 5.

strengths of the u population in turn. We see aggregations of u produced in both cases (Figure 4.13 and 4.14, blue lines; note that as we are considering only the u cell population, the v cell density, shown in red, is at 0). Note that the width of the aggregations approximately scales with the size of ξ_i, with aggregations being several cells in diameter.

Two populations, homotypic interactions only

We now move on to consider two populations, although we restrict ourselves to considering just homotypic interactions. Here, then, heterotypic terms are equal to 0. Again we look at ranges and strengths in turn, and again we see aggregations form in both cases. In Figure 4.15, we keep the range ξ_{uu} the same and vary ξ_{vv}. As ξ_{vv} increases, the width of the v aggregations (red) also increases, whilst those of the u

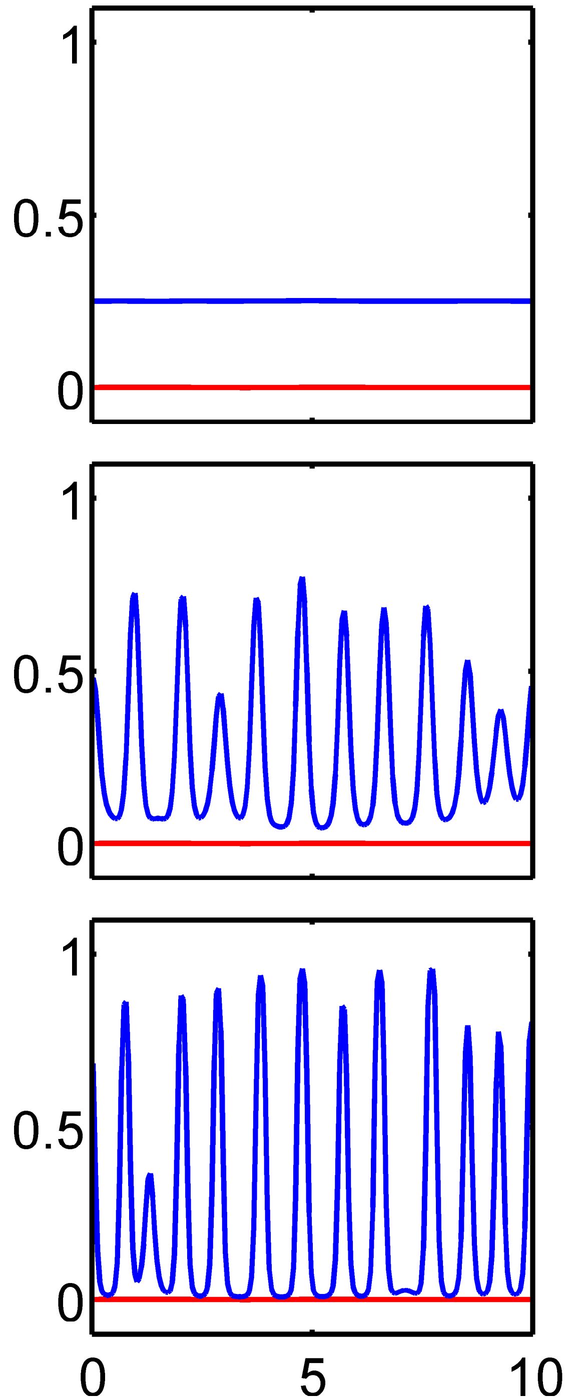

Figure 4.14: Simulations of the model equation (4.22). Instability at time $t = 0.5$ as μ_{uu} increases from 20 to 35 to 50. We see that as homotypic attraction increases, aggregations move further away from the steady state, whilst below a critical value for μ_{uu}, no aggregations are seen. Parameter μ_{uu} varies as described, with $\xi_{uu} = 0.1$. All other parameter values and numerical details are as in Figure 4.13.

population (blue) remain the same. Again, all aggregations are several cells wide, as in Figure 4.13. As in the one population case, as the homotypic signal strengths increase, aggregations move further away from the steady state (not shown).

Two populations, homotypic and heterotypic interactions

We begin by varying the heterotypic ranges of both populations, keeping all else fixed. We see aggregation width increasing as range increases, with the aggregations of u and v being in phase (not shown).

We now vary the heterotypic and homotypic range of one population, keeping the other ranges fixed. We see that whilst the aggregations of the two cell populations are in phase when the ranges of the two populations are similar (Figure 4.16, top two panels), if the heterotypic range of one population begins to differ greatly in size from both the heterotypic and homotypic ranges of the second population, narrower aggregations of the population type with the smaller heterotypic range will also form (Figure 4.16, lower two panels). This shows that our model is able to produce aggregations of multiple widths appearing alongside one another as is seen, for example, on the fish *Danio kerri*. Note however that these simulations do not tell us whether narrow aggregations will be permanent over long timescales

Note that the determination as to whether two coupled populations will experience in phase or out of phase patterning close to the steady state can be calculated, and we detail that process here. Recall that in our calculation of the dispersion relation (4.16), we assumed solutions proportional to $e^{ikx+\lambda t}$, with $\tilde{u} = e^{ikx+\lambda t}$ and $\tilde{v} = Ae^{ikx+\lambda t}$. This led us to equations (4.14) and (4.15). Multiplying these equations back through by $e^{ikx+\lambda t}$, as they were at an earlier stage in the calculation of the dispersion relation, we can then rearrange them such that we have the solution matrix

$$\begin{pmatrix} \lambda+q^2-iqU(1-(U+V))\mu_{uu}\widehat{\Omega}(q\xi_{uu}) & -iqU(1-(U+V))\mu_{uv}\widehat{\Omega}(q\xi_{uv}) \\ -iqV(1-(U+V))\mu_{vu}\widehat{\Omega}(q\xi_{vu}) & \lambda+\tilde{D}q^2-iqV(1-(U+V))\mu_{vv}\widehat{\Omega}(q\xi_{vv}) \end{pmatrix} \begin{pmatrix} \tilde{u} \\ \tilde{v} \end{pmatrix} = \begin{pmatrix} 0 \\ 0 \end{pmatrix} \tag{4.26}$$

when there are solutions. Straightforward rearrangement of this matrix now leads to two ratios of $\tilde{u}/\tilde{v}$. Either one of these ratios can be used to determine whether the solutions will be in phase, out of phase, or neither, depending on both the sign of the ratio and whether it is real or complex. If our eigenvalues λ are real, then because of the nature of our Fourier transform $\widehat{\Omega}$ for our specific example, our ratios $\tilde{u}/\tilde{v}$ will always be real, leading to all of our coupled solutions being either fully in phase if the ratio is positive, or fully out of phase if the ratio is negative. Note that it is unusual that by altering just one parameter, we are able to change whether aggregations form in phase or out of phase. Biologically speaking, this is the difference between seeing alternating aggregations of one cell population with another and seeing

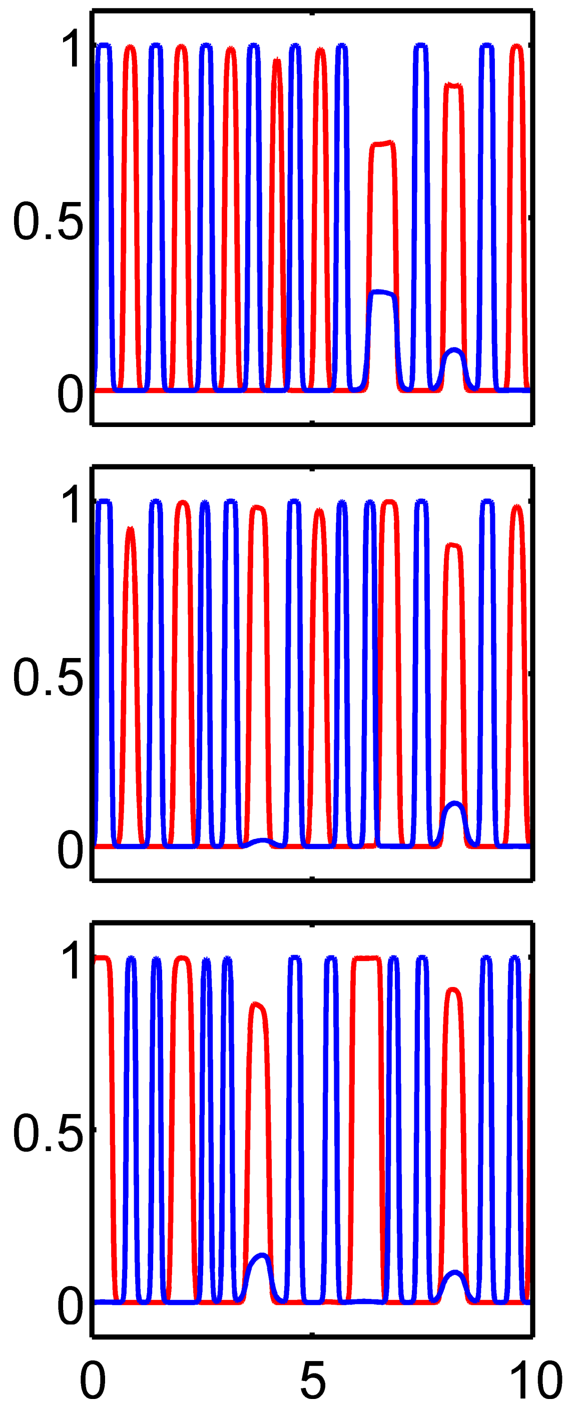

Figure 4.15: Simulations of the model equations (4.22) and (4.23). Instability at time $t = 0.5$ as $\xi_{uu} = 0.1$ and ξ_{vv} increases from 0.2 to 0.3 to 0.4. We see that as the homotypic range of v increases, moving further away in value from the homotypic range of u, wider v (red) aggregations form, whilst u (blue) aggregations remain narrow. Parameters ξ_{uu} and ξ_{vv} are as described, with $\tilde{D} = 1$, $U = V = 0.25$, $\mu_i = 100$ for $i = uu, vv$, and $\mu_i = 0$ for $i = uv, vu$. All numerical details are as in Figure 4.13.

single aggregations of mixed cell populations alternating with aggregations devoid of either cell type, two quite different scenarios. If, on the other hand, λ is complex, then we will see travelling solutions which are only partially in phase, with the phase difference measured by calculating the argument of $\tilde{u}/\tilde{v}$. Note that we do not see a partial phase structure for non-travelling solutions. For more on phase difference in reaction-diffusion-advection systems, see Satnoianu & Menzinger (2002).

We next move on to varying strength terms. We first vary heterotypic strength terms only (homotypic terms are positive but fixed). We see that in the attractive case, equally spaced and in-phase aggregations form (Figure 4.17), whilst in the repulsive case, out-of-phase narrow aggregations form (Figure 4.18). It is clear that whilst our analysis shows that both repulsive and attractive heterotypic strength terms do lead to instability, the kind of spatial patterning this instability leads to differ greatly. Note that the behaviour in Figure 4.17 is exactly as we would expect from considering the Differential Adhesion Hypothesis Model (Section 4.1; also see Gerisch & Painter, 2010), showing the connection of our model to another, well established model.

We now vary the heterotypic and homotypic strengths of one population, keeping the others fixed. Whilst the attractive case is similar to that above (not shown), the repulsive case is here stable, showing no patterning (Figure 4.19). This is as we would expect from considering the instability conditions (4.24) and (4.25), and clearly shows how the values of both the homotypic and the heterotypic terms can affect the stability of the system.

Note that, as mentioned above, these results show transient states. Experience from other models involving directional movement of a population with no kinetics (Painter, 2009; Hillen & Painter, 2009) suggests that the aggregations seen may coarsen over time, producing fewer, wider aggregations. We consider this coarsening in the following section.

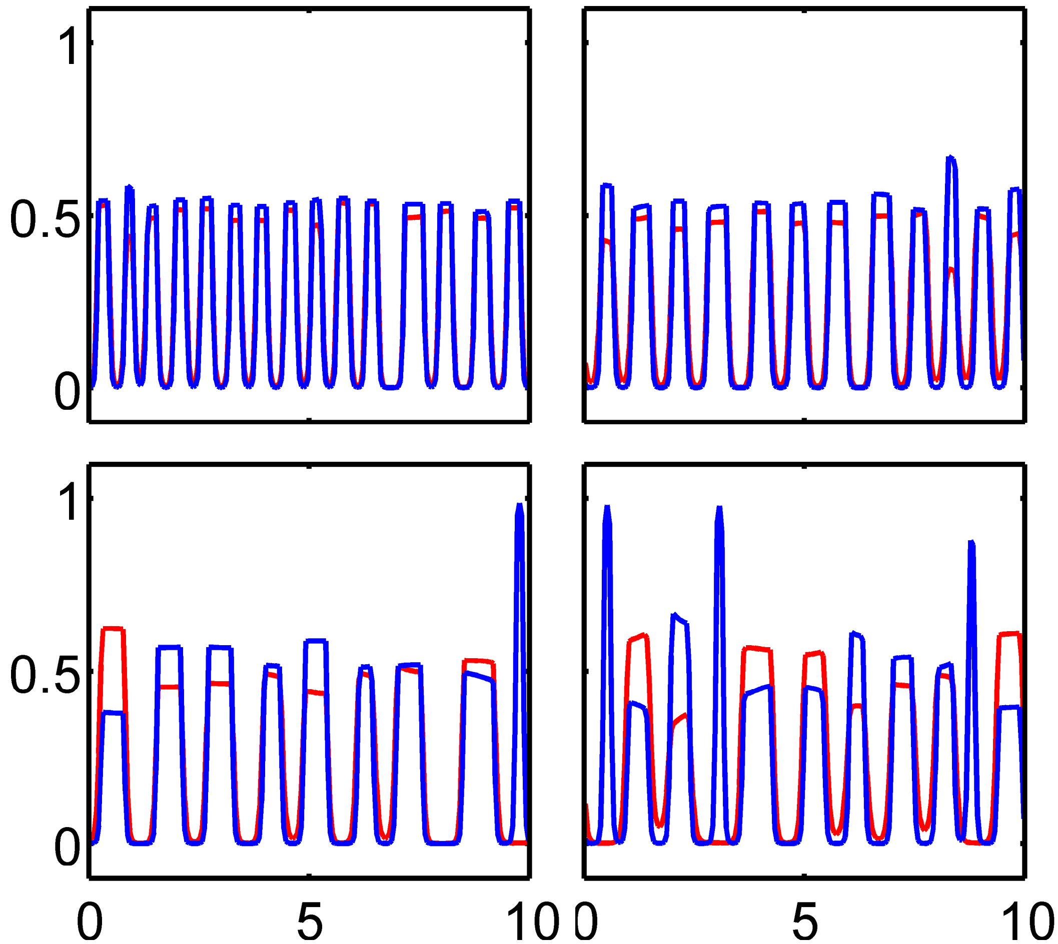

Figure 4.16: Simulations of the model equations (4.22) and (4.23). Instability at time $t = 0.5$ for the homotypic range $\xi_{vv} = 0.2$, with the heterotypic range ξ_{vu} increasing from 0.1 to 0.2 to 0.3 to 0.4. We see that as heterotypic range of v to u increases, the v population again begins to 'fill in' the gaps left between aggregations. While the mixed aggregations are quite wide, u only (blue) aggregations remain narrow. Results are similar for the $\xi_{vv} = 0.1$, $\xi_{vv} = 0.3$ and $\xi_{vv} = 0.4$ cases. All numerical and parameter details are as in Figure 4.15, except for ξ_{vv} and ξvu which vary as stated, and $\xi_{uu} = \xi_{uv} = 0.1$.

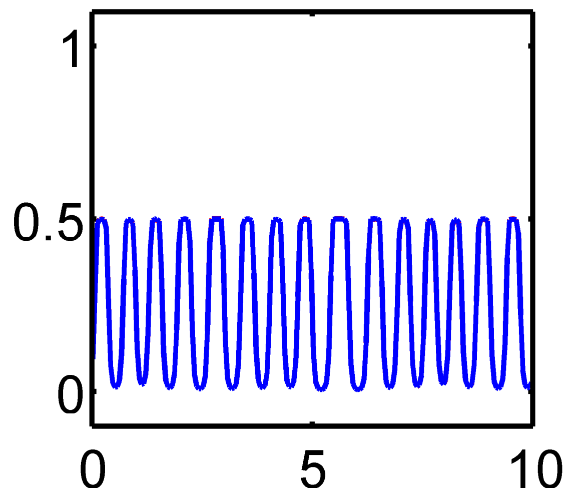

Figure 4.17: Simulations of the model equations (4.22) and (4.23). Instability at time $t = 0.5$ with $\mu_{uu} = \mu_{vv} = 50$, and $\mu_{uv} = \mu_{vu} = 60$. We see that both populations are unstable, with the aggregations of the two populations forming one on top of the other. Similar results are seen for values of $\mu_{uv} = \mu_{vu} = 50$ and $\mu_{uv} = \mu_{vu} = 40$. All parameters and numerical details are as in Figure 4.15, except for $\xi_i = 0.1$ for $i = uu, uv, vu, vv$, and μ_i for $i = uu, uv, vu, vv$ which are as described.

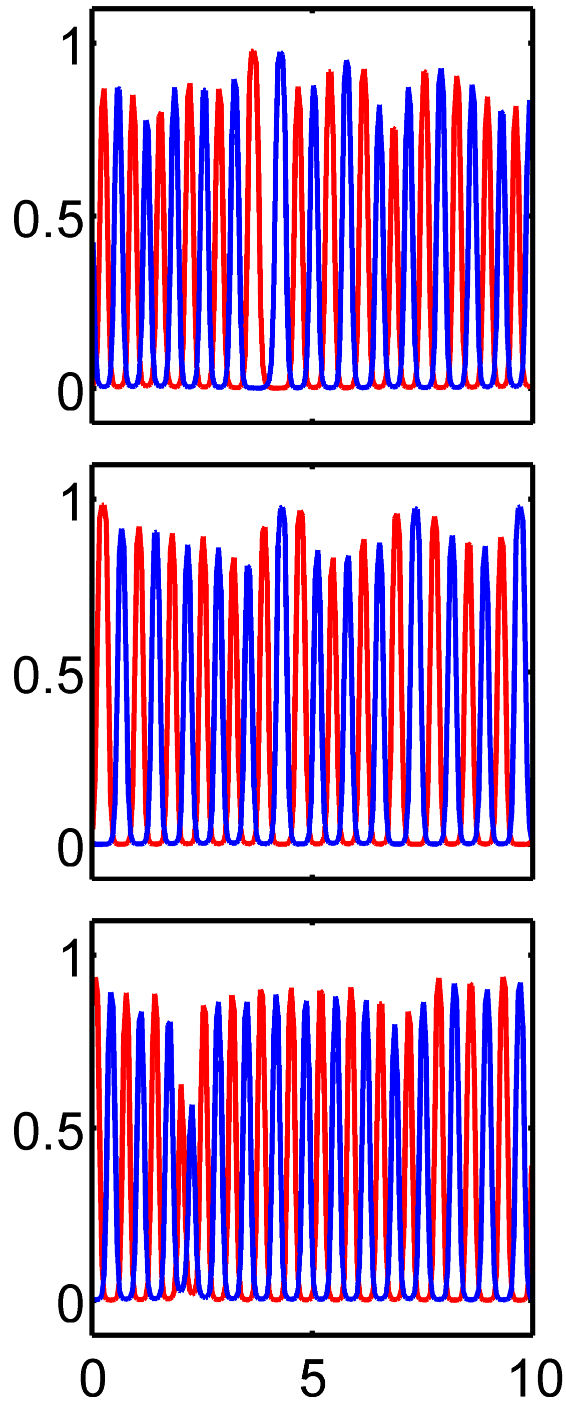

Figure 4.18: Simulations of the model equations (4.22) and (4.23). Instability at time $t = 0.5$ as $\mu_{uv} = -40$ and μ_{vu} decreases from -40 to -50 to -60. We see little change in aggregations as the heterotypic repulsion of u by v increases. We see similar results for $\mu_{uv} = -50$ and $\mu_{uv} = -60$. Homotypic strengths are fixed at 50. All parameters and numerical details are as in Figure 4.17, except for μ_i for $i = uu, uv, vu, vv$ which are as described.

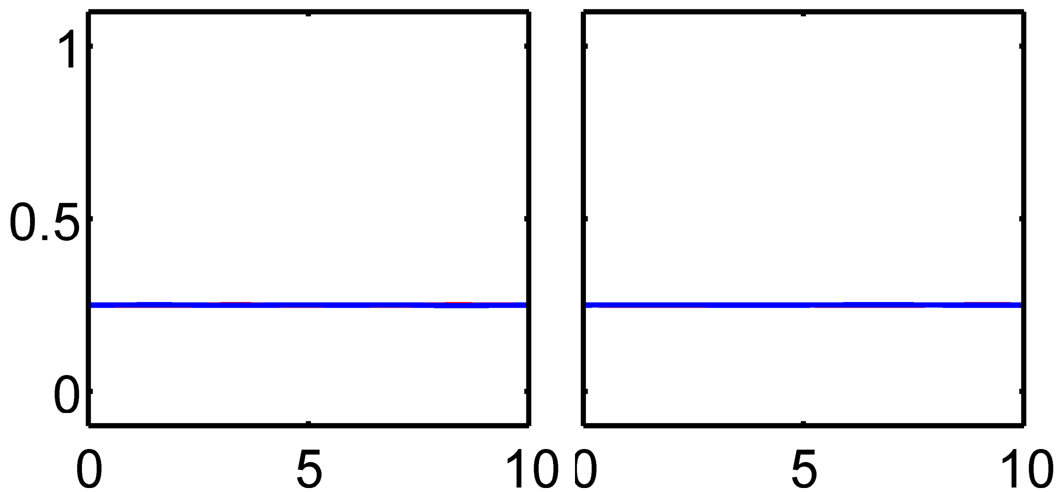

Figure 4.19: Simulations of the model equations (4.22) and (4.23). Patterning at time $t = 0.5$ as $\mu_{vv} = -40$ and μ_{vu} decreases from -40 to -60. We see that this is stable for both cases due to the negative v homotypic term, as can be understood from considering the instability conditions (4.24) and (4.25). All parameters and numerical details are as in Figure 4.17, except for μ_i for $i = uu, uv, vu, vv$ which are as described.

4.4.3 More detailed analysis

We see that we rarely reach stationary solutions in any of the plots above, and so are not sure if a final stable pattern will emerge. We therefore move to consider a longer timescale to dimensionless time $t = 20$, which is just over thirty three weeks (see Section 4.5 for a calculation of this). This time we vary only one parameter at a time in order to carry out a more focussed analysis. We begin by looking at the heterotypic range ξ_{uv}, before going on to vary the heterotypic strength μ_{uv}.

Varying one heterotypic range term only

We want to consider the effect that varying one range parameter will have on the spatial patterning seen. We vary the heterotypic range ξ_{uv} from 0.2 to 0.4, whilst keeping all other parameters fixed. We plot the results of these simulations below (Figures 4.20, 4.21, 4.22).

We see in all plots that aggregations form quickly in comparison to the time it takes for those aggregations to then widen (coarsen) . Stripes also coarsen over time, with the largest $\xi_{uv} = 0.4$ producing the widest aggregations, as one would expect (Figure 4.22). Note that the narrower aggregations, which are encouraged by the other, smaller, range parameters $\xi_{uu} = \xi_{vv} = \xi_{vu} = 0.1$, have disappeared by $t = 12$ (just over 1 day) in the $\xi_{uv} = 0.3$ and $\xi_{uv} = 0.4$ cases (Figure 4.21 and 4.22), whilst a narrow aggregation persists until $t = 20$ in the $\xi_{uv} = 0.2$ case (Figure 4.20). In terms of cell diameter, aggregations are again several cells wide in all cases.

Since aggregations are clearly still transient at this point, these simulations underline the importance of understanding the dimensional time for which our simulations are biologically relevant; many patterns that occur in the biological world have stripes of differing widths, and we may well wish to assess the relevance of our model to such biological scenarios, comparing the spatial patterning we see with that seen in biology. Whilst for some biological scenarios a timescale of 33 weeks or shorter, as here, will be relevant, thus making the results of these simulations useful, for others a longer time may be important. Since we are not at a stationary state by $t = 20$, this longer time could lead to different patterns forming, and hence simulations may need to be run for longer should the biological scenario under investigation require it.

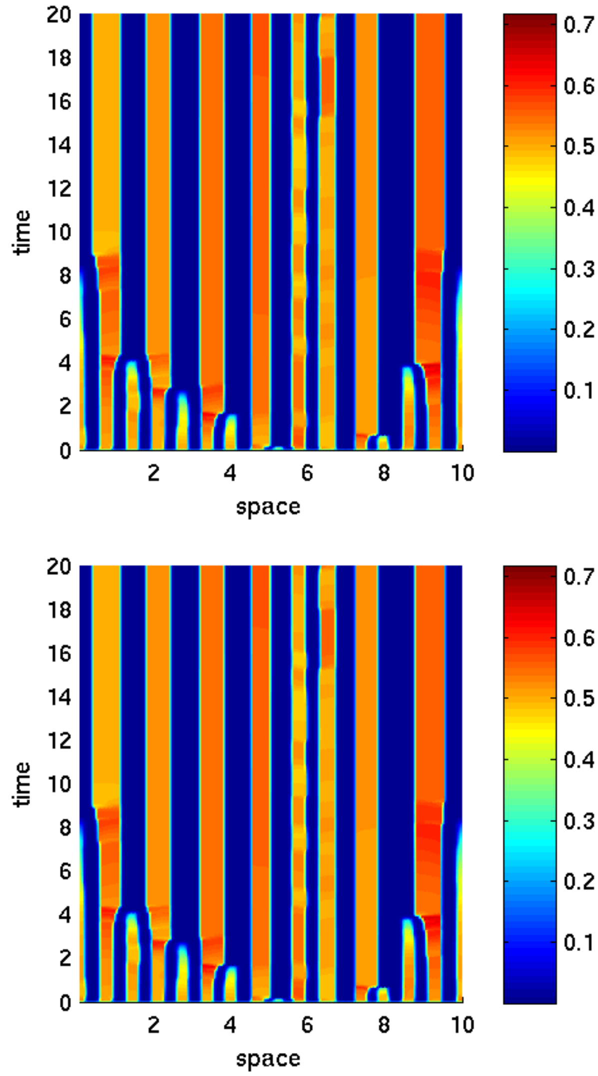

Figure 4.20: Space time plot of simulation of the model equations (4.22) and (4.23). Here we set the heterotypic range ξ_{uv} to 0.2, with all other ranges at 0.1. We plot the density of u (upper plot) and v (lower plot) through space over time, until $t = 20$. We see aggregations quickly form and then widen over time, with aggregations of different widths present. All parameters and numerical details are as in Figure 4.15, except for ξ_i for $i = uu, uv, vu, vv$ which are as described.

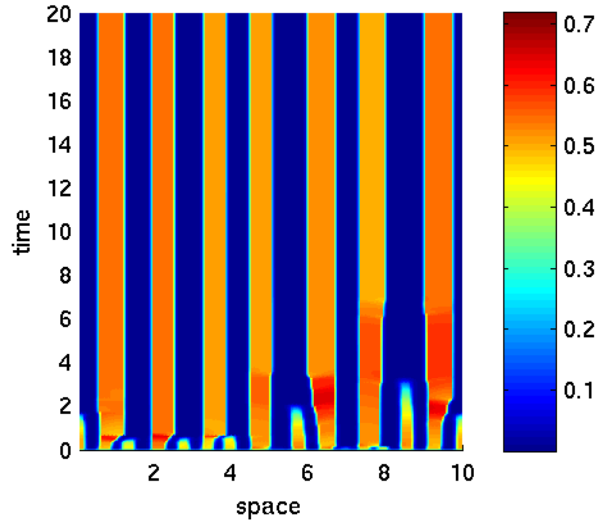

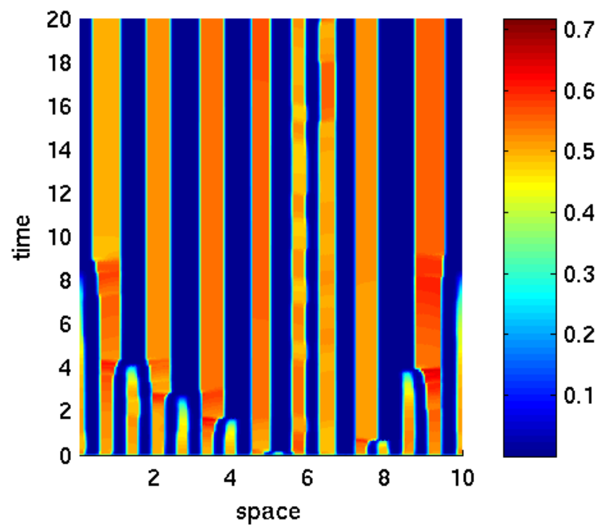

Figure 4.21: Space time plot of simulation of the model equations (4.22) and (4.23). Here the heterotypic range $\xi_{uv} = 0.3$, and again we plot the density of u (upper plot) and v (lower plot) through space over time until $t = 20$. Again aggregations quickly form and then widen. All parameters and numerical details are as in Figure 4.17, except for ξ_i for $i = uu, uv, vu, vv$ which are as described.

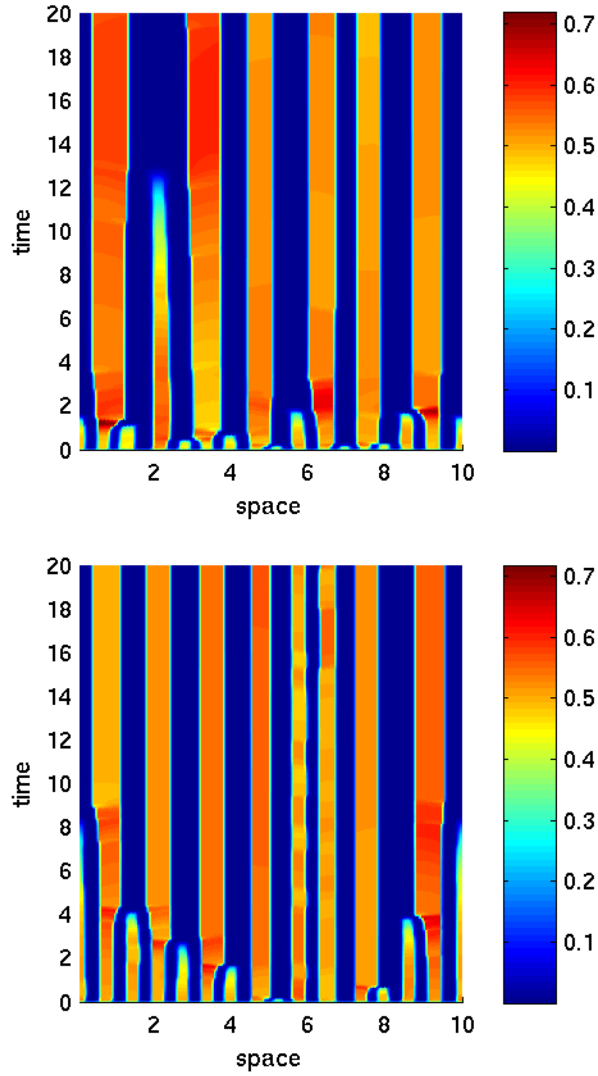

Figure 4.22: Space time plot of simulation of the model equations (4.22) and (4.23). Here the heterotypic range $\xi_{uv} = 0.4$, and again we plot the density of u (upper plot) and v (lower plot) through space over time, until $t = 20$. Again aggregations quickly form and then widen. All parameters and numerical details are as in Figure 4.17, except for ξ_i for $i = uu, uv, vu, vv$ which are as described.

Varying one heterotypic strength term only

We now vary the heterotypic strength μ_{uv} from -500 to 50 to 500, whilst keeping all other strengths the same at $\mu_i = 50$, $i = uu, vv, vu$. The results are below (Figure 4.23). We show plots for initial conditions of fixed density with noise. Note that we also tried flat initial conditions (i.e., no noise), and initial conditions of flat everywhere except for one small 'hump' for both populations half-way along the domain. However, over long times these different initial conditions had no impact on the final patterning seen, and so we do not show them here.

We see aggregations forming in both attractive cases, with aggregations consisting of exactly the same density of u and v cells in the $\mu_{uv} = 50$ case (Figure 4.23, top panels). In the $\mu_{uv} = 500$ case (Figure 4.23, middle panels), u is attracted strongly to v, and so forms high density peaks in places of high v density, while being scarcely present in places of low v density. Stripe widths increase over time, whilst the number of aggregations seen decreases. In the repulsive case, however (Figure 4.23, lower panels), we do not see such aggregations form. Rather the v population forms one wide, dense peak as it repels the u population away. Where the density of v is lower, the u population is able to form peaks, although these are unstable.

We see then that even up to $t = 20$, stationary solutions are not seen at all in the repulsion case, and that agglomerations that form in the other two cases are not stable, but rather continue to merge over time (Figure 4.23, left-hand panels). As a stationary pattern has clearly not yet been reached in any of the three cases, we now run them to $t = 100$, about 3 years in our chosen timescale scenario (Figure 4.24; see Section 4.5 for the calculation used to calculate this dimensional time). However, whilst past $t = 20$ we no longer see the merging of aggregations over time in the attractive cases (Figure 4.24, top two panels), we still do not see fixed patterning in the repulsive case (Figure 4.24, lower panel), underlining again the importance of timescale as discussed above.

We now zoom in on Figure 4.24, lower panel, looking at the transition between a few individual timepoints at a time to try and get a grasp of the seemingly arrhythmic dynamics (Figure 4.25). We see an increasingly defined criss-cross pattern form over time. This corresponds to the formation of irregular peaks which travel across the domain, only to die out near the band of high v density. New peaks constantly form in the centre of the domain, away from the high density band of v.

We now explore in more detail the kinds of patterning produced by a repulsion scenario such this one, as this is the only scenario that we have so far come across that has produced irregular spatial patterning.

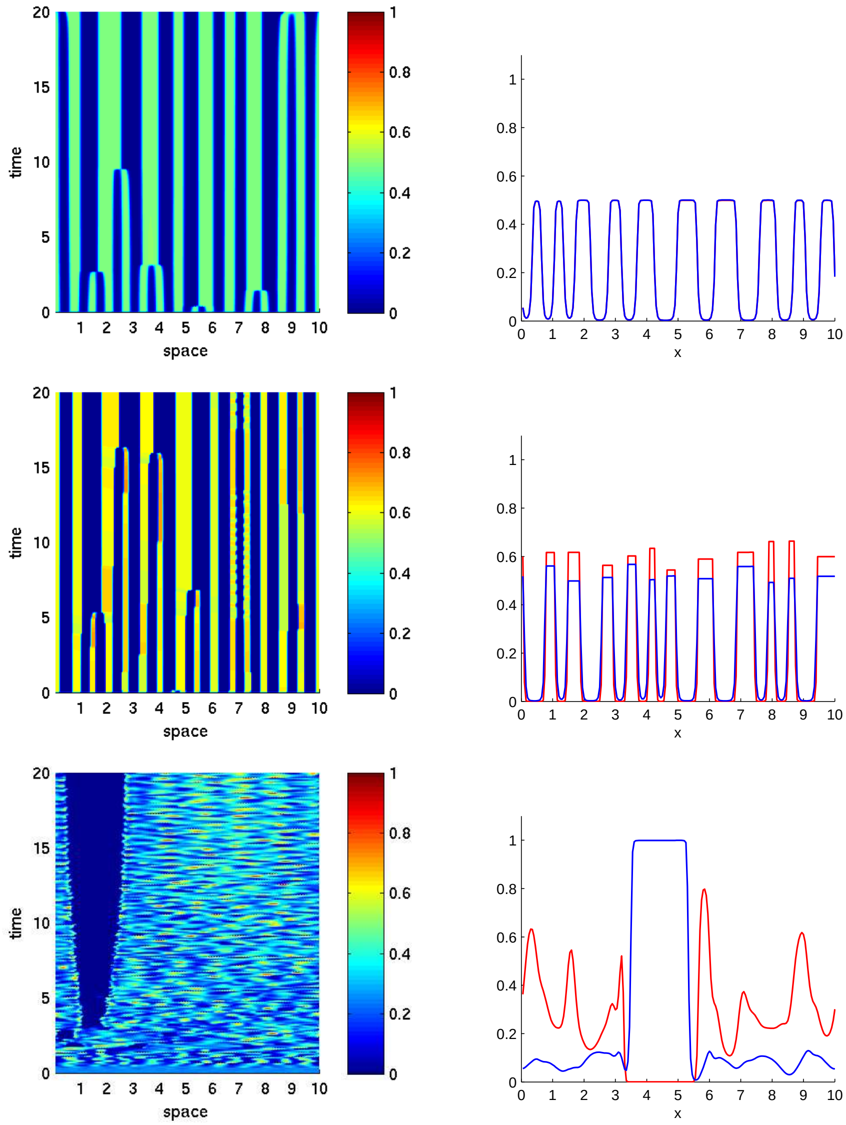

Figure 4.23: Simulations of the model equations (4.22) and (4.23). Space-time plots for the u population for, top to bottom, $\mu_{uv} = 50$, 500, -500 (left-hand panel), with space-density plots at $t = 20$ (right-hand panel) for both the u (red) and v (blue) populations. Left-hand panel: we plot the density of u through space at the time points indicated. In the case where all strengths are equal, we quickly see numerous agglomerations forming at a density of 0.5. These show exact mixing in the corresponding space-density plot. In the unequal attractive case we again see numerous agglomerations form, although here u has a high density (higher than that of v, as can be seen in the corresponding space-density plot). We see no clear pattern emerging in the repulsion case, although we do see agglomerations growing bigger with time. All parameters and numerical details are as in Figure 4.17, except for $\mu_i = 50$ for $i = uu, vu, vv$, and μ_{uv} which is as described.

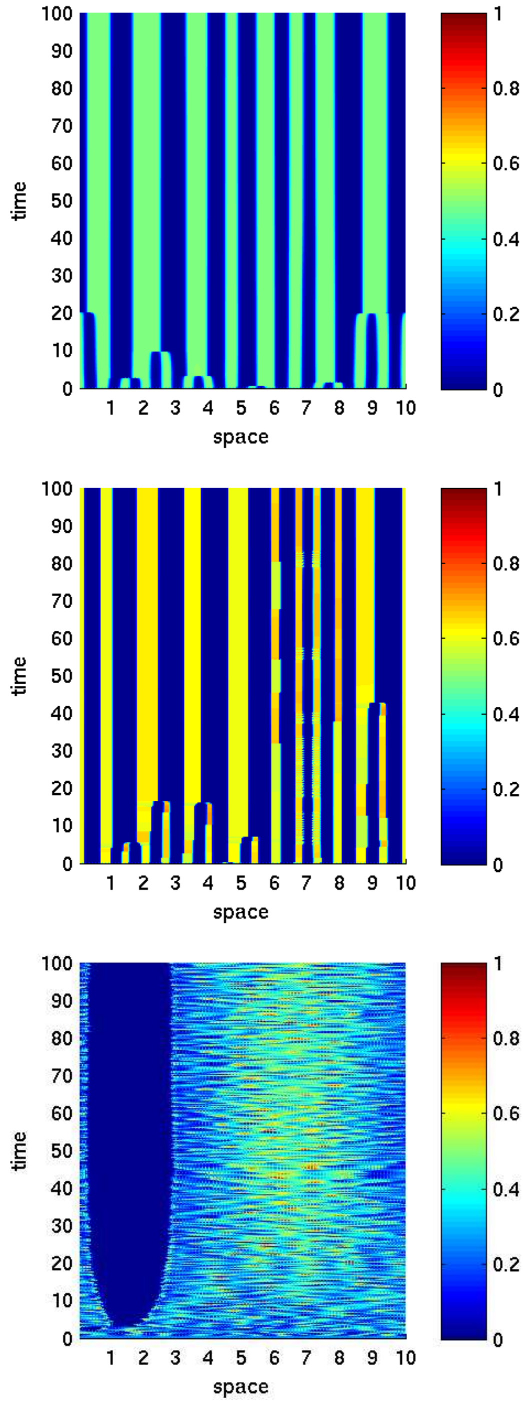

Figure 4.24: Simulations of the model equations (4.22) and (4.23). Again we plot space-time plots at the time points indicated, with, from top to bottom, μ_{uv} = 50, 500, -500. The attractive cases continue to lead to relatively constant agglomerations, although over the time of the plot, two of these agglomerations do aggregate to form one agglomeration. However, even over long times the repulsive $\mu_{uv} = -500$ case sees no stable pattern emerging. All parameters and numerical details are as in Figure 4.23.

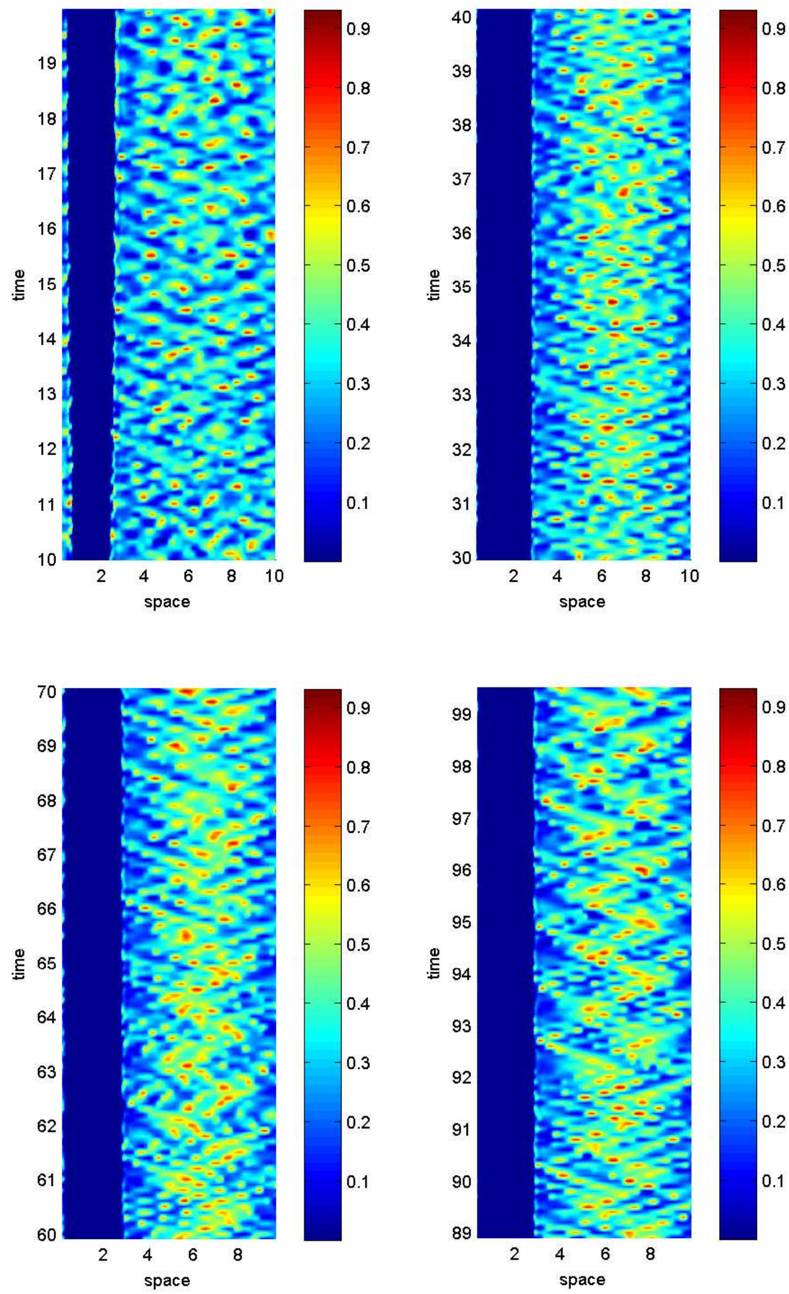

Figure 4.25: Close up snap shots of Figure 4.24 at times indicated, stretched to emphasise the transient dynamics of the u population. See text for further details.

Looking at the $\mu_{uv} < 0$ case in more detail

We now focus on a scenario similar to the repulsive case explored above, as it has shown highly unstable behaviour. We let our interaction strengths μ_i be $\mu_{uu} = 50\theta$, $\mu_{uv} = -100\theta$, $\mu_{vu} = 50\theta$ and $\mu_{vv} = 50\theta$, where θ is a parameter. We will vary our μ_i, $i = uu, uv, vv, vu$, by varying θ between 0.6 and 1.5, and look at the various different patterns which develop. Before doing so, we carry out some analysis to see what kind of behaviours we expect. We detail that analysis here.

We recall our dispersion relation (4.16) as in Section 4.3.2. In the θ scenario we have here, $\mu_{uu} = \mu_{vv}$, $\mu_{uv}\mu_{vu} < 0$, and all range parameters ξ_i are equal. Then the eigenvalues are always complex, with

$$\lambda_{1,2}(q) = -q^2 + q^2 AB \pm iq^2 A\sqrt{|\mu_{uv}\mu_{vu}|},$$

where $A = U(1-U-V)|\Gamma(q\xi_i)|/2q = V(1-U-V)|\Gamma(q\xi_i)|/2q$ and $B = 2\mu_{uu} = 2\mu_{vv}$. Note that there always exists an unstable solution for some q if B is sufficiently large. For our particular case, we need the homotypic strength term $\mu_{uu} = \mu_{vv}$ to be approximately 32 in order to see patterning. Meanwhile, the non-zero imaginary part of our eigenvalue indicates that close to bifurcation our unstable solutions will oscillate and travel. The period of these oscillations is given by $q^2 A\sqrt{|\mu_{uv}\mu_{vu}|}$ where q is the wavenumber, with the wavelength of each oscillation given by $2\pi/q$, demonstrating that we expect the period of oscillations to increase as $|\mu_{uv}|$ increases. Furthermore, we can determine if the solutions will be in phase, out of phase, or partially in phase by carrying out the calculation as detailed in (4.26), Section 4.4.2. We find that the ratio $\tilde{u}/\tilde{v}$ is complex, so we expect to see partially in phase solutions. In fact, the ratio is entirely imaginary for any q^2, meaning that the phase difference, which is given by the argument of $\tilde{u}/\tilde{v}$, will be simply $\pi/2$, as can be seen in Figure 4.28.

Turning to our simulations, we see that we do indeed have unstable solutions if $\mu_{uu} = \mu_{vv}$ is sufficiently large, whilst before then solutions are stable (Figure 4.26). The solutions oscillate in the early time steps for a low θ value (Figure 4.27), before beginning to travel. Travelling solutions with peaks partially in phase, as our analysis predicted, are seen for higher values of θ (Figures 4.28 and 4.29). The waves travel backwards, and in the $\theta = 0.8$ case, the waves have an irregular shape. As θ increases further to $\theta = 1.2$, a band of v cells forms, whilst the u population remains disorganised (Figure 4.30). Finally, we observe a band of each cell population forming across the domain, and see these bands 'breathing' (Figure 4.31). That is to say, the diameters of the bands of the two populations oscillate over time. This can be seen clearly by observing the space-density plots recorded at times $t = 20$ and $t = 25$ (Figure 4.31, lower panels): the band of u (red) notably increases in width. This width then decreases again, before once again increasing, as can be seen from considering the space-time plot (Figure 4.31, top panel). For more on breathing phenomena, see Vanag & Epstein (2007) and Guvrevich et al. (2006), both of whom discuss breathing in reaction diffusion systems.

Note that as our range of possible wavenumbers is large, we are unable to be sure of the exact values of our wavenumbers and periods for each simulation (we could find the value of q^2 for which $Re(\lambda)$ is maximum and use this as an estimate, as we would expect the largest wavenumber to be the dominant one in simulations, but this is not always the case and so is unsatisfactory). Note also that because we are dealing with the discrete case, the domain length of our simulations has an impact on wavelength, as with periodic boundary conditions there must be exactly $n \in \mathbb{N}$ wavelengths so that the waves at the left and right boundaries match up. Therefore we require $q = n\tilde{L}$, where $\tilde{L}$ is our domain length, so that in this discrete scenario the wavelength of each oscillation is in fact given by $2\tilde{L}\pi/q$.

In conclusion, we see that we move from complete mixing, to oscillatory behaviour, to travelling waves, to disorganised behaviour, to bands of single populations that breathe. The large range of patterning that we see demonstrates the importance of knowing precise parameter values when investigating spatial patterns – it is not sufficient to simply know the ratios of parameters to one another. Note that we still see no clear pattern emerging in the $\theta = 1.2$ case, suggesting that perhaps we should run our simulations for longer in order to see what stable patterns (if any) would emerge. Again, reference to the dimensional time required for a specific biological scenario under consideration would help us to make this decision.

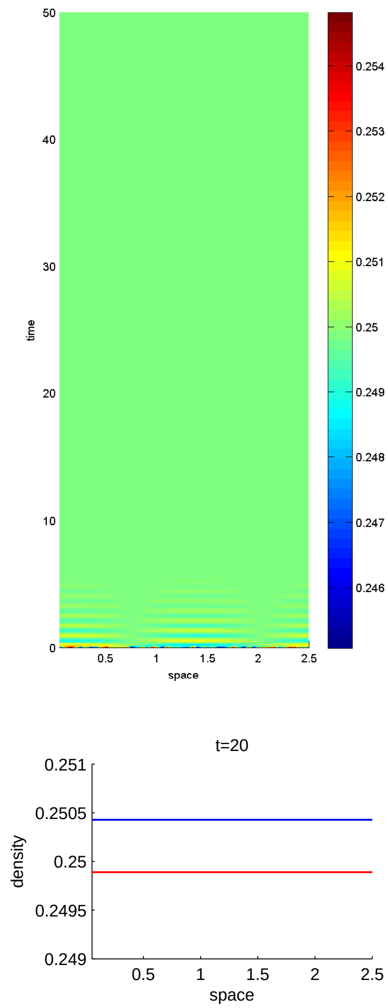

Figure 4.26: Simulations of the model equations (4.22) and (4.23). Space-time plot (top panel)for the u population for μ_i given by $\theta = 0.6$ (θ defined above), with space-density plot at $t = 20$ (lower panel) for both the u (red) and v (blue) populations. We see homogeneous mixing, as predicted by our analysis. All parameters and numerical details are as in Figure 4.23, except for μ_i for $i = uu, uv, vu, vv$ which are as described.

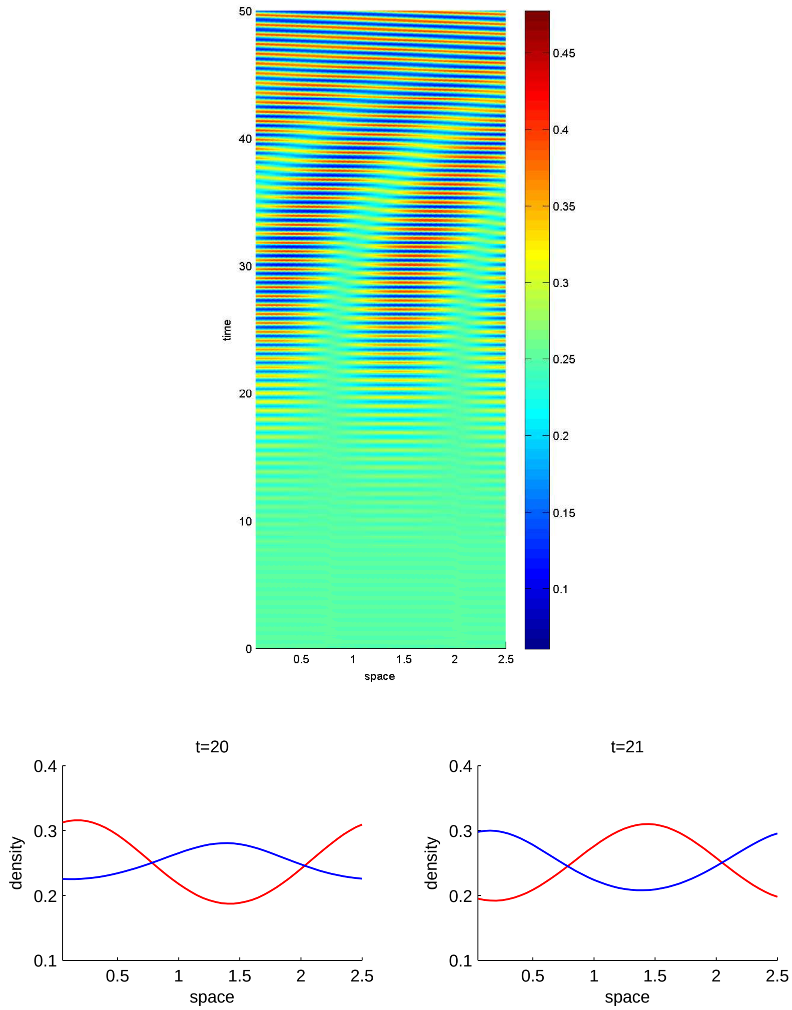

Figure 4.27: Simulations of the model equations (4.22) and (4.23). Space-time plot (top panel)for the u population for μ_i given by $\theta = 0.68$ (θ defined above), with space-density plot at $t = 20$ (lower left panel) and $t = 21$ (lower right panel) for both the u (red) and v (blue) populations. We see oscillatory behaviour at early times, with travelling waves forming later. All parameters and numerical details are as in Figure 4.23, except for μ_i for $i = uu, uv, vu, vv$ which are as described.

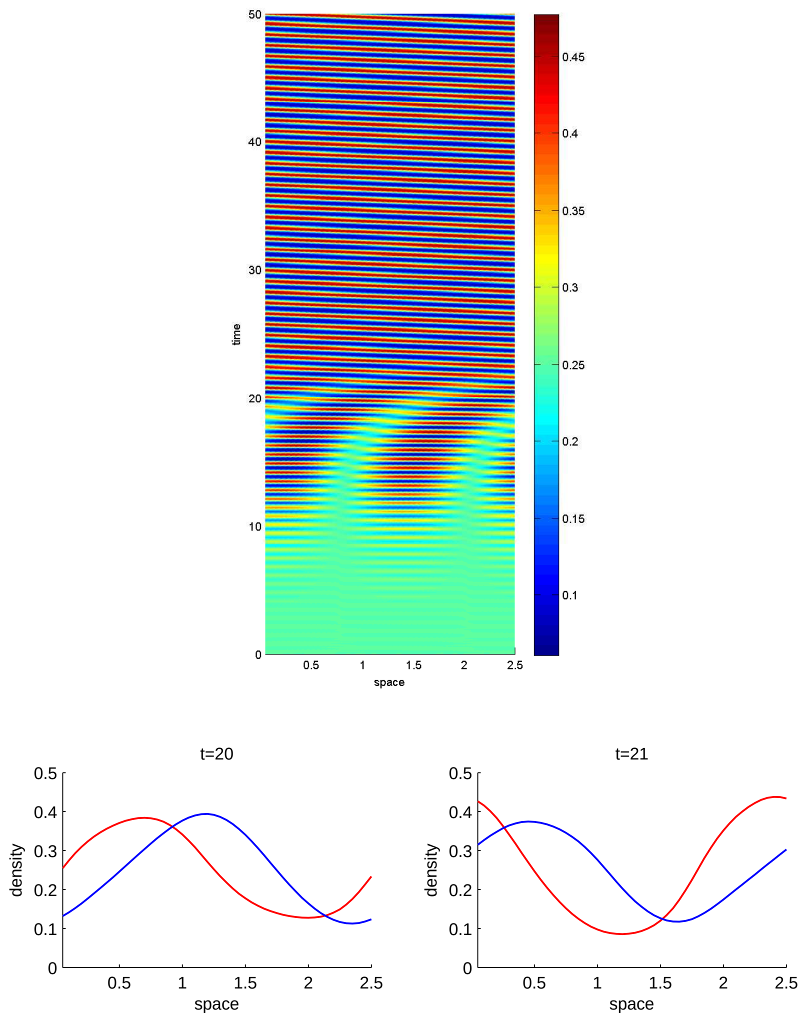

Figure 4.28: Simulations of the model equations (4.22) and (4.23). Space-time plot (top panel)for the u population for μ_i given by $\theta = 0.7$ (θ defined above), with space-density plot at $t = 20$ (lower left panel) and $t = 21$ (lower right panel) for both the u (red) and v (blue) populations. We see travelling wave behaviour. Peaks are smooth and waves travel from right to left. All parameters and numerical details are as in Figure 4.23, except for μ_i for $i = uu, uv, vu, vv$ which are as described.

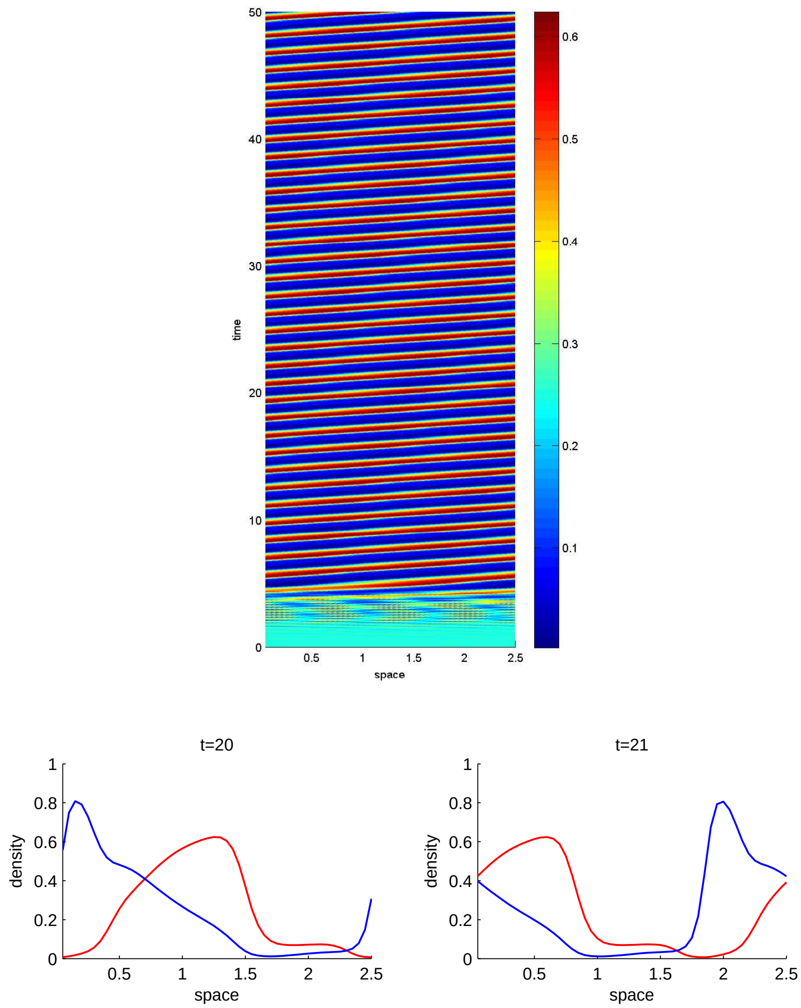

Figure 4.29: Simulations of the model equations (4.22) and (4.23). Space-time plot (top panel)for the u population for μ_i given by $\theta = 0.8$ (θ defined above), with space-density plot at $t = 20$ (lower left panel) and $t = 21$ (lower right panel) for both the u (red) and v (blue) populations. We again see travelling wave behaviour, although this time peaks are irregular in shape. All parameters and numerical details are as in Figure 4.23, except for μ_i for $i = uu, uv, vu, vv$ which are as described.

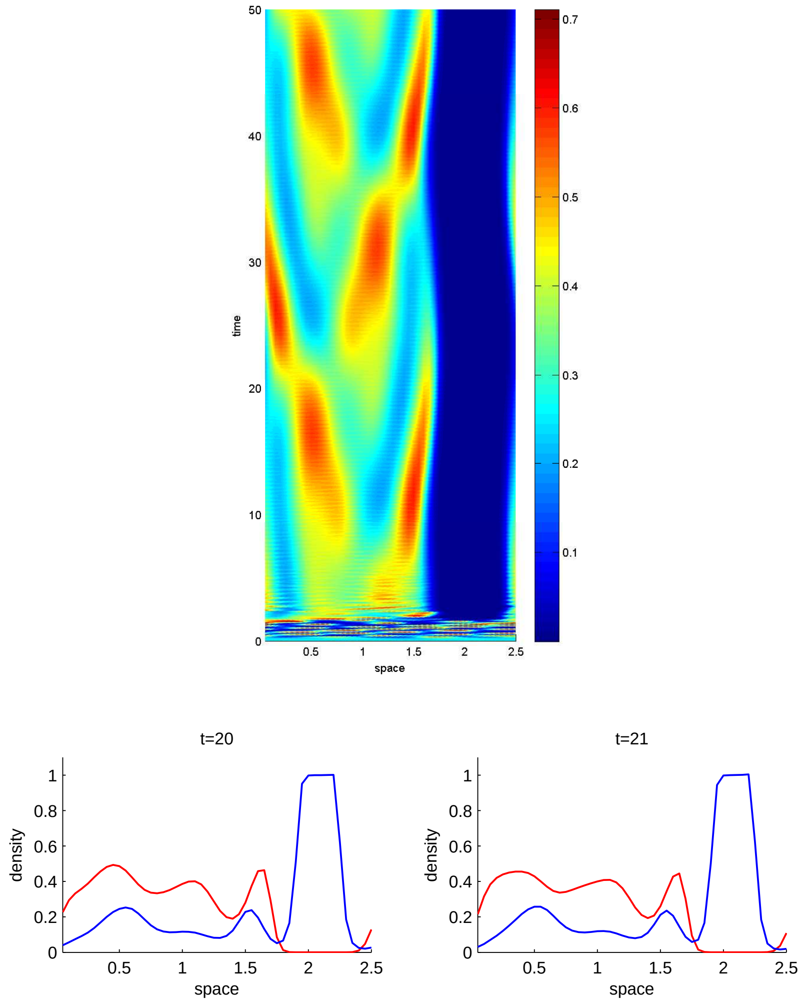

Figure 4.30: Simulations of the model equations (4.22) and (4.23). Space-time plot (top panel)for the u population for μ_i given by $\theta = 1.2$ (θ defined above), with space-density plot at $t = 20$ (lower left panel) and $t = 21$ (lower right panel) for both the u (red) and v (blue) populations. A band of population v forms, whilst the u population does not stabilise. All parameters and numerical details are as in Figure 4.23, except for μ_i for $i = uu, uv, vu, vv$ which are as described.

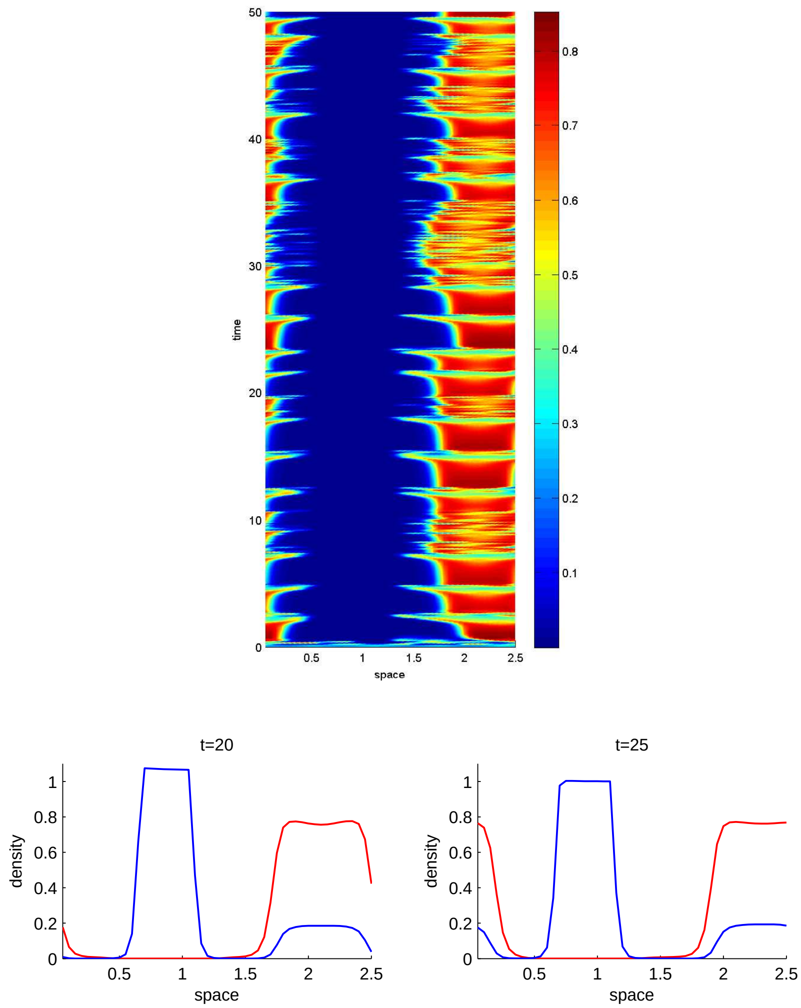

Figure 4.31: Simulations of the model equations (4.22) and (4.23). Space-time plot (top panel)for the u population for μ_i given by $\theta = 1.5$ (θ defined above), with space-density plot at $t = 20$ (lower left panel) and $t = 25$ (lower right panel) for both the u (red) and v (blue) populations. A band of u and a band of v form, with the widths of the bands oscillating, or breathing, over time. All parameters and numerical details are as in Figure 4.23, except for μ_i for $i = uu, uv, vu, vv$ which are as described.

4.5 Discussion

In this chapter we have presented a general model of contact-dependent interactions, and considered the role of both interaction ranges and strengths on patterning formation. Our analysis of the model equations (4.22) and (4.23) has shown that the magnitudes and signs of both of these terms affect whether the system will show instability or stability, as will the initial densities of each cell population. Furthermore, our simulations have shown that whilst increased ranges lead to increased aggregation widths, and attractive forces lead to stationary aggregations, repulsive forces can cause a range of behaviours, including travelling waves, oscillatory behaviour, and breathing bands.

Moreover, we have seen that many patterns change considerably over time; in particular, we see no stabilisation of the patterns seen in the repulsive strength cases presented in Figure 4.30, and we see the disappearance of aggregations of narrow width in Figures 4.21 and 4.22. Throughout Section 4.4 we discussed the dimensional timescale suggested by our model. We explain that calculation here.

In order to calculate dimensional time, we turn back to our nondimensionalisation of the system and consider nondimensional values of t. We have that t is dimensionalised by L^2/D_u (Section 4.3.1), and we have let L be the maximum signalling range of a single u cell. Let $L = 10^{-2}$cm, a reasonable dimensional value for a maximum signalling range if we take this to be ten times a cell diameter as in Section 4.4. We also let $D_u = 10^{-10}\text{cm}^2/\text{s}$, a reasonable dimensional value for cell motility. Then the corresponding dimensional time $t^* = 10^6 t$ s. So if we run simulations up to dimensionless time $t = 20$ as in Figures 4.23, 4.20, 4.21 and 4.22, then the corresponding dimensional time $t^* = 2 \times 10^7$s, which is approximately 33 weekss. Similarly, our simulations in Section 4.4.2 represent about 6 days.

We can use this calculation to decide how long we should run our simulations for, according to the biological scenario we are interested in. For example, if we want to investigate the morphogenesis of a zebrafish, which is completed within 28 days, we should compute up to dimensionless time $t = 3$.

There is obviously a great deal more work that can be done on this model in the future. For a start, a move into at least two dimensional simulations must be undertaken in order to fully reveal the types of spatial patterning that these various attractive and repulsive interactions can produce. Data available invariably pertains to two dimensional scenarios, and often three, and so an extension in this manner would be extremely useful. Also, since much patterning takes place during development, it would be beneficial to model a growing domain; this would allow a more accurate picture to be formed of the kind of patterns that these interactions could produce during growth.

Beyond these specific suggestions, there are other aspects of the model that can be altered and investigated in order to uncover what impact they have on patterning, and hence what impact their biological equivalent may have on patterning in real tissues. For example, assuming that all forms of the interaction term are alike is not necessary. Instead the signals from one cell population could be of a different form to those of a second population, so that in place of one signalling function Ω, we could have two or more different functions. On a similar theme, we could investigate the effect of u and v having different packing densities P_1 and P_2 say, or try the same packing functions for each cell, but different to the one we have used already. Finally, incorporating cell birth and death would make the model more accurate, especially when studying biological scenarios where cell turnover time is known. The incorporation of such kinetics is particularly important when considering long timescale dynamics that occur over several weeks.

Finally, this model could be used to explore specific biological scenarios. It could, for example, be used to look at zebrafish pigmentation patterning. This process takes place during development and occurs on the fish's epithelium, meaning that it could be modelled as a two-dimensional problem with the skin modelled as a monolayer. The cell dimensions of the melanophore and xanthophore pigment cells are known and there is detailed timeseries data of pattern production too (Moreira & Deutsch, 2005; Parichy, 2000), so that many of the parameters needed for the model are available. There are also conflicting hypotheses regarding the type of signalling interactions that occur between cells in order to form the zebrafish's stripes. Whilst some biologists believe that local cell-cell signals lead to the patterns seen (Maderspacher and Nüsslein-Volhard, 2003), others argue that much longer range signals are also key (Kondo et al., 2009). However there is general agreement that both attractive and repulsive signals are necessary. As the model could be easily extended to two dimensions, a domain size could be chosen which is an appropriate representation of the zebrafish skin. Initial conditions could be set to two horizontal stripes to mimic those found on the zebrafish epithelium after embryogenesis, and the model could then be used to explore pigmentation patterns during the transition to adulthood at approximately 28 days (Parichy, 2000). The two conflicting hypotheses could be modelled by choosing different forms of our signalling function Ω. Then a comprehensive investigation of the model's parameter regimes for which zebrafish-type stripes occur for these two different signalling functions could be undertaken to add some insight into the debate on whether local or non-local signals produce patterning, possibly leading to the verification or falsification of the opposing hypotheses.

With this application in mind we here attempt to reproduce the zebrafish ablation experiments of Yamaguchi et al. (2007). Note that whilst their experiments are well approximated to $2-D$ which they use in their simulations, our simulations are only in $1 - D$. Therefore we do not hope to reproduce their results exactly, but rather to see if the mechanism of our model is sufficient to form zebrafish-type stripes in the same timeframe as the experiments and simulations of Yamaguchi et al., using realistic parameter values. In these experiments, Yamaguchi and co-workers ablated the pigment cells of 20-day-old zebrafish using a laser and observed their regrowth over the course of three weeks (Figure 4.32, top panels). They then recreated the regrowth of these stripes via the simulation of a reaction-diffusion equation (Figure 4.32, lower panels). We now attempt to recreate the simulation results of Yamaguchi and co-workers using our integrodifferential model. We do this in order to explore whether direct cell-cell signals over small to medium distances, as opposed to much longer range signals, could be responsible for pattern formation in zebrafish. Note that we choose to recreate this particular experiment as it involves only the migration of pigment cells, and not also other processes such as cellular differentiation.

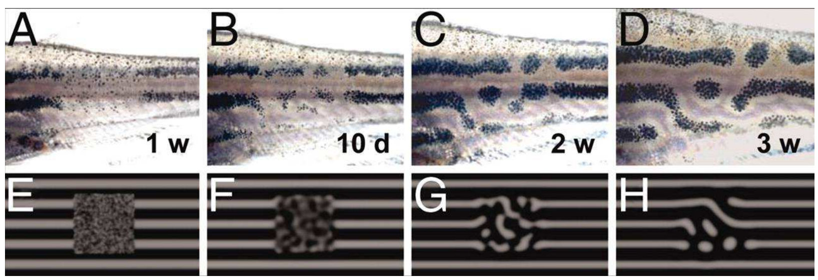

Figure 4.32: Regeneration process of the stripes of both zebrafish and computer simulation as carried out by Yamaguchi et al. (A-D) Regeneration of stripes without an inherent prepattern in zebrafish. Images were recorded after 1 week (A), 10 days (B), 2 weeks (C), and 3 weeks (D) after ablation of both melanophores and xanthophores in the wide region above the anal fin base. At the beginning of the regeneration, melanophores and xanthophores were randomly distributed in the ablated area (A). Then, each type of pigment cell began to segregate (B and C), and the stripe pattern without original anterior-posterior direction was regenerated (D). Note that this regeneration was achieved by autonomous migration of pigment cells. (E-H) Time-lapse captured images of the regeneration process outputted by computer simulation. Yamaguchi et al. used an activator-inhibitor reaction-diffusion model for the simulation. The white indicates an area where a concentration of the assumptive activator is the highest, whereas the black shows the highest concentration area of assumptive inhibitor. Parameters were selected to facilitate the stripe formation. As the initial condition for pattern regeneration, Yamaguchi et al. set a horizontal stripe pattern in the 256×128 field. For the ablation, the central region was replaced by a random pattern. Captures were produced after 500 (E), 1,000 (F), 3,000 (G), and 10,000 (H) iterations, respectively. Yamaguchi et al., (2007). Copyright of the National Academy of Sciences, with permission.

We begin by choosing our parameters. We let u be our xanthophore population and v be our melanophore population. Then u cells have diameters of about 0.1mm, and v cells have diameters of about 0.15mm (Moreira & Deutsch, 2005). We know that whilst melanophores and xanthophores experience homotypic attractions over medium and short ranges, xanthophores repel melanophores at short ranges (Maderspacher and Nüsslein-Volhard, 2003). We let a medium range be twice the average radius of a cell, and a short range be simply the average radius of a cell. Then we set $L = 0.1$mm (where, as above, L is the maximum signalling range of a u cell), with $\xi_{uu} = 1$, $\xi_{vv} = 1.5$ and $\xi_{uv} = 0.5$. For attractive strengths, we arbitrarily choose $\mu_{uu} = \mu_{vv} = 50$, and for repulsion we let $\mu_{uv} = -50$. These numbers allow our system to be unstable but as we do not know comparative strengths for the interactions between the two cell types, we set these three strengths to be of equal magnitude. Since nothing is known about melanophore-xanthophore interactions, we let $\mu_{vu} = 0$. Furthermore, we let $\tilde{D} = 1$ i.e., both cell types experience the same motility in the absence of directional cues. For our initial conditions we simply set each cell type to a density of 0.25 across the domain with noise, thus mimicking the conditions of the ablation experiments. We set the domain length to be 5mm long.

In order to know for how long we should run our simulations we calculate the dimensional value of one dimensionless timestep. We have that $L = 0.01$cm, and again let $D_u = 10^{-10}\text{cm}^2/\text{sec}$ as above. Then dimensionless time $t = 1$ is approximately 11.6 days. Therefore we will output our results at dimensionless times $t = 0.6$ (equivalent to the results at 1 week in the original experiment), $t = 0.85$ (3 days on, so equivalent to day 10 in the experiment), $t = 1.45$ (equivalent to day 14), and $t = 1.8$ (equivalent to day 21). We plot the results below (Figure 4.33).

Obviously, since our results are only in one dimension, we do not see the exact results of Yamaguchi et al. However, we do see an increase in distinct stripe formation of both melanophore stripes (blue) and xanthophore stripes (red) over time, and these stripes alternate across the domain. These two points match the original experiments. Moreover, gaps are seen between stripes, which is what we would expect to see in zebrafish (Parichy, 2000). Therefore it certainly seems possible that direct cell-cell signalling could produce the patterning seen in this experiment, and that a reaction-diffusion system is not the only way such patterning can be produced as proposed by Yamaguchi et al. A two dimensional simulation would confirm this.

Whilst we have not attempted to thoroughly investigate a specific biological application here, we hope that we have shown how the model may be used in this way. It has been designed to be amenable to many useful applications and studies, and we hope that the insights revealed by our preliminary investigations prove to be just the beginning.

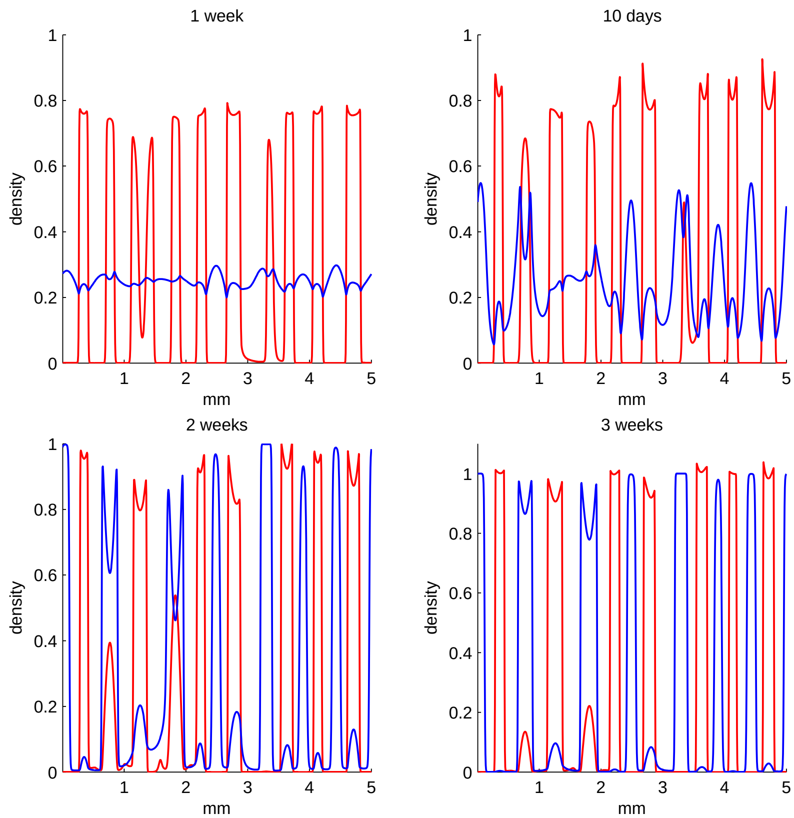

Figure 4.33: Results of a simulation of model equations (4.22) and (4.23), with all parameters and numerical details as described in the text. We see the formation of stripes over time. Initial conditions are set at $u = 0.25 + 0.01c$, $v = 0.25 + 0.01c$ across the domain, where $c \in [-0.5, 0.5]$ is randomly chosen for each numerical grid point. For all other numerical details, see Chapter 5.

Chapter 5

Numerical Methods

This chapter looks at the numerical methods used throughout this thesis, and explores some of the less expected behaviours of those numerics.

5.1 Cellular automata

On a square domain of 256×256 grid points, we simulate the two cellular automata models discussed in Chapter 2. We use a random-choice asynchronous updating method such that at each timestep, a cell is picked randomly across the domain. Note that a synchronous updating method leads to no appreciable difference in the outcome of our simulations (see Chapter 2, Sections 2.2.1 and 2.5.2 for more on this); we choose an asynchronous method as it matches more closely with realistic biological scenarios.

This randomly chosen cell is then updated according to the Majority algorithm or Single-Cell algorithm, as outlined in Chapter 2, Section 2.2.1, Figure 2.1. We use an eight neighbour Moore neighbourhood for all simulations, although note that in preliminary investigations with a four neighbour Von Neumann neighbourhood, no change in results was seen. Along the boundaries, we simply truncate the calculation: on the boundary and at the corners of the domain, only cells in the domain are considered, and an average is taken over that reduced number of cells in the Majority model, whilst in the Single-Cell model a cell that picks a neighbour outside the domain does not change state.

5.2 One dimensional integro-differential equations

We use our one dimensional results in Chapter 3 primarily to further our understanding of the stability of the system under certain conditions, before moving on to the more complicated two dimensional code. Therefore we are primarily interested in a straightforward numerical scheme. With this in mind, we opt for the most basic: the explicit Euler method. This scheme is given by

$$u^{n+1} = u^n + \delta t g(t^n, u^n),$$

where u^n is the state of population u at time n, and g represents the right hand side of our ordinary differential equations (ODEs). For details on the derivation of the explicit Euler method see, for example, Stuart & Humphries (1996). Note that we have ODEs not integro-differential equations to solve here as we first discretise uniformly through space, leaving us with an ODE at each grid point. For more on this technique, see Morton & Meyers (1994).

In order to calculate the line integral we first discretise it through space, setting our space discretisation to be $\delta x = 0.5$ on a grid of length 200. We then sum the integral over each point and average over the length, taking care to include any remainders at either end of the line which may lie over only part of a grid point. Note that we also investigated space discretisations of $\delta x = 0.\dot{3}$ and $\delta x = 0.25$. We carried out simulations of both the Community and Single Cell models 3.7 (Chapter 3, Section 3.2.1), repeating the simulations illustrated in Section 3.4.1, Figures 3.3 and 3.5, with $\delta x = 0.\dot{3}$ and $\delta x = 0.25$ in turn. When looking at the Community model, we saw no change in the density of stripes, and the overall behaviour of stripe patterns was consistent, i.e., whilst stripes in the $\alpha_1 = \alpha_2$ case remained stable over all time, as α_1 increased in size relative to α_2 stripes decayed more quickly. However we did see different numbers of stripes than in our original simulations (for both tests we saw three stripes across the domain in place of two). The decay rates of the stripes also differed: whilst in the $\delta x = 0.\dot{3}$ case the stripes decayed faster than in the original simulation, in the $\delta x = 0.25$ case a wide stripe appeared in the domain for all α_1 that led to an increase in time taken for each case to reach no stripes when $\alpha_1 \neq \alpha_2$. For the Single Cell model, again results were qualitatively the same but not quantitatively so: here the stable state was reached faster as the grid grew finer. These differences are possibly due to our calculation of the integral: since we approximate the remainder of the integral that lies over only part of a grid point, a coarse grid loses more of the integral at the boundary edge than a finer grid. This has the effect of slightly decreasing the integral radius. These results suggest that whilst our grid is sufficiently fine for understanding qualitative behaviour, a finer grid is necessary for quantitative observations.

Throughout our use of the Euler method, we let $\delta t = 0.01$, and calculated and recorded u^{n+1} at each grid point for each time output point. Note that we ensured that $\delta t = 0.01$ was sufficiently small by repeating simulations with $\delta t = 0.005$ and $\delta t = 0.001$; we found no difference in our results[1]. Initial conditions and our cellular

[1] Again we carried out simulations of Community and Single Cell models 3.7 (Chapter 3, Section 3.2.1), repeating the simulations illustrated in Section 3.4.1, Figures 3.3 and 3.5, this time with

differentiation functions for each simulation are as described in Chapter 3. Boundary conditions as such do not exist as there are no movement-type terms in our models in Chapter 3. However, when calculating the integral term within distance R of the boundary, we choose to truncate the integral and normalise it over the truncated area so as to model a closed system with no cells outside the boundary.

We are aware that the explicit Euler method is not the most accurate of schemes, but our testing of it has shown us that it is sufficiently robust for our purposes in the computation of solutions to our models in Chapter 3 and so, since it is also a simple scheme to implement, we use it here.

5.3 Two dimensional integro-differential equations

We begin by using the Method of Lines approach, which again allows us to transform our integro-differential equations into a system of ODEs (Morton & Meyers, 1994). For Chapters 2 and 3, our models involve only kinetic terms. As in the one dimensional code, we calculate the kinetic terms at each grid point across our two dimensional domain in order to calculate the right hand side of our system of ODEs. To solve this system, we then use ROWMAP (Weiner et al. 1997), a method that is particularly well suited to solving stiff ODE initial value problems, and which automatically controls and adjusts time-step size. As in the one dimensional case, we discretise uniformly through space. All details regarding specific values for δx, domain length, initial conditions and our bio-cellular functions for specific simulations can be found in Chapters 2 and 3. Again, boundary conditions are only relevant in calculating the integral, and we explain that integral calculation now.

Calculating the integral in two dimensions again involves discretising through space, here discretising the circular domain of the integral. We then sum the integral over each of the grid squares within the circle much like in the one dimensional scenario, although here some of the area of the circle is lost at the boundaries. The calculation is fast and, with a fine lattice, it is reasonably accurate. Note however that it is important to have a sufficiently fine grid, otherwise numerical artifacts can occur (see Section 5.5).

5.4 One dimensional integro-advection-diffusion partial differential equations

In Chapter 4, our focus is on an advection-diffusion problem, and so our numerical approach is significantly different. We begin by using a finite volume scheme on a

$\delta t = 0.005$ and $\delta t = 0.001$ in turn.

uniform grid to discretise space, with each grid point located at the centre of each numerical cell. We assume periodic boundary conditions. We use a Matlab code which uses the inbuilt Matlab time integrator 'ode45' to solve the the system of ODEs which we again formulate using Method of Lines approach, and this time we use a Fast Fourier Transform technique to calculate the integral. This method is extremely efficient and therefore preferable to other methods. Although it restricts us by its nature to a uniform grid, this does not matter in our largely abstract and non-problem specific investigations, and the gain in speed from previous codes amply makes up for any lost flexibility. See Gerisch (2010) for more details.

5.5 Numerical artifacts

In this section we describe our close examination of phenomena witnessed during preliminary implementations of the scheme described in section 5.3. These numerically driven phenomena occur when the two cell populations of the model 2.1, Chapter 2 separate into two distinct groups, with half of the domain filled by one cell population, the other half filled by the second (see Chapter 2, Section 2.3.1, Figure 2.6, lower panels). As a result of this close examination, we implemented a sufficiently fine grid for all subsequent simulations.

5.5.1 The necessity of a fine grid, part 1

When first observing the transition front that demarcates a change from one cell population to another (see Chapter 2, Section 2.3.1, Figure 2.6, lower panels), we initially believed these transition fronts to be flat (Figure 5.1, left panel). However, on studying our initial simulations more carefully, we saw that this was not the case, but rather from split initial conditions without noise (not shown), the transition front curved slightly. On closer inspection, this curving was seen to occur at the boundaries of the domain (Figure 5.1, middle and right panels). Although our boundary conditions are not unusual, they appeared to be affecting the dynamics of our solutions.

At the boundaries of our domain, the integral is truncated, so that only cells inside the domain are included in the integral calculation. At a transition front, this straightforward condition becomes more complicated. Imagine we wish to integrate over the transition front, at a point such that the majority of the integral is of cell type A, and the rest of B say. Away from the domain boundaries, this will return the same proportions of each cell type. However, at the boundary edge, this proportion changes as the area of our integral changes. For example, close to the boundary, we could lose from our integral cells of type A say, but none of type B (Figure 5.2). We realised that this could affect the shape of the transition front. In order to test this theory we ran two more simulations with different sensing radii. If our theory was correct then the curves witnessed along the transition front should scale with the length of the sensing radius. Indeed the size of the curves along the fronts, and the width of those fronts, changed accordingly (Figure 5.3).

This result highlighted the need to have a sufficiently fine grid in order to counteract this phenomena, which we then implemented throughout our simulations. Whilst it is clear that a more precise integral calculation would prevent this artifact from occurring, this work is primarily a work of mathematical modelling and not of numerical analysis so we do not seek to create a more accurate scheme here. Rather we highlight this curving as purely a numerical artifact to warn others who may wish to carry out similar simulations.

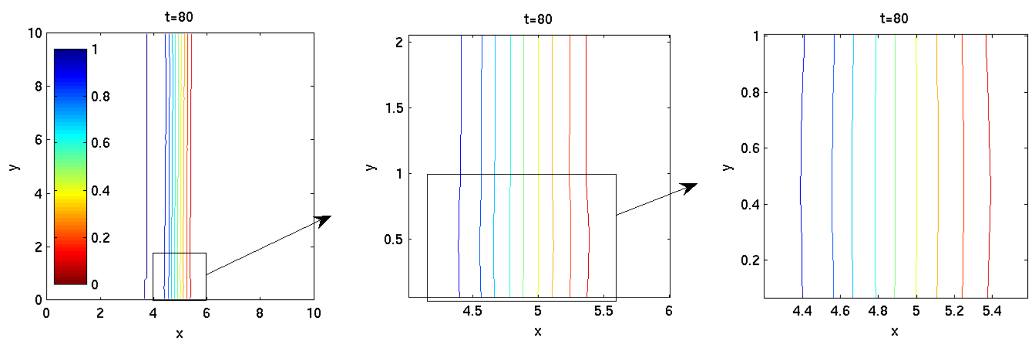

Figure 5.1: Simulation of the model 2.1, Chapter 2 with f non-linear. We plot the density of A in space at time $t = 80$. We see in the middle and right panels that the transition front is not flat, but in facts exhibits slight curving at the boundary (note the changed axis). Initial conditions are set at $a = 1.0$ when $x \leq 5$, $a = 0.0$ otherwise. The function f is given by $f(I) = 0.5\tanh(\tan(I\pi - 0.5\pi)) + 0.5$, a continuous approximation to a step function. The dimensionless parameter values are $R = 1.0$, $\alpha = 1.0$. The domain is of size 10 dimensionless space units, with 100×100 lattice points. We set absolute error tolerance in the ROWMAP scheme to 10^{-6}.

5.5.2 The necessity of a fine grid - part 2

A second phenomenon of our initial simulations was front movement. Again, the reader must be aware that if she or he chooses to repeat the simulations described, special care must be taken with grid coarseness. This is due to a numerical error that moves the front slowly across the domain (Figure 5.4), a movement which slows down over time (Figure 5.5). With a fine grid, such movement does not occur (Figure 5.6). This is because the finer the grid, the closer we remain to the original equation:

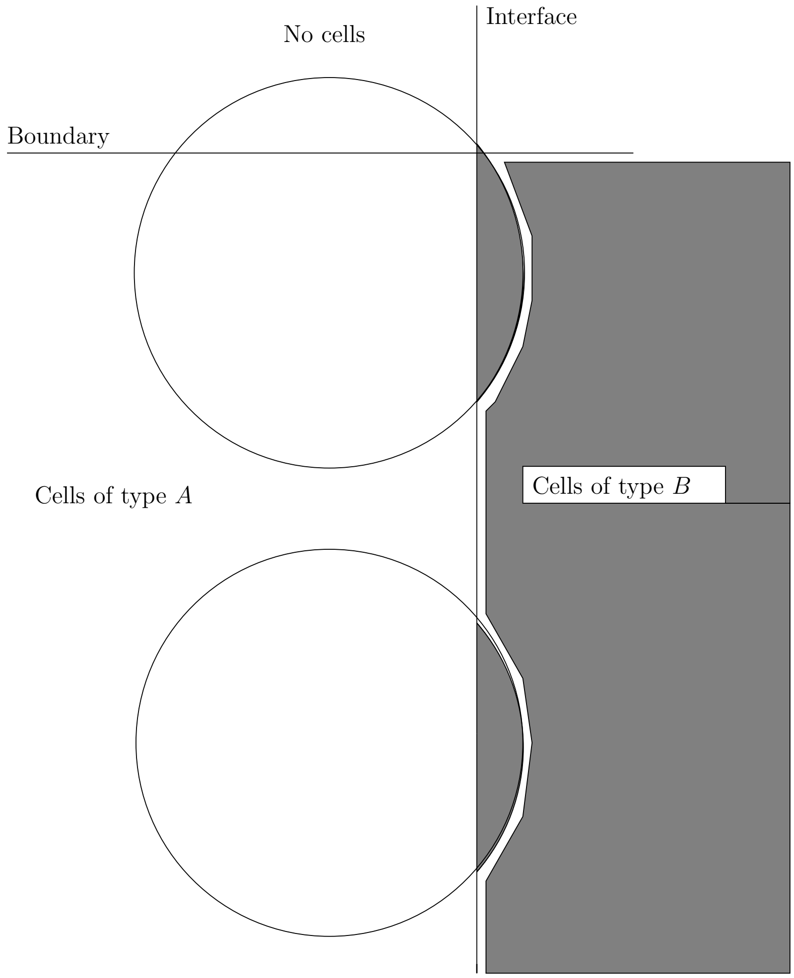

Figure 5.2: The lower circle shows an integral with a small portion of cells of type B (patterned), while a larger portion is of cells type A (white). However, the upper circle crosses the domain boundary and in doing so, it loses some of its white A cells, but retains all of its patterened B cells. As we integrate only over the area inside the domain boundary, the proportion of these two populations becomes altered at this point.

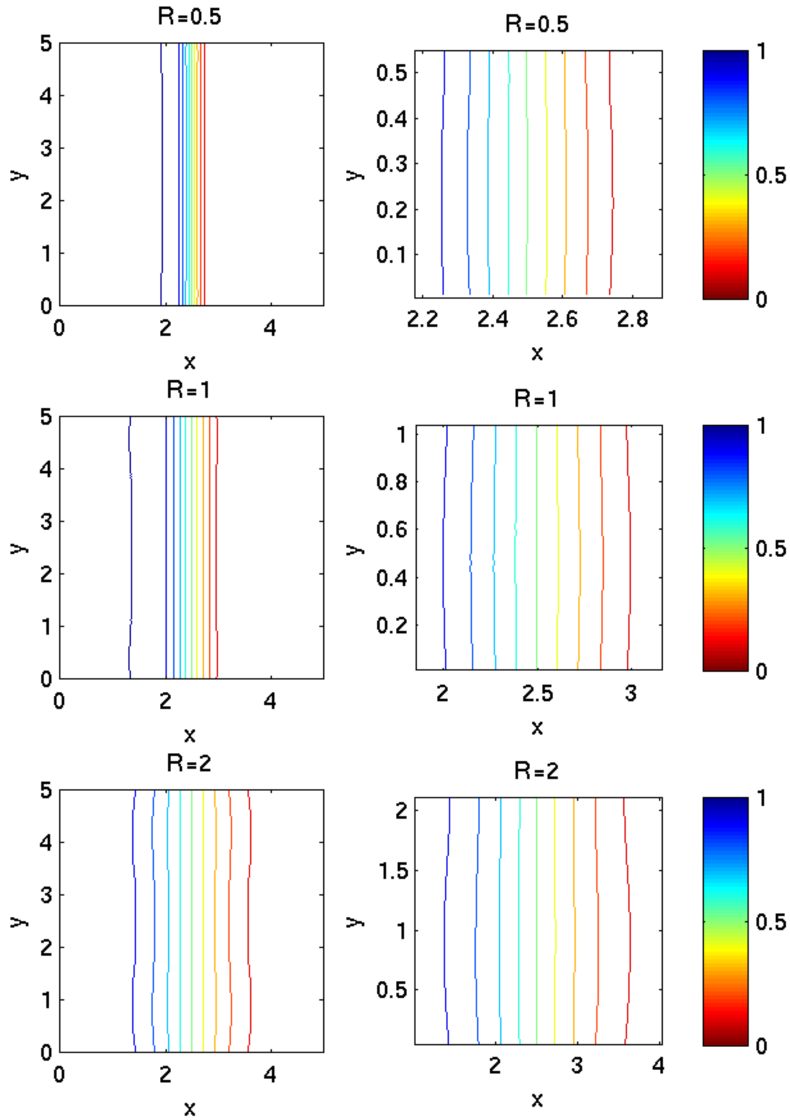

Figure 5.3: Simulation of the model 2.1, Chapter 2 with f non-linear, with three different sizes of sensing radius. We plot the desity of A at time $t = 50$ when the sensing radius is of length 0.5, 1.0 and 2.0. The right hand panels show a close-up view (note the change of axis in these figures), whilst the left hand panels show the full domain. We see that as the sensing radius increases, so too does the curve along the transition fronts, and the width of those fronts. All other numerical details are as in Figure 5.1.

as we discretise the model 2.1, Chapter 2, we move away from a balanced, bistable, integrodifferential equation to a system of balanced, bistable ordinary differential equations; in moving to the latter, we loose the non-local term and actually revert to equations very similar to those that exhibit metastabilty.

Metastability is the process by which a seemingly steady state evolves very slowly over time to the actual steady state solution; the original solution, although it seems stable, is in fact not. Such a phenomenon has been well documented, and has been shown to often occur in balanced, bistable equations, similar to those in the model (2.1), Chapter 2; therefore, front movement as we witness in coarse simulations seems plausible, in spite of this not being a genuine behaviour of the model 2.1, Chapter 2. We provide a detailed review of metastability in Section 5.6.

Note that, as in the situation described in Section 5.5.1 above, we could implement a better numerical scheme for the solution of the integral to resolve this problem, rather than relying on the choice of a sufficiently fine grid. However, the creation of such a scheme could take many months, and since we are primarily interested in modelling and not numerical analysis, we do not choose to undertake such a task. Rather, we here bring the reader's attention to the idiosyncracies of the scheme so that they can be avoided should the reader wish to carry out his or her own simulations.

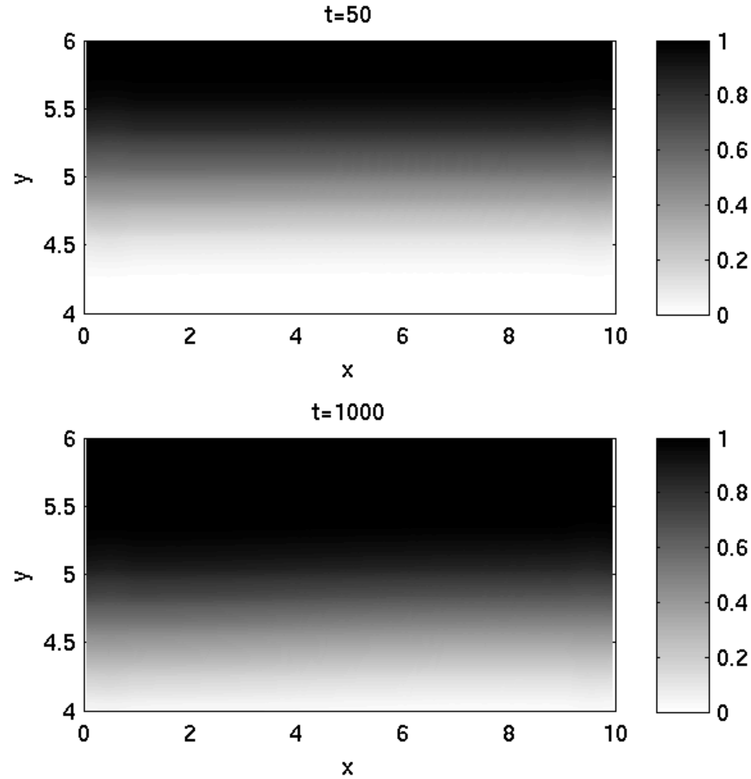

Figure 5.4: Simulation of the model (2.1) with f non-linear and split initial conditions. We plot the density of cell type A in space at times shown. We see that the transition front, which delimits where A cells exist and which has initial position $y = 5$, moves slowly through time towards $y = 4$. In this case the population of A cells increases at the expense of B cells. Note that the opposite can equally occur: see, for example, Figure 5.6, lower panel. We begin with initial conditions of $a = 0.0 + 0.02 \times c$ for points $y \leq 5$, and $a = 1.0 - 0.02 \times c$ otherwise, where c is chosen randomly between 0 and 1 at each numerical grid point. All other numerical details are as in Figure 5.1.

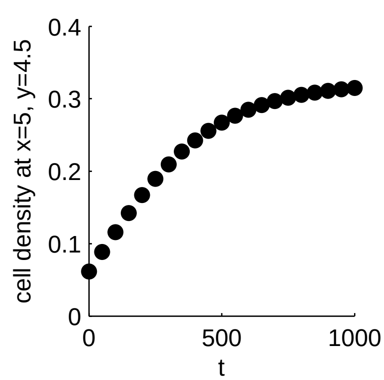

Figure 5.5: Cell density through time, at the point $x = 5$, $y = 4.5$ for the simulation shown in Figure 5.4. We see the cell density initially increase as the front moves forwards, but this increase is less over time, demonstrating that front movement increasingly slows. That this front movement eventually stops seems likely, but has not been investigated here due to long computational times.

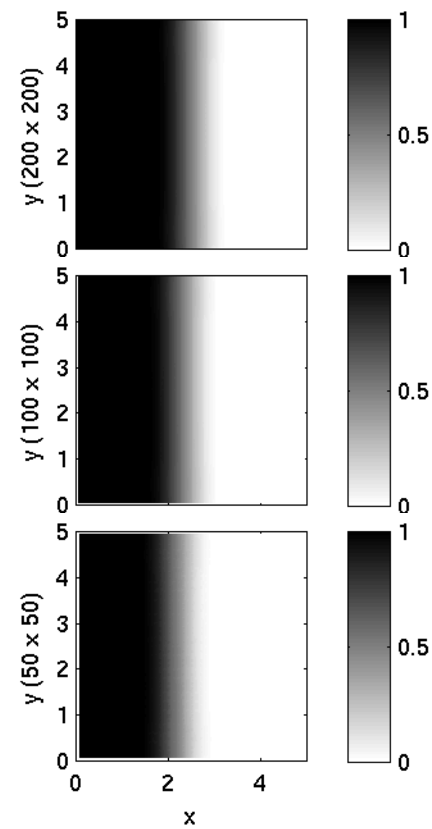

Figure 5.6: Simulation of the model (2.1) with f non-linear. We plot the density of A through space at $t = 1000$, and vary the coarseness of the grid in each simulation. From top to bottom, we have a grid with 200×200 lattice points, 100×100, and finally 50×50. We see that as the coarseness of the grid increases, the transition front moves further in the same time step, thus appearing to exhibit metastability. All other numerical details are as in Figure 5.1.

5.6 Literature review for equations of the form $u_t = \epsilon u_{xx} - f(u)$, f balanced bistable

As mentioned above, the model (2.1), Chapter 2 has balanced, bistable dynamics, and is very similar to the Ginzburg-Landau and Allen-Cahn equations. The dynamics of these bistable equations exhibit metastability – that is, solutions evolve very slowly over time, and hence in simulations they can appear to be stable when they are not. A whole body of literature has been produced to try and characterise the flow of the metastable transition layers which separate the two stable phases from each other, and that is what we will discuss here.

Metastable transition layers can briefly be described by the following: let us take, for example, the Ginzburg-Landau equation $u_t = \epsilon u_{xx} - f(u)$, f balanced and bistable (i.e. f is the derivative of a potential function that has two wells of equal depth), with minima at $u = \pm 1$. The travelling wave solution of this equation has wave speed $c = 0$ i.e. the waves which separate one stable phase at $u = +1$ from the other stable phase at $u = -1$ do not move. However these stationary waves are in fact unstable and the solutions evolve via movement of the transition layers, although with exponentionally small speeds and over very large timescales. It is the movement of these metastable transition layers or interfaces that we will discuss below.

This slow movement was first observed and discussed in physics, in relation to crystal growth, fluid dynamics, and chemical-reaction diffusion systems. In their 1988 paper, Dee & van Saarloos used numerical simulations to describe interface movement in detail, and concluded that almost all spatially bistable systems may produce moving transition layers. Other approaches of the time were also intuitive, based on microscopic models and thermodynamical considerations (see Fusco & Hale, 1989). However, within mathematics, a variety of rigorous approaches based on geometric and manifold techniques were developed, with the first such approach employed by Carr and Pego (1989) and Fusco and Hale (1989), although credited to the latter by the former. The basic idea behind the two papers is to construct a (non-invariant) manifold M that contains the essential dynamics of the equation in question. We explain Carr and Pego's approach here: they take a configuration $h = (h_1, ..., h_N)$ of N layer positions, and associate with it the function $u^h(x)$ which approximates a metastable state with N transition layers. This set of states forms an N-dimensional manifold, with careful attention paid to include only admissible transition layers (i.e. those which are a sufficient distance apart to still exhibit metastable dynamics[2]). Given a solution u near M, they can then write u in terms of u^h and a constructed coordinate v, where v is orthogonal to particular approximate tangent vectors to M. Through projection they obtain equations of motion for h and v, and hence, by linear

[2] Transition layers, once they are close to one another, quickly collapse (Carr & Pego, 1990).

analysis, can describe the flow of the transitional layers near M by $u = u^h$.

This manifold approach proved very successful, and spawned numerous results and extensions. Chen et al. (2006) explored entire solutions of the equation (i.e. those solutions which begin at $t = -\infty$) using invariant manifold techniques, following on from Yagisitia (2002) who proved their existence under various conditions. Chen et al. (2007) extended the manifold approach to obtain the precise dynamics of interfaces for cylindrically symmetric vertically moving solutions, while Carr and Pego (1990) considered the global unstable manifolds of equilibria to obtain numerous results on the shape, flow and timescale of transition layers. They found that there exists a global correspondence between the number of layer positions of metastable states and the dimension of the unstable manifold of unstable steady states of the equation, as originally conjectured by Fusco and Hale (1989). This led to the understanding that metastable states can be generated from a small perturbation of an unstable steady state. Other results from Carr and Pego (1990) include: finding the standing wave solutions of the transition layers; showing that layer positions repeat regularly in space; proving that the number of stationary states are of $O(\frac{1}{\epsilon})$ (where ϵ is the small diffusion coefficient). Carr and Pego also discussed layer collapse, which occurs when two transition layers approach each other. At this point, the layers speed up and annihilate each other, leading to a reduction in the total number of transition layers. This topic of layer collapse informed the next significant area of work on metastability, and was taken up by Ward (1994).

In a very thorough paper, Ward (1994) looked at various boundary conditions and their effects on the motion of metastable layers and their collapse. By numerical methods he solved various problems which describe layer collapse, and gave a quantitative confirmation of Carr and Pego's description of the coarsening process of the Ginzburg-Landau equation (Carr & Pego, 1990), including both the effects of boundary conditions and of the inclusion of layer collapse both internally and against a domain wall. Rougemont and Eckmann (1998), meanwhile, explored the collapse and annihilation of transition layers on the infinite line. By following and extending Carr and Pego's manifold techniques, they found initial conditions which led to infinite sequences of collapses of transition layers. The results were shown to hold for more general bistable equations than the Ginzburg-Landau equation, and included a formula for the speed of motion of these layers. Rougemont and Eckmann were able to predict with high precision the collision time and annihilation of a pair of transition layers, independently of the position of infinitely many other transition layers. Morita and Mimoto (2000) estimated the lifetime of layers before collapse, while Rougemont (1999) proved that all transition layers eventually disappear by colliding with each other. This opened up another area of work, namely what will happen to the remaining regions once all metastable transition layers have been annihilated, which

Rougemont proved must (eventually) occur.

Ward (1996) provided a partial answer to this question in the case of mass conservation in a multidimensional domain, assuming that the system will eventually collapse to one single closed interface (this had been shown to often be the case – see Bronsard, 1994, and Rubinstein, 1992 – but had not been proven for all instances: Rougemont's results on this only apply conclusively for one dimension). In a one dimensional domain, motion occurs due to the interaction of neighbouring layers, but interfaces in multidimensional domains move according to their curvature (Allen, 1979; Rubinstein, 1989). If there are several closed interfaces as a result of initial data, these may lead to a single surviving spherical interface and if movement at this point relied solely on curvature, this would not move at all. Ward (1996) showed that this is not the case, and produced many results on the shape and movement of such a surviving sphere using very different mathematical methods to those described so far.

First Ward used the method of matched asymptotic expansions to construct a canonical "bubble" solution to the steady state equation i.e. a solution with radial symmetry and exactly one internal layer. He then linearized the equation about this solution, and analysed the associated eigenvalue problem asymptotically. Using boundary layer analysis, Ward found estimates for the behaviour of eigenfunctions on the domain boundary. He then used these together with a projection method to accurately derive an explicit ODE for the motion of the centre of the sphere.

Stafford et al. (2001) extended this work to consider what happens once a bubble reaches the boundary of the domain. If the bubble becomes an arc, they showed that it will again move according to the mean curvature of the bubble, but if the length of the bubble interface is sufficiently small in comparison to that of the domain boundary, an approximate semi-circle will form which then moves according to the curvature of the domain boundary (see Alikakos, 2000). If, however, an exact semi-circle forms (i.e. the bubble hits a flat part of the boundary), Stafford et al. (2001) showed that this semi-circle is metastable, and they derived an asymptotic differential equation for its motion. Jorge et al. (2008) extended these ideas further to study, in detail, the boundary behaviour of the bubble, and in particular how the bubble readjusts in shape to its domain.

In comparison, Rougemont (2000) extended his use of invariant manifold techniques to provide a new proof of bubble movement according to mean curvature, or curve shortening. Although the proof of this movement had already been derived (Rubinstein, 1989), Rougemont's new proof gave insight into the dynamics of the orbits on the invariant manifold constructed by Carr and Pego (1989; 1990): namely, Rougemont found that these orbits also move according to a mean curvature law. Rougemont (2000) then explored the coalescence of two nearby bubbles, and gave criteria for both the merging and the non-interaction of two separate circular regions. By doing so, Rougemont underlined the fact that the long time behaviour of bubbles is not determined solely by mean curvature flow. Rougemont (2000) ended by discussing the disappearance of these circular bubbles over time.

Of particular relevance to our own problem is the small amount of previous work that exists on integro-differential equations in two dimensions. It has been proven that if the Allen-Cahn equation is perturbed by an integral term then any non-trivial steady state on a convex domain will always be unstable, with all interfaces eventually merging with the domain boundary and disappearing (Casten, 1978; Matano, 1979). This suggests that the inclusion of an integral term in the Allen-Cahn equation prevents steady states from forming, since in the non-perturbed case, nontrivial steady states do form (see Iron, 2009 for a discussion of this). Similarly, Duncan et al. (2000) looked directly at differences between the Allen-Cahn equation and an integro-differential variant, replacing the diffusion term in the Allen-Cahn equation with a positive integral of u. Duncan et al. found that the solution to this equation does not coarsen for a small enough integral coefficient i.e. the solution does not form large patches of all one phase or all the other. Rather a mix of the two phases across the domain remains. This is in contrast to the Allen-Cahn partial differential equation, which always exhibits coarsening in finite time, again demonstrating the difference that the inclusion of a nonlocal term can make to the dynamics of a balanced, bistable equation. Perhaps of most relevance to our work, Chen et al. (1997) considered an Allen-Cahn equation with a large nonlocal term. They found that, unlike in the Allen-Cahn equation, the nonlocal term here provides a source of nontrivial stationary patterns, and concluded that there is a balance between the effects of curvature and those of the nonlocal term (see also Rotstein, 2001). All of these results suggest that it will be difficult to apply much of the literature above, which does not consider integrodifferential equations, to our work. Having said that, Hutson and Grinfeld (2006) also looked at an integro-differential version of the Allen-Cahn equation, considering a more general form of integral than Duncan et al. (2000). By considering the initial value problem, they studied the convergence of solutions to equilibria. They proved that convergence holds for small diffusion coefficients, and hence do in fact show an analogy with the partial differential equation case.

Finally, a series of papers by Grant considers the differences between discrete and continuous balanced bistable systems. Grant and van Vleck (1995) looked at metastability in discrete versions of the Allen-Cahn equation, and found a bound for the speed of metastable transition layers, showing that the slow motion of these layers is preserved in the discrete case. Grant (2000) explored the size of "grains", those circular regions of phase equivalent to the closed interfaces of the multidimensional continuous system, in order to distinguish between genuine equilibria and those which will disappear over finite time. Using a discrete analogue of the Allen-Cahn equation, Grant produced results for a fixed lattice regarding the size of equilibria regions, finding lower bounds on their size which will ensure they are genuine equilibria (i.e. that they will not disappear). He also considered distribution patterns of these regions across the domain. In Grant (2001), he compared the solutions of (two different) discrete Allen-Cahn equations with its continuous counterpart, showing that the number of solutions of the discrete and the continuous equations do not necessarily agree, even when using an extremely fine lattice. This final paper throws up some interesting questions about how best to represent bistable dynamics discretely, for example in a numerical finite difference scheme, without losing the continuous dynamics, as well as suggesting that a discrete problem may exhibit different dynamics to the continuous problem by the very nature of its discreteness. Grant (2001) concluded by discussing the importance of the attractor, rather than the set of equilibria, in understanding the long-term behaviour of solutions.

In conclusion, one can understand why it would not be unexpected to see metatstability in the balanced, bistable equation of (2.1) and hence why it is vital to ensure proper care is taken to investigate the robustness of any numerical method used for simulations.

5.7 A one dimensional version of a two dimensional code

When carrying out our numerical simulations in Chapters 2 and 3, the length of time taken to complete one run of our code is several hours, making testing of different parameter values time consuming. This became a particular problem when attempting to find the limits on the birth and death rates for which an island of cells either grew or died out in Chapter 3: we needed a much faster numerical scheme. We saw a way that we could reduce the numerical problem to a one dimensional scenario, and we first explain our idea here, before demonstrating the mathematical analysis of it.

We want to consider how initial conditions of a circular 'island' of one cell type centred in a 'sea' of another, similar to those explored in Chapter 3, will change over time according to the Community Model. The number of simulations required for this figure made two-dimensional simulations unfeasible. Therefore we considered the case of the "island" being in the centre of a circular domain. The circular symmetry then makes the problem one-dimensional. However, the reduction to one dimension is somewhat involved, and we outline the details here.

We define x as a radial co-ordinate measured from the centre of the domain, and we denote by $\mathcal{C}(x)$ the circle, radius R, centred at x. We begin by considering the

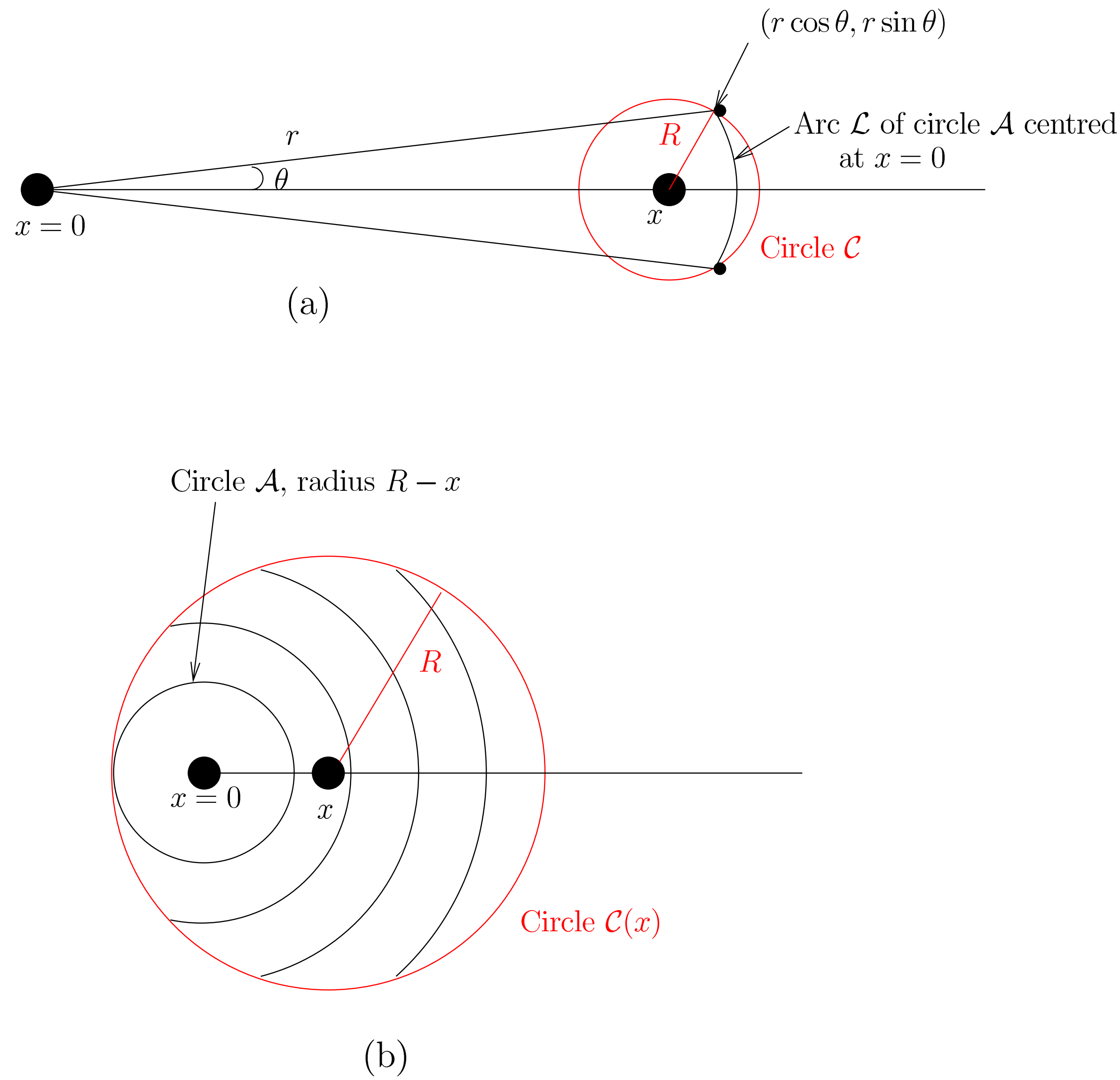

Figure 5.7: Upper panel: Figure of geometry of integral computation when $x - R$ is large. See text for details. Lower panel: Figure of geometry of integral computation near to the origin 0, shown large to allow more detail. If $x - R \leq 0$, the arcs $\mathcal{L}(r)$ of $\mathcal{A}$, three of which are shown (and each of which are distance r away from the origin), eventually form a circle. At the transition point between arcs and circumferences, $\mathcal{C}$ and $\mathcal{A}$ touch, and the radius is given by $R - x$. See text for further details.

case $x > R$. We wish to calculate

$$I = \iint_{\mathcal{C}(x)} F(x),$$

where $F(x)$ is the integrand in question. So, in the calculation of Figure 3.11, $F(x) = a(x)/\left(a(x)+b(x)\right)$ for our population of A cells. Then

$$I = \int_{r=x-R}^{r=x+R} L(r)F(r)dr$$

where $L(r)$ is the length of the arc $\mathcal{L}(r)$ contained within $\mathcal{C}(x)$ of the circle centred at the origin, with radius r; we refer to this circle as $\mathcal{A}$. Then the end points of $\mathcal{L}(r)$ are $(r\cos\theta, r\sin\theta)$ and $(r\cos\theta, -r\sin\theta)$, the intersection points with $\mathcal{C}$ (Figure 5.7). Thus $L = 2\theta r$, where

$$\theta = \arccos\left(1 - (R^2 - (r-x)^2)/2xr\right)$$

$$\Rightarrow I = 2\int_{r=x-R}^{r=x+R} \arccos\left(1 - \frac{R^2-(r-x)^2}{2xr}\right) rF(r)dr.$$

Note that the size of 'island' in the initial conditions does not effect this calculation at all: all arc lengths are centred at the origin and calculated appropriately according to the size of R, with the largest $\mathcal{A}$ marking the boundary of our original domain; the cell types present within the integral are considered purely in F, and their presence or otherwise should not be confused with the integration described. In particular the circle $\mathcal{A}$, which is used to calculate arc lengths, should not be confused with 'island' size.

The arguments above only apply if $x > R$. If $x \leq R$, the origin $x = 0$ lies inside $\mathcal{C}$, and for sufficiently small r the entire circle $\mathcal{A}$ lies inside $\mathcal{C}$. At the transition point between arcs and circumferences, $\mathcal{C}$ and $\mathcal{A}$ touch, and the radius is given by $R - x$ (Figure 5.7). Then

$$I = 2\int_{r=0}^{r=R-x} \pi rF(r)dr + 2\int_{r=R-x}^{r=x+R} \arccos\left(1 - \frac{R^2-(r-x)^2}{2xr}\right) rF(r)dr.$$

A simple test of the formulae above is given by considering $F = 1$, in which case $I = \pi R^2$. For $R = 1$, we found that in order for the one-dimensional formulae to give the answer π correct to 3 significant figures, we must set the spatial discretisation to $\delta x = 0.01$. The computational speed-up arising from the one-dimensional formulae is considerable. A typical simulation required for Figure 11 takes several hours in two dimensions but only 1 to 2 minutes in one dimension at the same accuracy level (for a 3.2GHz processor with 4096 megabytes of memory).

Chapter 6

Discussion

The investigations in this thesis explore how interactions between two cell populations and their local environment can affect the types of patterning produced by those cell populations. We have found that in cell renewal and cell differentiation, the type of interaction that takes place within a cell's local environment greatly affects the patterning produced, with a community effect-type mechanism leading to the production of clear stripe patterns, and a linear mechanism leading to no patterns. When considering local environment-mediated cell migration on the other hand, we found that the attraction or repulsion between cells dictates the kind of patterning seen. In cases of attraction, we always see stripes, whereas repulsion leads to a variety of patterning behaviours.

In Chapter 2, we showed that small changes in the type of interaction that cells have with their local cellular environment can lead to very different outcomes for the composition of mosaic tissues, and we investigated differing hypotheses regarding the patterning seen in some mosaics of organ development. Our results suggest that the variation in patterns seen in organ parenchymas may be driven purely by the process of cell replacement, with different interaction scenarios creating different patterns.

Such a proposal could be tested by the use of flourescent marking, which would allow one to track individual cells *in vitro* in order to see whether or not they renew via the mechanism predicted by our model. If they do not, we could extend the model to investigate other hypotheses, such as one that proposes that both cell renewal and directed migration create the patterns witnessed. Beyond this, extending the model to incorporate growth and proliferation would be particularly helpful in the exploration of developmental mosaics, where growth is obviously an important factor. A three dimensional model would also be useful here.

In Chapter 3, we adapted the model to explore cellular differentiation. We found that pattern formation only occurs when differentiation is regulated by a strong community effect. In this case, permanent spatial patterns only occur under a precise relationship between the parameters characterising cell dynamics, although transient patterns can persist for biologically relevant timescales when this conditon is relaxed. In all cases, the long lived patterns consist only of stripes, not spots.

Such a restriction on the parameter values for which patterns are seen could be used to verify the model mechanism in applications. Working with experimentalists, precise values could be obtained for a number of parameters. These could then be used to discover if the patterning mechanism of a strong community effect is likely to be the mechanism behind the patterns being investigated or not, thus falsifying biological hypotheses. Such a procedure was carried out in Chapter 3 for zebrafish, and it is clear that this could be repeated for other suitable applications.

Finally, in Chapter 4 we moved on to consider the role of cell migration in tissue patterning. Here we created a general model that explored both the attractive and repulsive forces that occur between cells and that generate movement. As different cell types have different affinities to one another, their interactions can produce patterning. We see stable stipes, oscillations, travelling waves and breathing stripes, showing that this model mechanism for migration can produce a range of patterning behaviours.

An obvious area for future work here is to look at two dimensional patterning. This would allow us to see if spots or spirals can be generated by the model. It would also allow for a clear application of the model to biological processes, as certainly patterning that develops on the skin's surface can be modelled as a monolayer, and the vast majority of biological scenarios are in two or three dimensions. Some specific applications for both a two dimensional and three dimensional version of the model that could be looked at include: pigmentation patterning in fish, amphibians and mammals; swarming patterns in animal migration systems; aggregations of bacteria in quorum sensing.

In conclusion, the studies in this thesis have tested hypotheses for the mechanisms that control patterning in mosaic tissues and in skin pigmentation in zebrafish, leading to the rejection of the community effect hypothesis in the latter and support for the proliferation hypothesis in the former. Empirical studies must now be undertaken to confirm or refute our results. Furthermore, the work in Chapter 4 in this thesis has led to the creation of a non-local cell migration model that it is hoped will be used to investigate numerous migration scenarios and hence provide clear insights into complex biological systems.

Bibliography

[1] B. Alberts, A. Johnson, J. Lewis, M. Raff, K. Roberts, and P. Walter. *Molecular Biology of the Cell*. Garland Science, Fifth edition, 2008.

[2] N. D. Alikakos, X. Chen, and G. Fusco. Motion of a droplet by surface tension along the boundary. *Calculus of Variations and P.D.E.s*, 11(3):233–305, 2000.

[3] S. M. Allen and J. W. Cahn. A microscopic theory for antiphase boundary motion and its application to antiphase domain coarsening. *Acta Metallurgica*, 27(6):1085–1095, 1979.

[4] A. R. A. Anderson, M. A. J. Chaplain, and A. Rejniak Katarzyna. *Single-cell-based models in biology and medicine*. Springer, 2007.

[5] N. Armstrong. *Continuum modelling of cell-cell adhesion*. Heriot Watt University, 2007.

[6] N. J. Armstrong, K. J. Painter, and J. A. Sherratt. A continuum approach to modelling cell-cell adnesion. *Journal of Theoretical Biology*, 243:98–113, 2006.

[7] N. J. Armstrong, K. J. Painter, and J. A. Sherratt. Adding Adhesion to a Chemical Signaling Model for Somite Formation. *Bulletin of Mathematical Biology*, 71(1):1–24, 2009.

[8] A. Asplund, Z. Guo, X. Hu, C. Wassberg, and F. Ponten. Mosaic pattern of maternal and paternal keratinocyte clones in normal human epidermis revelaed by analysis of x-chromosome inactivation. *The Journal of Investigative Dermatology*, 117(1):128–131, 2001.

[9] S. Atkinson and P. Williams. Quorum sensing and social networking in the microbial world. *Journal of the Royal Society Interface*, 6:959–978, 2009.

[10] G. Aubin-Houzelstein, F. Bernex, C. Elbaz, and J. J. Panthier. Survival of patchwork melanoblasts is dependent upon their number in the hair follicle at the end of embryogenesis. *Developmental Biology*, 198:266–276, 1998.

[11] A. L. Bauer, T. L. Jackson, and Y. Jiang. A cell-based model exhibiting branching and anastomosis during tumor-induced angiogenesis. *Biophysical Journal*, 92(9):3105 – 3121, 2007.

[12] J. M. Bloomfield, K. J. Painter, and J. A. Sherratt. How does cellular contact affect differentiation mediated pattern formation? *Bull. Math. Bio.*, 73:1529–1558, 2011.

[13] J. M. Bloomfield, J. A. Sherratt, K. J. Painter, and G. Landini. Cellular automata and integrodifferential equation models for cell renewal in mosaic tissues. *Journal of the Royal Society Interface*, 7:1525–1535, 2010.

[14] A. J. Bray. Theory of phase-ordering kinetics. *Advances in Physics*, 43(3):357–459, 1994.

[15] L. Bronsard and R. V. Kohn. Motion by mean curvature as the singular limit of Ginzburg-Landau dynamics. *Journal of Differential Equations*, 90:211–237, 1991.

[16] M. Buckingham. How the community effect orchestrates muscle differentiation. *Bioessays*, 25:13–16, 2003.

[17] H. M. Byrne and M. A. J. Chaplain. Modelling the role of cell-cell adhesion in the growth and development of carcinomas. *Mathematical and Computer Modelling*, 24(12):1–17, 1996.

[18] C. E. Caicedo-Carvajal and T. Shinbrot. In silico zebrafish pattern formation. *Developmental Biology*, 315(2):397–403, 2008.

[19] C. Carmona-Fontaine, H. K. Matthews, S. Kuriyama, M. Moreno, G. A. Dunn, M. Parsons, C. D. Stern, and R. Mayor. Contact inhibition of locomotion in vivo controls neural crest directional migration. *Nature*, 456(5):957–61, 2008.

[20] J. Carr and R. Pego. Metastable patterns in solutions of $u_t = \epsilon u_{xx} - f(u)$. *Communications on Pure and Applied Mathematics*, 42:523–576, 1989.

[21] J. Carr and R. Pego. Invariant manifolds for metastable patterns in $u_t = \epsilon u_{xx} - f(u)$. *Proceedings of the Royal Society of Edinburgh*, 116A:133–160, 1990.

[22] G. Casten and J. Holland. Instability results for reaction diffusion equations with neumann boundary conditions. *Journal of Differential Equations*, 27:266–273, 1978.

[23] M. A. J. Chaplain. Avascular growth, angiogenesis and vascular growth in solid tumours: The mathematical modelling of the stages of tumour development. *Mathematical and Computer Modelling*, 23(6):47–87, 1996.

[24] X. Chen, J. Guo, F. Hamel, H. Ninomiya, and J. Roquejoffre. Traveling waves with paraboloid like interfaces for balanced bistable dynamics. *Ann.I.H.Poincare*, 24:369–393, 2007.

[25] X. Chen, J. Guo, and H. Ninomiya. Entire solutions of reaction-diffusion equations with balaced bistable nonlinearities. *Proceedings of the Royal Society of Edinburgh*, 136A:1207–1237, 2006.

[26] X. Chen, D. Hilhorst, and E. Logak. Asymptotic behavior of solutions of an allen-cahn equation with a nonlocal term. *Nonlinear Analysis*, 28(7):1283–1298, 1997.

[27] G. Cossu, R. Kelly, S. Di Donna, E. Vivarelli, and M. Buckingham. Myoblast differentiation during mammalian somitogenesis is dependent upon a community effect. *Proceedings of the National Academy of Sciences of the United States of America*, 92(6):2254–2258, 1995.

[28] J. T. Cox and R. Durrett. *Random walks, Brownian motion, and interacting particle systems*, chapter Nonlinear Voter Models. Birkhäuser, 1991.

[29] J. T. Cox and D. Griffeath. Diffusive clustering in the two dimensional voter model. *Annals of Probability*, 14(2):347–370, 1986.

[30] V. Cristini, J. Lowengrub, and Q. Nie. Nonlinear simulation of tumor growth. *Journal of Mathematical Biology*, 46:191–224, 2003.

[31] G.T. Dee and W. van Saarlos. Bistable systems with propagating fronts leading to pattern formation. *Physical Review Letters*, 60(25):2641–2644, 1988.

[32] A. Deutsch and S. Dormann. *Cellular Automaton Modelling of Biological Pattern Formation*. Birkhauser, 2005.

[33] I. Dornic, H. Chaté, J. Chave, and H. Hinrichsen. Critical coarsening without surface tension: The universality class of the voter model. *Physical Review Letters*, 87(4):045701, 2001.

[34] D. B. Duncan, M. Grinfeld, and I. Stoleriu. Coarsening in an integro-differential model of phase transitions. *European Journal of Applied Mathematics*, 11:561–572, 2000.

[35] J.P. Eckmann and J. Rougemont. Coarsening by Ginzberg-Landau dynamics. *Communications in Mathematical Physics*, 199:441–470, 1998.

[36] R. Eftimie, G. de Vries, and M. Lewis. Weakly nonlinear analysis of a hyperbolic model for animal group formation. *Journal of Mathematical Biology*, 59:37–74, 2009.

[37] R. Eftimie, G. de Vries, M. Lewis, and F. Lutscher. Modeling group formation and activity patterns in self-organizing collectives of individuals. *Bulletin of Mathematical Biology*, 69:1537–1565, 2007.

[38] R. Eftimie, G. de Vries, and M. A. Lewis. Complex spatial group patterns result from different animal communication mechanisms. *Proceedings of the National Academy of Sciences*, 104(17):6974–6979, 2007.

[39] H. B. Frieboes, Xiaoming Z., Chung-Ho S., Bruce T., Robert G., and Vittorio C. An Integrated Computational/Experimental Model of Tumor Invasion. *Cancer Research*, 66(3):1597–1604, 2006.

[40] G. Fusco and J. K. Hale. Slow-motion manifolds, dormant instability, and singular perturbations. *Journal of Dynamics and Differential Equations*, 1(1):75–94, 1989.

[41] J. Galle, G. Aust, G. Schaller, T. Beyer, and D. Drasdo. Individual cell-based models of the spatial-temporal organization of multicellular systemsachievements and limitations. *Cytometry Part A*, 69A(7):704–710, 2006.

[42] R. Galli, U. Borello, A. Gritti, M. G. Minasi, C. Bjornson, M. Coletta, M. Mora, M. G. De Angelis, R. Fiocco, G. Cossu, and A. L. Vescovi. Skeletal myogenic potential of human and mouse neural stem cells. *Nature Neuroscience*, 3:986–991, 2000.

[43] A. Gerisch. On the approximation and efficient evaluation of integral terms in pde models of cell adhesion, in preparation. *IMA Journal of Numerical Analysis*, 30:173–194, 2010.

[44] A. Gerisch and M. A. J. Chaplain. Robust numerical methods for taxis-diffusion-reaction systems: Applications to biomedical problems. *Mathematical and Computer Modelling*, pages 49–75, 2006.

[45] A. Gerisch and M.A.J. Chaplain. Mathematical modelling of cancer cell invasion of tissue: Local and non-local models and the effect of adhesion. *Journal of Theoretical Biology*, 250(4):684 –704, 2008.

[46] A. Gerisch and K. J. Painter. *Cell Mechanics: From Single Scale-Based Models to Multiscale Modeling*. CRC Press, 2010.

[47] S. F. Gilbert. *Developmental Biology*. Sinauer Associates Inc., Ninth edition, 2010.

[48] J. A. Glazier and F. Graner. Simulation of the differential adhesion driven rearrangement of biological cells. *Physical Review E*, 47:2128–2154, 1993.

[49] B. Graham and A. van Ooyen. Mathematical modelling and numerical simulation of the morphological development of neurons. *BMC Neuroscience*, 7(Suppl 1):S9, 2006.

[50] F. Graner and J. A. Glazier. Simulation of biological cell sorting using a two-dimensional extended potts model. *Phys. Rev. Lett.*, 69(13):2013–2016, 1992.

[51] C. P. Grant. Grain sizes in the discrete Allen-Cahn andCahn-Hilliard equations. *Discrete and Continuous Dynamical Systems*, 1(1):1–33, 2000.

[52] C. P. Grant. Superabudance of stationary solutions for the discrete Allen-Cahn equation. *Dynamics of Continuous, Discrete and Impulsive Systems*, pages 71–92, 2001.

[53] C. P. Grant and E. S. Van Vleck. Slowly-migrating transition layers for the discrete Allen-Cahn and Cahn-Hilliard equations. *Nonlinearity*, 8:861–876, 1995.

[54] J.E.F. Green, S.L. Waters, J.P. Whiteley, L. Edelstein-Keshet, K.M. Shakesheff, and H.M. Byrne. Non-local models for the formation of hepatocyte-stellate cell aggregates. *Journal of Theoretical Biology*, 267(1):106–120, 2010.

[55] J. B. Gurdon. A community effect in animal development. *Nature*, 336:772–774, 1988.

[56] J. B. Gurdon, P. Lemaire, and K. Kato. Community effects and related phenomena in development. *Cell*, 75:831–834, 1993.

[57] J. B. Gurdon, E. Tiller, J. Roberts, and K. Kato. A community effect in muscle development. *Current Biology*, 3:1–11, 1993.

[58] S. V. Gurevich, Sh. Amiranashvili, and H.-G. Purwins. Breathing dissipative solitons in three-component reaction-diffusion system. *Phys. Rev. E*, 74(6):066201, 2006.

[59] R. Happle. X-chromosome inactivation: role in skin disease expression. *Acta Paediatrica*, 95:16–23, 2006.

[60] T. Hillen and K. J. Painter. A user's guide to PDE models for chemotaxis. *Journal of Matematical Biology*, 58:183–217, 2009.

[61] K. A. Hultman and S. L. Johnson. Differential contribution of direct-developing and stem cell-derived melanocytes to the zebrafish larval pigment pattern. *Dev. Biol.*, 337(2), 2010.

[62] V. Hutson and M. Grinfeld. Non-local dispersal and bistability. *European Journal of Applied Mathematics*, 17:221–232, 2006.

[63] P. Iannaccone, S. Morley, T. Skimina, J. Mullins, and G. Landini. Cord-like mosaic patches in the adrenal cortex are fractal: Implications for growth and development. *FASEB*, 2002.

[64] P. M. Iannaccone and W. C. Weinberg. The histogenesis of the rat adrenal cortex: A study based on histological analysis of mosaic pattern in chimeras. *The Journal of Experimental Zoology*, 243(2):217–223, 1987.

[65] D. Iron, T. Kolokolonikov, J. Rumsey, and J. Wei. Stability of curved interfaces in the perturbed two-dimensional allen–cahn system. *SIAM Journal on Applied Mathematics*, 69(5):1228–1243, 2009.

[66] M. C. Jorge, A. A. Minzoni, and C. A. Vargas. Influence of corner layers in the variational determination of bubble solutions of the constrained allen-cahn equation. *European Journal of Applied Mathematics*, 19:561–574, 2008.

[67] T. Kaneko, K. Kojima, and K. Yasuda. Dependence of the community effect of cultured cardiomyocytes on the cell network pattern. *Biochemical and Biophysical Research Communications*, 356(2):494–498, 2007.

[68] K. Kato and J. B. Gurdon. Single-cell transplantation determines the time when Xenopus muscle precursor cells acquire a capacity for autonomous differentiation. *Proceedings of the National Acadamy of Sciences of the United States of America*, 90:1310–1314, 1993.

[69] M. K. Khokha, G. Landini, and P. M. Iannaccone. Fractal geometry in rat chimeras demonstrates that a repetitive cell division program may generate liver parenchyma. *Developmental Biology*, 165:545–555, 1994.

[70] D. Kim, S. Chi, K. H. Lee, S. Rhee, Y. K. Kwon, C. H. Chung, H. Kwon, and M. S. Kang. Neuregulin stimulates myogenic differentiation in an autocrine manner. *Journal of Biolical Chemistry*, 274:15395–15400, 1999.

[71] K. Kojima, T. Kaneko, and K. Yasuda. Role of the community effect of cardiomyocyte in the entrainment and reestablishment of stable beating rhythms. *Biochemical and Biophysical Research Communications*, 351(1):209–215, 2006.

[72] S. Kondo, M. Iwashita, and M. Yamaguchi. How animals get their skin patterns: fish pigment pattern as a live Turing wave. *International Journal of Developmental Biology*, 53:851–856, 2009.

[73] G. Landini and P. M. Iannaccone. Modelling of mosaic paterns in chimeric liver and adrenal cortex: algorithmic organogenesis? *FASEB*, 14:823–827, 2000.

[74] S. J. Landy and D. Donnai. Incontinentia pigmenti (bloch-sulzberger syndrome). *Journal of Medical Genetics*, 30:53–59, 1993.

[75] T. M. Liggett. *Interacting Particle Systems*, chapter The Voter Model. Springer-Verlag, 1985.

[76] M. Lyon. Gene action in the x-chromosome of the mouse. *Nature*, 190:372–373, 1961.

[77] P. Macklin and J. Lowengrub. Nonlinear simulation of the effect of microenvironment on tumor growth. *Journal of Theoretical Biology*, 245:677–704, 2007.

[78] F. Maderspacher and C. Nusslein-Volhard. Formation of the adult pigment pattern in zebrafish requires leopard and obelix dependent cell interactions. *Development*, 130(15):3447–3457, 2003.

[79] H. Matano. Asymptotic behaviour and stability of solutions of semilinear diffusion equations. *Publ. Res. Inst. Math. Sci.*, 15:401–454, 1979.

[80] A. Mogilner and L. Edelstein-Keshet. A non-local model for a swarm. *Journal of Mathematical Biology*, 38:534–570, 1999.

[81] N. A. M. Monk. The community effect and ectoderm-mesoderm interaction in Xenopus muscle differentiation. *Bulletin of Mathematical Biology*, 59(3):409–425, 1997.

[82] J. Moreira and A. Deutsch. Pigment pattern formation in zebrafish during late larval stages: A model based on local interactions. *Developmental Dynamics*, 232(1):33–42, 2005.

[83] Y. Morita and Y. Mimoto. Colision and collapse of layers in a 1d scalar reaction-diffusion equation. *Physica D*, 140:151–170, 2000.

[84] S. D. Morley, I. Viard, B. Chung, Y. Ikeda, K. L. Parker, and J. J. Mullins. Variegated expression of a mouse steroid 21-hydroxylase/beta-galactosidase transgene suggests centripetal migration of adrenocortical cells. *Molecular Endocrinology*, 10(5):585–598, 1996.

[85] K. W. Morton and D. F. Mayers. *Numerical Solution of Partial Differential Equations*. Cambridge University Press, 1994.

[86] J. D. Murray. *Mathematical Biology*, volume 1. Springer, third edition, 2002.

[87] T. Nagai, S. Otani, T. Saito, S. Maegawa, K. Inoue, K. Arai, and E. Yamaha. Germ-line chimera produced by blastoderm transplantation in zebrafish. *Nippon Suisan Gakkaishi*, 71(1):1–9, 2005.

[88] C. L. Nehaniv. Asynchronous automata networks can emulate any synchronous automata network. *International Journal of Algebra and Computation*, 2004.

[89] Y. K. Ng and P. M. Iannaccone. Experimental chimeras: current concepts and controversies in normal development and pathogenesis. *Current Topics in Developmental Biology*, 27:235–274, 1992.

[90] P. D. Nieuwkoop. Short historical survey of pattern formation in the endo-mesoderm and the neural anlage in the vertebrates: the role of vertical and planar inductive actions. *Cellular and Molecular Life Sciences*, 53:305–318, 1997.

[91] M. R. Owen, J. A. Sherratt, and S. R. Myers. How far can a juxtacrine signal travel? *Proceedings of the Royal Society of London Series B - Biological Sciences*, 266(1419):579–585, 1999.

[92] K. Painter. Continuous models for cell migration in tissues andapplications to cell sorting via differential chemotaxis. *Bulletin of Mathematical Biology*, 71:1117–1147, 2009.

[93] K. J. Painter, N. J. Armstrong, and J. A. Sherratt. The impact of adhesion on cellular invasion processes in cancer and development. *Journal of Theoretical Biology*, 264, 2010.

[94] C. Paratore, L. Hagedorn, J. Floris, L. Hari, M. Kleber, U. Suter, and L. Sommer. Cell-intrinsic and cell-extrinsic cues regulating lineage decisions in multipotent neural crest-derived progenitor cells. *International Journal of Developmental Biology*, 46(1, Sp. Iss. SI):193–200, 2002.

[95] D. M. Parichy. Homology and the evolution of novelty during Danio adult pigment pattern development. *Journal of Experimental Zoology Part B - Molecular and Developmental Evolution*, 308B(5):578–590, 2007.

[96] D. M. Parichy, D. G. Ransom, B. Paw, L. I. Zon, and S. L. Johnson. An orthologue of the kit-related gene fms is required for development of neural crest-derived xanthophores and a subpopulation of adult melanocytes in the zebrafish, Danio rerio. *Development*, 127:3031–3044, 2000.

[97] A. J. Perumpanani, J. A. Sherratt, J. Norbury, and H. M. Byrne. Biological inferences from a mathematical model for malignant invasion. *Invasion and Metastasis*, 16:209–221, 1996.

[98] A. Poliakov, M. Cotrina, and D. G. Wilkinson. Diverse roles of eph receptors and ephrins in the regulation of cell migration and tissue assembly. *Developmental Cell*, 7(4):465–480, 2004.

[99] I. K. Quigley and D. M. Parichy. Pigment pattern formation in zebrafish: A model for developmental genetics and the evolution of form. *Microscopy Research and Technique*, 58:442–455, 2002.

[100] J. F. Rawls and S. L. Johnson. Zebrafish kit mutation reveals primary and secondary regulation of melanocyte development during fin stripe regeneration. *Development*, 127(17):3715–3724, 2000.

[101] P. Rørth. Collective cell migration. *Cell and Developmental Biology*, 25:407–429, 2009.

[102] H. G. Rotstein, I. Mitkov, A. M. Zhabotinsky, and I. R. Epstein. Dynamics of kinks in one- and two-dimensional hyperbolic models with quasidiscrete nonlinearities. *Physical Review E*, 63(6):066613, 2001.

[103] J. Rougemont. Dynamics of kinks in the Ginzberg-Landau equation: approach to a metastable shape and collapse of embedded pairs of kinks. *Nonlinearity*, 12:539–554, 1999.

[104] J. Rougemont. Evaporation of droplets in the two-dimensional Ginzberg-Landau equation. *Physica D*, 140:267–282, 2000.

[105] J. Rubinstein and P. Sternberg. Nonlocal reaction–diffusion equations and nucleation. *IMA Journal of Applied Mathematics*, 48(3):249–264, 1992.

[106] J. Rubinstein, P. Sternberg, and J. B. Keller. Fast reaction, slow diffusion, and curve shortening. *SIAM Journal on Applied Mathematics*, 49(1):116–133, 1989.

[107] I. Salazar-Ciudad, J. Jernvall, and S. A. Newman. Mechanisms of pattern formation in development and evolution. *Development*, 130:2027–2037, 2003.

[108] B. Sandstede. Stability of travelling waves. In B Fiedler, editor, *Handbook of Dynamical Systems II*, pages 983–1055. North-Holland, 2002.

[109] R. A. Satnoianu and M. Menzinger. A general mechanism for 'inexact' phase differences in reaction-diffusion-advection systems. *Physics Letters A*, 304(5-6):149–156, 2002.

[110] N. J. Savill and J. A. Sherratt. Control of epidermal stem cell clusters by notch-mediated lateral induction. *Developmental Biology*, 258(1):141 – 153, 2003.

[111] B. Schönfisch and A. de Roos. Synchronous and asynchronous updating in cellular automata. *BioSystems*, 51:123–143, 1999.

[112] T. Sekimura, M. Zhu, J. Cook, P. K. Maini, and J. D. Murray. Pattern formation of scale cells in lepidoptera by differential origin-dependent cell adhesion. *Bulletin of Mathematical Biology*, 61:807–828, 1999.

[113] N. M. Sherer and W. Mothes. Cytonemes and tunneling nanotubules in cell-cell communication and viral pathogenesis. *Trends in Cell Biology*, 18(9):414–420, 2008.

[114] J. A. Sherratt, S. A. Gourley, N. J. Armstrong, and K. J. Painter. Boundedness of solutions of a non-local reaction-diffusion model for adhesion in cell aggregation and cancer invasion. *European Journal of Applied Mathematics*, 20(Part 1):123–144, 2009.

[115] T. Shinbrot. Simulated morphogenesis of developmental folds due to proliferative pressure. *Journal of Theoretical Biology*, 242(3):764–773, 2006.

[116] M. J. Simpson, K. A. Landman, B. D. Hughes, and D. F. Newgreen. Looking inside an invasion wave of cells using continuum models: Proliferation is the key. *Journal of Theoretical Biology*, 243:343–360, 2006.

[117] M. J. Simpson, A. Merrifield, K. A. Landman, and B. D. Hughes. Simulating invasion with cellular automata: Connecting cell-scale and population-scale properties. *Physical Review E*, 76, 2007.

[118] M. J. Simpson, D. C. Zhang, M. Mariani, K. A. Landman, and D. F. Newgreen. Cell proliferation drives neural crest cell invasion of the intestine. *Developmental Biology*, 302(553–568), 2007.

[119] D. Stafford, M.J. Ward, and B. Wetton. The dynamics of drops and attached interfaces for the constrained allen-cahn equation. *European Journal of Applied Mathematics*, 12:1–24, 2001.

[120] H. J. Standley, A. M. Zorn, and J. B. Gurdon. eFGF and its mode of action in the community effect during xenopus myogenesis. *Development*, 128(8):1347–1357, 2001.

[121] M. S. Steinberg. Mechanism of tissue reconstruction by dissociated cells, ii. time course of events. *Science*, 137:762–763, 1962a.

[122] M. S. Steinberg. On the mechanism of tissue reconstruction by dis- sociated cells, i. population kinetics, differential adhesiveness, and the absence of directed migration. *Proceedings of the National Academy of Science U.S.A.*, 48:1577–1582, 1962b.

[123] M. S. Steinberg. On the mechanism of tissue reconstruction by dis- sociated cells, iii. free energy relations and the reorganization of fused, heteronomic tissue fragments. *Proceedings of the National Academy of Science U.S.A.*, 48:1769–1776, 1962c.

[124] M. S. Steinberg. Reconstruction of tissues by dissociated cells. *Science*, 141(3579):401–408, 1963.

[125] M. S. Steinberg. Differential adhesion in morphogenesis: a modern view. *Current Opinion in Genetics and Development*, 17:281–286, 2007.

[126] A. M. Stuart and A. R. Humphries. *Dynamical Systems and Numerical Analysis*. Cambridge University Press, 1996.

[127] C. Topaz and A. L. Bertozzi. Swarming patterns in a two-dimensional kinematic model for biological groups. *SIAM Journal on Applied Mathematics*, 65:152–174, 2004.

[128] R. P. Tucker and C. A. Erickson. The control of pigment cell pattern formation in the California newt, *Taricha torosa*. *Journal of Embryology and Experimental Morphology*, 97:141–168, 1986.

[129] S. Turner and J. A. Sherratt. Intercellular adhesion and cancer invasion: A discrete simulation using the extended potts model. *Journal of Theoretical Biology*, 216(1):85 – 100, 2002.

[130] V. K. Vanag and I. R. Epstein. Localized patterns in reaction-diffusion systems. *Chaos*, 17(3):037110 (11 pages), 2007.

[131] M. J. Ward. Metastable patterns, layer collapses, and coarsening for a one-dimensional Ginzburg-Landau equation. *Studies in Applied Mathematics*, 91(1):51–93, 1994.

[132] M. J. Ward. Metastable bubble solutions for the Allen-Cahn equation with mass conservation. *SIAM Journal on Applied Mathematics*, 56(5):1247–1279, 1996.

[133] F. M. Watt, C. Lo Celso, and V. Silva-Vargas. Epidermal stem cells: an update. *Current Opinion in Genetic Development*, 16:518–524, 2006.

[134] S. D. Webb and M. R. Owen. Intra-membrane ligand diffusion and cell shape modulate juxtacrine patterning. *Journal of Theoretical Biology*, 230:99–117, 2004.

[135] R. Weiner, B.A. Schmitt, and H. Podhaisky. ROWMAP - a ROW-code with Krylov techniques for large stiff ODEs. *Applied Numerical Math*, 25:303–319, 1997.

[136] J. D. West. 2 insights into development and genetics from mouse chimeras. volume 44 of *Current Topics in Developmental Biology*, pages 21–66. Academic Press, 1998.

[137] M. J. D. Weston, K. Kato, and J. B. Gurdon. A community effect is required for amphibian notochord differentiation. *Development Genes and Evolution*, 203(5):250–253, 1994.

[138] L. Wolpert, R. Beddington, T. Jessell, P. Lawrence, E. Meyerowitz, and J. Smith. *Principles of Development*. Oxford University Press, Second edition, 2004.

[139] H. Yagisita. Backward global solutions characterizing annihilation dynamics of traveling fronts. *Publications of the Research Institue for Mathematical Sciences*, 39:117–164, 2002.

[140] M. Yamaguchi, E. Yoshimoto, and S. Kondo. Pattern regulation in the stripe of zebrafish suggests an underlying dynamic and autonomous mechanism. *Proceedings of the National Acadamy of Sciences of the United States of America*, 104(12):4790–4793, 2007.

[141] H. Yang, P. Jensen, and D. Goldowitz. The Community Effect and Purkinje Cell Migration in the Cerebellar Cortex: Analysis of Scrambler Chimeric Mice. *Journal of Neuroscience*, 22(2):464–470, 2002.

[142] W. Zhong. Timing cell-fate determination during asymmetric cell divisions. *Current Opinion in Neurobiology*, 18:472–478, 2008.